This is to certify that the
dissertation entitled

PURIFICATION, KINETIC ANALYSIS, AND SPECTROSCOPIC CHARACTERIZATION OF WILD-TYPE *Aspergillus nidulans* XANTHINE HYDROXYLASE AND SELECTED VARIANTS

presented by

Meng Li

has been accepted towards fulfillment
of the requirements for the

PhD degree in CHEMISTRY

Robert A. Rousseau
Major Professor's Signature

8/17/07
Date

PURIFICATION, KINETIC ANALYSIS, AND SPECTROSCOPIC CHARACTERIZATION OF WILD-TYPE *Aspergillus nidulans* XANTHINE HYDROXYLASE AND SELECTED VARIANTS

By

Meng Li

A DISSERTATION

Submitted to
Michigan State University
In partial fulfillment of the requirements
For the degree of

DOCTOR OF PHILOSOPHY

Department of Chemistry

2007

ABSTRACT

PURIFICATION, KINETIC ANALYSIS, AND SPECTROSCOPIC CHARACTERIZATION OF WILD-TYPE *Aspergillus nidulans* XANTHINE HYDROXYLASE AND SELECTED VARIANTS

By

Meng Li

Xanthine hydroxylase (XanA) is the first member in the Fe(II)/α-ketoglutarate dependent dioxygenase superfamily to catalyze the hydroxylation of a purine base. His_6-tagged XanA of *Aspergillus nidulans* was purified from both the fungal mycelium and recombinant *Escherichia coli* cells. Comparison studies revealed very different quaternary structures and posttranslational modifications; however, the kinetic properties of XanA purified from both hosts are very similar. Extensive kinetic studies were carried out for His_6-tagged XanA isolated from bacterial host. The enzyme exhibits no significant isotope effect when using 8-^{2}H-xanthine whereas it demonstrates a two-fold solvent isotope effect. XanA is Fe(II)-specific and has high selectivity for substrates. A homology model of XanA was generated on the basis of the structure of the related enzyme taurine/αKG dioxygenase (TauD). The putative active site residues were mutated to alanine, and the variants were purified and kinetically characterized by using native substrate and chemical analogues. The three mutants of the predicted metal ligands showed an increased K_d of Fe(II), H149A and D151A are completely inactive and H340A exhibited only trace amount of activity. Asn358 is crucial for catalysis. The Q356A and N358A variants had significantly increased K_i^{app} over control protein for 6,8-DHP, suggesting that Gln356 and Asn358

hydrogen bond with the C-6 hydroxyl group of substrate. The E137A and D138A variants demonstrated enhanced activity with 9-methylxanthine, consistent with Glu137 and Asp138 being proximal to N-9 of substrate. Based on the extensive kinetic studies and the homology model, a preliminary xanthine binding mode was proposed and this is the first step to understand substrate binding for XanA when an enzyme crystal structure is not available. Electronic spectroscopy and one- and two-dimensional electron spin echo envelope modulation (ESEEM) experiments have been used to study the coordination chemistry at the nitric oxide (NO)-bound non-heme Fe(II) sites of XanA and TauD. Electron paramagnetic resonance (EPR) spectra indicated the electronic environment perturbation of the $\{FeNO\}^7$ center were perturbed after addition of primary substrate for both enzymes. ESEEM and HYSCORE (hyperfine sublevel correlation spectroscopy) detected hyperfine couplings from ^1H and ^{14}N nuclei in different protein complexes, and XanA exhibited patterns very similar to TauD. Interestingly, a new coupling coming from a non-exchangeable ^1H approximately 3.2 Å from the metal ion of TauD was detected in the NO-bound ternary complex. A particular residue from the enzyme probably contributes to this signal and one candidate, Trp248, was examined by analysis of the W248F variant. This study represents the first biochemical characterization of purified xanthine/αKG dioxygenase. It suggests the substrate binding mode through mutagenesis studies, it provides the first spectroscopic information for this enzyme, and it yields insights into the coordination properties of Fe(II) in this protein.

To my dearest father, mother
&
Beloved husband

ACKNOWLEDGMENTS

I would not have been able to complete a PhD without the aid and support of countless people over the past five years. I must first express my deepest gratitude towards my advisor, Prof. Robert Hausinger, for his guidance, encouragement and continuous support through the course of my work. The extensive knowledge, vision, and creative thinking of Dr. Hausinger have always been the source of inspiration for me. Also, I would like to thank Prof. Joan Broderick who had been an excellent advisor and great teacher to me for the first three years of my PhD.

I would like to thank many people for their help during my studies: Prof. Claudio Scazzocchio and his graduate student Gabriela M. Montero-Moran initiated this project and provided the *xanA* gene. Prof. John McCracken assisted with EPR and ESEEM analyses and performed the HYSCORE simulations. Prof. Michael Feig and Andrew W. Stumpff-Kane constructed the homology model. Prof. David J. Lowe and Fabrice Jourdan synthesized the 8-hydroxypurine, 2,8-dihydroxypurine and 6,8-dihydroxypurine. Christine Drevet provided the alignment figure of XanA with putative orthologous sequences from several fungi. Dr. Tina Müller constructed the XanA variants and carried out ferroxidase assays. Efhalia Kalliri and Dr. Piotr Grzyska provided wild-type and W248F TauD samples. Prof. James Geiger provided a model of NO-bound TauD. J. C. Price and Prof. Marty Bollinger provided deuterium-labeled taurine. Prof. Nicholas Burzlaff provided NOG. Dr. Rajendra Bose

Muthukumaran initiated the HYSCORE studies. Prof. Dan Jones provided mass spectrometry assistance.

I also thank the many graduate and undergraduate students I have worked with in Prof. Hausinger's group: Jana, Kim, Piotr, Scott, Soledad, Thalia, Tina, Aaron, Andrea, Bruce, Kimberly, Melody and Rachel. The friendly and supportive atmosphere inherent to the whole group contributed essentially to the final outcome of my studies. I wish to thank Bruce in particular who has been a great help and assisted me during the mutagenesis study. They each helped make my time in the PhD program more fun and interesting.

Last but not least, I wish to thank my family who have always supported me, and my husband, Jihua, who always believes in me. I could not finish this long journey without you.

TABLE OF CONTENTS

LIST OF TABLES

CHAPTER 4

LIST OF FIGURES

(Images in this dissertation are presented in color.)

CHAPTER 1

CHAPTER 2

CHAPTER 3

CHAPTER 4

ABBREVIATIONS

αKG	α-Ketoglutarate
ABTS	2,2'-Azino-bis(3-ethylbenzthiazoline-6-sulfonic acid)
CAS	Clavaminate synthase
2,4-D	2,4-Dichlorophenol
DAOCS	Deacetoxycephalosporin C synthase
DEA/NO	Diethylammonium (Z)-1-(*N*,*N*-diethylamino)diazen-1-ium -1,2-diolate
2,8-DHP	2,8-Dihydroxypurine
6,8-DHP	6,8-Dihydroxypurine
DSBH	Double-stranded β-helix
DTNB	5,5'-Dithiobis(2-nitrobenzoic acid)
EPR	Electron paramagnetic resonance
ESEEM	Electron spin-echo envelope modulation
F3H	Flavanone 3β-hydroxylase
FIH	HIF-α-specific asparaginyl hydroxylases
HIF	Hypoxia –inducible factor
HPPD	4-Hydroxyphenylpyruvate dioxygenase
HYSCORE	Hyperfine sublevel correlation spectroscopy
IPNS	Isopenicillin N synthase
JHDM	JmjC domain-containing histone demethylase
LMCT	Ligand-to-metal charge-transfer

MLCT	Metal-to-ligand charge-transfer
Moco	Molybdopterin cofactor
NO	Nitric acid
NOG	*N*-oxalylglycine
NTA	Nitrilotriacetic acid
OPDA	*o*-Phenylenediamine
P3H	Proline 3-hydroxylase
P4H	Prolyl 4-hydroxylases
PNGase F	*N*-glycosidase F
SDS-PAGE	Sodium dodecyl sulfate-polyacrylamide gel electrophoresis
TauD	Taurine/αKG dioxygenase
TfdA	2.4-D dioxygenase
XAS	X-ray absorption spectroscopy
XanA	Xanthine/αKG dioxygenase.
XO	Xanthine oxidase

CHAPTER 1

INTRODUCTION

Fe(II)/α-KETOGLUTARATE-DEPENDENT HYDROXYLASES

Fe(II)/α-ketoglutarate (αKG)-dependent hydroxylases catalyze a wild range of reactions including protein side-chain modification (some of which are involved in transcriptional regulation), repair of alkylated DNA/RNA, biosynthesis of antibiotics and plant products, lipid metabolism, and synthesis or decomposition of a wide variety of small molecules (*1-13*). Structural studies reveal a conserved double-stranded β-helix (DSBH) core of this superfamily, also called a β-strand "jellyroll" structure. This conserved structure is responsible for binding the iron through three amino acid side chains in a His^1-X-Asp/Glu-X_n-His^2 motif (where n can range from 44 to over 150). In addition, the metal is bound by αKG using its C-1 carboxylate and C-2 keto groups. Binding of co-substrate and substrate triggers the ligation of dioxygen to metal, stimulates the oxidative decomposition of αKG to succinate and CO_2, and leads to the formation of a highly reactive Fe(IV)-oxo species which is proposed to hydroxylate the primary substrate. The overall reaction is illustrated in Figure 1.1. In this chapter, I briefly introduce several representatives of this superfamily of enzymes, including selected Fe(II)/αKG-dependent hydroxylases as well as others that are structurally or mechanistically related. I discuss the general structural and mechanistic features of these enzymes based on kinetic and spectroscopic studies. Finally, I provide an outline of my thesis to highlight the purpose of my studies.

FIGURE 1.1: General reaction of Fe(II)/αKG-dependent hydroxylases.

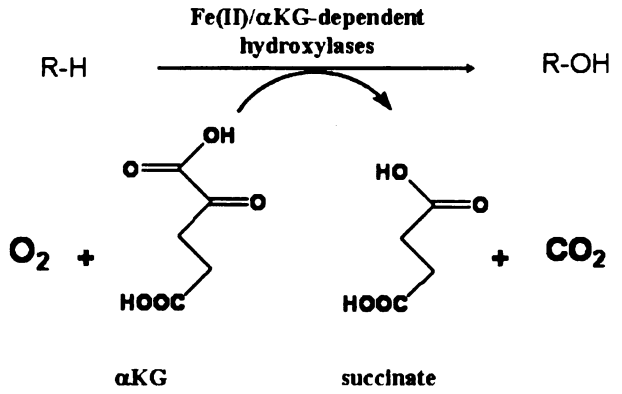

FIGURE 1.2: General reaction of prolyl 4-hydroxylases (P4H).

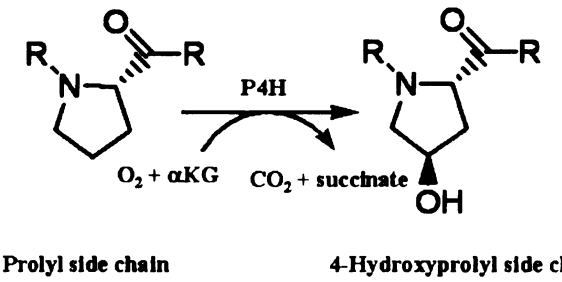

FIGURE 1.3: General reaction of HIF-α-specific asparaginyl hydroxylases (FIH).

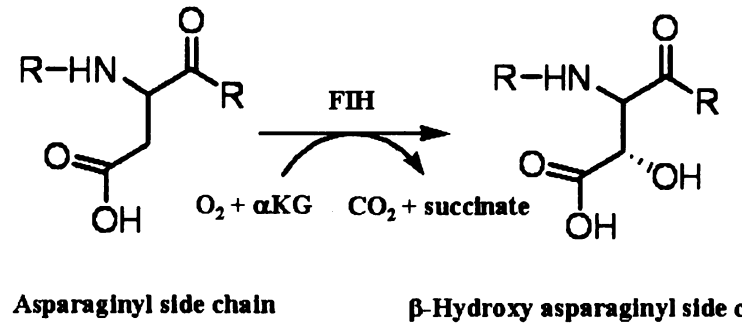

Protein Modification

Prolyl 4-hydroxylase

Prolyl 4-hydroxylase (P4H), the first Fe(II)/αKG-dependent hydroxylase identified (*14*), catalyzes the hydroxylation of proline residues to yield the trans-4-hydroxyprolyl group as shown in Figure 1.2. In mammals, P4H is the key enzyme in the biosynthesis of collagens (*2*), a family of extracellular matrix proteins, as 4-hydroxyproline residues are essential for the folding of the newly synthesized collagen polypeptide chains into triple-helical structure. The enzyme recognizes the Gly-X-Pro motif and about 10% of the Pro position is modified. P4H has also been isolated from plants (*15, 16*), where it hydroxylates proline-rich structural glycoproteins of the cell walls. Genes encoding P4H have been cloned from human, plant, insect, nematode, and other sources, including *Paramecium bursaria Chlorella* virus-1 (*15-20*). Generally, the protein is composed of two subunits, a catalytic subunit α, which contains separate catalytic and peptide substrate-binding domains, and a protein disulfide isomerase subunit, β, except for algal and plant enzymes which are identified as monomer (*15, 16*). His412, Asp414 and His483 were proposed to be the metal ligands for human enzyme via a mutagenesis study (*21, 22*), and αKG is thought to chelate the Fe(II) center in a bidentate fashion as described above with the C-5 carboxylate forming a salt bridge with Lys493. The peptide substrate-binding domain consisting of residues 144-244 of the human α subunit was crystallized and diffracted to at least 3Å (*23*), however, there is no complete structure reported since the catalytic domain was not included in the crystal.

Transcriptional Regulation

Prolyl hydroxylase domain-containing enzymes & Factor-inhibiting HIF

Fe(II)/αKG-dependent hydroxylases were known for decades to catalyze protein post-translational modifications (*24-26*), and included the prolyl, lysyl, and aspartyl(asparaginyl) hydroxylases. Recently, some representatives of these enzymes were shown to play a novel role involving regulation of the hypoxic response, one of the most important ways in which animals respond to reduced levels of dioxygen (*3, 4, 27-29*). Hypoxia –inducible factor (HIF) is an αβ heterodimeric transcription factor enabling the transcription of an array of genes that work to compensate for the effects of low oxygen tension. Under low oxygen condition, the HIF-α subunit translocates to the nucleus, dimerizes with HIF-β and together they recruit coactivators, such as p300, to initiate a transcriptional response. Under normal dioxygen concentraions, HIF-α is targeted for degradation by two independent pathways. One path involves hydroxylation of either Pro402 or Pro564 by HIF-α-specific prolyl hydroxylase domain-containing enzymes, using an oxygen, Fe(II), and αKG-dependent reaction (*3, 4, 30*). The hydroxylated HIF-α forms a complex with the von Hippel-Lindau tumor suppressor protein, elongin B, and elongin C, resulting in polyubiquitinylation and destruction of the transcription factor subunit. The other pathway involves hydroxylation at the *pro*-S position of the β-carbon of Asn803 in HIF-α through factor-inhibiting HIF (FIH) (*5, 31-33*) as shown in Figure 1.3, The action of this HIF-α-specific asparaginyl hydroxylase prevents interaction of HIF-α with the p300 transcription coactivator, thus repressing HIF transcriptional activity. An X-ray

crystallography study predicted that FIH is comprised of a β-strand jellyroll core with both Fe(II) and the co-substrate αKG bound in the active site (*34*). The metal ligands are His199, Asp201, and His279, whereas Tyr145, Thr196, and Lys214 stabilize binding of the αKG C-5 carboxylate in a unique type of interaction. The crystal structure of FIH, in complex with Fe(II), αKG and the C-terminal transactivation domain of HIF-α, was also obtained. Asn803 of CAD is precisely orientated in the active site to allow hydroxylation to occur at its β carbon; however, oxidation was prevented by the anaerobic conditions used for crystallization. Similarly, anaerobic conditions in the cell prevents HIF hydroxylation allowing it to function as a transcription factor.

Jumonji C (JmjC)- domain-containing histone demethylases

Covalent histone modifications have an important role in regulating a wide range of processes including gene activity, chromatin structure, dosage compensation and epigenetic memory (*35*). One such modification is methylation, occurring on arginine and lysine residues, the extent of which is controlled by a balance between enzymes that catalyze the addition and removal of this modification (*36*). It was long thought that histone methylation was irreversible until a novel JmjC domain-containing protein, JHDM1 (JmjC domain-containing histone demethylase 1), that specifically demethylates histone H3 at lysine 36 (H3K36) was discovered in 2005 (*37*). From then on, more JHDM members have been identified and JHDMs have become the third and largest class of demethylase enzymes. PADI4 (petidylarginine deiminase 4) converts methyl-arginine to citrulline as opposed to directly reversing arginine

methylation, so it cannot strictly be considered a histone demethylase (*38, 39*). LSD1 (lysine specific demethylase 1), a representative of a second class of enzymes, directly reverses histone H3K4 or H3K9 modifications by an oxidative demethylation reaction in which flavin is cofactor (*40, 41*). It is worth noticing that the state of histone methylation, in addition to the site of lysine modification, is important in determining the functional outcome of this epigenetic modification. Unlike the other two classes, which can only remove mono- and dimethyl lysyl modifications, the JHDMs can remove all three histone lysine-methylation states. In this very active area of investigation, JHDMs already have been shown to reverse H3K36 (JHDM1) (*37*), H3K9 (JHDM2A) (*42*) and both H3K9 and H3K36 (JHDM3 and JMJD2A-D) methylation (*43-46*). A set of 98 JmjC-domain-containing proteins from human to yeast has been reported based on the analysis of public protein-domain databases (*47*). Curiously, FIH, functioning as an asparagine hydroxylase for the HIF-α transcription factor, was included in this enzyme family. Even though FIH is only found in higher eukaryotes such as mice and humans, it is still a useful template for study of other JmjC-domain-containing proteins.

The reaction catalyzed by JHDMs uses Fe(II) and αKG as cofactors to hydroxylate the methyl group of the modified lysyl side chain of histones, with the resulting intermediate spontaneously decomposing as shown in Figure 1.4. In agreement with the reaction, formaldehyde and succinate were detected during the demethylation by JHDM1A (a human JHDM1 homologue) (*37*). Based on the recently solved structure (2.28 Å) of the catalytic domain of JMJD2A (*48*), the JmjC

domain folds into eight conserved β-sheets forming the typical jellyroll-like structure. The iron atom is chelated by three absolutely conserved residues: His188, Glu190, and His276. Two water molecules binding to the metal center also were observed in the native structure. In the presence of αKG, the two water molecules are replaced by two oxygen atoms from αKG which associate with Fe(II) via the C-1 carboxylate and C-2 keto groups. αKG is further stabilized by three hydrogen bonds formed between αKG and the side chains of Tyr132, Asn198 and Lys206. The potential substrate binding site and binding mechanism were proposed, but a complex structure of JMJD2A and its cognate substrate peptide is still required to verify this model.

Repair of Alkylated DNA/RNA

AlkB

Cellular DNA can be damaged by various intracellular and environmental alkylating agents to produce alkylation base lesions which may cause genetic changes that lead to diseases such as cancer (*49-51*). In *E. coli*, an adaptive responsive pathway mediated by Ada protein is initiated by this treatment (*52*). Methyl transfer to Cys69 of Ada converts it into an activator that increases expression of *alkB* and two other genes, *alkA* and *aidB*. AlkA is a glycosylase that cleaves specific methylated bases from DNA and performs the first step of the well-known base excision repair pathway of base lesions. The precise function of AidB is still unknown. The activity of AlkB was unknown for almost 20 years after its involvement in alkylation damage was shown; however, based on phenotypic studies, AlkB was known to function as a DNA repair enzyme that demethylates 1-methyladenine and 3-methylcytosine of

FIGURE 1.4: General reaction of JmjC-domain-containing histone demethylases (JHDM).

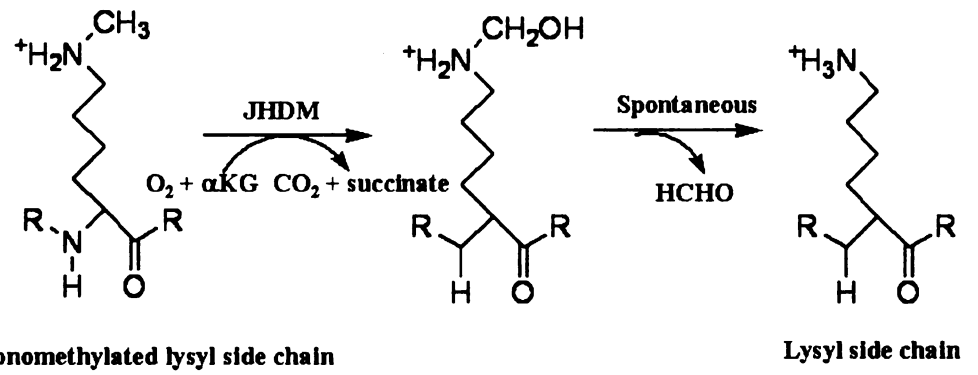

FIGURE 1.5: General reactions of AlkB.

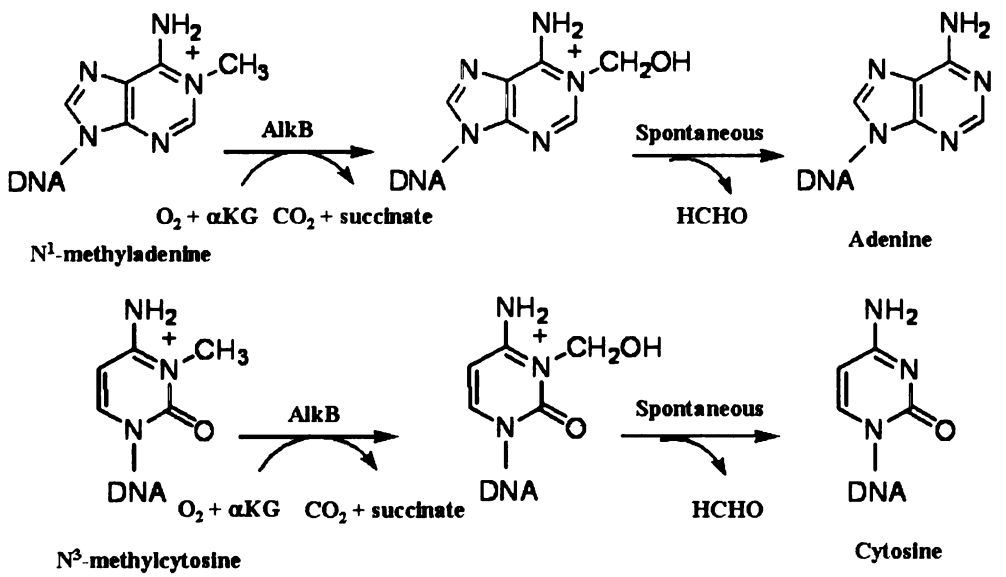

single-strand polynucleotides (*53, 54*). Sequence profile analysis revealed that AlkB belongs to the Fe(II)/αKG-dependent dioxygenase superfamily (*55*). In 2002, two groups confirmed the biochemical activity of AlkB at the same time by detecting the formation of formaldehyde and showing that the AlkB enzyme utilizes an oxidative demethylation pathway to repair base lesions (*1, 56*). In this pathway, oxidation of the methyl group gives a hydroxylated intermediate, which spontaneously decomposes to release the repaired base and formaldehyde as illustrated in Figure 1.5. So far, *in vitro* studies have shown that the sites repaired by AlkB include 1-methyladenine and 3-methylcytosine in DNA or RNA, as well as adducts containing ethyl, hydroxyethyl, propyl, and hydroxylpropyl groups (*57, 58*).

Homologs of AlkB have been discovered based on sequence and fold similarity, and the *alkB* gene is conserved from bacteria to human (*55, 59-61*). At least eight homologs exist in the human genome, and the functions of two of them, ABH2 and ABH3, as well as two mouse homologs mAbh2 and mAbh3 have been characterized (*57, 62*). In contrast, ABH1, which is 52% similar and 23% identical to *E. coli* AlkB, along with ABH4, ABH6 and ABH7 did not show any activity on any of the known substrates for AlkB. In 2006, crystal structures of substrate and product complexes of *E. coli* AlkB were resolved from 1.8 Å to 2.3 Å (*63*). The catalytic core contains a DSBH in which eight β-strands form a jellyroll-like structure matching that observed in other superfamily members. Fe is bound through the His131, Asp133 and His187 facial triad and αKG chelates to Fe(II) via its C-1 carboxylate and C-2 keto groups with Arg204 and Arg210 forming salt bridges to C-5 carboxylate. The alkylated

1-methyladenine base is bound in a deep, predominantly hydrophobic cavity and the nucleotide backbone is bound in a cooperative hydrogen bonding network. Interestingly, there is a unique subdomain, 90 N-terminal residues, that holds the methylated trinucleotide substrate into the active site through contact to the polynucleotide backbone. Through amide hydrogen exchange studies and crystallographic analyses (*63*), this substrate-binding "lid" was shown to be flexible but its flexibility is reduced on binding the substrate. This suggested that AlkB has evolved an elegant molecular design in which this flexible nucleotide-recognition lid recognizes invariant nucleic acid backbone features to produce high-affinity docking of chemically diverse modified bases into its conserved catalytic core. Analysis of crystal structures of substrate and product complexes provided valuable information about the mechanism of AlkB demethylation which will be elucidated in later sections of this chapter.

Biosynthesis of Antibiotics and Plant Products

Clavaminate synthase

Soon after the introduction of β-lactam compounds (like penicillin) as antibiotics, bacteria developed resistance mechanisms involving β-lactamases, that hydrolyze the antibiotic to give biologically inactive products (*64*). Clavulanic acid is a natural compound which inhibits β-lactamase mediated hydrolysis and clavaminate synthase (CAS) is a remarkable Fe(II)/αKG-dependent dioxygenase that catalyzes three separate oxidative reactions in the biosynthesis of clavulanic acid (*65*), Figure 1.6. At first, CAS catalyzes the hydroxylation of a monocylic β-lactam to give a

guanidine-containing alcohol which is hydrolyzed by proclavaminate amidinohydrolase to yield proclavaminic acid. CAS then catalyzes an oxidative cyclization reaction to give dihydroclavaminic acid which is subsequently desaturated by CAS to form clavulanic acid. There are two functionally identical isozymes (CAS1 and CAS2) with a sequence identity of 87% from *Streptomyces clavuligerus* and one single isozyme from *Streptomyces antibioticus* mostly used to carry out the trifunctional activities (*66, 67*). CAS1 was used to obtain an X-ray crystal structure of CAS-Fe(II)-αKG-substrate (*6*). It showed that iron is ligated by the side chains of His144, Glu146 and His279. Of interest, the presence of a glutamyl rather an aspartyl iron ligand is pretty rare in this superfamily and this might reflect the need for flexibility to perform its trifunctional role since glutamate is generally less rigid than aspartate. αKG binds Fe(II) via its C-1 carboxylate and C-2 keto groups and interacts with Arg293 and Thr172 though its C-5 carboxylate. N-α-acetyl-L-arginine and proclavaminic acid were used to study the enzyme-substrate binding, with subtle differences observed in the structures that provide some insight into the mechanisms of oxidative cyclization and desaturation.

Flavanone 3-hydroxylase

Flavonoids, including flavones, isoflavones, flavonols, anthocyanins, and other compounds, are widely distributed in plants where they fulfill many functions including producing yellow or red/blue pigmentation in flowers and protecting them from attack by microbes and insects (*68*). Flavanone 3β-hydroxylase (F3H) catalyzes one of the key steps of flavonoid biosynthesis by hydroxylating (2S)- flavanones to

FIGURE 1.6: Reactions of clavaminate synthase (CAS).

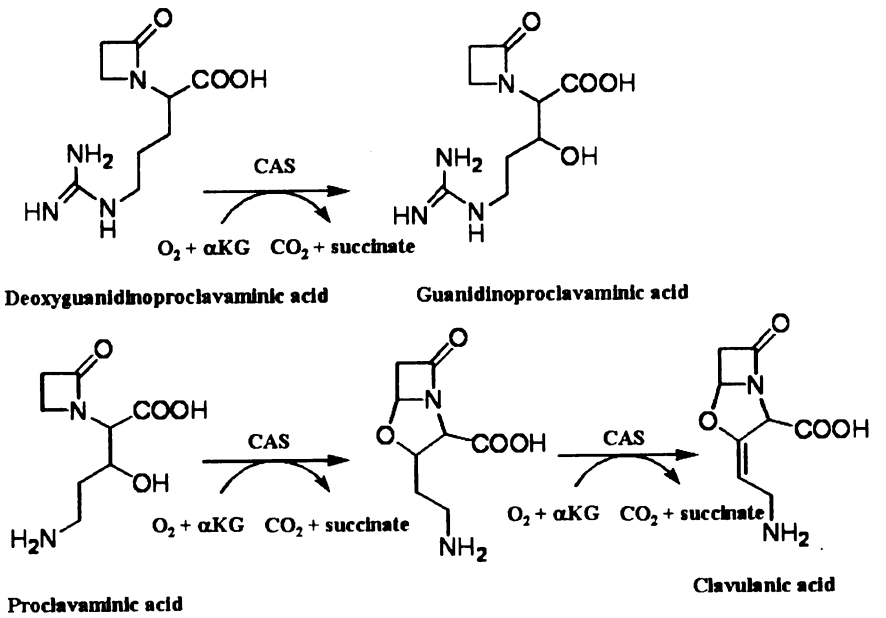

FIGURE 1.7: General reaction of Flavanone 3β-hydroxylase (F3H).

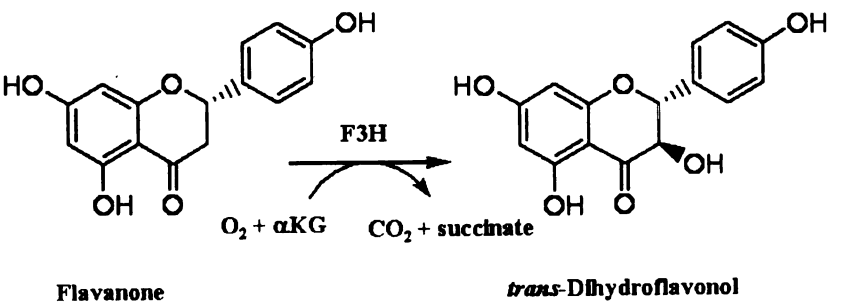

FIGURE 1.8: General reaction of TauD.

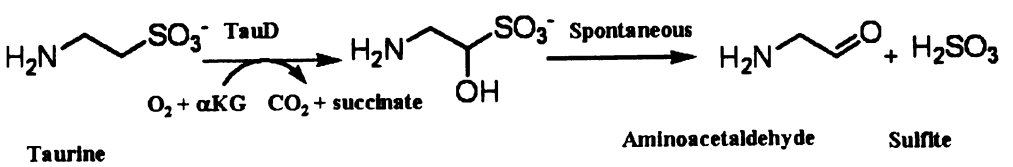

(2R,3R)-dihydroflavonols (*69*). F3H activity was first demonstrated in crude extracts of *Matthiola incana* flower buds (*70*). The enzyme expressed in *E. coli* was purified from *Petunia hybrida* in 1986 and for the first time, this recombinant F3H was shown to be an Fe(II)/αKG-dependent dioxygenase (*71*), as shown in Figure 1.7. In 2000, recombinant *P. hybrida* enzyme was purified by a more convenient two-step protocol with higher yield (*72*). Mutagenesis studies of the recombinant *P. hybrida* gene indicated that His220, Asp222, and His278 comprise the iron binding site, while Arg288 and Ser290 assist in binding αKG (*8, 73*).

Synthesis or Decomposition of Small Molecules

Taurine/αKG dioxygenase

In the absence of sulfate, *E. coli* can utilize aliphatic sulfonates, such as ethanesulfonate, butanesulfonate, L-cysteate, isethionate (2-hydroxylethanesulfonate), and taurine (2-aminoethanesulfonate), as sulfur sources for growth (*74, 75*). The *tauABCD* gene cluster on the *E. coli* chromosome is involved in the utilization of taurine as sulfur source with *tauABC* encoding an uptake system for taurine and the *tauD* gene product showing similarity to Fe(II)/αKG-dependent dioxygenases (*13, 76*). Biochemical characterization confirmed that TauD belongs to this superfamily (*77*) and extensive kinetic, structural and spectroscopic studies have been carried out since then. Indeed, TauD is the most well-characterized member of this enzyme family. This enzyme hydroxylates taurine to create an unstable intermediate that decomposes to aminoacetaldehyde and sulfite (*77*), which is subsequently used as a sulfur source. Substrate hydroxylation is coupled to the oxidative decarboxylation of

αKG to succinate and CO_2 as shown in Figure 1.8. The X-ray crystal structure of anaerobic TauD in the presence of αKG and taurine reveals a pentacoordinate ferrous iron bound to the protein through a 2-His-1-carboxylate facial triad made up of residues His99, Asp101 and His255 (*78, 79*). The αKG is bound in a bidentate manner with the C-1 carboxylate and the C-2 keto groups coordinated to Fe, while the C-5 carboxylate forms a salt bridge with Arg266 and a hydrogen bond with Thr126. Primary substrate binding induces protein conformational changes (*79*). More detailed structural and mechanical studies will be discussed in the later sections of this chapter.

2,4-Dichlorophenoxyacetate /αKG dioxygenase

The 2,4-dichloropheoxyacetic acid (2,4-D) biodegradation pathway has been studied as a model for microbial decomposition of chloroaromatic compounds. In *Alcaligenes eutrophus*, there are five genes, *tfdABCDE*, responsible for this pathway and the *tfdA* gene product (TfdA) catalyzes the hydroxylation of 2,4-D with subsequent decomposition of the hydroxyl-intermediate to yield glyoxylate and 2,4-dichlorophenol, coupled with oxidative cleavage of αKG to CO_2 plus succinate (*13, 76, 80*), as shown in Figure 1.9. TfdA has a relatively broad substrate range, including other phenoxyacetic acid derivatives, thiophenoxyacetic acid, naphthoxyacetic acid, benzofuran-2-carboxylate, and various cinnamic acids (*81*). Of interest, some orthologs from *Alcaligenes denitrificans, Sphingomonas herbicidovorans* MG, and *Delftia acidovorans* MC1 had shown stereospecficity to degradation when examined with enantiomeric 2-phenoxypropionate analogues (*82-85*). Biophysical methods had been applied to study the coordination chemistry of

Fe(II)- and Cu(II)-bound TfdA, including electron paramagnetic resonance (EPR), electron spin-echo envelope modulation (ESEEM) and X-ray absorption spectroscopy (XAS) (*86-89*). On the basis of observations by EPR and ESEEM, the presence of two histidine ligands was proposed, with the ligand geometry undergoing changes upon co-substrate and substrate binding (*87*). Mutagenesis studies indicated that Fe(II) is coordinated by His114, Asp116, and His263, with Arg274 assisting in binding of αKG (*88, 89*). A TfdA model was constructed using the TauD structure as a template, since these two are closely related proteins (~30% sequence identity) (*78*). The model is consistent with mutagenesis and spectroscopy studies.

Xanthine hydroxylase

Most organisms that metabolize xanthine possess a molybdopterin cofactor (Moco)-containing enzyme that hydroxylates the substrate to form uric acid while transferring electrons to NAD (xanthine dehydrogenase) or oxygen (xanthine oxidase) (*90*), Figure 1.10. These enzymes are conserved throughout living organisms, including archaea, bacteria, fungi, plants, and metazoans. In 2005, a novel mechanism for xanthine metabolism was discovered in certain fungi (*91*). All mutants of *Aspergillus nidulans* defective in xanthine dehydrogenase (i.e., with mutations affecting the structural gene *hxA*, the *cnx* genes for Moco synthesis, or *hxB* for sulfuration of Moco) retained the ability to grow on xanthine as sole nitrogen source. Genetic studies revealed that *xanA* was responsible for this capability. The XanA sequence is 18% identical to TauD, suggesting that it is an Fe(II)/αKG-dependent dioxygenase and is the first member of this superfamily to hydroxylate a free purine

FIGURE 1.9: General reaction of TfdA.

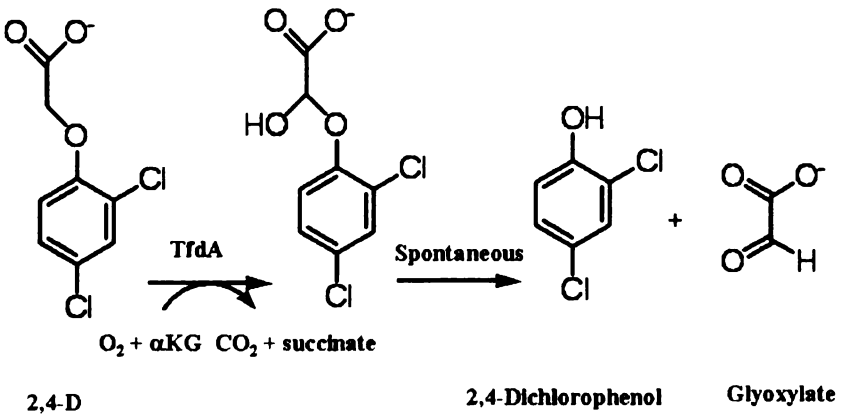

FIGURE 1.10: General reaction of Moco-containing xanthine oxidase (XO).

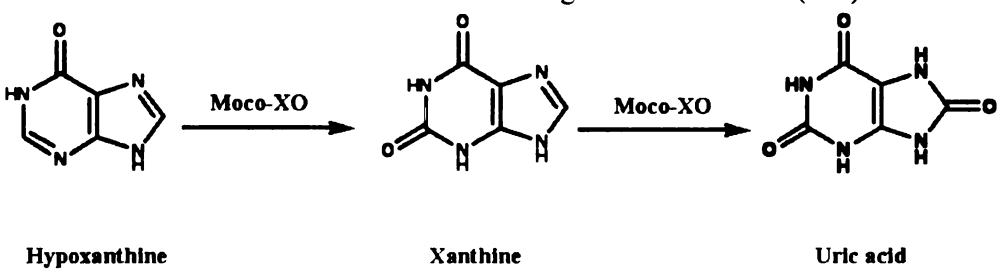

FIGURE 1.11: General reaction of isopenicillin N synthase (IPNS).

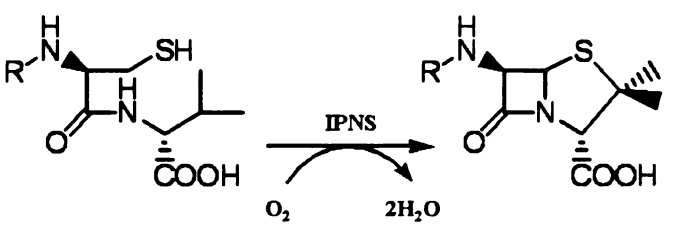

FIGURE 1.12: General reaction of 4-hydroxyphenylpyruvate dioxygenase (HPPD).

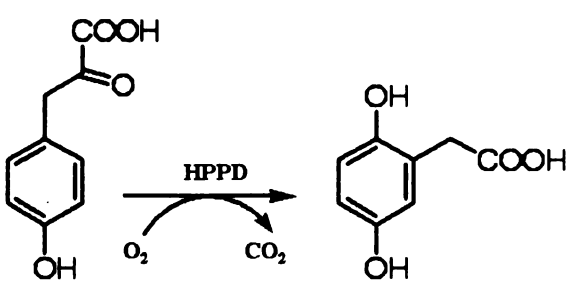

base (*91*). This thesis will present the purification and extensive kinetic and spectroscopic studies on this enzyme to understand its biochemical characteristics and coordination chemistries at different stages of enzymatic reaction.

RELATED ENZYMES

The following section will focus on several enzymes that function independently of αKG but are related to the Fe(II)/αKG-dependent hydroxylases by sequence or mechanism.

Isopenicillin N synthase

Isopenicillin *N* synthase (IPNS) is a non-heme Fe(II)-dependent enzyme found in β-lactam antibiotic-producing microorganisms. It catalyzes the formation of isopenicillin *N* from δ-(L-α-aminoadipoyl)-L-cysteinyl-D-valine (ACV) (*92, 93*), as illustrated in Figure 1.11. IPNS is structurally related to the Fe(II)/αKG-dependent hydroxylases, but it does not utilize αKG as a cosubstrate. Furthermore, unlike Fe(II)/αKG-dependent dioxygenases which incorporate the elements of dioxygen into their substates, the two oxidative ring closures of ACV forming β-lactam and thiazolidine rings catalyzed by IPNS result in the complete four-electron reduction of 1 equiv of dioxygen to 2 equiv of water. The monomeric enzyme has been purified from a variety of fungi and bacteria (*94-96*). The first cloning, characterization and expression in *E. coli* of the gene encoding the IPNS protein in *Cephalosporium acremonium* was reported in 1985 (*97*), and studies on the mechanism of the action of IPNS have focused mainly on the structure of the ferrous iron active site and its role in catalysis. Mössbauer, EPR and UV-Vis spectra all show substrate perturbation of

the iron site, and nitric acid (NO) was used to complex with iron to create EPR and UV-Vis detectable species (*98, 99*). UV-Vis absorption spectra suggested a possible thiol coordination to iron of the IPNS-Fe(II)-ACV complex (*98*). High spin Fe(II) was indicated by the Mössbauer spectrum of IPNS-Fe(II) and IPNS-Fe(II)-ACV (*98*). ESEEM was used to study the active site structure of the IPNS from *Cephalosporium acremonium* with Cu(II) as a spectroscopic probe (*99*). This study revealed two nearly magnetically equivalent, equatorially coordinated His ligands, whereas ^{1}H nuclear magnetic resonance spectra of Fe(II) and Co(II) derivatives indicated the likely presence of three His ligands. Also, a comparison study of ESEEM spectra of Cu(II) IPNS in D_2O and H_2O suggested that water is a ligand of Cu(II) and this is displaced on the addition of substrate. In 1993, Fe K-edge X-ray absorption studies provided more insight into the iron coordination environment with three His ligands and one carboxylate associating with iron (*100, 101*). In the presence of substrate, an Fe-S interaction was observed indicating the coordination of substrate cysteine thiolate to the metal center. The first crystal structure of recombinant *Aspergillus nidulans* IPNS was obtained in complex with manganese and determined at a resolution of 2.5 Å (*102*). Eight of the β-strands fold to form a jelly-roll motif where the active site is buried. The metal is attached by four protein ligands (His214, Asp216, His270, and Gln330) in the absence of substrate. Of interest, Gln330 is not conserved in Fe(II)/αKG-dependent dioxygenases and is only observed in IPNS. This might reflect the differences in their mechanism and substrate specificity, in particular the fact that IPNS does not use an α-keto acid as a co-substrate. Additional mutagenesis studies

have shown this residue is not important to catalysis (*103*), and a more recent crystal structure has shown that this Gln residue is replaced by substrate binding (*104*). In particular, a thiol-metal bond is formed in the IPNS-Fe(II)-ACV complex.

4-Hydroxyphenylpyruvate dioxygenase

4-Hydroxyphenylpyruvate dioxygenase (HPPD) is a non-heme Fe(II) oxygenase that catalyzes the conversion of 4-hydroxyphenylpyruvate to homogentisate (*105*) as illustrated in Figure 1.12. This reaction involves decarboxylation, substituent migration, and aromatic oxygenation. It shows close chemical parallels to Fe(II)/αKG-dependent dioxygenases but is not related in sequence to this superfamily. Rather, the motif, $HX_{\sim 80}HX_{\sim 80}E$, is more similar to that of extradiol dioxygenases $HX_{\sim 65}HX_{\sim 50}E$ (*105*). αKG is not used as a co-substrate and both atoms of dioxygen are incorporated into the aromatic product. This conversion is the second step of a catabolic pathway of tyrosine and has both agricultural and therapeutic significance (*106*).

This enzyme has been purified from human as dimers and from bacteria as tetramers (*107-109*). Aerobic purification of HPPD from *Pseudomonas* sp. strain P. J. 874 was blue (*110*). It is found that this 595 nm absorbance is linked to enzyme-bound Fe(III) and the reduction of iron, which caused the disappearance of the color, restores enzyme activity. This form of enzyme was investigated by resonance Raman spectroscopy, indicating that this absorbance probably arises from coordination of an active site Fe(III) atom by the hydroxyl oxygen atom of tyrosine in the phenolate form (*111*). The crystal structure of *Pseudomona fluorescens* HPPD was solved at 2.4 Å,

and the active site metal ion of HPPD was found to be surrounded by a bower of β-sheet structure with iron liganded to the side chains of His161, His240 and Glu322 (*112*). Significantly, no tyrosine residue side chain is within contact distance of the active site metal ion. This structure raises the possibility of self-hydroxylation of nearby Phe residues to account for the spectroscopic results. Four fully conserved phenylalanines lie close to the active site, and it was postulated that they could be hydroxylated then subsequently ligate to the metal ion (*113*). The structure of substrate binding to the active site is currently unknown, but a hypothetical mode of binding was proposed by Serre et al.(*112*). Similar to Fe(II)/αKG-dependent dioxygenases, the α-keto acid moiety may bind the metal ion in a bidentate fashion, which is consistent with results from the UV-Vis spectrum reported by Moran et al. in 2003 (*114*). A different binding mode was proposed based on the crystal structure of HPPD doped with inhibitor NTBC (*115, 116*). In that proposal, the substrate α-keto acid moiety makes bidentate contact with the active metal ion; however, the phenol is sandwiched between two conserved phenylalanine rings.

STRUCTURAL STUDIES OF Fe(II)/αKG-DEPENDENT HYDROXYLASES

Crystal structures have been determined for more than twenty Fe(II)/αKG-dependent dioxygenases and related enzymes as briefly introduced in the previous sections. These structural studies provide valuable information to understand the enzyme reaction mechanisms. Here, I will further discuss these structural studies, highlight the similarities, point out the differences, and relate these analyses to

enzyme mechanism investigations.

All identified Fe(II)/αKG-dependent dioxygenases appear to contain a DSBH (or jellyroll) fold. The DSBH topology normally consists of eight β-strands that form a β-sandwich structure comprised of two four-stranded antiparallel β-sheets, which twist in a right-handed fashion as shown in Figure 1.13. Sequentially adjacent strands of the DSBH are in different sheets with the exception of the "hairpin" connected fourth and fifth β-strands (*117*). In some members, such as deacetoxycephalosporin C synthase (DAOCS), which catalyzes the conversion of penicillin N to deacetoxycephalosporin C, this connection is a tight loop (*118*). But in the others, such as TauD and CAS, this connection has a highly extended conformation which is able to form part of the substrate binding pocket (*6, 78*). Crystallographic analyses have revealed that the DSBH is stabilized by hydrophobic interactions and is supported by conserved α-helices, which pack alongside the major β-sheet. DSBH enzymes can exist in various oligomeric forms. For examples, IPNS and CAS are monomeric proteins (*6, 102*); DAOCS equilibrates between monomeric and trimeric species in solution, but crystallizes as a trimeric protein (*119*); FIH and TauD are dimeric proteins (*5, 34, 78, 79*); AtsK, catalyzing the oxygenolytic cleavage of a variety of different alkyl sulfate esters to the corresponding aldehyde and sulfate, is tetrameric (*120*) and CarC, which is involved in carbazole degradation, is hexameric (*121*).

The DSBH appears to act as a stable platform to anchor the Fe(II) and αKG. The metal ion is ligated by the three residues forming a conserved HXD/EX_nH motif,

which is located within the minor β-sheet (*122*). (The eight β-sheets can be distinguished by two kinds (i) minor (β-strands 2, 7, 4, 5), referred to as minor due to its shorter strand length (ii) major (β-strands 1, 8, 3, 6), which is often extended with additional strands. See Figure 1.13. The HXD/E of the motif is located at the end of the second strand of the DSBH and the distal histidine of the motif is found on the seventh strand of the DSBH. This 2-His-1-carboxylate motif has been termed a facial triad and also is found in other non-heme oxygenases, including the catechol dioxygenases and the cyclooxygenases (*123, 124*). Exceptions to this arrangement are known as in the enzyme that catalyzes hydroxylation of aspartate and asparagines residues in epidermal growth factor domains where the distal His appears to be missing (*125*).

Compared to the nearly identical arrangements of the three amino acid side chains that bind to the metal, the αKG binding mode is less rigid and resolved into two distinct categories. In both cases, the C-1 carboxylate and C-2 keto groups chelate the metal and the C-5 carboxylate is stabilized by a salt bridge to an Arg residue or by ionic interaction with a Lys side chain. In all reported structures, the 2-keto group coordinates the iron in the position *trans*, or approximately *trans*, to the Asp or Glu residue of the HXE/DX$_n$H motif (*122, 126*). However, the coordination position of the 1-carboxylate of αKG varies between being *trans* to the proximal histidine residues or *trans* to the distal histidine of the triad. One category is represented by CAS, TauD and FIH (*6, 34, 78*). In these enzymes, the 1-carboxylate of αKG is *trans* to the proximal histidine, with the open coordination site either occupied by a water

molecule or vacant, as seen in Figure 1.14A. Primary substrate binding near the active site could replace this water molecule so oxygen could bind in this position. In this case, the open metal coordination site exists near the primary substrate, called the "in line" binding mode. By contrast, some enzyme representatives have the open coordination site oriented away from the substrate binding site, a situation known as the "off line" binding mode, shown in Figure 1.14B. In this category, the 1-carboxylate of αKG is *trans* to the distal histidine and the vacant site is *trans* to the distal histidine, represented by CarC and DAOCS (*121, 127, 128*). Sometimes, these two modes are exchangeable. This αKG binding flexibility reflects that different protein structures tend to stabilize one mode over the other. For example, the C-1 carboxylate of αKG flips from the "in line" to the "off line" mode when Fe(II) is replaced by sodium in AtsK (*120*). For CAS, the addition of NO to substrate-αKG-Fe-ACS complex causes the C-1 carboxylate of αKG to flip from the "in line" to the "off line" binding mode, as shown in Figure1.14 (*129*). Significantly, this discovery suggests that ligand migration involving an intermediate species may be a general feature of Fe(II)/αKG-dependent dioxygenase reaction chemistry.

Structural studies indicate that αKG typically binds prior to the primary substrate, but they also provide insight about the release of the products, whether CO_2 and succinate dissociate during turnover, or they depart only after turnover is complete. First, there are some contradictary opinions on the existence of ferryl-oxo intermediate with CO_2 bound. On one side, stoichiometric accumulation of CO_2 was detected before the completion of the catalytic cycle (*130*). The crystal structure of a

FIGURE 1.13: Double-stranded β-helix structure. A, Eight β-strands forming a double-stranded β-helix (DSBH or jellyroll). B, cartoon of the DSBH motif better illustrating the connections between the strands, modified from (*131*).

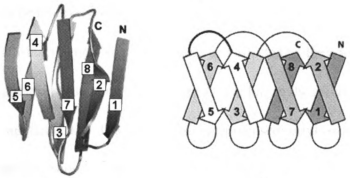

FIGURE 1.14: αKG binding modes. A , on-line, and B, off line. The encircled S represents the substrate binding site.

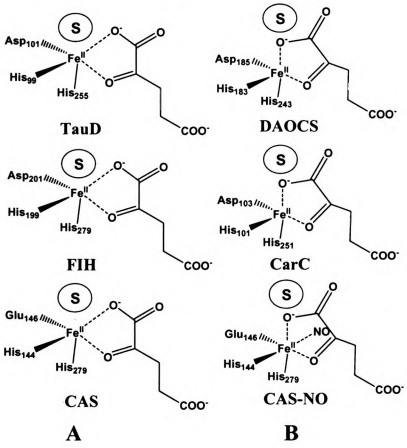

of a C-terminal truncated mutant of DAOCS complexed with Fe(II), succinate, and unhydrated linear CO_2 was determined (*128*), supporting the proposals for a metal-bound CO_2 intermediate during catalysis.This evidence suggests that Fe-CO_2 may be relatively stable and the CO_2 is not always immediately released. Furthermore, a self-inactivation reaction of TauD was affected by the addition of bicarbonate (*132*), suggesting another mechanism of CO_2 binding to the metallocenter. On the other side, computational studies suggest that the proposed ferryl-oxo intermediate can not form with CO_2 bound. (*133*). Early steady state investigations indicated that CO_2 is the first product to dissociate, followed by succinate (*108, 126, 130, 134, 135*). In 2006, co-crystallization of AlkB with succinate yielded a structure with monodentate coordination of Fe by the product plus a second water molecule bound at the site previously occupied by the C-1 carboxylate of αKG, supporting the proposal that the release of CO_2 from αKG occurs prior to release of succinate during turnover, and in some cases its release is suggested to allow migration of the ferryl-oxo intermediate to oxidize substrate (*63*). Succinate is believed to leave the active site after CO_2 departs, and this usually occurs after primary substrate reactivity. An interesting exception involves DAOCS, where the enzyme-substrate complex structure could only be obtained in the absence of αKG and succinate and the αKG decomposition is thought to occur temporily separated from substrate hydroxylation (*128*). Existence of a product complex also is reported in the non-αKG enzyme HPPD, and product release is the rate-limiting step as observed for TauD (*130, 136*).

Another interesting structure feature for this enzyme family is the primary

substrate binding mode. There is more variation in the way the substrate binds than is apparent in either Fe(II) or αKG binding. The substrates range from small molecules, such as taurine, to large polymers, such as proteins or DNA/RNA. With the available evidence, there is no clear link between the structural sub-family and the type of reaction catalyzed. However, there are some common characteristics of substrate binding. First, for some small molecule dioxygenase, such as DAOCS, the sequence and length of the flexible C-terminus is important for substrate selectivity. For example, mutation of the C-terminus of DAOCS, which has a polar side-chain, enabled it to bind penicillin N, whereas, mutation to a hydrophobic side chain favored selectivity toward penicillin G (*137*). Further mutation of the C-terminus resulted in uncoupling of αKG decomposition from substrate oxidation (*119*). Second, the addition of primary substrate induces movement of the flexible elements of the enzyme. For example, in IPNS Arg279 changes its direction from pointing towards the exterior of the protein to one orientated in position to bind the C-terminal carboxylate of the substrate (*102, 104*). Another example is TauD, which undergoes dramatic changes of secondary structures upon adding primary substrate. In the absence of taurine, several key hydrogen bonds in the active site are lost resulting in the releases of a random coil region (*79*). Third, some large substrates can change their conformations to fit into the active site better, such as FIH-α (*34*).

MECHANISTIC STUDIES OF Fe(II)/αKG-DEPENDENT HYDROXYLASES

Prior to the detailed descriptions for each intermediate, I would like to briefly

summarize the reaction mechanism of Fe(II)/αKG-dependent hydroxylases, highlight some common features and point out uncertainties. Hydroxylation is the most common reaction type catalyzed by this superfamily, so it is chosen to represent the general mechanism.

In essence, substrate is oxidized by dioxygen coupled with oxidative decarboxylation of αKG to generate succinate and CO_2, with one of the oxygen atoms incorporated into succinate and the other into the product hydroxyl group. In all cases, Fe(II) binds to the active site before the co-substrates and substrates, as shown by Figure 1.15A. Usually, the addition of substrates begins with the binding of αKG, Figure 1.15B, with two H_2O molecules being displaced (*138-141*). It was proposed that subsequent addition of the primary substrate displaces another H_2O and creates a site for oxygen binding; this mechanism will limit the ability of the enzyme to reduce dioxygen until such time that all organic substrates are appropriately localized and oriented with respect to the active-site metal ion and thus avoids uncoupled or abortive reactive intermediate pathways (*142*). The primary substrate is proposed to coordinate in the vicinity of, not directly to, the metal ion, as shown in Figure 1.15C, creating a five-coordinated Fe(II) site (*6, 78, 143*). Subsequent binding of dioxygen leads to an Fe(III)-superoxo or Fe(IV)-peroxo species, Figure 1.15D, the anion of which attacks the 2-oxo group of αKG, which is activated by the Lewis acidity of the iron (*126*). This reaction can lead to bicyclic peroxide or a persuccinate species Figure 1.15E (*126*). Notably, hybrid density-functional theory calculations have supported the existence of such a persuccinate species (*144*). The ferryl-oxo species, Figure

1.15F, is formed after the collapse of the bicyclic peroxide or persuccinate and is thought to oxidize the substrate by radical rebound-type chemistry, restoring the ferrous species (Figure 1.15, F to A) (*126*).

Intermediate A is the resting state of enzyme, in which Fe(II) is six-coordinate with the 2-His-1-Asp/Glu facial triad ligands and three H_2O molecules that are clearly revealed from the crystal structure of holoenzyme DAOCS (*118*). Until now, only two structures of unliganded holoenzyme have been published: those for DAOCS and proline 3-hydroxylase (P3H) (*7, 118*). Near-infrared magnetic circular dichroism (MCD) spectroscopy of CAS detected two d→d transitions belonging to the six-coordinated distorted octahedral center; these investigations also showed that αKG binding is reduced in the absence of metal ion, confirming that the metal ion binds prior to the co-substrate (*138, 145, 146*).This octahedral arrangement of the Fe(II) ion was also indicated by the XAS studies with TfdA (*86*). Moreover, the Mössbauer spectrum of ^{57}Fe-TauD shows a signal with an isomer shift δ= 1.27 ±0.05 mm/s and quadrupole splitting ΔE_Q = 3.06 ±0.05 mm/s, consistent with high-spin Fe(II) in the active site (*143*). In summary, the holoenzyme species of this superfamily contains a distorted six-coordinated high-spin Fe(II) ion center, surrounded by two His, one Asp/Glu and three water molecules.

Two of the solvent molecules were replaced upon binding of αKG which exhibits bidentate interactions with the iron atom via C-1 carboxylate and C-2 keto groups, Figure 1.15B. Crystal structures showing this bidentate association of αKG

FIGURE 1.15: Proposed mechanism for the hydroxylation reaction catalyzed by Fe(II)/αKG-dependent dioxygenase. See text for a description of the various intermediates.

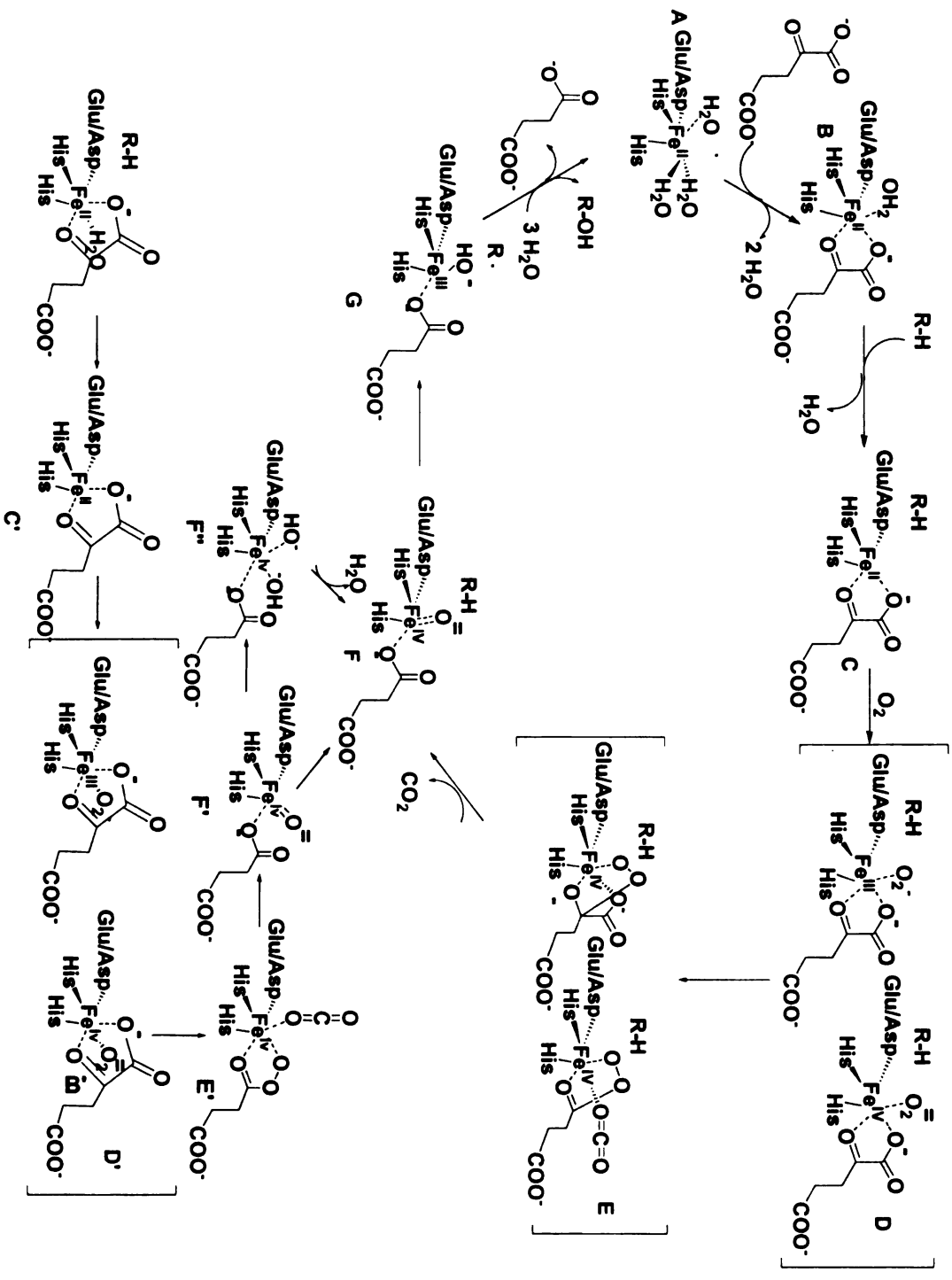

are available for many enzymes, such as FIH, CAS, DAOCS and AtsK (*5, 6, 118, 120*). The five-membered ring formed by αKG binding to the metal is associated with the metal-to-ligand charge-transfer (MLCT) absorption transitions with visible maxima around 500 nm that can be observed in the absence of oxygen. These transitions are now accepted as characteristic of bidentate αKG binding to the metal ion even though the intensities and maxima of these transitions differ slightly in each enzyme, indicating differences in overlap between d orbitals of Fe and π^* orbitals of αKG among different enzymes (*142*). The lilac-colored chromophore exhibits a λ_{max} at 530 nm for both αKG-Fe(II)-TauD and αKG-Fe(II)-TfdA (*140, 141*), whereas the feature is observed at 500 nm in αKG-Fe(II)-AlkB (*1*). Resonance Raman (RR) spectroscopy detected two vibrational transitions with the complex αKG-Fe(II)-TauD in H_2O: 470 cm^{-1} indicative of metal-ligand stretching vibrations, and 1688 cm^{-1} due to the C=O vibration of αKG (*147*). There are two types of coordination chemistry shown in Figure 1.15 for the αKG bound state, intermediate B (in line) and B' (off line). As described before, the C-1 carboxylate is *trans* to the proximal His ligand for the in-line binding mode while it is *trans* to the distal His ligand for the off-line binding mode. Under the off-line binding mode, the ferryl-oxo initially is oriented away from the substrate binding site. In order to accomplish substrate oxidation, migration is required of either the metal ligands or the ferryl intermediate in the later step of the catalytic cycle.

The primary substrate is bound nearby, but not in contact with, the metal ion at the active site, Figure 1.15C, however, substrate binding has a direct influence on the

metal's coordination number. Crystal structures of substrate-αKG-Fe(II)-enzyme complex has been resolved for a few proteins, such as FIH, CAS, TauD and AlkB (*6, 34, 78, 79*). These structures indicate that substrate binding induces a conversion from six-coordinate octahedral to five-coordinate square-pyramidal geometry by the release of the last H_2O molecule. CAS is an exception by only exhibiting an enlonged metal to H_2O bond distance (*6*). The departure of the H_2O molecule is critical for enzyme activity since O_2 is supposed to bind in this open site to carry out the hydroxylation reaction. It was shown that poor substrate binding sometimes retains six-coordination while inclusion of native substrate almost invariably induces five-coordinate rearrangements (*6, 78, 121*). One exception is AlkB, where the substrate-bound enzyme retains a six-coordinate metal site (*63, 148*). Multiple types of spectroscopies have been applied to monitor the effects of primary substrate binding on the active site in the presence of αKG. Upon substrate binding, the UV/Vis spectra often exhibit a perturbation of the MLCT features including a slight increase in intensity, greater resolution of the transitions, and a blue shift (resulting in maxima at 520 nm for TauD and 515 nm for TfdA) (*140, 141*). For TauD, RR also exhibited 10-cm^{-1} shift in features to 470 cm^{-1} and 1688 cm^{-1} in the presence of taurine (*147*); this result was attributed to a switch from six-coordination to five-coordination. Also, the Mössbauer spectra of taurine-αKG-Fe(II)-TauD complex gave a signal with an isomer shift δ = 1.16 ±0.05 mm/s and quadrupole splitting ΔE_Q = 2.76 ±0.05 mm/s, in accord with a reduction in coordination number (*143*). For CAS, the d→d transitions in the presence of substrate identified by near-infrared MCD were in agreement with a

five-coordination site (*145, 146*). Substrate binding in the off-line mode is shown as Figure 1.15C'. It was reported that at least one third of the available crystal structures of this superfamily indicate that the sixth site on the ferrous ion in the tertiary complex is orthogonal to the substrate (*142*). Crystal structure studies on CAS and AlkB provide good examples of enzymes that likely require rearrangements around the active site (*6, 63, 129*).

From intermediate C to the end of catalytic cycle is the least understood part of the mechanism. Only one intermediate, a ferryl-oxo species, has been directly identified. This species was first detected in TauD, but has also been observed in prolyl-4-hydroxylase (P4H) and the halogenase CytC3 (*143, 149-151*). This intermediate from TauD has been investigated most thoroughly. The presumed ferryl-oxo species exhibited an absorption near 318 nm by UV/Vis stopped-flow spectroscopy (*143*). Using rapid freeze-quench techniques to trap the intermediate and carrying out subsequent analysis by EPR and Mössbauer spectroscopy, a species with isomer shift δ= 0.31 ±0.03 mm/s and quadrupole splitting ΔE_Q = 0.88 ±0.03 mm/s was detected and assigned to an integer spin with $S \geq 2$ (*143*). Cryoreduction of this intermediate formed a high-spin Fe(III) species; thus, the intermediate was identified as some type of Fe(IV) species (*143*). Use of C-1 deuterated taurine decreased the rate of decay of this intermediate by 37 fold, indicating that the Fe(IV) species participates in hydrogen abstraction from the substrate (*152*). Furthermore, RR and cryogenic continuous flow were applied to directly identify this intermediate as Fe(IV)=O^{2-} by detecting its isotope-sensitive vibrations (787 cm^{-1} for ^{18}O and 821 cm^{-1} for ^{16}O) (*149*).

The Fe-O distance of 1.62 Å was determined by EXAFS, consistent with literature Fe(IV)-oxo models (*153-155*). The identification of $Fe(IV)=O^{2-}$ is a big step for understanding the mechanism of this enzyme superfamily, but there are still many unsolved questions. None of the O_2-dependent intermediates leading to or following $Fe(IV)=O^{2-}$ has been identified. Even though we knew that $Fe(IV)=O^{2-}$ is responsible for the hydrogen atom abstraction from TauD, whether or not this highly reactive species has the capacity to facilitate all of the observed reactions of this superfamily is unknown. Alternatively, different enzymes might use different activated oxygen species to carry out their unique reactions. Nevertheless, this general mechanism involving formation of $Fe(IV)=O^{2-}$ is very appealing and could reasonably accommodate the desaturation, ring-expansion, epimerization, halogenation and other reactions of this enzyme superfamily. For instance, CAS catalyzes cyclization and desaturation reactions from proclavaminic acid. The ferryl-oxo species could abstract the C4' (*S*) hydrogen as illustrated in Figure 1.16, which leads to intermediate B, with Fe(III)-OH and the C4'-centered radical (*156*). An attack of the C3-bound hydroxyl at C4' coupled with hydrogen atom transfer to Fe(III)-OH leads to the product complex C. Desaturation can be explained in a similar way. The $Fe(IV)=O^{2-}$ species could first hydroxylate the substrate, followed by a dehydration reaction to form the double bond. Alternatively, the $Fe(IV)=O^{2-}$ could initiate two hydrogen atom transfers from the substrate directly to the product, Figure 1.17. Regardless of the diversity of overall reactions that are observed, the initial processes of hydrogen abstraction could be quite similar for each of the enzymes. The most recently discovered subgroup of

Fe(II)/αKG-dependent dioxygenase, the halogenases, replace the monodentate carboxylate of the facial triad with a halide ion, Figure 1.18. The $Fe(IV)=O^{2-}$ is thought to abstract hydrogen atom from the substrate, then the newly formed radical and chloride atom will combine together to give halogenated product (*151, 157*).

For the "in line" mode, the $Fe(IV)=O^{2-}$ points to the intended position of the primary substrate allowing the hydrogen abstraction and subsequent reactions to proceed directly. In contrast, the $Fe(IV)=O^{2-}$ points away from the substrate for the " off line" mode and migration of this ferryl-oxo species or shifting of the metal ligands is necessary. One possibility is that αKG reorients from "off line" (Figure 1.15B') to "in line" (Figure 1.15B) binding mode, so that the subsequent steps will follow those of Figure 1.15 B to F. Another option is that αKG retains its off-line orientation resulting in the formation of $Fe(IV)=O^{2-}$ pointing away from the substrate, as shown in Figure 1.15 B' to F'. Release of CO_2 will provide an open site for one H_2O molecule to bind, resulting in the formation of dihydroxylated intermediate, Figure 1.15F", which can lose a molecule of water to complete the ferryl-oxo migration, Figure 1.15 F' → F" →F. Subsequently, $Fe(IV)=O^{2-}$ is positioned near the substrate and the following steps are equivalent to those in Figure 1.15 F to A.

Currently, the crystal structures of O_2 adducts have only been determined for two mononuclear non-heme iron enzymes, naphthalene dioxygenase and homoprotocatechuate 2,3-dioxygenase (*158, 159*). Both of these proteins contain 2-His-1-carboxylate facial triad, but their proposed reaction mechanisms are totally different from that of the Fe(II)/αKG dependent dioxygenases and neither use αKG as

co-substrate. For both enzymes, in the presence of primary substrate, O_2 binds to the iron center through a side-on rather than end-on mode which is favored by theoretical calculations (*160*). Even though these enzymes provide valuable information about an O_2 binding mode, the Fe(II)/αKG dioxygenases are unlikely share this side-on O_2 binding fashion due to their different protein structure and reaction mechanism.

It is well known that reactive oxygen species can cause severe damage to the cell, and effective control of these reactive species is very important *in vivo* (*161-163*). As mentioned earlier, oxygen generally is the last substrate to bind to the metal ion so that activation of oxygen will not occur until all the necessary cofactors or co-substrates are in the proper position. This strategy guarantees a high coupling efficiency, so the substrate coverts into product concomitant with the oxidative decarboxylation of αKG. This is not always the situation *in vitro*, where the primary substrates may be absent or inhibitors or poor substrates may be present. Under these conditions uncoupled reactions may take place and lead to enzyme inactivation and self-modification, such as reported TfdA, AlkB, TauD, and HPPD (*1, 111, 164-168*). Aerobic purification of HPPD resulted in a blue chromophore consistent with an Fe(III) tyrosinate and the tyrosinate probably is formed from hydroxylation of one of the phenyl rings near the active site (*110*). When TfdA reacted with dioxygen and αKG in the absence of primary substrate, a weak chromophore with λ_{max} around 580 nm was observed (*164*). RR and EPR were applied to identify this species as a Fe(III) hydroxyindolate product arising from the hydroxylation of Trp112 adjacent to the metal ion. A similar result was also observed using TauD, which first forms a

FIGURE 1.16: Proposed mechanism for oxidative cyclization catalyzed by CAS.

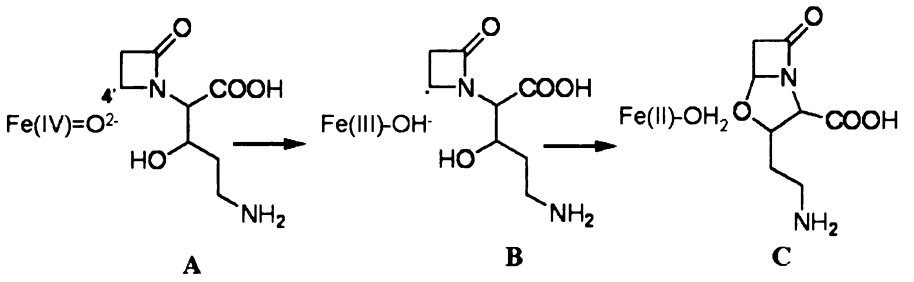

FIGURE 1.17: Proposed mechanism for a desaturation reaction.

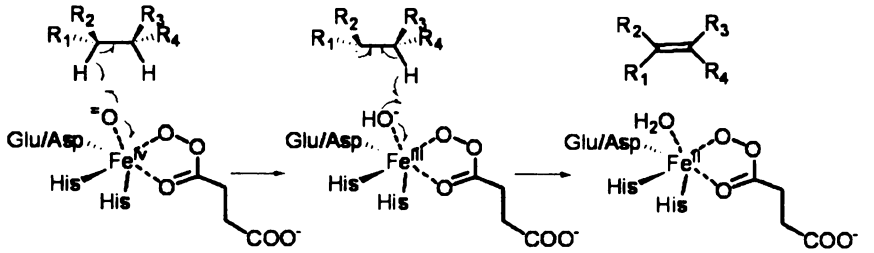

FIGURE 1.18: General reaction of halogenase.

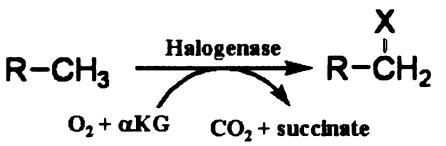

tyrosyl radical then catalyzes the self-hydroxylation of Tyr73 to form a catechol which binds Fe(III) to develop a chromophore with with λ_{max} near 550 nm, as identified by RR as a Fe(III)-catecholate species (*166*). These enzymes in their ferric states are inactive, but some reductants, such as ascorbate and DTT, were reported to be able to restore part of the enzyme activity (*132*). Completing reaction cycles in uncoupled turnover reactions is commonly thought of as the reason for the ascorbate requirement of many Fe(II)/αKG-dependent hydroxylases. Of interest, representatives of these enzymes operate in organisms where ascorbate is not present (*131*), so they could not be restored to a functional state by this reductant. It's still unclear if the self-hydroxylation observed *in vitro* is of physiological relevance. It's been suggested that the enzyme builds in a number of sacrificial amino acids that are susceptible to oxygenation adjacent to the active site metal ion, so that in the absence of substrates or when substrate is not positioned properly, the enzyme internally quenches the reactive oxygen species rather than releasing it to solvent (*131*). Given the facts that the uncoupling reactions rates are much slower than the catalytic reactions involving substrate (*132, 166*), and the relatively low cellular dioxygen concentration, self-inactivation is unlikely to be physiologically relevant *in vivo*.

THESIS OUTLINE

The following chapters describe my studies on the purification and characterization of recombinant xanthine hydroxylase (XanA) from *Aspergillus nidulans*, including the investigation of the substrate-binding mode by site-directed

mutagensis and examination of the metallocenter coordination chemistry by various kinds of spectroscopies. In Chapter 2, I describe the purification of recombinant *A. nidulans* XanA as a His-tag version, and I provide evidence that XanA belongs to the family of Fe(II)/αKG-dependent hydroxylases. I also examine the effects of pH, different kinds of buffers, and salt concentration on the enzymatic activity to optimize the assay conditions. In addition, I characterize the substrate and co-substrate concentration dependence to characterize the kinetic properties of XanA. Of interest, comparison of XanA expressed in different hosts revealed very different quaternary structures and posttranslational modifications. In Chapter 3, I describe more extensive kinetic characterizations, including effects of different divalent metals, co-substrate analogs, and substrate analogs to understand their binding modes to the active site. Finally, I use a homology model, created by a colleague using TauD as the template, to help understand the active site structure. The studies described in Chapter 1 and 2 were published in Biochemistry 2007, *46*, 5293-5304. In Chapter 4, I describe the preparation and characterization of mutant proteins with putative active site residues mutated to alanine based on the homology model constructed from Chapter 3. Xanthine, αKG, alternative substrate analogs, inhibitors and chemical regents were applied to characterize the kinetic properties of the seven active mutants. Kinetic parameters from single mutants were compared with wild-type XanA to gain more insight into the substrate binding mode. The study of oxygen consumption when assayed without primary substrate provided more information on the potential of the relevance of these residues to the active site. Combining the kinetic characterization

and oxygen consumption studies, several important substrate binding interactions are proposed. In Chapter 5, I show that binding of αKG and xanthine to anaerobic Fe(II)-XanA generated MLCT transitions typical of this enzyme family. In addition, I show that nitric oxide (NO), a good oxygen surrogate, can be used to prepare various $\{FeNO\}^7$ complexes, which were extensively characterized by various kinds of spectroscopies, including UV/Vis, EPR, and one- and two-dimensional ESEEM. I used these different $\{FeNO\}^7$ intermediates of XanA to investigate the coordination chemistry at different reaction stages. For comparision, I used TauD, a well characterized member of this superfamily, as a reference to better interpret the results of my spectroscopic studies on XanA. Finally, I provide a concluding chapter that summarizes the remaining questions and places my investigations in broader perspective.

REFERENCES

(1) Trewick, S. C., Henshaw, T. F., Hausinger, R. P., Lindahl, T., and Sedgwick, B. (2002) Oxidative demethylation by *Escherichia coli* AlkB directly reverts DNA base damage. *Nature 419*, 174-178.

(2) Kivirikko, K. I., and Pihlajaniemi, T. (1998) Collagen hydroxylases and the protein disulfide isomerase subunit of prolyl 4-hydroxylase. *Adv. Enzymol. Rel. Areas Mol. Biol. 72*, 325-398.

(3) Ivan, M., Kondo, K., Yang, H., Kim, W., Valiando, J., Ohh, M., Salic, A., Asara, J. M., Lane, W. S., and Kaelin, W. G., Jr. (2001) HIFα targeted for VHL-mediated destruction by proline hydroxylation: implications for O_2 sensing. *Science 292*, 464-467.

(4) Jaakkola, P., Mole, D. R., Tian, Y.-M., Wilson, M. I., Gielbert, J., Gaskell, S. J., von Kriegsheim, A., Hebestreit, H. F., Mukherji, M., Schofield, C. J., Maxwell, P. H., Pugh, C. W., and Ratcliffe, P. J. (2001) Targeting of HIF-α to the von Hippel-Lindau ubiquitylation complex by O_2-regulated prolyl hydroxylation. *Science 292*, 468-472.

(5) Dann, C. E., III, Bruick, R. K., and Deisenhofer, J. (2002) Structure of a factor-inhibiting hypoxia-inducible factor 1: an essential asparaginyl hydroxylase involved in the hypoxic response pathway. *Proc. Natl. Acad. Sci. USA 99*, 15351-15356.

(6) Zhang, Z., Ren, J., Stammers, D. K., Baldwin, J. E., Harlos, K., and Schofield, C. J. (2000) Structural origins of the selectivity of the trifunctional oxygenase clavaminic acid synthase. *Nature Struct. Biol. 7*, 127-133.

(7) Clifton, I. J., Hsueh, L.-C., Baldwin, J. E., Harlos, K., and Schofield, C. J. (2001) Structure of proline 3-hydroxylase. Evolution of the family of 2-oxoglutarate dependent dioxygenases. *Eur. J. Biochem. 268*, 6625-6636.

(8) Lukacin, R., Groning, I., Pieper, U., and Matern, U. (2000) Site-directed mutagenesis of the active site serine290 in flavanone 3β-hydroxylase from *Petunia hybrida*. *Eur. J. Biochem. 267*, 853-860.

(9) Hedden, P., and Phillips, A. L. (2000) Gibberellin metabolism: new insights revealed by the genes. *Trends Plant Sci. 5*, 523-528.

(10) De Carolis, E., Chan, F., Balsevich, J., and De Luca, V. (1990) Isolation and

characterization of a 2-oxoglutarate dependent dioxygenase involved in the second-to-last step in vindoline biosynthesis. *Plant Physiol. 94*, 1323-1329.

(11) Hashimoto, T., and Yamada, Y. (1987) Purification and characterization of hyoscyamine 6β-hydroxylase from root cultures of *Hyoscyamus niger* L. Hydroxylase and epoxidase activities of enzyme preparations. *Eur. J. Biochem. 164*, 277-285.

(12) Jansen, G. A., Mihalik, S. J., Watkins, P. A., Jakobs, C., Moser, H. W., and Wanders, R. J. A. (1998) Characterization of phytanoyl-coenzyme A hydroxylase in human liver and activity measurements in patients with peroxisomal disorders. *Clin. Chim. Acta 271*, 203-211.

(13) Fukumori, F., and Hausinger, R. P. (1993) Purification and characterization of 2,4-dichlorophenoxyacetate/α-ketoglutarate dioxygenase. *J. Biol. Chem. 268*, 24311-24317.

(14) Hutton, J. J., Jr., Trappel, A. L., and Udenfriend, S. (1966) Requirement for α-ketoglutarate, ferrous ion and ascorbate for collagen proline hydroxylase. *Biochem. Biophys. Res. Commun. 24*, 179-184.

(15) Hieta, R., and Myllyharju, J. (2002) Cloning and characterization of a low molecular weight prolyl 4-hydroxylase from *Arabidopsis thaliana*. Effective hydroxylation of proline-rich, collagen-like, and hypoxia-inducible transcription factor α-like peptides. *J. Biol. Chem. 277*, 23965-23971.

(16) Kaska, D. D., Myllylä, R., Günzler, V., Gibor, A., and Kivirikko, K. I. (1988) Prolyl 4-hydroxylase from *Volvox carteri*. A low-M_r enzyme antigenically related to the α subunit of the invertebrate enzyme. *Biochem. J. 256*, 257-263.

(17) Helaakoski, T., Vuori, K., R., M., Kivirikko, K. I., and Pihlajaniemi, T. (1989) Molecular cloning of the α-subunit of human prolyl 4-hydroxylase: the complete cDNA-derived amino acid sequence and evidence for alternative splicing of RNA transcripts. *Proc. Natl. Acad. Sci. USA 86*, 4392-4396.

(18) Annunem, P., Koivunen, P., and Kivirikko, K. I. (1999) Cloning of the α-subunit of prolyl 4-hydroxylase from *Drosophila* and expression and characterization of the corresponding enzyme tetramer with some unique properties. *J. Biol. Chem. 274*, 6790-6796.

(19) Veijola, J., Koivunen, P., Annunem, P., Pihlajaniemi, T., and Kivirikko, K. I. (1994) Cloning, Baculovirus expression, and characterization of the α subunit of prolyl 4-hydroxylase from the nematode *Caenorhaditis elegans*. This α subunit forms an active αβ dimer with the human protein disulfide

isomerase/β subunit. *J. Biol. Chem. 269*, 26746-26753.

(20) Ericksson, M., Myllyharju, J., Tu, H., Hellman, M., and Kivirikko, K. I. (1999) Evidence for 4-hydroxyproline in viral proteins. Characterization of a viral prolyl 4-hydroxylase and its peptide substrates. *J. Biol. Chem. 274*, 22131-22134.

(21) Lamberg, A., Pihlajaniemi, T., and Kivirikko, K. I. (1995) Site-directed mutagenesis of the α subunit of human prolyl 4-hydroxylase. Identification of three histidine residues critical for catalytic activity. *J. Biol. Chem. 270*, 9926-9931.

(22) Myllyharju, J., and Kivirikko, K. I. (1997) Characterization of the iron- and 2-oxoglutarate-binding sites of human prolyl 4-hydroxylase. *The EMBO J. 16*, 1173-1180.

(23) Pekkala, M., Hieta, R., Kursula, P., Kivirikko, K. I., Wierenga, R. K., and Myllyharju, J. (2003) Crystallization of the proline-rich-peptide binding domain of human type I collagen prolyl 4-hydroxylase. *Acta Crystallogr. D59*, 940-942.

(24) Myllyharju, J. (2003) Prolyl 4-hydroxylases, the key enzymes of collagen biosynthesis. *Matrix Biol. 22*, 15-24.

(25) Pirskanen, A., Kaimio, A. M., Myllyla, R., and Kivirikko, K. I. (1996) Site-directed mutagenesis of human lysyl hydroxylase expressed in insect cells. Identification of histidine residues and an aspartic acid residue critical for catalytic activity. *J. Biol. Chem. 271*, 9398-402.

(26) Walsh, G., and Jefferis, R. (2006) Post-translational modifications in the context of therapeutic proteins. *Nat. Biotechnol. 24*, 1241-52.

(27) Semenza, G. L. (2000) HIF-1 and human disease: one highly involved factor. *Genes Dev. 14*, 1983-91.

(28) Schofield, C. J., and Ratcliffe, P. J. (2004) Oxygen sensing by HIF hydroxylases. *Nat. Rev. Mol. Cell Biol. 5*, 343-54.

(29) Hewitson, K. S., McNeill, L. A., Elkins, J. M., and Schofield, C. J. (2003) The role of iron and 2-oxoglutarate oxygenases in signalling. *Biochem. Soc. Trans. 31*, 510-515.

(30) Bruick, R. K., and McKnight, S. L. (2001) A conserved family of prolyl-4-hydroxylases that modify HIF. *Science 294*, 1337-1340.

(31) Hewitson, K. S., McNeill, L. A., Riordan, M. V., Tian, Y.-M., Bullock, A. N., Welford, R. W., Elkins, J. M., Oldham, N. J., Bhattacharya, S., Gleadle, J. M., Ratcliffe, P. J., Pugh, C. W., and Schofield, C. J. (2002) Hypoxia-inducible factor (HIF) asparagine hydroxylase is identical to factor inhibiting HIF (FIH) and is related to the cupin structural familly. *J. Biol. Chem. 277*, 26351-26355.

(32) Lando, D., Peet, D. J., Whelan, D. A., Gorman, J. J., and Whitelaw, M. L. (2002) Asparagine hydroxylation of the HIF transactivation domain: a hypoxic switch. *Science 295*, 858-861.

(33) McNeill, L. A., Hewitson, K. S., Claridge, T. D., Seibel, J. F., Horsfall, L. E., and Schofield, C. J. (2002) Hypoxia-inducible factor asparginyl hydroxylase (FIH-1) catalyses hydroxylation at the β-carbon of asparagine-803. *Biochem. J. 367*, 571-575.

(34) Elkins, J. M., Hewitson, K. S., McNeill, L. A., Seibel, J. F., Schlemminger, I., Pugh, C. W., Ratcliffe, P. J., and Schofield, C. J. (2003) Structure of factor-inhibiting hypoxia-inducible factor (HIF) reveals mechanism of oxidative modification of HIF-1α. *J. Biol. Chem. 278*, 1802-1806.

(35) Martin, C., and Zhang, Y. (2005) The diverse functions of histone lysine methylation. *Nat. Rev. Mol. Cell Biol. 6*, 838-49.

(36) Strahl, B. D., and Allis, C. D. (2000) The language of covalent histone modifications. *Nature 403*, 41-5.

(37) Tsukada, Y.-I., Fang, J., Erdjument-Bromage, H., Warren, M. E., Borchers, C. H., Tempst, P., and Zhang, Y. (2006) Histone demethylation by a family of JmjC domain-containing proteins. *Nature 439*, 811-816.

(38) Wang, Y., Wysocka, J., Sayegh, J., Lee, Y.-H., Perlin, J. R., Leonelli, L., Sonbuchner, L. S., McDonald, C. H., Cook, R. G, Dou, Y., Roeder, R. G, Clarke, S., Stallcup, M. R., Allis, C. D., and Coonrod, S. A. (2004) Human PAD4 regulates histone arginine methylation levels via demethylimination. *Science 306*, 279-283.

(39) Cuthbert, G L., Daujat, S., Snowden, A. W., Erdjument-Bromage, H., Hagiwara, T., Yamada, M., Schneider, R., Gregory, P. D., Tempst, P., Bannister, A. J., and Kouzarides, T. (2004) Histone deimination antagonizes arginine methylation. *Cell 118*, 545-53.

(40) Shi, Y., Lan, F., Matson, C., Mulligan, P., Whetstine, J. R., Cole, P. A., Casero, R. A., and Shi, Y. (2004) Histone demethylation mediated by the nuclear amine oxidase homolog LSD1. *Cell 119*, 941-53.

(41) Metzger, E., Wissmann, M., Yin, N., Muller, J. M., Schneider, R., Peters, A. H., Gunther, T., Buettner, R., and Schule, R. (2005) LSD1 demethylates repressive histone marks to promote androgen-receptor-dependent transcription. *Nature 437*, 436-9.

(42) Yamane, K., Toumazou, C., Tsukada, Y.-I., Erdjument-Bromage, H., Tempst, P., Wong, J., and Zhang, Y. (2006) JHDM2A, a JmjC-containing H3K9 demethylase, facilitates transcription activation by androgen receptor. *Cell 125*, 1-13.

(43) Cloos, P. A. C., Christensen, J., Agger, K., Maiolica, A., Rappsilber, J., Antal, T., Hansen, K. H., and Helin, K. (2006) The putative oncogene GASC1 demethylates tri- and dimethylated lysine 9 on histone H3. *Nature 442*, 307-311.

(44) Whetstine, J. R., Nottke, A., Lan, F., Huart, M., Smolikov, S., Chen, Z., Spooner, E., Li, E., Zhang, G., Colaiacovo, M., and Shi, Y. (2006) Reversal of histone lysine trimethylation by the JMJD2 family of histone demethylases. *Cell 125*, 467-481.

(45) Klose, R. J., Yamane, K., Bae, Y., Zhang, D., Erdjument-Bromage, H., Tempst, P., Wong, J., and Zhang, Y. (2006) The transcriptional repressor JHDM3A demethylates trimethyl histone H3 lysine 9 and lysine 36. *Nature 442*, 312-316.

(46) Fodor, B. D., Kubicek, S., Yonezawa, M., O'Sullivan, R. J., Sengupta, R., Perez-Burgos, L., Opravil, S., Mechtler, K., Schotta, G., and Jenuwein, T. (2006) Jmjd2b antagonizes H3K9 trimethylation at pericentric heterochromatin in mammalian cells. *Genes Dev 20*, 1557-62.

(47) Klose, R. J., Kallin, E. M., and Zhang, Y. (2006) JmjC-domain-containing proteins and histone demethylation. *Nat. Rev. Genet. 7*, 715-27.

(48) Chen, Z., Zang, J., Whetstine, J., Hong, X., Davrazou, F., Kutateladze, T. G., Simpson, M., Mao, Q., Pan, C. H., Dai, S., Hagman, J., Hansen, K., Shi, Y., and Zhang, G. (2006) Structural insights into histone demethylation by JMJD2 family members. *Cell 125*, 691-702.

(49) Sedgwick, B., and Lindahl, T. (2002) Recent progress on the Ada response for inducible repair of DNA alkylation damage. *Oncogene 21*, 8886-8894.

(50) Sedgwick, B. (2004) Repairing DNA-methylation damage. *Nat. Rev. Molec. Cell Biol. 5*, 148-157.

(51) Rydberg, B., and Lindahl, T. (1982) Nonenzymatic methylation of DNA by the intracellular methyl group donor S-adenosyl-L-methionine is a potentially mutagenic reaction. *EMBO J. 1*, 211-6.

(52) Teo, I., Sedgwick, B., Kilpatrick, M. W., McCarthy, T. V., and Lindahl, T. (1986) The intracellular signal for induction of resistance to alkylating agents in *E. coli*. *Cell 45*, 315-24.

(53) Kataoka, H., Yamamoto, Y., and Sekiguchi, M. (1983) A new gene (*alkB*) of *Escherichia coli* that controls sensitivity to methyl methane sulfonate. *J. Bacteriol. 153*, 1301-1307.

(54) Chen, B. J., Carroll, P., and Samson, L. (1994) The *Escherichia coli* AlkB protein protects human cells against alkylation-induced toxicity. *J. Bacteriol. 176*, 6255-6261.

(55) Aravind, L., and Koonin, E. V. (2001) The DNA-repair protein AlkB, EGL-9, and leprecan define new families of 2-oxoglutarate-dependent- and iron-dependent dioxygenases. *Genome Biology 2*, 7.1-7.8.

(56) Falnes, P. O., Johansen, R. F., and Seeberg, E. (2002) AlkB-mediated oxidative demethylation reverses DNA damage in *Escherichia coli*. *Nature 419*, 178-182.

(57) Duncan, T., Trewick, S. C., Koivisto, P., Bates, P. A., Lindahl, T., and Sedgwick, B. (2002) Reversal of DNA alkylation damage by two human dioxygenases. *Proc. Natl. Acad. Sci. USA 99*, 16660-16665.

(58) Koivisto, P., Duncan, T., Lindahl, T., and Sedgwick, B. (2003) Minimal methylated substrate and extended substrate range of *Escherichia coli* AlkB protein, a 1-methyladenine-DNA dioxygenase. *J. Biol. Chem. 278*, 44348-44354.

(59) Wei, Y.-F., Carter, K. C., Wang, R.-P., and Shell, B. K. (1996) Molecular cloning and functional analysis of a human cDNA encoding an *Escherichia coli* AlkB homolog, a protein involved in DNA alkylation damage repair. *Nucl. Acids Res. 24*, 931-937.

(60) Kurowski, M. A., Bhagwat, A. S., Papaj, G., and Bujnicki, J. M. (2003) Phylogenomic identification of five new human homologues of the DNA repair enzyme AlkB. *BMC Genomics 4*, 48.

(61) Colombi, D., and Gomes, S. L. (1997) An *alkB* gene homolog is differentially transcribed during the *Caulobacter crescentus* cell cycle. *J. Bacteriol. 179*,

3139-45.

(62) Aas, P. A., Otterlei, M., Falnes, P. O., Vagbe, C. B., Skorpen, F., Akbari, M., Sundheim, O., Bjoras, M., Slupphaug, G., Seeberg, E., and Krokan, H. E. (2003) Human and bacterial oxidative demethylases repair alkylation damage in both RNA and DNA. *Nature 421*, 859-863.

(63) Yu, B., Edstrom, W. C., Hamuro, Y., Weber, P. C., Gibney, B. R., and Hunt, J. F. (2006) Crystal structures of catalytic complexes of the oxidative DNA/RNA repair enzyme AlkB. *Nature 439*, 879-884.

(64) Matagne, A., Dubus, A., Galleni, M., and Frere, J. M. (1999) The beta-lactamase cycle: a tale of selective pressure and bacterial ingenuity. *Nat Prod Rep 16*, 1-19.

(65) Lloyd, M. D., Merrit, K. D., Lee, V., Sewell, T. J., Wha-Son, B., Baldwin, J. E., Schofield, C. J., Elson, S. W., Baggaley, K. H., and Nicholson, N. H. (1999) Product-substrate engineering by bacteria: studies on clavaminate synthase, a trifunctional dioxygenase. *Tetrahedron 55*, 10201-10220.

(66) Busby, R. W., Chang, M. D.-T., Busby, R. C., Wimp, J., and Townsend, C. A. (1995) Expression and purification of two isozymes of clavaminate synthase and initial characterization of the iron binding site. General error analysis in polymerase chain reaction amplification. *J. Biol. Chem. 270*, 4262-4269.

(67) Marsh, E. N., Chang, M. D.-T., and Townsend, C. A. (1992) Two isozymes of clavaminate synthase central to clavulanic acid formation: cloning and sequencing of both genes from *Streptomyces clavuligerus*. *Biochemistry 31*, 12648-12657.

(68) Bohm, B. A. (1998) *Introduction to Flavonoids*, Harwood Academic Publishers, Amsterdam, The Netherlands.

(69) Prescott, A. G. (1993) A dilemma of dioxygenases (or where biochemistry and molecular biology fail to meet). *J. Exper. Bot. 44*, 849-861.

(70) Heller, W., and Forkmann, G. (1993) *The flavonoids, advances in research since 1986*, 399-425.

(71) Britsch, L., and Grisebach, H. (1986) Purification and characterization of (2*S*)-flavanone 3-hydroxylase from *Petunia hybrida*. *Eur. J. Biochem. 156*, 569-577.

(72) Lukacin, R., Gröning, I., Schiltz, E., Britsch, L., and Matern, U. (2000)

Purification of recombinant flavanone 3β-hydroxylase from *Petunia hybrida* and assignment of the primary site of proteolytic degradation. *Arch. Biochem. Biophys. 375*, 364-370.

(73) Lukacin, R., and Britsch, L. (1997) Identification of strictly conserved histidine and arginine residues as part of the active site in *Petunia hybrida* flavanone 3β-hydroxylase. *Eur. J. Biochem. 249*, 748-757.

(74) Uria-Nickelsen, M. R., Leadbetter, E. R., and Godchaux, W., III. (1993) Sulfonate utilization by enteric bacteria. *J. Gen. Microbiol. 139*, 203-208.

(75) Van Der Ploeg, J. R., Weiss, M. A., Saller, E., Nashimoto, H., Saito, N., Kertesz, M. A., and Leisinger, T. (1996) Identification of sulfate starvation-regulated genes in *Escherichia coli*: a gene cluster involved in the utilization of taurine as a sulfur source. *J. Bacteriol. 178*, 5438-5446.

(76) Fukumori, F., and Hausinger, R. P. (1993) *Alcaligenes eutrophus* JMP134 "2,4-dichlorophenoxyacetate monooxygenase" is an α-ketoglutarate-dependent dioxygenase. *J. Bacteriol. 175*, 2083-2086.

(77) Eichhorn, E., van der Ploeg, J. R., Kertesz, M. A., and Leisinger, T. (1997) Characterization of α-ketoglutarate-dependent taurine dioxygenase from *Escherichia coli*. *J. Biol. Chem. 272*, 23031-23036.

(78) Elkins, J. M., Ryle, M. J., Clifton, I. J., Dunning Hotopp, J. C., Lloyd, J. S., Burzlaff, N. I., Baldwin, J. E., Hausinger, R. P., and Roach, P. L. (2002) X-ray crystal structure of *Escherichia coli* taurine/α-ketoglutarate dioxygenase complexed to ferrous iron and substrates. *Biochemistry 41*, 5185-5192.

(79) O'Brien, J. R., Schuller, D. J., Yang, V. S., Dillard, B. D., and Lanzilotta, W. N. (2003) Substrate-induced conformational changes in *Escherichia coli* taurine/α-ketoglutarate dioxygenase and insight into the oligomeric structure. *Biochemistry 42*, 5547-5554.

(80) Hausinger, R. P., Fukumori, F., Hogan, D. A., Sassanella, T. M., Kamagata, Y., Takami, H., and Saari, R. E. (1997) Biochemistry of 2,4-D degradation: evolutionary implications, in *Microbial Diversity and Genetics of Biodegradation* (Horikoshi, K., Fukuda, M., and Kudo, T., Eds.) pp 35-51, Japan Scientific Press, Tokyo.

(81) Dunning Hotopp, J. C., and Hausinger, R. P. (2001) Alternative substrates for 2,4-dichlorophenoxyacetate/α-ketoglutarate dioxygenase. *J. Molec. Catalysis B 15*, 155-162.

(82) Tett, V. A., Willetts, A. J., and Lappin-Scott, H. M. (1997) Biodegradation of the chlorophenoxy herbicide (*R*)-(+)-mecoprop by *Alcaligenes denitrificans*. *Biodegradation 8*, 43-52.

(83) Nickel, K., Suter, M. J.-F., and Kohler, H.-P. E. (1997) Involvement of two α-ketoglutarate-dependent dioxygenases in enantioselective degradation of (*R*)- and (*S*)-mecoprop by *Sphingomonas herbicidovorans* MH. *J. Bacteriol. 179*, 6674-6679.

(84) Westendorf, A., Müller, A., and Babel, W. (2003) Purification and characterization of the enantiospecific dioxygenases from *Delftia acidovorans* MC1 initiating the degradation of phenoxypropionate and phenoxyacetate herbicides. *Acta Biotechnol 23*, 3-17.

(85) Müller, T. A., Zavodszky, M. I., Feig, M., Kuhn, L. A., and Hausinger, R. P. (2006) Structural basis for the enantiospecificities of *R*- and *S*-phenoxypropionate/α-ketoglutarate dioxygenases. *Prot. Science 15*, 1356-1368.

(86) Cosper, N. J., Stålhandske, C. M. V., Saari, R. E., Hausinger, R. P., and Scott, R. A. (1999) X-ray absorption spectroscopic analysis of Fe(II) and Cu(II) forms of an herbicide-degrading α-ketoglutarate dioxygenase. *J. Biol. Inorg. Chem. 4*, 122-129.

(87) Whiting, A. K., Que, L., Jr., Saari, R. E., Hausinger, R. P., Fredrick, M. A., and McCracken, J. (1997) Metal coordination environment of a Cu(II)-substituted α-keto acid-dependent dioxygenase that degrades the herbicide 2,4-D. *J. Am. Chem. Soc. 119*, 3413-3414.

(88) Dunning Hotopp, J. C., and Hausinger, R. P. (2002) Probing the 2,4-dichlorophenoxyacetate/α-ketoglutarate dioxygenase substrate binding site by site-directed mutagenesis and mechanism-based inactivation. *Biochemistry 41*, 9787-9794.

(89) Hogan, D. A., Smith, S. R., Saari, E. A., McCracken, J., and Hausinger, R. P. (2000) Site-directed mutagenesis of 2,4-dichlorophenoxyacetic acid/α-ketoglutarate dioxygenase. Identification of residues involved in metallocenter formation and substrate binding. *J. Biol. Chem. 275*, 12400-12409.

(90) Hille, R. (2005) Molybdenum-containing hydroxylases. *Arch. Biochem. Biophys. 433*, 107-116.

(91) Cultrone, A., Scazzocchio, C., Rochet, M., Montero-Morán, G., Drevet, C.,

and Fernández-Martín, R. (2005) Convergent evolution of hydroxylation mechanisms in the fungal kingdoms: molybdenum cofactor-independent hydroxylation of xanthine via α-ketoglutarate dependent dioxygenase. *Molec. Microbiol. 57*, 276-290.

(92) Kreisberg-Zakarin, R., Borovok, I., Yanko, M., Aharonowitz, Y., and Cohen, G. (1999) Recent advances in the structure and function of isopenicillin N synthase. *Antonie van Leeuwenhoek 75*, 33-39.

(93) Schofield, C. J., Baldwin, J. E., Byford, M. F., Clifton, I. J., Hensgens, C., and Roach, P. L. (1997) Proteins of the penicillin biosynthesis pathway. *Curr. Opinion Struct. Biol. 7*, 857-864.

(94) Pang, C. P., Chakravarti, B., Adlington, R. M., Ting, H. H., White, R. L., Jayatilake, G. S., Baldwin, J. E., and Abraham, E. P. (1984) Purification of isopenicillin N synthetase. *Biochem J 222*, 789-95.

(95) Baldwin, J. E., and Abraham, E. (1988) The biosynthesis of penicillins and cephalosporins. *Nat. Prod. Rep. 5*, 129-45.

(96) Castro, J. M., Liras, P., Laiz, L., Cortes, J., and Martin, J. F. (1988) Purification and characterization of the isopenicillin N synthase of Streptomyces lactamdurans. *J. Gen. Microbiol. 134*, 133-41.

(97) Samson, S. M., Belagaje, R., Blankenship, D. T., Chapman, J. L., Perry, D., Skatrud, P. L., VanFrank, R. M., Abraham, E. P., Baldwin, J. E., Queener, S. W., and et al. (1985) Isolation, sequence determination and expression in *Escherichia coli* of the isopenicillin *N* synthetase gene from *Cephalosporium acremonium*. *Nature 318*, 191-4.

(98) Chen, V. J., Orville, A. M., Harpel, M. R., Frolik, C. A., Surerus, K. K., Munck, E., and Lipscomb, J. D. (1989) Spectroscopic studies of isopenicillin N synthase. A mononuclear nonheme Fe^{2+} oxidase with metal coordination sites for small molecules and substrate. *J. Biol. Chem. 264*, 21677-21681.

(99) Jiang, F., Peisach, J., Ming, L.-J., Que, L., Jr., and Chen, V. J. (1991) Electron spin echo envelope modulation studies of the Cu(I)-substituted derivative of isopenicillin N synthase: a structural and spectroscopic model. *Biochemistry 30*, 11437-11445.

(100) Randall, C. R., Zang, Y., True, A. E., Que, L., Jr., Charnock, J. M., Garner, C. D., Fujishima, Y., Schofield, C. J., and Baldwin, J. E. (1993) X-ray absorption studies of the ferrous active site of isopenicillin N synthase and related model complexes. *Biochemistry 32*, 6664-6673.

(101) Scott, R. A., Wang, S., Eidsness, M. K., Kriauciunas, A., Frolik, C. A., and Chen, V. J. (1992) X-ray absorption spectroscopic studies of the high-spin iron(II) active site of isopenicillin N synthase: evidence for Fe-S interaction in the enzyme-substrate complex. *Biochemistry 31*, 4596-4601.

(102) Roach, P. L., Clifton, I. J., Fülöp, V., Harlos, K., Barton, G. J., Hajdu, J., Andersson, K., Schofield, C. J., and Baldwin, J. E. (1995) Crystal structure of isopenicillin *N* synthase is the first from a new structural family of enzymes. *Nature (London) 375*, 700-704.

(103) Landman, O., Borovok, I., Aharonowitz, Y., and Cohen, G. (1997) The glutamine ligand in the ferrous iron active site of isopenicillin N synthase of *Streptomyces jumonjinensis* is not essential for catalysis. *FEBS Lett. 405*, 172-174.

(104) Roach, P. L., Clifton, I. J., Hensgens, C. M. H., Shibata, N., Schofield, C. J., Hajdu, J., and Baldwin, J. E. (1997) Structure of isopenicillin *N* synthase complexed with substrate and the mechanism of penicillin formation. *Nature (London) 387*, 827-830.

(105) Moran, G. R. (2005) 4-Hydroxyphenylpyruvate dioxygenase. *Arch. Biochem. Biophys. 433*, 117-128.

(106) Gissen, P., Preece, M. A., Willshaw, H. A., and McKiernan, P. J. (2003) Ophthalmic follow-up of patients with tyrosinaemia type I on NTBC. *J. Inherit. Metab. Dis. 26*, 13-6.

(107) Wada, G. H., Fellman, J. H., Fujita, T. S., and Roth, E. S. (1975) Purification and properties of avian liver p-hydroxyphenylpyruvate hydroxylase. *J. Biol. Chem. 250*, 6720-6.

(108) Lindblad, B., Lindstedt, G., Lindstedt, S., and Rundgren, M. (1977) Purification and some properties of human 4-hydroxyphenylpyruvate dioxygenase (I). *J. Biol. Chem. 252*, 5073-84.

(109) Buckthal, D. J., Roche, P. A., Moorehead, T. J., Forbes, B. J., and Hamilton, G. A. (1987) 4-Hydroxyphenylpyruvate dioxygenase from pig liver. *Metholds Enzymol. 142*, 132-8.

(110) Lindstedt, S., and Rundgren, M. (1982) Blue color, metal content, and substrate binding in 4-hydroxyphenylpyruvate dioxygenase from Pseudomonas sp. strain P. J. 874. *J. Biol. Chem. 257*, 11922-31.

(111) Bradley, F. C., Lindstedt, S., Lipscomb, J. D., Que, L., Jr., Roe, A. L., and

Rundgren, M. (1986) 4-Hydroxyphenylpyruvate dioxygenase is an iron-tyrosinate protein. *J. Biol. Chem. 261*, 11693-11696.

(112) Serre, L., Sailland, A., Sy, D., Boudec, P., Rolland, A., Pebay-Peyroula, E., and Cohen-Addad, C. (1999) Crystal structure of *Pseudomonas fluorescens* 4-hydroxyphenylpyruvate dioxygenase: an enzyme involved in the tyrosine degradation pathway. *Structure 7*, 977-988.

(113) Ryle, M. J., and Hausinger, R. P. (2002) Non-heme iron oxygenases. *Curr. Opinion Chem. Biol. 6*, 193-201.

(114) Johnson-Winters, K., Purpero, V. M., Kavana, M., Nelson, T., and Moran, G. R. (2003) (4-Hydroxyphenyl)pyruvate dioxygenase from *Streptomyces avermitilis*: the basis for ordered substrate addition. *Biochemistry 42*, 2072-2080.

(115) Gunsior, M., Ravel, J., Challis, G. L., and Townsend, C. A. (2004) Engineering *p*-hydroxyphenylpyruvate dioxygenase to a *p*-hydroxymandelate synthase and evidence for the proposed benzene oxide intermediate in homogentisate formation. *Biochemistry 43*, 663-674.

(116) Brownlee, J. M., Johnson-Winters, K., Harrison, D. H. T., and Moran, G. R. (2004) Structure of the ferrous form of (4-hydroxyphenyl)pyruvate dioxygenase from *Streptomyces avermitilis* in complex with the therapeutic herbicide, NTBC. *Biochemistry 43*, 6370-6377.

(117) Stirk, H. J., Woolfson, D. N., Hutchinson, E. G., and Thornton, J. M. (1992) Depicting topology and handedness in jellyroll structures. *FEBS Lett 308*, 1-3.

(118) Valegård, K., Terwisscha van Scheltinga, A. C., Lloyd, M. D., Hara, T., Ramaswamy, S., Perrakis, A., Thompson, A., Lee, W.-J., Baldwin, J. E., Schofield, C. J., Hajdu, J., and Andersson, I. (1998) Structure of a cephalosporin synthase. *Nature (London) 394*, 805-809.

(119) Lloyd, M. D., Lee, H.-J., Harlos, K., Zhang, Z.-H., Baldwin, J. E., Schofield, C. J., Charnock, J. M., Garner, C. D., Hara, T., Terwisscha Van Scheltinga, A. C., Valegard, K., Viklund, J. A. C., Hajdu, J., Andersson, I., Danielsson, A., and Bhikhabhai, R. (1999) Studies on the active site of deacetoxycephalosporin C synthase. *J. Mol. Biol. 287*, 943-960.

(120) Müller, I., Kahnert, A., Pape, T., Sheldrick, G. M., Meyer-Klaucke, W., Dierks, T., Kertesz, M., and Usòn, I. (2004) Crystal structure of the alkylsulfatase AtsK: insights into the catalytic mechanism of the Fe(II) α-ketoglutarate-dependent dioxygenase superfamily. *Biochemistry 43*,

3075-3088.

(121) Clifton, I. J., Doan, L. X., Sleeman, M. C., Topf, M., Suzuki, H., Wilmouth, R. C., and Schofield, C. J. (2003) Crystal structure of carbapenem synthase (CarC). *J. Biol. Chem. 278*, 20843-20850.

(122) Clifton, I. J., McDonough, M. A., Ehrismann, D., Kershaw, N. J., Granatino, N., and Schofield, C. J. (2006) Structural studies on 2-oxoglutarate oxygenases and related double-stranded β-helix fold protein. *J. Inorg. Biochem. 100*, 644-669.

(123) Broderick, J. B. (1999) Catechol dioxygenases. *Essays Biochem. 34*, 173-189.

(124) Costas, M., Mehn, M. P., Jensen, M. P., and Que, L., Jr. (2004) Dioxygen activation at mononuclear nonheme iron active sites: enzymes, models, and intermediates. *Chem. Rev. 104*, 939-986.

(125) Lancaster, D. E., McDonough, M. A., and Schofield, C. J. (2004) Factor inhibiting hypoxia-inducible factor (FIH) and other asparaginyl hydroxylases. *Biochem. Soc. Trans. 32*, 943-5.

(126) Hausinger, R. P. (2004) Fe(II)/α-ketoglutarate-dependent hydroxylases and related enzymes. *Crit. Rev. Biochem. Mol. Biol. 39*, 21-68.

(127) Valegard, K., Terwisscha van Scheltinga, A. C., Dubus, A., Ranghino, G., Oster, L. M., Hajdu, J., and Andersson, I. (2004) The structural basis of cephalosporin formation in a mononuclear ferrous enzyme. *Nat. Struct. Mol. Biol. 11*, 95-101.

(128) Lee, H. J., Lloyde, M. D., Clifton, I. J., Baldwin, J. E., and Schofield, C. J. (2001) Kinetic and crystallographic studies on deacetoxycephalosporin C synthase (DAOCS). *J. Mol. Biol. 308*, 937-948.

(129) Zhang, Z., Ren, J.-s., Harlos, K., McKinnon, C. H., Clifton, I. J., and Schofield, C. J. (2002) Crystal structure of a clavaminate synthase-Fe(II)-2-oxoglutarate-substrate-NO complex: evidence for metal centred rearrangements. *FEBS Lett. 517*, 7-12.

(130) Price, J. C., Barr, E. W., Hoffart, L. M., Krebs, C., and Bollinger, J. M., Jr. (2005) Kinetic dissection of the catalytic mechanism of taurine:α-ketoglutarate dioxygenase (TauD) from *Escherichia coli*. *Biochemistry 44*, 8138-8147.

(131) Hewitson, K. S., Granatino, N., Welford, R. W., McDonough, M. A., and

Schofield, C. J. (2005) Oxidation by 2-oxoglutarate oxygenases: non-haem iron systems in catalysis and signalling. *Philos. Transact. A Math. Phys. Eng. Sci. 363*, 807-28; discussion 1035-40.

(132) Ryle, M. J., Koehntop, K. D., Liu, A., Que, L., Jr., and Hausinger, R. P. (2003) Interconversion of two oxidized forms of TauD, a non-heme iron hydroxylase: evidence for bicarbonate binding. *Proc. Natl. Acad. Sci. USA 100*, 3790-3795.

(133) Neidig, M. L., Decker, A., Choroba, O. W., Huang, F., Kavana, M., Moran, G. R., Spencer, J. B., and Solomon, E. I. (2006) Spectroscopic and electronic structure studies of aromatic electrophilic attack and hydrogen-atom abstraction by non-heme iron enzymes. *Proc Natl Acad Sci U S A 103*, 12966-73.

(134) Holme, E. (1975) A kinetic study of thymine 7-hydroxylase from *Neurospora crassa*. *Biochemistry 14*, 4999-5003.

(135) Tuderman, L., R., M., and Kivirikko, K. I. (1977) Mechanism of prolyl hydroxylase reaction. 1. Role of co-substrates. *Eur. J. Biochem. 80*, 314-348.

(136) Johnson-Winters, K., Purpero, V. M., Kavana, M., and Moran, G. R. (2005) Accumulation of multiple intermediates in the catalytic cycle of (4-hydroxyphenyl)pyruvate dioxygenase from *Streptomyces avermitilis*. *Biochemistry 44*, 7189-7199.

(137) Lee, H.-J., Lloyd, M. D., Clifton, I. J., Harlos, K., Dubus, A., Baldwin, J., E., Frere, J.-M., and Schofield, C. J. (2001) Alteration of the co-substrate selectivity of deacetoxycephalosporin C synthase. The role of arginine 258. *J. Biol. Chem. 276*, 18290-18295.

(138) Pavel, E. G., Zhou, J., Busby, R. W., Gunsior, M., Townsend, C. A., and Solomon, E. I. (1998) Circular dichroism and magnetic circular dichroism spectroscopic studies of the non-heme ferrous active site in clavaminate synthase and its interaction with α-ketoglutarate cosubstrate. *J. Am. Chem. Soc. 120*, 743-753.

(139) Neidig, M. L., Kavana, M., Moran, G. R., and Solomon, E. I. (2004) CD and MCD studies of the non-heme ferrous active site in (4-hydroxyphenyl)pyruvate dioxygenase: correlation between oxygen activation in the extradiol and alpha-KG-dependent dioxygenases. *J. Am. Chem. Soc. 126*, 4486-7.

(140) Ryle, M. J., Padmakumar, R., and Hausinger, R. P. (1999) Stopped-flow kinetic analysis of *Escherichia coli* taurine/α-ketoglutarate dioxygenase:

interactions with α-ketoglutarate, taurine, and oxygen. *Biochemistry 38*, 15278-15286.

(141) Hegg, E. L., Whiting, A. K., Saari, R. E., McCracken, J., Hausinger, R. P., and Que, L., Jr. (1999) Herbicide-degrading α-keto acid-dependent enzyme TfdA: metal coordination environment and mechanistic insights. *Biochemistry 38*, 16714-16726.

(142) Purpero, V., and Moran, G. R. (2007) The diverse and pervasive chemistries of the α-keto acid dependent enzymes. *J. Biol. Inorg. Chem. 12*, 587-601.

(143) Price, J. C., Barr, E. W., Tirupati, B., Bollinger, J. M., Jr., and Krebs, C. (2003) The first direct characterization of a high-valent iron intermediate in the reaction of an α-ketoglutarate-dependent dioxygenase: a high-spin Fe(IV) complex in taurine/α-ketoglutarate dioxygenase (TauD) from *Escherichia coli*. *J. Biol. Chem. 42*, 7497-7508.

(144) Borowski, T., Bassan, A., and Siegbahn, P. E. M. (2004) Mechanism of dioxygen activation in 2-oxoglutarate-dependent enzymes: a hybrid DFT study. *Chem. Eur. J. 10*, 1031-1041.

(145) Zhou, J., Gunsior, M., Bachmann, B. O., Townsend, C. A., and Solomon, E. I. (1998) Substrate binding to the α-ketoglutarate-dependent non-heme iron enzyme clavaminate synthase 2: coupling mechanism of oxidative decarboxylation and hydroxylation. *J. Am. Chem. Soc. 120*, 13539-13540.

(146) Zhou, J., Kelly, W. L., Bachmann, B. O., Gunsior, M., Townsend, C. A., and Solomon, E. I. (2001) Spectroscopic studies of substrate interactions with clavaminate synthase 2, a multifunctional α-KG-dependent non-heme iron enzyme: correlation with mechanisms and reactivities. *J. Am. Chem. Soc. 123*, 7388-7398.

(147) Ho, R. Y. N., Mehn, M. P., Hegg, E. L., Liu, A., Ryle, M. A., Hausinger, R. P., and Que, L., Jr. (2001) Resonance Raman studies of the iron(II)-α-keto acid chromophore in model and enzyme complexes. *J. Am. Chem. Soc. 123*, 5022-5029.

(148) Bleijlevens, B., Shivarattan, T., Sedgwick, B., Rigby, S. E., and Matthews, S. J. (2007) Replacement of non-heme Fe(II) with Cu(II) in the α-ketoglutarate dependent DNA repair enzyme AlkB: spectroscopic characterization of the active site. *J. Inorg. Biochem.*, ASAP.

(149) Proshlyakov, D. A., Henshaw, T. F., Monterosso, G. R., Ryle, M. J., and Hausinger, R. P. (2004) Direct detection of oxygen intermediates in the

non-heme Fe enzyme taurine/α-ketoglutarate dioxygenase. *J. Am. Chem. Soc. 126*, 1022-1023.

(150) Hoffart, L. M., Barr, E. W., Guyer, R. B., Bollinger, J. M., Jr., and Krebs, C. (2006) Direct spectroscopic detection of a C-H-cleaving high-spin Fe(IV) complex in a prolyl-4-hydroxylase. *Proc. Natl. Acad. Sci. USA 103*, 14738-14743.

(151) Galonic, D. P., Barr, E. W., Walsh, C. T., Bollinger, J. M., Jr., and Krebs, C. (2007) Two interconverting Fe(IV) intermediates in aliphatic chlorination by the halogenase CytC3. *Nat Chem Biol 3*, 113-6.

(152) Price, J. C., Barr, E. W., Glass, T. E., Krebs, C., and Bollinger, J. M., Jr. (2003) Evidence for hydrogen abstraction from C1 of taurine by the high-spin Fe(IV) intermediate detected during oxygen activation by taurine:α-ketoglutarate dioxygenase (TauD). *J. Am. Chem. Soc. 125*, 13008-13009.

(153) Wolter, T., Meyer-Klaucke, W., Muther, M., Mandon, D., Winkler, H., Trautwein, A. X., and Weiss, R. (2000) Generation of oxoiron (IV) tetramesitylporphyrin pi-cation radical complexes by m-CPBA oxidation of ferric tetramesitylporphyrin derivatives in butyronitrile at - 78 degrees C. Evidence for the formation of six-coordinate oxoiron (IV) tetramesitylporphyrin pi-cation radical complexes FeIV = O(tmp*)X (X = Cl-, Br-), by Mossbauer and X-ray absorption spectroscopy. *J. Inorg. Biochem. 78*, 117-22.

(154) Penner-Hahn, J. E., McMurry, T. J., Renner, M., Latos-Grazynsky, L., Eble, K. S., Davis, I. M., Balch, A. L., Groves, J. T., Dawson, J. H., and Hodgson, K. O. (1983) X-ray absorption spectroscopic studies of high valent iron porphyrins. Horseradish peroxidase compounds I and II and synthetic models. *J. Biol. Chem. 258*, 12761-4.

(155) Riggs-Gelasco, P. J., Price, J. C., Guyer, R. B., Brehm, J. H., Barr, E. W., Bollinger, J. M., Jr., and Krebs, C. (2004) EXAFS spectroscopic evidence for an Fe=O unit in the Fe(IV) intermediate observed during oxygen activation by taurine:alpha-ketoglutarate dioxygenase. *J. Am. Chem. Soc. 126*, 8108-9.

(156) Borowski, T., de Marothy, S., Broclawik, E., Schofield, C. J., and Siegbahn, P. E. (2007) Mechanism for cyclization reaction by clavaminic acid synthase. Insights from modeling studies. *Biochemistry 46*, 3682-91.

(157) Blasiak, L. C., Vaillancourt, F. H., Walsh, C. T., and Drennan, C. L. (2006) Crystal structure of the non-haem iron halogenase SyrB2 in syringomycin biosynthesis. *Nature 440*, 368-71.

(158) Karlsson, A., Parales, J. V., Pareles, R. E., Gibson, D. T., Eklund, H., and Ramaswamy, S. (2003) Crystal structure of naphthalene dioxygenase: side-on binding of dioxygen to iron. *Science 299*, 1039-1042.

(159) Kovaleva, E. G., and Lipscomb, J. D. (2007) Crystal structures of Fe2+ dioxygenase superoxo, alkylperoxo, and bound product intermediates. *Science 316*, 453-7.

(160) Goddard, W. A., 3rd, and Olafson, B. D. (1975) Ozone model for bonding of an O2 to heme in oxyhemoglobin. *Proc Natl Acad Sci U S A 72*, 2335-9.

(161) Valko, M., Rhodes, C. J., Moncol, J., Izakovic, M., and Mazur, M. (2006) Free radicals, metals and antioxidants in oxidative stress-induced cancer. *Chem. Biol. Interact. 160*, 1-40.

(162) Weiss, S. J. (1982) Neutrophil-mediated methemoglobin formation in the erythrocyte. The role of superoxide and hydrogen peroxide. *J. Biol. Chem. 257*, 2947-53.

(163) Simon, R. H., Scoggin, C. H., and Patterson, D. (1981) Hydrogen peroxide causes the fatal injury to human fibroblasts exposed to oxygen radicals. *J. Biol. Chem. 256*, 7181-6.

(164) Saari, R. E., and Hausinger, R. P. (1998) Ascorbic acid-dependent turnover and reactivation of 2,4-dichlorophenoxyacetic acid/α-ketoglutarate dioxygenase using thiophenoxyacetic acid. *Biochemistry 37*, 3035-3042.

(165) Welford, R. W. D., Schlemminger, I., McNeill, L. A., Hewitson, K. S., and Schofield, C. J. (2003) The selectivity and inhibition of AlkB. *J. Biol. Chem. 278*, 10157-10161.

(166) Ryle, M. J., Liu, A., Muthukumaran, R. B., Ho, R. Y. N., Koehntop, K. D., McCracken, J., Que, L., Jr., and Hausinger, R. P. (2003) O_2- and α-ketoglutarate-dependent tyrosyl radical formation in TauD, an α-keto acid-dependent non-heme iron dioxygenase. *Biochemistry 42*, 1854-1862.

(167) Lindstedt, S., and Rundgren, M. (1982) Blue color, metal content, and substrate binding in 4-hydroxyphenylpyruvate dioxygenase from *Pseudomonas* sp. strain P. J. 874. *J. Biol. Chem. 257*, 11922-11931.

(168) Liu, A., Ho, R. Y. N., Que, L., Jr., Ryle, M. J., Phinney, B. S., and Hausinger, R. P. (2001) Alternative reactivity of an α-ketoglutarate-dependent iron(II) oxygenase: enzyme self-hydroxylation. *J. Am. Chem. Soc. 123*, 5126-5127.

CHAPTER 2

PURIFICATION AND PROPERTIES OF *ASPERGILLUS NUDULANS* XANTHINE HYDROXYLASE

The work described in this chapter was combined with additional studies and published: Montero-Moran*, G. M.; Li*, M.; Rendon-Huerita, E.; Jourdan, F.; Lowe, D. J.; Stumpff-Kane, A. W; Feig, M.; Scazzocchio, C.; and Hausinger, R. P. "Purification and characterization of the Fe(II)- and α-Ketoglutarate-Dependent *Aspergillus nidulans* Xanthine Hydroxylase from *Aspergillus nidulans*" *Biochemistry*, 2007, *46 (18)*, 5293-5304 (* Co-first author). The studies briefly mentioned here regarding purification, M_r estimation, kinetic characterzaion, glycosylation analysis and phosphorylation testing of protein from the *A. nudulans* host were carried out by other authors. One figure included here (the subunit size comparison from both hosts examined by SDS-PAGE) was provided by Dr. Montero-Moran.

ABSTRACT

His_6-tagged xanthine/α-ketoglutarate (αKG) dioxygenase (XanA) of *Aspergillus nidulans* was purified from both the fungal mycelium and recombinant *Escherichia coli* cells, and the properties of the two forms of the protein were compared. The kinetic parameters were similar for XanA from the two sources (k_{cat} 30-70 s^{-1}, K_m of αKG 31-50 μM, K_m of xanthine ~45 μM, and pH optima at 7.0-7.4); however, the protein properties were markedly distinct. Evidence was obtained for both *N*- and *O*-linked glycosylation on the fungus-derived XanA, which aggregated into an apparent dodecamer, while bacterial-derived XanA was free of glycosylation and behaved as a monomer. Furthermore, the phosphorylation status differed for the two enzyme forms and the fungus-derived sample was shown to undergo extensive truncation at its amino terminus. The sites of posttranslational modification on the two forms of the enzyme are discussed in terms of a homology model of XanA. These studies represent the first biochemical characterization of purified xanthine/αKG dioxygenase.

INTRODUCTION

Most organisms that metabolize xanthine possess a molybdopterin cofactor (Moco)-containing enzyme that hydroxylates the substrate to form uric acid while transferring electrons to NAD (xanthine dehydrogenase) or oxygen (xanthine oxidase) (*1*). These enzymes, referred to here as xanthine hydroxylases, are conserved throughout living organisms, including archaea, bacteria, fungi, plants, and metazoans.

In 2005, a novel mechanism for xanthine metabolism was discovered in certain fungi (*2*). This finding arose out of the observation that all mutants of *Aspergillus nidulans* defective in xanthine dehydrogenase (i.e., with mutations affecting the structural gene *hxA*, the *cnx* genes for Moco synthesis, or *hxB* for sulfuration of Moco) retained the ability to grow on xanthine as sole nitrogen source (*2, 3*). A mutation affecting this alternative process was identified, and the cognate gene *xanA* was localized to chromosome VIII (*4*). Subsequently, the *xanA* gene and its homologues from *Schizosaccharomyces pombe* and *Neurospora crassa* were cloned and further homologues were identified in several other fungi (but not outside the fungal kingdom). The XanA sequence shows some similarity with the TauD group of Fe(II)- and α-ketoglutarate (αKG)-dependent dioxygenases (*2*), including a clear conservation of the Fe(II)- and αKG-binding sites. This homology suggested that the alternative xanthine oxidation mechanism present in some fungi might utilize an Fe(II)-dependent xanthine/αKG dioxygenase. Such activity, depicted in Figure 2.1, was demonstrated in both crude and partially purified extracts of fungal mycelia of strains that expressed the

FIGURE 2.1: General mechanism of Fe(II)/αKG-dependent xanthine hydroxylases.

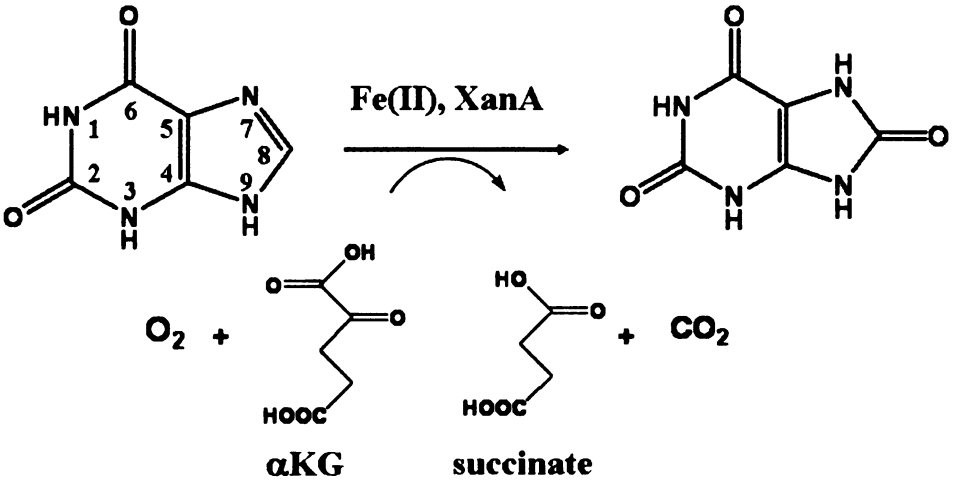

xanA gene (*2*).

The wide range of Fe(II)/αKG hydroxylases utilize a diverse array of primary substrates (reviewed in (*5*)); however, XanA is the first described enzyme of this group to hydroxylate a free purine base. In the fungal kingdom, this enzyme coexists with the classical xanthine hydroxylase; i.e., some fungi possess both xanthine hydroxylase and xanthine/αKG dioxygenase, while others possess only one or the other. Notably, yeasts as evolutionarily distant as *S. pombe* and *Kluveromyces lactis* are able to metabolize xanthine through the activity of a XanA homologue (*2*). They lack a classical xanthine dehydrogenase, and they are incapable of synthesizing Moco, which is universally present in the classical xanthine hydroxylases. The discovery of the novel Fe(II)/αKG-dependent XanA enzyme poses both evolutionary and mechanistic problems. Is the xanthine-binding site of the newly identified enzyme at all similar to that of the classical xanthine hydroxylases (*6, 7*) or to the recently described xanthine transporters (*8, 9*) Is the mechanism of hydroxylation similar to that described for TauD (*10, 11*) What are the evolutionary advantages and disadvantages of possessing the Moco-containing and Fe(II)/αKG-dependent enzymes.

As a first step towards answering the above questions, I purified the His_6-tagged versions of XanA from *Escherichia coli* and compared it to the corresponding protein purified from fungal mycelium. I confirm that the enzyme is an Fe(II)/αKG dioxygenase and determine the pH dependence and kinetic parameters associated with the Fe(II), αKG, and xanthine concentration dependencies. Comparison studies with mycelium-derived

enzyme show similar kinetic properties but the proteins differ in quaternary structure and identity of posttranslational modifications. In addition, fungus-derived protein is truncated at its amino terminus. Finally, I use a homology model of XanA to provide insights into the sites of posttranslational modification. These studies present the first detailed biochemical analysis of a purified Fe(II)-dependent xanthine/αKG dioxygenase. More detailed kinetic inhibition and homology modeling studies are described in Chapter 3.

EXPERIMENTAL PROCEDURES

The plasmid pxanA-His_6 was provided by Gabriela M. Montero-Morán, Institut de Génétique et de Microbiologie, Université Paris-Sud, Bâtiment 409, UMR 8621 CNRS, 91405 Orsay Cedex, France.

Growth of E. coli *Cells Overproducing* A. nidulans XanA. Plasmid pxanA-His_6 was transformed into XL1Blue *E. coli* cells (Stratagene) as described by Hanahan (*12*). A single colony of *E. coli* XL1Blue (pxanA-His_6) was used to inoculate 50 mL of Luria Base Broth (Difco) containing 100 μg mL^{-1} ampicillin. The cells were grown to saturation at 37 °C for 16 h and used to inoculate 1 L of LB media. The culture was grown at 37 °C with vigorous shaking until reaching OD_{600} 0.5-0.7, adjusted to contain 0.4 mM isopropyl-β-D-thiogalactopyranoside, transferred to 25 °C, and vigorously shaken for 16 h. Alternatively, *E. coli* XL1Blue (pxanA-His_6) was grown aerobically in 200 mL LB-ampicillin medium at 37 °C to an OD_{600} of 0.6, induced with 0.75 mM IPTG, and incubated at 25 °C for 14 h with constant shaking (140 rpm). In either case, cultures were harvested by centrifugation at 8,000-9,000 rpm for 10 min at 4 °C.

Purification of His_6-tagged XanA from E. coli. Approximately 5 g of *E. coli* XLBlue (pxanA-His_6) cell paste was suspended in 10-15 mL of lysis buffer containing 100 mM Tris, pH 8.0, 300 mM NaCl, 25 mM imidazole, and trace amounts of lysozyme, leupeptin, DNase I and RNase A. This suspension was incubated at room temperature for 30 min, transferred to an ice bath for 30 min, disrupted by using a French pressure cell at ~500 psi at 4 °C, and spun for 45 min at 100,000 *g*. The soluble cell extracts (30 mL) were loaded

onto a 10 mL Ni-nitrilotriacetic acid (NTA) column using 100 mM Tris buffer, pH 8.0, containing 300 mM NaCl and 25 mM imidazole, followed by elution with 100 mM Tris buffer, pH 8.0, with 300 mM NaCl, 250 mM imidazole and 15 % glycerol. The fractions containing XanA were collected and incubated with 1 mM EDTA at 4 °C for 5 h, then concentrated to 5-10 mg mL^{-1} by using a Centriprep (Amicon Corp.) with a YM-10 membrane.

Enzyme Assays. Xanthine/αKG dioxygenase activity was measured at 25 °C by using the following typical assay conditions (total volume of 1 mL): 1 mM αKG, 40 μM $Fe(NH_4)_2(SO_4)_2$, and 200 μM xanthine in 50 mM MOPS buffer, pH 7.4. Variations of these conditions included use of alternate buffers, different pH values, and varied concentrations of substrates. The absorbance at 294 nm was monitored to determine the uric acid production (ε_{294} 12,200 M^{-1} cm^{-1}) with a correction for loss of the xanthine absorbance at this wavelength (measured ε_{294} 2,000 M^{-1} cm^{-1}) for an overall change in ε_{294} of 10,200 M^{-1} cm^{-1}. Units of activity (U) were defined as μmol min^{-1} of uric acid produced and the specific activity (U mg^{-1}) was measured as μmol min^{-1} (mg of purified XanA)$^{-1}$.

In addition to the above spectroscopic assay, xanthine/αKG dioxygenase activity was measured by two alternative methods. Oxygen consumption measurements were carried out in air-saturated MOPS medium (pH 7) at 25 °C by using a Clark-type oxygen electrode. Quantification of αKG consumed during the reaction was assessed by HPLC. Aliquots (300 μL) of the reaction mixtures were quenched by addition of 5 μL 6 M H_2SO_4, the

samples were centrifuged for 5 min at 20,000 *g*, and the supernatant was chromatographed on an Aminex HPX-87H column (Bio-Rad Laboratories) in 0.013 M H_2SO_4 with detection by using a differential refractometer (Waters, Model R401).

Metal Analyses. The iron concentration was measured by utilizing the $KMnO_4$ oxidation, ascorbate reduction, and ferrozine chelation protocol of Bienert (*13*).

Protein Analytical Methods. Routine determinations of protein concentration were carried out by the method of Bradford (*14*) with bovine serum albumin used as the standard. Qualitative measurement of protein overexpression and assessment of protein purity made use of sodium dodecyl sulfate polyacrylamide gel electrophoresis (SDS-PAGE) (*15*), with stacking and running gels containing 5 % and 12 % acrylamide. Standard proteins used for comparison included phosphorylase b, M_r 97,400; bovine serum albumin, M_r 66,200; ovalbumin, M_r 45,000; carbonic anhydrase, M_r 31,000; trypsin inhibitor, M_r 21,500; and lysozyme, M_r 14,400 (Bio-Rad Laboratories). The native size of XanA isolated from *E. coli* was estimated by gel filtration chromatography using a Protein-pak Diol(OH) 10 μm column (Waters, 0.5 or 1 min mL^{-1}, room temperature in 100 mM Tris buffer, pH 7.5, containing 300 mM NaCl), a Superose™ 6 HR 10/30 GL column (Pharmacia, 1 mL min^{-1} in 50 mM MOPS, pH 6.8, containing 0.15 M NaCl). The calibration proteins were thyroglobulin, M_r 670,000; γ-globulin, M_r 158,000; ovalbumin, M_r 44,000; myoglobin, M_r 17,000; and vitamin B_{12}, M_r 1,350 (Bio-Rad).

Mass Spectrometry. (Assisted by Dan Jones, Department of Biochemistry & Chemistry, MSU). Mass spectrometry analyses were performed by using a Waters

(Milford, MA) LCT Premier mass spectrometer coupled to a Shimadzu (Columbia, MD) LC-20AD HPLC and SIL-5000 autosampler. Samples were analyzed using electrospray ionization in positive ion mode. On-line desalting and separation from detergents was performed using a Thermo Hypersil-Keystone BetaBasic cyano column (1.0 x 10 mm) coupled to the electrospray ionization probe. Aliquots were injected onto the column using a flow rate of 0.1 mL/min of 95% solvent A (0.15% aqueous formic acid)/5% solvent B (acetonitrile). Gradient elution was performed by using the following parameters: (0-1 min: 95%A/5%B; linear gradient to 30%A/70%B at 6 min; hold at 30%A/70%B until 9 min). Electrospray spectra were processed using MassLynx software (Waters, Milford, MA), and zero-charge state mass spectra were obtained by deconvolution using the MaxEnt1 algorithm.

MALDI mass spectra were generated on a Voyager-DE STR mass spectrometer (Applied Biosystems, Foster City, CA) in positive ion linear mode using sinapinic acid as matrix. Samples were processed using strong cation exchange ZipTips (ZipTipSCX, Millipore, Billerica, MA) to remove detergent and reversed phase C18 ZipTips for desalting, following the manufacturer's recommended protocols, before spotting the MALDI target.

Structural Homology Modeling. (Assisted by Michael Feig and Andrew W. Stumpff-Kane, Department of Biochemistry and Molecular Biology, MSU.) Details related to the creation of the homology model using TauD (PDB code 1OS7, chain A) as a template structure (*16, 17*) are described in Chapter 3 (*18*).

RESULTS

Properties of Recombinant XanA in E. coli *Cell Extracts.* When assayed by using standard conditions (1 mM αKG, 40 μM $Fe(NH_4)_2(SO_4)_2$, and 200 μM xanthine in 50 mM MOPS buffer, pH 7.4, 25 °C), fresh extracts of *E. coli* cells overproducing His_6-tagged XanA exhibited xanthine/αKG dioxygenase specific activity of approximately 19 U (mg protein)$^{-1}$ (Figure 2.2A). As expected, the activity was strictly dependent on the presence of αKG in the assay as previously described for the crude enzyme extracted from *A. nidulans* (Figure 2.2B) (*2*). Unlike the earlier findings, however, significant activity was detected in the absence of added Fe(II) (16.9 U mg^{-1}) (Figure 2.2C) and some activity was retained when 5 mM EDTA was included in the assay buffer (2.01 U mg^{-1}), Figure 2.2D. These data indicate that endogenous Fe(II) is tightly bound to the bacterial-produced enzyme sample. The activity of these extracts was irreversibly lost over 3 weeks when stored at 4 °C using a protein concentration of 15-17 mg mL^{-1}, or after 1 week in the added presence of 1 mM EDTA. While long-term incubation of cell extracts with EDTA was undesirable, studies with enriched enzyme samples showed that EDTA treatment provided stable apoprotein (when maintained at high protein concentrations) that could be activated by addition of ferrous ions.

Purification of XanA from the E. coli. XanA produced in *E. coli* XL1Blue (pxan-His_6) was purified to homogeneity from cell extracts (Figure 2.3A) by Ni-NTA chromatography. Inclusion of 15 % glycerol in the chromatography buffers, which were maintained on ice, helped to minimize protein precipitation during purification. About 5 % of the soluble

FIGURE 2.2: Activity assay of XanA cell extracts. (A) Complete assay: 15 μg XanA crude extract, 40 μM Fe(II), 1 mM αKG, 100 μM xanthine in 50 mM MOPS, pH=7.4, 25 °C. (B) without αKG. (C) without Fe(II). (D) with 5 mM EDTA. UV-Vis spectra were recorded from 240 to 320 nm every 15 seconds after initiating the enzymatic reaction by adding primary substrate.

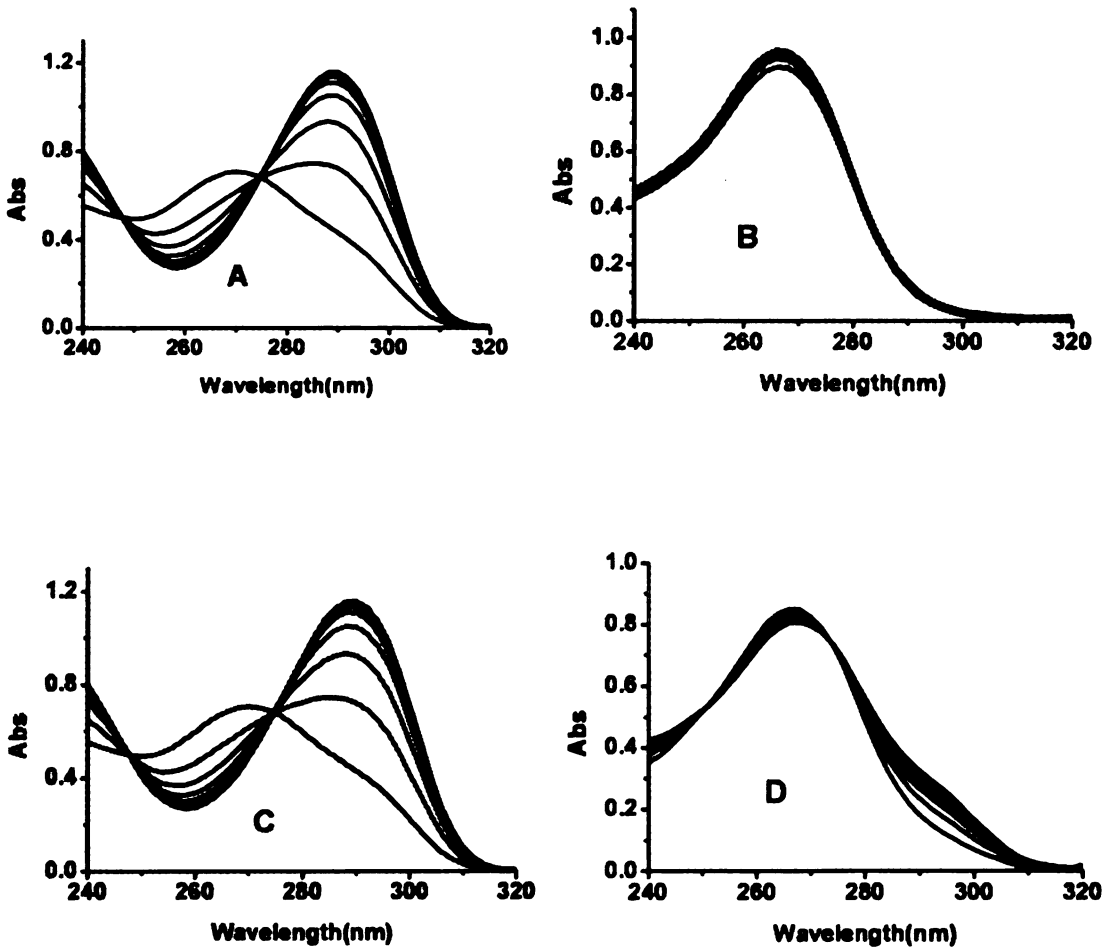

activity was located in the flow-though fractions, perhaps indicating that some XanA interacts tightly with other proteins that fail to bind the resin. As measured by the standard assay protocol, the Ni-NTA column fractions containing purified XanA accounted for 33 % of the activity that had been observed in cell extracts. When this pool was treated with 1 mM EDTA at 4 °C for 5 h and then concentrated to 5-12 mg mL^{-1}, the activity increased such that 60 % of the activity of cell extracts was recovered and yielded a final specific activity for the purified enzyme of 70-80 U $(mg\ protein)^{-1}$ at 25 °C which corresponds to a k_{cat} of 49-56 s^{-1} (assuming M_r = 42 kDa per subunit). The enzyme recovered from the Ni-NTA column contained 0.26 to 0.5 moles of Fe per mole of subunit according to the colorimetric assay, while that incubated with EDTA lacked detectable Fe, and a sample incubated with exogenous Fe(II) and then chromatographed on a Sephadex G-25 gel filtration column contained 1.3 moles of Fe per mole of subunit. Concentrated XanA derived from *E. coli* was stable for at least one month at 4 °C when stored in 100 mM Tris buffer, pH 8.0, containing 300 mM NaCl, 250 mM imidazole, 1 mM EDTA and 15 % glycerol, or at least two months if frozen at -80 °C.

For comparison, the specific activity of the isolated protein from the fungal host was measured as 22-40 U $(mg\ protein)^{-1}$ at 30 °C equivalent to a k_{cat} of 15.4-30 s^{-1} (again assuming M_r = 42 kDa per subunit), comparable with those from bacterial host. (The activity of XanA isolated from fungal host was measured by Gabriela M. Montero-Morán, Institut de Génétique et de Microbiologie, Université Paris-Sud, Bâtiment.)

FIGURE 2.3: SDS-PAGE analysis of the purified XanA from *E. coli* and *A. nidulans*. (A) Analysis of fractions during purification of XanA from *E. coli*. Lane 1, molecular weight standards; lanes 2 and 3, suspension of cultures before and after induction by IPTG; lane 4, cell extracts after lysis; lane 5, cell pellet after lysis; lane 6, flow-through fraction from Ni-NTA chromatography; lane 7-13, fractions of purified XanA obtained after Ni-NTA chromatography. (B) Comparison of the purified XanA protein derived from *A. nidulans* and *E. coli*. Lane M, markers; lane 1, sample purified from the fungus; lane 2, protein isolated from the bacterium (7 μg each). Stacking and running gels contain 5 % and 12 % acrylamide.

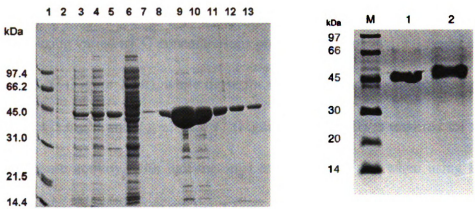

Effects of pH on Stability and Activity of XanA from E. coli. The effect of pH on the stability of XanA was examined. After incubating the XanA samples in various pH buffers at 4 °C for 3 h, the activity remaining was examined by using the standard assay procedure. The results (data not shown) indicate that each purified enzyme is stable over a wide pH range (7.0-11.0).

The effect of pH on the activity of the enzyme was also examined. XanA isolated from *E. coli* was assayed by using a series of different buffers as depicted in Figure 2.4. The enzyme activity exhibited a narrow pH optimum of 7.0-8.0 with pH 7.4 yielding optimal activity for most buffers (Tris, MOPS, MES, imidazole, and HEPES).

Kinetic Analyses of XanA from E. coli. For the *E. coli*-derived enzyme, the results of studies using varied αKG concentrations provided a K_m of 31.1 ± 1.6 μM and k_{cat} of 66.5 s^{-1} at 25 °C (Figure 2.5A), while those for varied xanthine concentrations provided a K_m of 45.2 ± 3.6 μM and k_{cat} of 71.4 s^{-1} (Figure 2.5B). Fe(II) is required for xanthine/αKG dioxygenase activity, with half-maximal activity at ~7 μM when using the apoprotein isolated from the bacterium (Figure 2.6).

The kinetic parameters were very similar for XanA isolated from the two sources. When the protein isolated from *A. nidulans* enzyme was assayed at 30 °C with varied αKG or xanthine concentrations the measured K_m values were 50 μM ± 6 and 46 ± 4 μM, respectively, but with a smaller k_{cat} that ranged from 15 s^{-1} to 30 s^{-1} depending on the preparation provided by Gabriela M. Montero-Morán.

FIGURE 2.4: pH dependence of XanA activity. The activity of XanA (0.51 μg ml^{-1}) derived from *E. coli* was assayed in the following buffers (50 mM) and pH values at 25 °C: imidazole, pH 6.0-8.2 (♦);MES, pH 6.6-6.8 (+); MOPS, pH 6.6-7.8 (×); HEPES, pH 7.0-8.2 (▼); Tris, pH 7.4-9.0 (○); CHES, pH 9.4-9.8 (▲); CAPS, pH 9.6-10.0 (●). Assay solutions also contained 1 mM αKG, 40 μM $Fe(NH_4)_2(SO_4)_2$, and 200 μM xanthine.

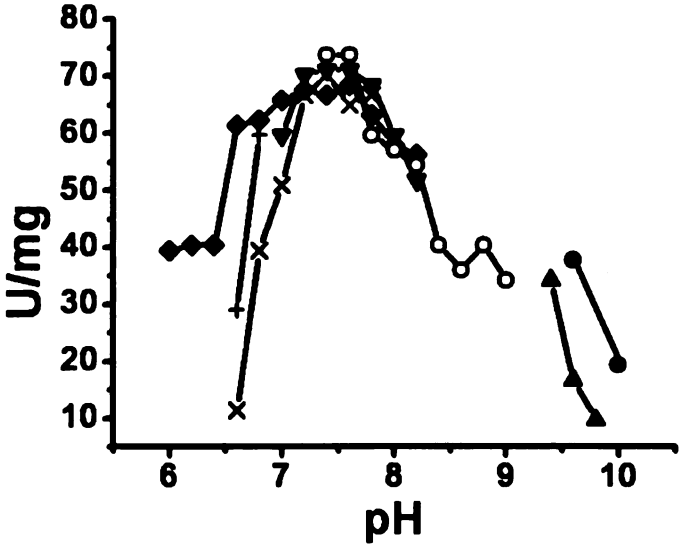

FIGURE 2.5: Substrate and co-substrate concentration dependencies of XanA. The effects of varying the concentrations of (A) αKG and (B) xanthine on xanthine/αKG dioxygenase activity were examined for the *E. coli*-derived protein at 25 °C. Except for the compound being varied, the assay solutions contained 40 μM Fe(II), 1 mM αKG, and 200 μM xanthine in 50 mM MOPS buffer, pH 7.4. The data were fit to the Michaelis-Menten equation.

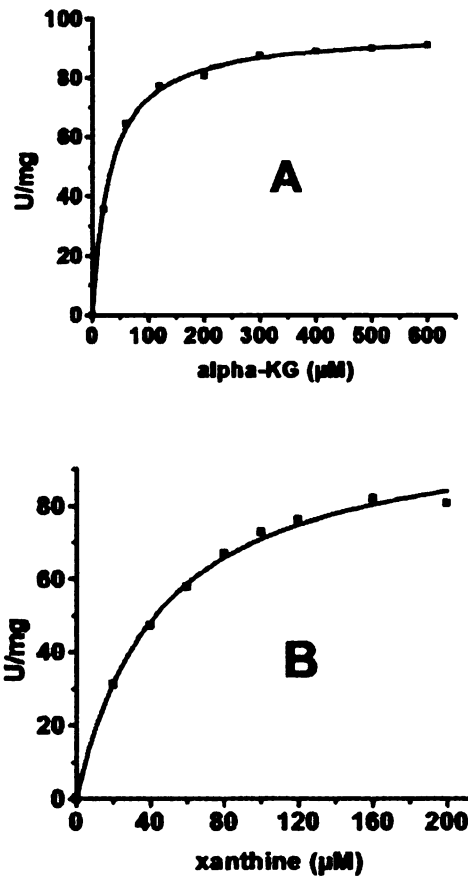

The stoichiometry of the enzymatic reaction was examined for XanA by UV-Vis spectroscopy and O_2 electrodes. The degradation of 100 μM xanthine was accompanied by the production of 92 μM uric acid as measured by UV-Vis spectrosocopy, and this coincided with the consumption of 110 μM oxygen determined by O_2 electorde (data not shown).

Differential Protein Properties of XanA Purified from the Two Host Cells. Gel filtration chromatography provided an estimated M_r of 39-42 kDa for the native enzyme isolated from the bacterial host (consistent with a monomeric structure) (Figure 2.7); however, similar analysis of the protein from the fungal host showed that it was oligomeric, with an approximate M_r of 500 kDa that was consistent with about twelve subunits per native molecule (data from Gabriela M. Montero-Morán.) (*18*).The SDS-PAGE results highlight a key difference between the XanA proteins isolated from the two sources; i.e., the apparent M_r of the *E. coli*-derived protein is larger than that of the protein derived from the fungus (Figure 2.3B) (Provided by Montero-Morán). This finding led us to investigate the possibility of unique posttranslational modifications in the proteins produced in the bacterial and eukaryotic hosts. G. M. Montero-Morán and co-workers have shown the presence of *N*-glycosylation, *O*-glycosylation and Thr phosphorylation in the protein purified from *A. nidulans*, but both Thr and Ser phosphorylation in the one isolated from bacterial host (*18*).

Mass spectrometric methods were used to further characterize the two enzyme forms. Electrospray ionization mass spectrometry of bacteria-derived XanA indicated a single

FIGURE 2.6: Fe(II) concentration dependence of XanA. The effects of varying the concentration of Fe(II) on xanthine/αKG dioxygenase activity were examined by using the *E. coli*-derived protein at 25 °C in solutions containing 1 mM αKG and 200 μM xanthine in 50 mM MOPS buffer, pH 7.4.

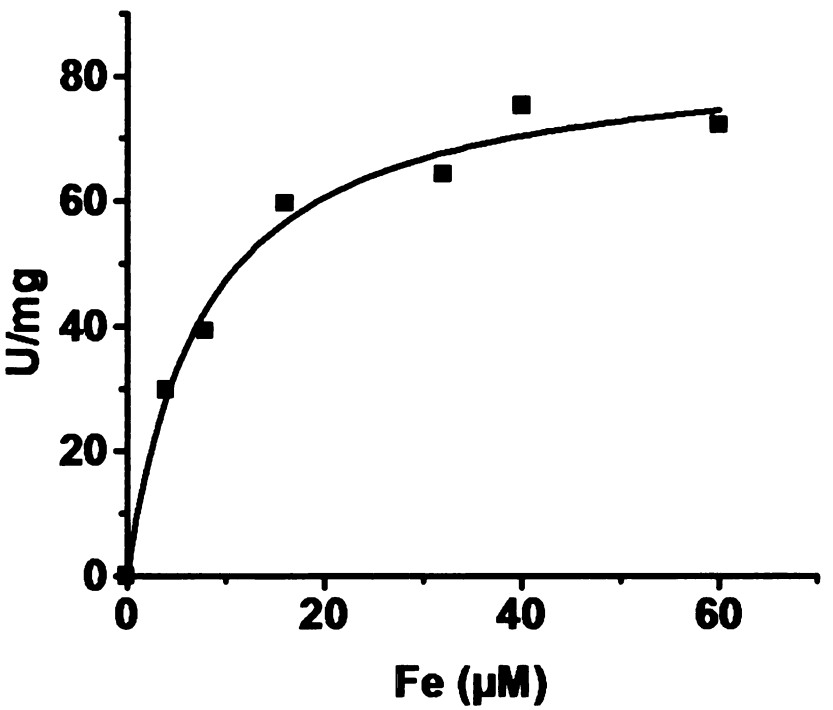

FIGURE 2.7: Measurement of native size of XanA derived from *E. coli.* (■) represents the standards and (□) represents the XanA isolated form *E. coli.*

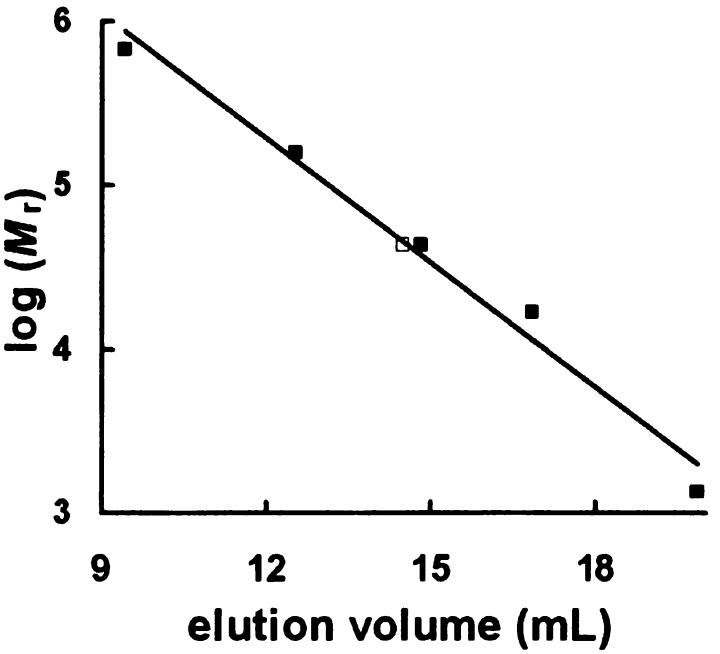

species with a molecular mass of 41,992 Da (data not shown), which matches very well to the theoretical mass (41,996.50 Da; using the ExPASY Compute pI/Mw tool at ca.expasy.org) for the His_6-tagged protein missing its amino-terminal Met residue. This sample provided no evidence of phosphorylation (differing from the immunological detection of phosphoserine and phosphothreonine by our collaborators) or glycosylation. In contrast to this single species, the fungus-derived protein sample exhibited a complex electrospray ionization mass spectrum centered near 36,000 Da (Figure 2.8). The spectrum of Figure 2.8 includes features separated by 162 mass units, consistent with glycosylation involving hexose sugars, as well as features separated by 80 mass units, indicating phosphorylation. The smallest component of the spectrum exhibits a mass of 35,171 Da, indicating that the non-glycosylated and non-phosphorylated fungal protein is severely truncated compared to the theoretical mass of full-length protein of 42,127.69. This truncation must occur at the N-terminus, since the C-terminal His_6-tag was used for enzyme purification, and consists of approximately 60 residues.

FIGURE 2.8: Mass spectrometric analysis of fungus-derived XanA. The XanA protein isolated from *A. nidulans* was analyzed by electrospray ionization mass spectrometry. The figure depicts a series of peaks separated by 162 mass units and 80 mass units, consistent with glycosylation and phosphorylation, respectively.

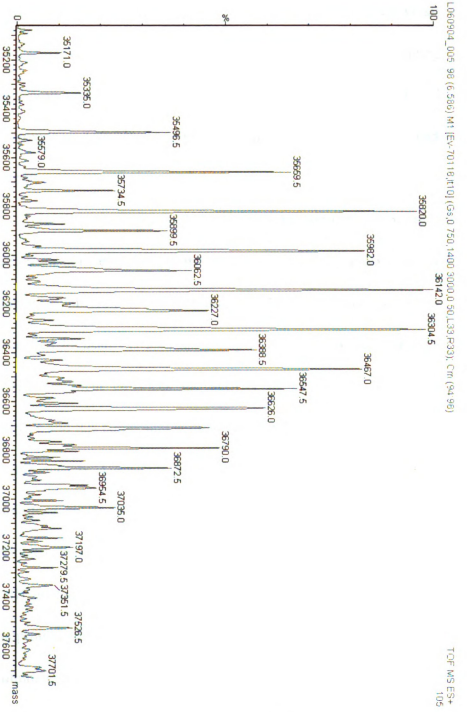

DISCUSSION

In this study I describe the isolation and general properties of xanthine/αKG dioxygenase, a novel enzyme found exclusively in the fungal kingdom (*2*).

Purification. Immobilized metal ion chromatography is very effective for purifying recombinant XanA from the bacterial host cells. His-tagged versions of several other representative Fe(II)/αKG dioxygenases have been studied, including AlkB, RdpA, SdpA, phytanoyl-CoA hydroxylase, and the oxygen-sensing prolyl 4- and asparaginyl hydroxylases (*19-23*). The His-rich sequences generally have modest if any effect on activity.

XanA Enzyme Stability. Purified XanA is unstable at room temperature (denaturing within an hour even in buffers containing 15 % glycerol), when agitated (e.g., during stirring in an Amicon concentrator), or when incubated at pH values below 6.5 (the pI estimated for XanA is 5.82 according to the ExPASy ProtParam tool at ca.expasy.org). EDTA treatment enhances the activity of the highly concentrated bacterial-derived enzyme and this compound is maintained in the storage buffer to ensure maximal lifetime of the activity. I attribute the enhancement effect of EDTA to its ability to remove inhibitory Ni(II) (co-eluted with the enzyme from the NTA resin) and Fe(III) (the oxidized, inactive state of the metal) from the enzyme so that the apoprotein can bind Fe(II) in the assay buffer. Several other Fe(II)/αKG dioxygenases are purified as their apoprotein forms by inclusion of chelators (*24, 25*) to prevent Fe(II) oxidation and to eliminate Ni(II), if purified using an NTA column. In contrast, some representatives of

these enzymes have been purified anaerobically to assure that the metal remains in its reduced form (*26, 27*).

XanA Enzyme Activity. The kinetic properties of XanA as purified from *E. coli* (~70 U mg^{-1}, K_m of 31 μM for αKG, and K_m of 45 μM for xanthine at pH 7.4) compare well with those of XanA isolated from *A. nidulans* (30 U mg^{-1}, and K_m values of 50 μM and 46 μM at pH 7.0), and these results are compatible with those reported earlier for enriched sample from the fungus (40 U mg^{-1}, 50 μM, and 23 μM) (*2*). The reaction requires Fe(II) (half-maximal activity at 7 μM for standard conditions), consistent with the results of related family members.

Posttranslational Modifications. My comparison of recombinant XanA purified from *E. coli* with that of *A. nidulans* provided by my collaborators reveals very different quaternary structures and posttranslational modifications. Whereas the protein derived from the bacterial source chromatographs on a size exclusion column as a monomer, that isolated from the fungus is much larger, with apparent M_r of 500 kDa. The sample from the fungus was also glycosylated and phosphorylated while the one from bacterial was suggested to contain both phosphoserine and phosphothreonine by our collaborators. Treatment of the fungal protein with PNGase F was found to result in a dramatic shift in electrophoretic mobility, but not all glycosylation was removed by this process indicating the presence of both *N*- and *O*-glycoconjugates. Comparing the size of the subunit from both sources along with the mass spectrometry results suggested an extensive truncation takes place at the N-terminus of the fungal enzyme. Despite the extensive differences in

post-translational modifications between the two forms of the enzyme the kinetic parameters are nearly identical, consistent with the modifications not affecting catalytic activity. Analogous biochemical comparisons between the enzyme form isolated from its native eukaryotic host and the form isolated from *E. coli* have not been reported for other Fe(II)/αKG dioxygenase family members.

An extant question is the role of the extensive N-terminal processing of enzyme isolated from its natural fungal host. I speculate that this feature may relate to cellular targeting of the XanA enzyme. It is not unreasonable to propose that an oxidoreductase such as XanA could be peroxisomal. In fact, the immediate downstream enzyme, urate oxidase, has been shown to be peroxisomal in every organism where its localization has been investigated, including amoebas, mammals and plants (*28-31*). A urate oxidase-green fluorescent protein fusion shows a particulate intracellular distribution in *Aspergillus nidulans*, fully consistent with a peroxisomal localization (G. Langousis and G. Diallinas, unpublished data). XanA does not possess a C-terminal peroxisomal targeting signal (variations of an SKL tripeptide, denoted PTS1); however, it contains a RSALYTHL sequence (residues 40-47) that resembles the PTS2 N-terminal import sequence (variations of RLX_5HL) found in a minority of peroxisomal proteins throughout the eukaryotes (*32-34*). In some instances, including mammalian (*35*), yeast (*36*), and plant (*37*) peroxisomal proteins, it has been shown that the PST2 is contained in a pre-sequence that is cleaved upon peroxisomal entry. The function of XanA glycosylation could be understood in this context as a mechanism to protect the protein from further proteolysis.

FIGURE 2.9: Location of potential sites of glycosylation and phosphorylation in XanA. The positions of selected residues are depicted in a homology model, described in the chapter 3, with the potential *N*-glycosylation site (Asn118) in blue, Thr and Ser residues that could be either glycosylated or phosphorylated (Thr5 and Ser37) in orange and magenta, potential *O*-glycosylation sites (Thr10, Thr195, and Ser316) in red, and other possible phosphothreonines (Thr38, Thr58, Thr66, Thr120, and Thr274) or phosphoserines (Ser15, Ser142, Ser199, Ser208, Ser217, Ser218, and Ser341) illustrated in yellow and cyan. The amino terminus of the fungus-derived protein is truncated through the first approximately 60 residues. The brown sphere shows the postulated position of Fe(II). Additional glycosylation (Ser231) and phosphorylation (Thr177 and Ser184) are not shown because they are located on non-modeled protein loops that represent insertions compared to the template structure (TauD, PDB code 1OS7, chain A).

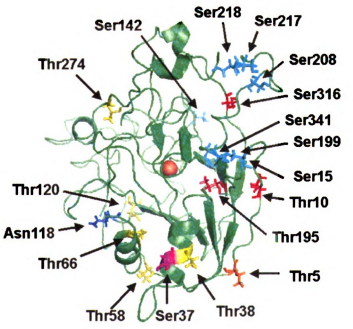

Insights from a Homology Model. A XanA homology model (Figure 2.9), whose generation is described in detail in Chapter 3 (*18*), provides critical insights into the likely sites of posttranslational modification in the protein. This model is based on the full-length sequence of the XanA protein, but we assume that the overall fold is maintained even in the truncated version derived from the fungal host because this region of the protein is external to the DSBH core of the protein. Consistent with the PNGase F results that demonstrate the presence of *N*-glycosylation sites in the fungus-derived protein, the NetNGlyc 1.0 server (R. Gupta, E. Jung, and S. Brunak, unpublished) predicts glycosylation of Asn118, and the homology model places this residue on the protein surface. The PNGase F-treated fungal-derived protein still stains as a glycoprotein, consistent with *O*-linked glycoconjugates in the protein. Thr5 and Thr10 are predicted to be glycosylated by the NetOGlyc 3.1 server (*38*) while the YingOYang 1.2 server (R. Gupta, J. Hansen, and S. Brunak, unpublished) predicts Thr5, Ser37, Thr195, Ser231, and Ser316 as possible sites of glycosylation. The XanA homology model reveals that all of these positions except for Thr195 are surface exposed or, for Ser231, on surface loops that were not modeled. On the basis of my mass spectrometry results showing truncation of approximately 60 residues from the N-terminus, I suggest Ser231 or Ser316 as the most likely sites of O-glycosylation.

A wide range of potential Ser, Thr, or Tyr phosphorylation sites are identified in XanA by the NetPhos 2.0 server (*39*) and by Prosite (www.expasy.org). Phosphoproteins are common in eukaryotes and are well known in *E. coli* (*40*). Given the immunological

evidence for phosphothreonine in XanA from both sources, the Thr phosphorylation sites are of special interest and are predicted by at least one program to include Thr5, Thr38, Thr58, Thr66, Thr120, Thr177, and Thr274. The first three residues are likely to be missing in the fungus-derived protein based on the mass spectrometry results. The homology model predicts that Thr66 and Thr120 are buried (although their disposition is less clear for the truncated protein), whereas the other residues are exposed to the surface or, for Thr177, on a loop that was not modeled. The bacterial-derived protein also reacts with antibodies directed against phosphoserine, whereas XanA derived from the fungus reacted only weakly with these antibodies. We attribute this difference in reactivity between the two proteins to the phosphorylation site being inaccessible in the fungal-derived sample, either due to nearby glycosylation or due to being located at a subunit interface in the multimeric protein. Sites of Ser phosphorylation predicted by at least one program include Ser15, Ser37, Ser142, Ser184, Ser199, Ser208, Ser217, Ser218, and Ser341. The first two residues are likely to be absent in the fungus-derived protein. Residues Ser199 and Ser341 are predicted to be somewhat buried in the model, Ser184 occurs on a loop that could not be modeled, and the other residues are predicted to be surface exposed. Of note, Ser341 would be made more inaccessible by glycosylation of Thr195; thus, potentially explaining the source specificity behavior for Ser phosphorylation.

REFERENCES

(1) Hille, R. (2005) Molybdenum-containing hydroxylases. *Arch. Biochem. Biophys. 433*, 107-116.

(2) Cultrone, A., Scazzocchio, C., Rochet, M., Montero-Morán, G., Drevet, C., and Fernández-Martín, R. (2005) Convergent evolution of hydroxylation mechanisms in the fungal kingdoms: molybdenum cofactor-independent hydroxylation of xanthine via α-ketoglutarate dependent dioxygenase. *Molec. Microbiol. 57*, 276-290.

(3) Darlington, A. J., and Scazzocchio, C. (1968) Evidence for an alternative pathway of xanthine oxidation in *Aspergillus nidulans*. *Biochim. Biophys. Acta 166*, 557-568.

(4) Sealy-Lewis, H. M., Scazzocchio, C., and Lee, S. (1978) A mutation defective in xanthine alternative pathway of *Aspergillus nidulans*: its use to investigate the specificity of *uaY* mediated induction. *Molec. Gen. Genet. 164*, 303-308.

(5) Hausinger, R. P. (2004) Fe(II)/α-ketoglutarate-dependent hydroxylases and related enzymes. *Crit. Rev. Biochem. Mol. Biol. 39*, 21-68.

(6) Glatigny, A., Hof, P., Romao, M. J., Huber, R., and Scazzocchio, C. (1998) Altered specificity mutations define residues essential for substrate positioning in xanthine dehydrogenase. *J. Mol. Biol. 278*, 431-438.

(7) Truglio, J. J., Theis, K., Leimkühler, S., Rappa, R., Rajagopalan, K. V., and Kisker, C. (2002) Crystal structure of the active and alloxanthine-inhibited forms of xanthine dehydrogenase from *Rhodobacter capsulatus*. *Structure 10*, 115-125.

(8) Goudela, S., Karatza, P., Koukaki, M., Frilingos, S., and Diallinas, G. (2005) Comparative substrate recognition by bacterial and fungal purine transporters of the NAT/NCS2 family. *Molec. Membrane Biol. 22*, 263-275.

(9) Koukaki, M., Vlanti, A., Goudela, S., Pantazopoulou, A., Gioule, H., Tournaviti, S., and Diallinas, G. (2005) The nucleobase-ascorbate transporter (NAT) signature motif in UapA defines the function of the purine translocation pathway. *J. Mol. Biol. 350*, 499-513.

(10) Eichhorn, E., van der Ploeg, J. R., Kertesz, M. A., and Leisinger, T. (1997) Characterization of α-ketoglutarate-dependent taurine dioxygenase from *Escherichia coli*. *J. Biol. Chem. 272*, 23031-23036.

(11) Grzyska, P. K., Ryle, M. J., Monterosso, G. R., Liu, J., Ballou, D. P., and Hausinger, R. P. (2005) Steady-state and transient kinetic analyses of taurine/α-ketoglutarate dioxygenase: effects of oxygen concentration, alternative sulfonates, and active site variants on the Fe(IV) intermediate. *Biochemistry 44*, 3845-3855.

(12) Hanahan, D. (1983) Studies on transformation of *Escherichia coli* with plasmids. *J. Mol. Biol. 166*, 557-580.

(13) Beinert, H. (1978) Micro methods for the quantitative determination of iron and copper in biological material. *Meth. Enzymol. 54*, 435-445.

(14) Bradford, M. M. (1976) A rapid and sensitive method for the quantitation of microgram quantities of protein utilizing the principle of protein-dye binding. *Anal. Biochem. 72*, 248-254.

(15) Laemmli, U. K. (1970) Cleavage of structural proteins during the assembly of the head of bacteriophage T4. *Nature (London) 227*, 680-685.

(16) Elkins, J. M., Ryle, M. J., Clifton, I. J., Dunning Hotopp, J. C., Lloyd, J. S., Burzlaff, N. I., Baldwin, J. E., Hausinger, R. P., and Roach, P. L. (2002) X-ray crystal structure of *Escherichia coli* taurine/α-ketoglutarate dioxygenase complexed to ferrous iron and substrates. *Biochemistry 41*, 5185-5192.

(17) O'Brien, J. R., Schuller, D. J., Yang, V. S., Dillard, B. D., and Lanzilotta, W. N. (2003) Substrate-induced conformational changes in *Escherichia coli* taurine/α-ketoglutarate dioxygenase and insight into the oligomeric structure. *Biochemistry 42*, 5547-5554.

(18) Montero-Morán, G. M., Li, M., Rendon-Huerta, E., Jourdan, F., Lowe, D. J., Stumpff-Kane, A. W., Feig, M., Scazzocchio, C., and Hausinger, R. P. (2007) Purification and characterization of the Fe(II)- and α-ketoglutarate-dependent xanthine hydroxylase from *Aspergillus nidulans*. *Biochemistry 46*, 5293-5304.

(19) Trewick, S. C., Henshaw, T. F., Hausinger, R. P., Lindahl, T., and Sedgwick, B. (2002) Oxidative demethylation by *Escherichia coli* AlkB directly reverts DNA base damage. *Nature 419*, 174-178.

(20) Müller, T. A., Zavodszky, M. I., Feig, M., Kuhn, L. A., and Hausinger, R. P. (2006) Structural basis for the enantiospecificities of *R*- and *S*-phenoxypropionate/α-ketoglutarate dioxygenases. *Prot. Science 15*, 1356-1368.

(21) Searls, T., Butler, D., Chien, W., Mukherji, M., Lloyd, M. D., and Schofield, C. J. (2005) Studies on the specificity of pro- and mature-forms of phytanoyl-CoA 2-hydroxylase and mutation of the iron binding ligands. *J. Lipid Res. 46*, 1660-1670.

(22) McDonough, M. A., Li, V., Flashman, E., Chowdhury, R., Mohr, C., Liénard, B. M. R., Zondlo, J., Oldham, N. J., Clifton, I. J., Lewis, J., McNeill, L. A., Kurzeja, R. J. M., Hewitson, K. S., Yang, E., Jordan, S., Syed, R. S., and Schofield, C. J. (2006) Cellular oxygen sensing: crystal structure of hypoxia-inducible factor prolyl hydroxylase (PHD2). *Proc. Natl. Acad. Sci. USA 103*, 9814-9819.

(23) Dann, C. E., III, Bruick, R. K., and Deisenhofer, J. (2002) Structure of a factor-inhibiting hypoxia-inducible factor 1: an essential asparaginyl hydroxylase involved in the hypoxic response pathway. *Proc. Natl. Acad. Sci. USA 99*, 15351-15356.

(24) Ryle, M. J., Padmakumar, R., and Hausinger, R. P. (1999) Stopped-flow kinetic analysis of *Escherichia coli* taurine/α-ketoglutarate dioxygenase: interactions with α-ketoglutarate, taurine, and oxygen. *Biochemistry 38*, 15278-15286.

(25) Fukumori, F., and Hausinger, R. P. (1993) Purification and characterization of 2,4-dichlorophenoxyacetate/α-ketoglutarate dioxygenase. *J. Biol. Chem. 268*, 24311-24317.

(26) Mishina, Y., Chen, L. X., and He, C. (2004) Preparation and characterization of the native iron(III)-containing DNA repair AlkB protein directly from *Escherichia coli*. *J. Am. Chem. Soc. 126*, 16930-16936.

(27) Vaillancourt, F. H., Yin, J., and Walsh, C. T. (2005) SyrB2 in syringomycin E biosynthesis is a nonheme Fe^{II} α-ketoglutarate- and O_2-dependent halogenase. *Proc. Natl. Acad. Sci. USA 102*, 10111-10116.

(28) Muller, M., and Moller, K. M. (1969) Urate oxidase and its association with peroxisomes in Acanthamoeba sp. *Eur. J. Biochem. 9*, 424-430.

(29) Leighton, F., Poole, B., Lazarow, P. B., and de Duve, C. (1969) The synthesis and

turnover of rat liver peroxisomes. I. Fractionation of peroxisome proteins. *J. Cell. Biochem. 41*, 521-535.

(30) Nguyen, T., Zelechowska, M., Foster, V., Bergmann, H., and Verma, D. P. S. (1985) Primary structure of the soybean nodulin-35 gene encoding uricase II localized in the peroxisomes of uninfected cells of nodules. *Proc. Natl. Acad. Sci. USA 82*, 5040-5044.

(31) Breidenbach, R. W., Kahn, A., and Beevers, H. (1968) Characterization of glyoxysomes from castor bean endosperm. *Plant Physiol. 43*, 705-713.

(32) de Hoop, M. J., and Ab, G. (1992) Import of proteins into peroxisomes and other microbodies. *Biochem. J. 286*, 657-669.

(33) Petriv, O. I., Tang, L., Titorenko, V. I., and Rachubinski, R. A. (2004) A new definition for the consensus sequence of the peroxisome targeting signal type 2. *J. Mol. Biol. 341*, 119-134.

(34) Reumann, S. (2004) Specification of the peroxisome targeting signals type 1 and type 2 of plant peroxisomes by bioinformatics analyses. *Plant Physiol. 135*, 783-800.

(35) Swinkels, B. W., Gould, S. J., Bodnar, A. G., Rachubinski, R. A., and Subramaniam, S. (1991) A novel, cleavable peroxisomal targeting signal at the amino-terminus of rat 3-ketoacyl-CoA thiolase. *EMBO J. 10*, 3255-3262.

(36) Lee, J. G., Lee, Y. J., Lee, C. H., and Maeng, P. J. (2006) Mutational and functional analysis of the cryptic N-terminal targeting signal for both mitochondria and peroxisomes in yeast peroxisomal citrate synthase. *Biochem (Tokyo) 140*, 121-133.

(37) Kato, A., Hayashi, M., Kondo, M., and Nishimura, M. (2000) Transport of peroxisomal proteins synthesized as large precursors in plants. *Cell Biochem. Biophys. 32*, 269-275.

(38) Julenius, K., Molgaard, A., Gupta, R., and Brunak, S. (2005) Prediction, conservation analysis and structural characterization of mammalian mucin-type O-glycosylation sites. *Glycobiology 15*, 153-164.

(39) Blom, N., Gammeltoft, S., and Brunak, S. (1999) Sequence- and structure-based prediction of eukaryotic protein phosphorylation sites. *J. Mol. Biol. 295*,

1351-1362.

(40) Cortay, J.-C., Rieul, C., Duclos, B., and Cozzone, A. J. (1986) Characterization of the phosphoproteins of *Escherichia coli* cells by electrophoretic analysis. *Eur. J. Biochem. 159*, 227-237.

CHAPTER 3

KINETIC CHARACTERIZATION, ISOTOPE EFFECTS, AND EFFECTS OF ALTERNATE METAL IONS, SALTS, AND SUBSTRATE ANALOGUES ON *ASPERGILLUS NIDULANS* XANTHINE HYDROXYLASE

The studies described in this chapter were combined with additional investigations and published: Montero-Moran*, G. M.; Li*, M.; Rendon-Huerita, E.; Jourdan, F.; Lowe, D. J.; Stumpff-Kane, A. W; Feig, M.; Scazzocchio, C.; and Hausinger, R. P. "Purification and characterization of the Fe(II)- and α-Ketoglutarate-Dependent *Aspergillus nidulans* Xanthine Hydroxylase from *Aspergillus nidulans*" *Biochemistry*, 2007, *46 (18)*, 5293-5304 (* Co-first author). Michael Feig and Andrew W. Stumpff-Kane constructed the homology model, David J. Lowe and Fabrice Jourdan synthesized the 8-hydroxypurine, 2,8-dihydroxypurine and 6,8-dihydroxypurine, and Christine Drevet provided the alignment figure of XanA with putative orthologous sequences from several fungi.

ABSTRACT

Xanthine/α-ketoglutarate (αKG) dioxygenase (XanA) of *Aspergillus nidulans* was previously purified from fungal mycelium and recombinant *Escherichia coli* cells, and the two forms of the enzyme were shown to exhibit distinct posttranslational modifications while retaining similar kinetic parameters as described in Chpater 2. Here, I characterize several additional kinetic properties of the XanA isolated form *E. coli*. The enzyme exhibits no significant isotope effect when using 8-^{2}H-xanthine; however, it demonstrates a two-fold solvent deuterium isotope effect. Cu(II) and Zn(II) potently inhibit the Fe(II)-specific enzyme, presumably by binding to the Fe(II) site, whereas Co(II), Mn(II), and Ni(II) are weaker inhibitors. NaCl inhibits the enzyme, resulting in decreases in k_{cat} and increases in K_m of both αKG and xanthine. The αKG cosubstrate can be substituted by α-ketoadipate (resulting in a 9-fold decrease in k_{cat} and a 5-fold increase in the K_m compared to the normal α-keto acid), while the αKG analogue *N*-oxalylglycine is an effective competitive inhibitor (K_i 0.12 μM). No alternative purines are able to effectively substitute for xanthine as a substrate, and only one purine analogue (6,8-dihydroxypurine, DHP) results in significant inhibition. A homology model of XanA was generated on the basis of the structure of the related enzyme TauD (PDB code 1OS7) and used to provide insights into the mode of substrate and inhibitor binding. These studies present the first analysis of xanthine/αKG dioxygenase isotope effects, interactions with alternative metal ions and NaCl, and behavior with substrate analogues.

INTRODUCTION

In Chapter 2, I described the purification and basic properties of the Fe(II)-dependent xanthine/α-ketoglutarate (αKG) dioxygenase (XanA) of *Aspergillus nidulans*. This enzyme, exclusively associated with the fungal kingdom, catalyzes the oxidative decarboxylation of αKG, forming succinate and carbon dioxide, concomitant with xanthine hydroxylation to uric acid, as shown in Figure 2.1. I showed that fungus-derived XanA differed from the recombinant form isolated from *Escherichia coli* both in quaternary structure and identity of posttranslational modifications, but the two enzyme forms exhibited very similar kinetic parameters. In contrast to the phylogenetically restricted XanA enzyme, a molybdopterin cofactor (Moco)-containing enzyme xanthine oxidoreductase or xanthine hydroxylase (*1*) is present in all kingdoms of life, including fungi, and carries out an analogous reaction, the key step of which is depicted in Figure 3.1. A glutamic acid general base activates the hydroxyl group coordinated to Mo(VI) (chelated by an enedithiolate moiety of the pterin) and the resulting nucleophile attacks the C-8 position of xanthine with concomitant hydride transfer to Mo=S. The product subsequently dissociates and the resulting Mo(IV)-SH intermediate reoxidizes by sequential electron transfer steps through two [2Fe-2S] clusters and an enzyme bound flavin adenine dinucleotide. The reduced flavin passes on the electrons to NAD (xanthine dehydrogenase) or in some cases to oxygen (xanthine oxidase). Whereas the Moco-containing xanthine hydroxylases have been extensively characterized, little is known of the Fe(II)/αKG-dependent XanA.

FIGURE 3.1: General mechanism of Moco-containing xanthine oxidases

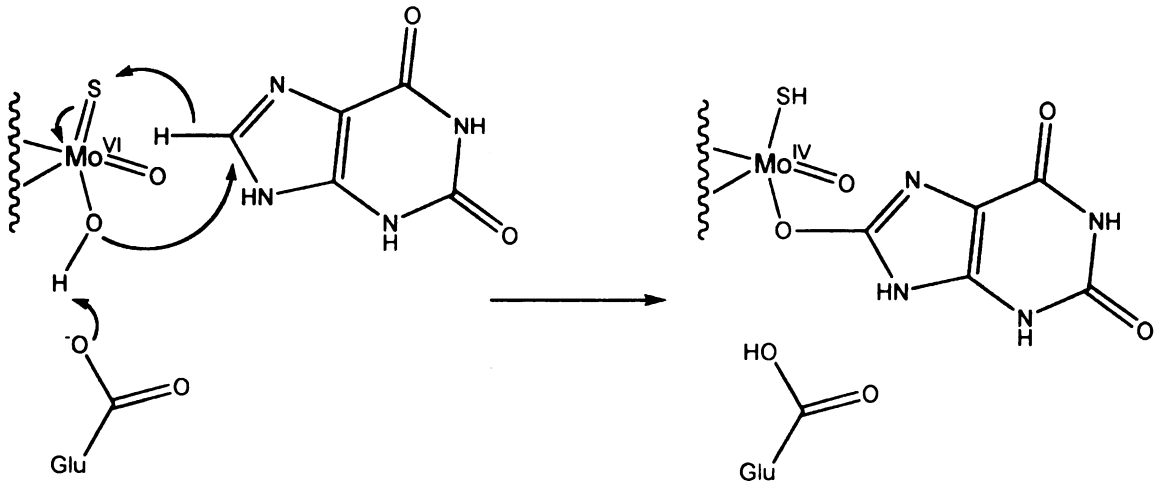

The Fe(II)/αKG hydroxylases encompass a wide range of enzymes with diverse primary substrates (reviewed in (*2*)). The prolyl, lysyl, and aspartyl(asparaginyl) hydroxylases catalyze posttranslational modifications of proteins, in some cases associated with hypoxic signaling (*3*). JmjC domain-containing proteins have been shown to catalyze methylated-histone demethylation reactions (*4*). AlkB repairs 1-methyl-A or 3-methyl-C lesions in DNA (or RNA) by using an analogous oxidative dealkylation reaction (*5, 6*). The lipid-metabolizing enzyme phytanoyl-CoA hydroxylase participates in the metabolism of phytanic acid, and deficiency of this enzyme leads to Refsum disease (*7*). Finally, a wide variety of small molecules are synthesized or decomposed by members of this enzyme family. For example, plants synthesize gibberellins, flavonoids, and some alkaloids by action of these enzymes (*8*), thymine 7-hydroxylase sequentially hydroxylates the methyl group of free thymine (*9*), and TfdA, RdpA, and SdpA decompose specific phenoxyalkanoic acid herbicides by hydroxylation of the side chain (*10, 11*). The best-characterized representative of this protein family is taurine/αKG dioxygenase (TauD), responsible for the decomposition of taurine (2-aminoethanesulfonate) to aminoacetaldehyde and sulfite (*12*). In particular, a series of transient kinetic studies have demonstrated the intermediacy of an Fe(IV)-oxo species in the TauD catalytic mechanism (*13-19*). In addition, the TauD crystal structure has been solved (*20, 21*) and aberrant chemistry leading to side chain hydroxylation reactions has been extensively defined (*22-24*). The XanA sequence shows some similarity with the TauD group of dioxygenases (*25*), including a clear conservation of the Fe(II)- and

αKG-binding sites.

The studies reported here continue our characterization of the bacteria-derived forms of *A. nidulans* XanA. I describe its solvent and substrate kinetic isotope effects, define the effects of different divalent metal ions and several αKG and xanthine analogues, and I identify alternate substrates and inhibitors. Finally, a homology model of XanA was generated and I use it to provide insights into the mode of substrate/inhibitor binding. These studies present the first analysis of isotope effects, interactions with alternative metal ions and NaCl, and behavior of substrate analogues for xanthine/αKG dioxygenase.

EXPERIMENTAL PROCEDURES

Purification of Bacterial-Derived XanA. XanA was purified from recombinant *E. coli* cells as previously described in Chapter 2 (*26*).

Enzyme Assays. Xanthine/αKG dioxygenase activity was measured at 25 °C by using the following typical assay conditions (total volume of 1 mL): 1 mM αKG, 40 μM $Fe(NH_4)_2(SO_4)_2$, and 200 μM xanthine in 50 mM MOPS buffer, pH 7.4. Variations of these conditions included use of varied concentrations of these and other additives. The absorbance at 294 nm was monitored to determine the uric acid production (ε_{294} 12,200 M^{-1} cm^{-1}) with a correction for loss of the xanthine absorbance at this wavelength (measured ε_{294} 2,000 M^{-1} cm^{-1}) for an overall change in ε_{294} of 10,200 M^{-1} cm^{-1}. Initial rates were calculated by using linear data collected over a time period where 10% or less of the substrate was consumed. Units of activity (U) were defined as μmol min^{-1} of uric acid produced and the specific activity (U mg^{-1}) was measured as μmol min^{-1} (mg of purified XanA)$^{-1}$.

Sources and Synthesis of Chemical Analogues of αKG and Xanthine. αKG, α-ketoadipate, α-ketobutyric acid, pyruvate, phenylpyruvate, 4-hydroxyphenylpyruvate, purine, 6-methylpurine, 2-hydroxypurine, 2-hydroxy-6-methylpurine, hypoxanthine, xanthine, 1-methylxanthine, 3-methylxanthine, 7-methylxanthine, 9-methylxanthine, allopurinol, and allantoin were from Sigma-Aldrich. *N*-oxalylglycine (NOG) was a gift from Dr. Nicolai Burzlaff.

8-Hydroxypurine and 6,8-dihydroxypurine (6,8-DHP) were prepared from the

commercially available (Sigma Aldrich) 4,5-diaminopyrimidine and 4,5-diamino-6-hydroxypyrimidine, respectively, following a modified method described previously (*27*). 2,8-Dihydroxypurine (2,8-DHP) was prepared following a published method (*28*). Each of these compounds was provided by David J. Lowe and Fabrice Jourdan.

8-^{2}H-Xanthine Preparation. 8-^{2}H-xanthine was prepared by incubating a 1 % (w/v) xanthine solution in ^2H_2O (99.9 %, Sigma & Aldrich), with 0.3 M NaO^2H (> 99 % ^2H, Sigma-Aldrich) in a serum vial sealed with a butyl rubber stopper for 20 h in a 100 °C oven. The proton-deuterium exchange was monitored by using NMR spectroscopy to integrate the resonance at 6.9 ppm due to the proton on C-8. The final solution was diluted and neutralized to pH 7.0. The 8-^{2}H-xanthine precipitated from the solution and was dried under vacuum for at least 3 h. Yields were approximately 90 %. The purity of 8-^{2}H-xanthine was monitored by electrospray ionization mass spectrometry, and the conversion was shown to be 98.4 % as a molar ratio.

^2H_2O Solvent Isotope Effect. In 1 mL 50 mM MOPS, p^{2}H 8.0 (p^{2}H values were determined by adding 0.4 to the pH 7.6 electrode reading), 0.51 μg of purified XanA was assayed in 40 μM $Fe(NH_4)_2(SO_4)_2$, 1 mM αKG and 0-200 μM xanthine. All buffers were prepared in ^2H_2O. These data were compared to assays carried out in the same conditions at pH 7.6. Of note, the *E. coli*-derived enzyme exhibits optimal activity over a range from pH 7.0 to 8.0.

Structural Modeling. (Assisted by Andrew W. Stumpff-Kane and Michael Feig,

Department of Biochemistry and Molecular Biology, MSU.) A homology model of XanA was generated on the basis of the structure of the related enzyme TauD (PDB code 1OTJ, chain A, and PDB code 1OS7, chain A) (*21*). XanA is 18 % identical to TauD over 280 residues, and has three significant additional regions of 15, 22, and 18 amino acids. Multiple templates for the XanA structure were obtained with PSI-BLAST (*29, 30*) starting both from the amino acid sequence of XanA and from that of several closely related proteins for which no structure has yet been reported, and with 3D-Jury (*31*) using the Bioinfo Meta Server (http://bioinfo.pl/Meta). Additional suboptimal alignments for each template were generated using probA (*32*) to produce a large pool of possible models. A structural model was constructed from each alignment, with side chains reconstructed using the MMTSB Tool Set (*33, 34*), and the best model from the entire set of models was selected according to combined energy scores from DFIRE (*35*), MMGB/SA (*36*), and RAPDF (*37*), using a correlation-based approach (*38*) in combination with clustering. The αKG and iron were placed into the active site according to the TauD structure.

RESULTS

Isotope Effects. To test for substrate or solvent isotope effects on the overall reaction rate, activity assays were carried out by using 8-^{2}H-xanthine or in $^{2}H_2O$ and compared to control studies with unlabeled xanthine in H_2O. No significant isotope effect was observed when the reaction was carried out with 8-^{2}H-xanthine (98.4 % enriched with ^{2}H) and compared to non-labeled substrate (data not shown). In contrast, a significant solvent deuterium isotope effect was observed (Figure 3.2), with V_{max} reduced by 50 % (72.1 U mg^{-1} dropping to 34.0 U mg^{-1}) while K_m was nearly unaffected (45.2 and 48.9 mM, respectively).

Effect of Other Metal Ions and Salt. Metal ions other than Fe(II) were tested and found to be unable to stimulate activity when added to the apoprotein. When various metal ions were added to the assay buffer in concentrations equivalent to that of Fe(II), both Cu(II) and Zn(II) completely inhibited the xanthine/αKG dioxygenase activity, with partial inhibition observed with Co(II), Mn(II), and (much less pronounced) Ni(II) (Figure 3.3). The inactive metal ions are presumed to compete for the Fe(II)-binding site. The activity of XanA was shown to decrease in buffers containing NaCl (Figure 3.4A). Kinetic analyses revealed that 0.5 M NaCl salt increased the K_m of αKG to 0.74 ± 0.08 mM (Figure 3.4B), increased the K_m of xanthine to 105 ± 5.8 μM (Figure 3.4C), and decreased the k_{cat} to 35.4 s^{-1} and 43.2 s^{-1}, respectively in the two studies. These findings indicate that the K_m of αKG is significantly affected by ionic strength, while the K_m of xanthine and k_{cat} are less affected, and demonstrate that the salt content of fractions

FIGURE 3.2: Solvent deuterium isotope effect on XanA activity. The effects of varying the concentration of xanthine on xanthine/αKG dioxygenase activity were examined at 25 °C in 50 mM MOPS buffer, p^2H 8.0 (■) (p^2H values were determined by adding 0.4 to the pH electrode reading) or pH 7.6 (▲) containing 40 μM Fe(II), 1 mM αKG, and 0-200 μM xanthine.

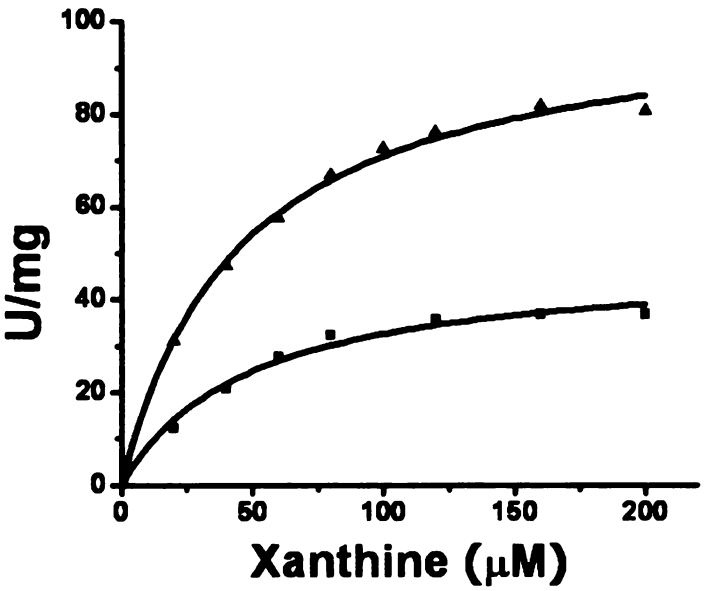

FIGURE 3.3: Divalent cation inhibition of XanA. The effects of several divalent cations (M^{II}, at 40 μM concentration) on xanthine/αKG dioxygenase activity were examined by using the *E. coli*-derived protein at 25 °C in solutions containing 40 μM Fe(II), 1 mM αKG and 200 μM xanthine in 50 mM MOPS buffer, pH 7.4. Samples included (1) Fe(II) only and Fe(II) plus (2) Mg(II), (3) Mn(II), (4) Co(II), (5) Ni(II), (6) Zn(II), (7) Cu(II).

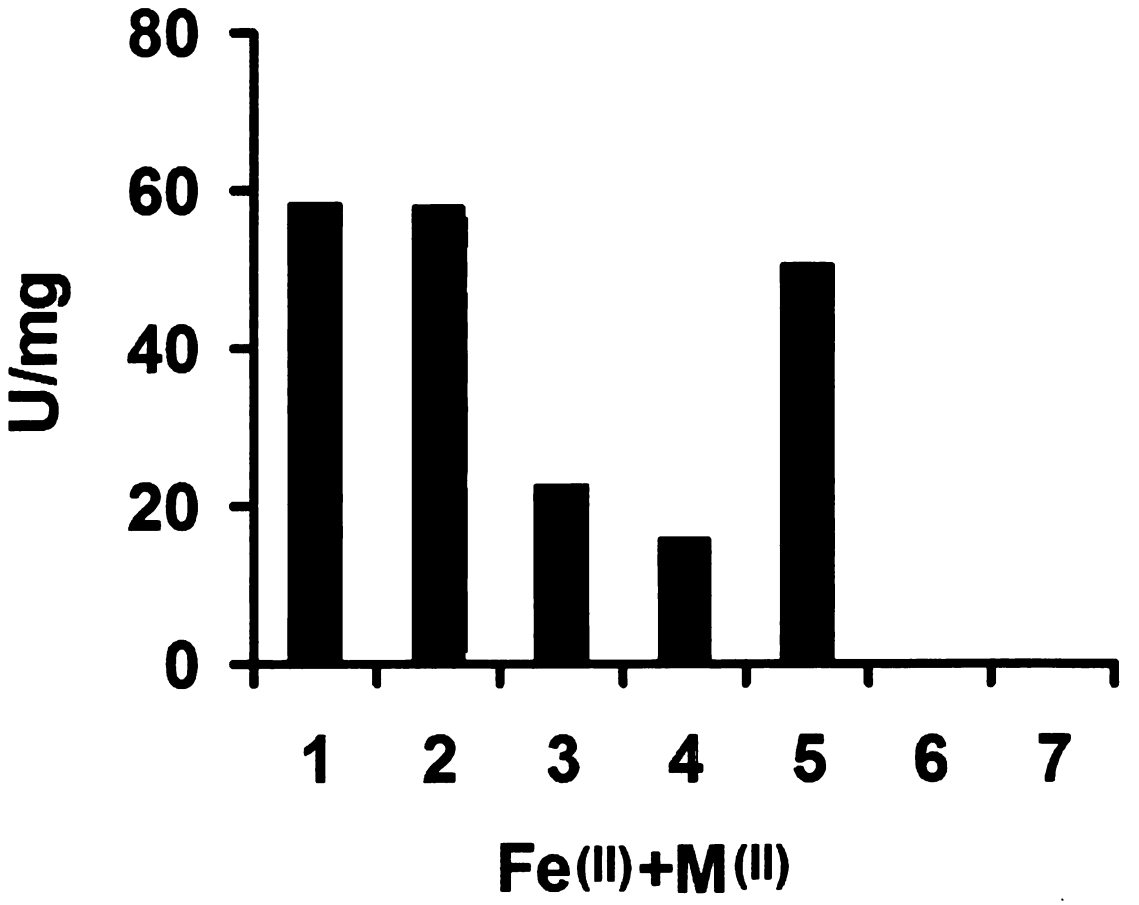

FIGURE 3.4: NaCl inhibition of XanA. (A) The effects of varying NaCl concentrations on xanthine/αKG dioxygenase activity were examined by monitoring the absorbance at 294 nm over time for the *E. coli*-derived protein at 25 °C in solutions containing 40 μM Fe(II), 1 mM αKG and 200 μM xanthine in 50 mM MOPS buffer, pH 7.4. The concentrations of NaCl examined were: 0 mM (♦); 200 mM (■); 400 mM (▲); 600 mM (▼); 800 mM (●). Using 0.5 M NaCl, the effects of varying the concentrations of (B) αKG and (C) xanthine were examined. Data in panels B and C represent initial rates and were fit to the Michaelis-Menten equation.

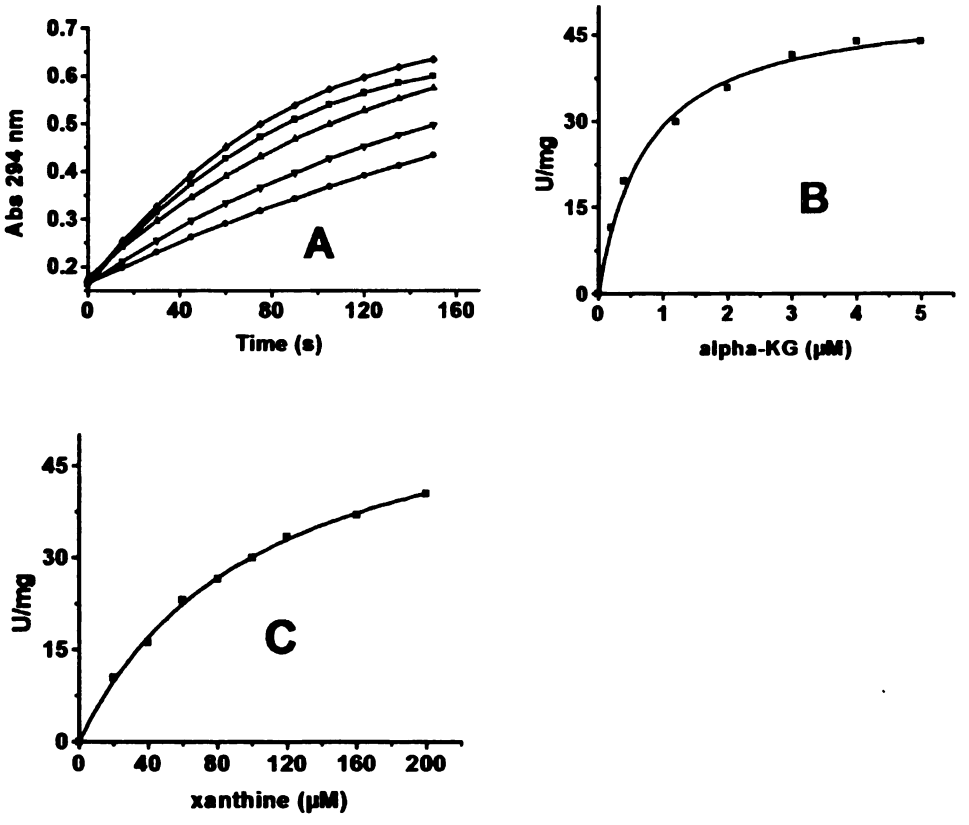

recovered during protein isolation must be considered when assaying the enzyme.

αKG Analogues. In addition to αKG, α-ketoadipic acid is a cosubstrate of XanA and results in an activity of 9.2 U (mg protein)$^{-1}$ or about 1/10 of that observed with αKG. Kinetic analyses revealed a k_{cat} of 7.6 s^{-1} and a K_m of 0.16 mM for this alternative co-substrate compared to a k_{cat} of 61 s^{-1} and K_m of 31 μM for αKG (*26*). In contrast, pyruvate, α-ketobutyric acid, phenylpyruvate, and 4-hydroxyphenylpyruvate were not used as co-substrates. NOG, a known inhibitor of several Fe(II)/αKG-dependent dioxygenase family members (*39-43*), was shown to compete with αKG and provided a K_i of 0.12 μM for inhibition of the enzyme (Figure 3.5).

Xanthine Analogues. XanA was shown to be highly specific for xanthine. On the basis of the spectroscopic assay using standard conditions with 12 nM enzyme, no activity was detected when the enzyme was assayed with 80, 100, or 200 μM hypoxanthine, 1-methylxanthine, 3-methylxanthine, 7-methylxanthine, 9-methylxanthine, purine, 6-methylpurine, 2-hydroxypurine, 8-hydroxypurine, 2,8-dihydroxypurine, 2-hydroxy-6-methylpurine, allopurinol, allantoin, or adenosine diphosphate. Similarly, significant inhibitory effects were not observed with 100 or 200 μM of any of these compounds (although very modest inhibition was noted with 2,8-DHP). The one xanthine-like compound that does inhibit the enzyme, but does not serve as a substrate, is 6,8-DHP. The kinetic inhibition mechanism of 6,8-DHP will be discussed in more detail in Chapter 4.

Structural Model of XanA. XanA was aligned with TauD and a homology model was

FIGURE 3.5: NOG inhibition of XanA. (A) The effects of varying concentrations of NOG (0, 0.2, 0.6, 1.2, and 2 μM) on xanthine/αKG dioxygenase activity were examined by using the *E. coli*-derived protein at 25 °C in solutions containing 40 μM Fe(II), 1 mM αKG and 200 μM xanthine in 50 mM MOPS buffer, pH 7.4. Each set of initial rate data was fit to the Michaelis-Menten equation. (B) A replot of the values of apparent K_m divided by apparent V_{max} as a function of inhibitor concentration.

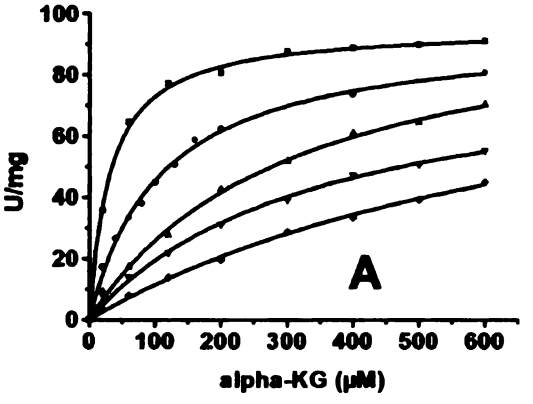

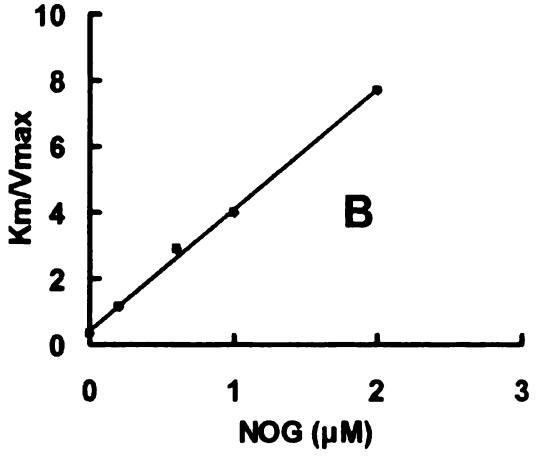

created by my collaborators using the TauD structure (*20, 21*) as the template. The overall sequence identity is 18%, however the sequence identity of the most relevant structural regions near the active site is 33%. Moreover, given recent advances in structure prediction, sequence identities as low as 18% identity are commonly sufficient to support comparative modeling with a good match of predicted secondary structure elements (*44, 45*) as in the case of XanA. Consequently, it is reasonable to assume that our model of the XanA structure captures the overall features correctly, while structural details near the active site are likely represented more accurately. Nevertheless, any predicted model without further experimental validation remains speculative and is subject to some level of uncertainty.

As illustrated in Figure 3.6A, the XanA protein is predicted to contain the DSBH fold comprised of eight β-strands with connecting loops, as is typical of this enzyme family (*2, 46*). Three loops in the sequence, comprising residues 72-88, 173-190, and 219-231, had no counterparts in TauD and were not modeled (indicated by boxes at the appropriate positions in the figure), but these are all distant from the putative active site region. The homology model contains the Fe(II)-binding site (His149, Asp151, and His340) expected from prior sequence alignments (*25*). The co-substrate (shown in yellow) was positioned into the model so as to chelate Fe(II) in a similar fashion as αKG occurs in TauD. The αKG C-5 carboxylate is predicted to form a salt bridge with Arg352 (depicted in red), while Lys122 (in green) is well positioned to stabilize the C-1 carboxylate of the co-substrate.

FIGURE 3.6: Homology model of XanA. A, Ribbon diagram depicting the XanA homology model that was predicted using TauD (PDB code 1OS7) as a template. The polypeptide chain is depicted in blue to red coloration (*N*-terminus to *C*-terminus) with gaps indicated by boxes for the non-modeled loops involving residues 72-88, 173-190, and 219-231. The postulated metal ligands (His149, Asp151, and His340) are illustrated in green, yellow, and red, respectively, to the right of the magenta Fe(II) sphere. Bound αKG (yellow) chelates the metals and is suggested to be stabilized by a salt bridge to the C-5 carboxylate involving Arg352 (red) and a hydrogen bond to the C-1 carboxylate via Lys122 (green). B, Putative active site pocket derived from the XanA homology model. A closeup view (20 Å slab) of the XanA homology model depicting possible positions of residues at the active site pocket, shown in the same orientation as illustrated in Figure 9. αKG in stick form is shown chelating the metal with its carbon atoms colored yellow. The three side chains that bind the metal are shown in stick form using green (His149), yellow (Asp151), and red (His340) coloration, as in Figure 9. Residues predicted to line the active site pocket are shown in stick form with their carbon atoms in white, while other residues are shown as lines with green carbon atoms.

FIGURE 3.6:

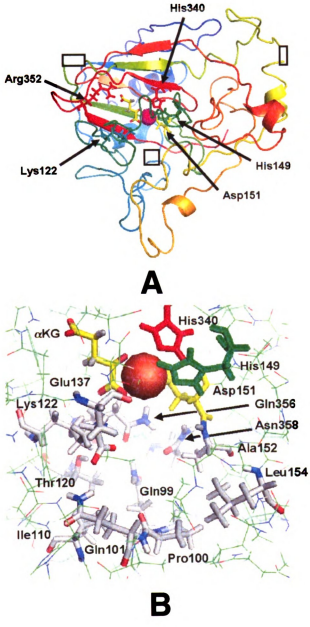
His340
Arg352
Lys122
His149
Asp151
A
αKG
His340
His149
Glu137
Asp151
Lys122
Gln356
Asn358
Ala152
Leu154
Thr120
Gln99
Ile110
Gln101
Pro100
B

DISCUSSION

In this study I describe several properties of xanthine/αKG dioxygenase, a novel xanthine-metabolizing enzyme found exclusively in the fungal kingdom (*25*). Below, I place my findings on isotope effects, interactions with various metal ions, salts, and substrate analogues, into the larger context of other Fe(II)/αKG dioxygenases, and I relate key findings to our homology model of the protein.

Isotope Effects. Although the xanthine C-H bond is broken at C-8 during turnover, substitution of the proton at this position by ^2H did not lead to a substrate isotope effect. This result demonstrates that C-H cleavage is not the rate-determining step in the reaction. The deuterated substrate might be useful in future experiments to examine individual steps in the reaction by using transient kinetic approaches, as was elegantly demonstrated with deuterated substrate and stopped-flow techniques for TauD (*15*) and, more recently, prolyl 4-hydroxylase (*47*). In contrast to the situation with labeled xanthine, a solvent isotope effect was observed upon substituting H_2O with D_2O (Figure 3.2). This substitution had little effect on the K_m of xanthine while decreasing V_{max} by 40 % compared to the assay in H_2O. This result suggests that a chemical group possessing an exchangeable proton is important in the rate-determining step of the overall reaction. Options for the protonatable group include a general base or general acid protein side chain or a metallocenter species such as Fe(III)-OOH or Fe(III)-OH. The finding of a solvent deuterium isotope effect contrasts with the case of TauD, where product release is the slow step in catalysis and no solvent isotope effect is observed (*13, 19*).

Metal Ion and Salt Effects. Zn(II) and Cu(II) are potent inhibitors of XanA, and several other metals also inhibit the enzyme (Figure 3.3). This situation resembles that known for related enzymes such as TauD where Co(II) and Ni(II) inhibition has been studied (*39*), clavaminate synthase where Co(II) inhibition was characterized (*48*), or TfdA where the Cu(II)-inhibited enzyme was analyzed (*49*). The inhibitory metal ions are likely to substitute for Fe(II) and utilize the same set of amino acid side chain ligands.

The inhibitory effects of NaCl on XanA (Figure 3.4) represent, to my knowledge, the only systematic characterization of any salt effect on an Fe(II)/αKG dioxygenase. The presence of salt leads to a large increase in K_m of αKG, a small increase in K_m of xanthine, and a reduction in k_{cat}. I attribute the K_m effect to the ability of salt to interfere with salt bridge formation and other stabilizing interactions between αKG or xanthine and the protein. Similar salt effects are likely to apply to a wide range of other family members; thus, one must exercise caution in the choice of ionic strength when doing enzyme assays.

Co-Substrate and Substrate Specificity. The co-substrate specificity of XanA is somewhat more relaxed than that for the primary substrate, with α-ketoadipic acid (with one extra carbon compared to αKG) also yielding activity. The increase in K_m and decrease in k_{cat} for the incorrectly-sized analogue is easily rationalized in terms of the XanA homology model where both the C-1 and C-5 carboxylates of αKG are predicted to interact with the protein (with Lys122 and Arg352, respectively) while also chelating the active site metal ion. Alternative α-ketoacids are known to support αKG-dependent

activities of several other enzyme family members including TauD, TfdA, RdpA, SdpA, and an alkyl sulfatase (*10, 12, 50, 51*). The αKG homologue NOG is a competitive inhibitor of XanA (Figure 3.5), consistent with its known inhibition of several other representatives of the Fe(II)/αKG-dependent hydroxylases. Of interest, the measured K_i of NOG for XanA (0.12 μM) is well below the K_m of αKG in this enzyme and much below the reported 290 μM K_i for inhibition of TauD (*39*). More generally, the K_i of NOG can vary widely among family members (e.g., it is reported to be 1.9-7.0 μM for collagen prolyl 4-hydroxylase (*40*) and 1.2 mM for an oxygen-sensing asparaginyl hydroxylase (*43*)), presumably due to distinct interactions with the active site protein side chains in the target enzymes.

XanA proved to be exquisitely specific to its primary substrate. For example, allopurinol (a known substrate and inhibitor of xanthine oxidase (*52*)), 1-methylxanthine and 2-hydroxy-6-methylpurine (alternative substrates of the Moco-containing enzyme (*53, 54*), and several other purine-type compounds were neither substrates nor inhibitors of XanA. Of the compounds tested, only 6,8-DHP bound tightly to the enzyme (more date and discussion of this inhibitor are provided in Chapter 4). For comparison, other members of the Fe(II)/αKG-dependent dioxygenases range widely in their substrate specificities. The prolyl hydroxylases involved in the hypoxic response appear to be highly specific for recognizing a single prolyl residue in the HIF1α protein (*55, 56*). By contrast, TfdA utilizes a wide range of phenoxyacetic acids (*10*) and a yeast αKG/sulfonate dioxygenase metabolizes a diverse array of sulfonates (*57*).

Postulated Substrate-Binding Mode. Additional structural or mutagenesis studies are required to characterize the mode of substrate binding to XanA; however, our homology model (Figure 3.6) allows me to identify potential key active site residues (Figure 3.6B). the model depicts a pocket adjacent to the metallocenter and lined by a series of putative active site residues (Gln99, Pro100, Gln101, Ile110, Thr120, Lys122, Glu137, Ala152, leu154, Gln356, and Asn358) that are generally well conserved in sequences of XanA orthologues (Figure 3.7). Pro100, Gln101, Gln356, and Asn358 are universally conserved in the XanA sequences. Gln99 counterparts also are present often, but Val occupies this position in some representatives. Lys122, which is suggested to stabilize the αKG C-1 carboxylate and bind substrate, either is retained or conservatively replaced by Arg or Thr. In some fungi, various residues (Lys, Gln, Arg, Asn, and Glu) replace Thr120, but all of these are ble to function in hydrogen bonding. Similarly, Asp, Gln, and Ser, all capable of similar hydrogen bond interactions, replace Glu137 in other XanA homologues. Among the hydrophobic residues predicted to surround the active site, Ile110 is replaced by Val or Phe, Ala152 is retained or replaced by Ser, Leu154 is strictly conserved, and Leu251 (not shown) is retained or replaced by other large side chains in other homologues. Aromatic groups, often involved in π-π stacking interactions with nucleic acids and known to occur in xanthine hydroxylase (*58, 59*) and uric acid oxidase (*60*), do not appear to be important for binding xanthine in xanthine/αKG dioxygenase. These predictions set the stage for future chemical modification, mutagenesis, and structural efforts to test these interactions.

FIGURE 3.7: Comparison of sequences from XanA orthologues in selected fungi. Black shading represents identical sequences and gray shading indicates conservative replacements.

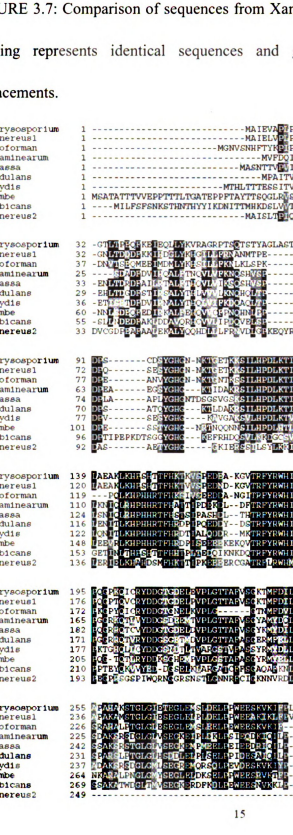

FIGURE 3.7:

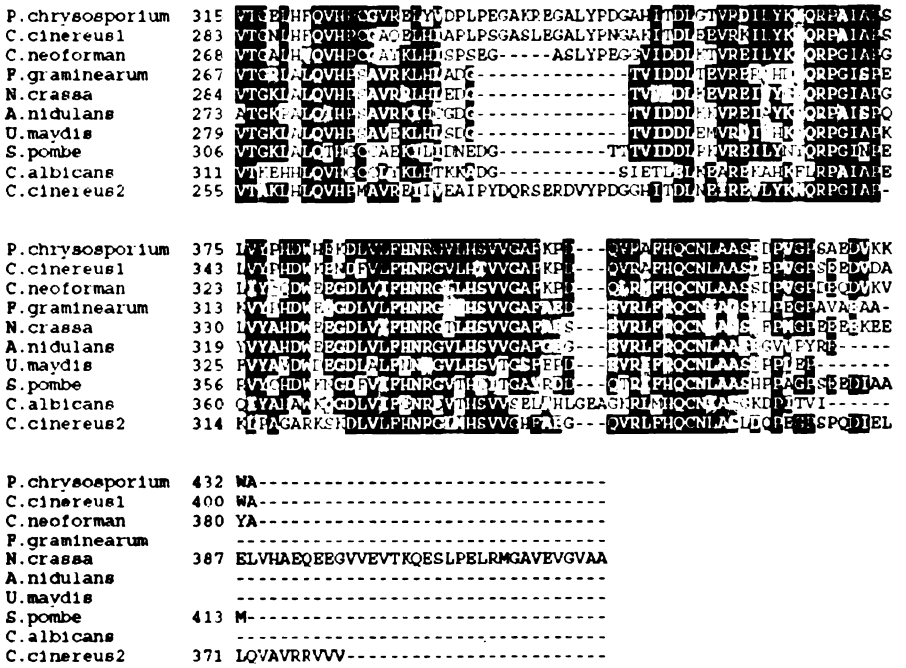
P.chrysosporium 315
C.cinereus1 283
C.neoforman 268
P.graminearum 267
N.crassa 264
A.nidulans 273
U.maydis 279
S.pombe 306
C.albicans 311
C.cinereus2 255
P.chrysosporium 375
C.cinereus1 343
C.neoforman 323
P.graminearum 313
N.crassa 330
A.nidulans 319
U.maydis 325
S.pombe 356
C.albicans 360
C.cinereus2 314
P.chrysosporium 432 WA
C.cinereus1 400 WA
C.neoforman 380 YA
P.graminearum
N.crassa 387 ELVHAEQEEGVVEVTKQESLPELRMGAVEVGVAA
A.nidulans
U.maydis
S.pombe 413 M
C.albicans
C.cinereus2 371 LQVAVRRVVV

REFERENCES

(1) Hille, R. (2005) Molybdenum-containing hydroxylases. *Arch. Biochem. Biophys. 433*, 107-116.

(2) Hausinger, R. P. (2004) Fe(II)/α-ketoglutarate-dependent hydroxylases and related enzymes. *Crit. Rev. Biochem. Mol. Biol. 39*, 21-68.

(3) Schofield, C. J., and Ratcliffe, P. J. (2004) Oxygen sensing by hydroxylases. *Nat. Rev. Molec. Cell Biol. 5*, 343-354.

(4) Tsukada, Y.-I., Fang, J., Erdjument-Bromage, H., Warren, M. E., Borchers, C. H., Tempst, P., and Zhang, Y. (2006) Histone demethylation by a family of JmjC domain-containing proteins. *Nature 439*, 811-816.

(5) Trewick, S. C., Henshaw, T. F., Hausinger, R. P., Lindahl, T., and Sedgwick, B. (2002) Oxidative demethylation by *Escherichia coli* AlkB directly reverts DNA base damage. *Nature 419*, 174-178.

(6) Aas, P. A., Otterlei, M., Falnes, P. O., Vagbe, C. B., Skorpen, F., Akbari, M., Sundheim, O., Bjoras, M., Slupphaug, G., Seeberg, E., and Krokan, H. E. (2003) Human and bacterial oxidative demethylases repair alkylation damage in both RNA and DNA. *Nature 421*, 859-863.

(7) Mukherji, M., Chien, W., Kershaw, N. J., Clifton, I. J., Schofield, C. J., Wierzbicki, A. S., and Lloyd, M. D. (2001) Structure-function analysis of phytanoyl-CoA 2-hydroxylase mutations causing Refsum's disease. *Human Molec. Genet. 10*, 1971-1982.

(8) Prescott, A. G., and John, P. (1996) Dioxygenases: molecular structure and role in plant metabolism. *Annu. Rev. Plant Physiol. Plant Molec. Biol. 47*, 245-271.

(9) Thornburg, L. D., Lai, M.-T., Wishnok, J. S., and Stubbe, J. (1993) A non-heme iron protein with heme tendencies: an investigation of the substrate specificity of thymine hydroxylase. *Biochemistry 32*, 14023-14033.

(10) Fukumori, F., and Hausinger, R. P. (1993) Purification and characterization of 2,4-dichlorophenoxyacetate/α-ketoglutarate dioxygenase. *J. Biol. Chem. 268*, 24311-24317.

(11) Müller, T. A., Zavodszky, M. I., Feig, M., Kuhn, L. A., and Hausinger, R. P. (2006) Structural basis for the enantiospecificities of *R*- and *S*-phenoxypropionate/α-ketoglutarate dioxygenases. *Prot. Science 15*, 1356-1368.

(12) Eichhorn, E., van der Ploeg, J. R., Kertesz, M. A., and Leisinger, T. (1997) Characterization of α-ketoglutarate-dependent taurine dioxygenase from *Escherichia coli*. *J. Biol. Chem. 272*, 23031-23036.

(13) Ryle, M. J., Padmakumar, R., and Hausinger, R. P. (1999) Stopped-flow kinetic analysis of *Escherichia coli* taurine/α-ketoglutarate dioxygenase: interactions with α-ketoglutarate, taurine, and oxygen. *Biochemistry 38*, 15278-15286.

(14) Price, J. C., Barr, E. W., Tirupati, B., Bollinger, J. M., Jr., and Krebs, C. (2003) The first direct characterization of a high-valent iron intermediate in the reaction of an α-ketoglutarate-dependent dioxygenase: a high-spin Fe(IV) complex in taurine/α-ketoglutarate dioxygenase (TauD) from *Escherichia coli*. *J. Biol. Chem. 42*, 7497-7508.

(15) Price, J. C., Barr, E. W., Glass, T. E., Krebs, C., and Bollinger, J. M., Jr. (2003) Evidence for hydrogen abstraction from C1 of taurine by the high-spin Fe(IV) intermediate detected during oxygen activation by taurine:α-ketoglutarate dioxygenase (TauD). *J. Am. Chem. Soc. 125*, 13008-13009.

(16) Proshlyakov, D. A., Henshaw, T. F., Monterosso, G. R., Ryle, M. J., and Hausinger, R. P. (2004) Direct detection of oxygen intermediates in the non-heme Fe enzyme taurine/α-ketoglutarate dioxygenase. *J. Am. Chem. Soc. 126*, 1022-1023.

(17) Riggs-Gelasco, P. J., Price, J. C., Guyer, R. B., Brehm, J. H., Barr, E. W., Bollinger, J. M., Jr., and Krebs, C. (2004) EXAFS spectroscopic evidence for an Fe=O unit in the Fe(IV) intermediate observed during oxygen activation by taurine:α-ketoglutarate dioxygenase. *J. Am. Chem. Soc. 126*, 8108-8109.

(18) Price, J. C., Barr, E. W., Hoffart, L. M., Krebs, C., and Bollinger, J. M., Jr. (2005) Kinetic dissection of the catalytic mechanism of taurine:α-ketoglutarate dioxygenase (TauD) from *Escherichia coli*. *Biochemistry 44*, 8138-8147.

(19) Grzyska, P. K., Ryle, M. J., Monterosso, G. R., Liu, J., Ballou, D. P., and Hausinger, R. P. (2005) Steady-state and transient kinetic analyses of taurine/α-ketoglutarate dioxygenase: effects of oxygen concentration, alternative sulfonates, and active site variants on the Fe(IV) intermediate. *Biochemistry 44*,

3845-3855.

(20) Elkins, J. M., Ryle, M. J., Clifton, I. J., Dunning Hotopp, J. C., Lloyd, J. S., Burzlaff, N. I., Baldwin, J. E., Hausinger, R. P., and Roach, P. L. (2002) X-ray crystal structure of *Escherichia coli* taurine/α-ketoglutarate dioxygenase complexed to ferrous iron and substrates. *Biochemistry 41*, 5185-5192.

(21) O'Brien, J. R., Schuller, D. J., Yang, V. S., Dillard, B. D., and Lanzilotta, W. N. (2003) Substrate-induced conformational changes in *Escherichia coli* taurine/α-ketoglutarate dioxygenase and insight into the oligomeric structure. *Biochemistry 42*, 5547-5554.

(22) Ryle, M. J., Liu, A., Muthukumaran, R. B., Ho, R. Y. N., Koehntop, K. D., McCracken, J., Que, L., Jr., and Hausinger, R. P. (2003) O_2- and α-ketoglutarate-dependent tyrosyl radical formation in TauD, an α-keto acid-dependent non-heme iron dioxygenase. *Biochemistry 42*, 1854-1862.

(23) Ryle, M. J., Koehntop, K. D., Liu, A., Que, L., Jr., and Hausinger, R. P. (2003) Interconversion of two oxidized forms of TauD, a non-heme iron hydroxylase: evidence for bicarbonate binding. *Proc. Natl. Acad. Sci. USA 100*, 3790-3795.

(24) Koehntop, K. D., Marimanikkuppam, S., Ryle, M. J., Hausinger, R. P., and Que, L., Jr. (2006) Self-hydroxylation of taurine/α-ketoglutarate dioxygenase. Evidence for more than one oxygen activation mechanism. *J. Biol. Inorg. Chem. 11*, 63-72.

(25) Cultrone, A., Scazzocchio, C., Rochet, M., Montero-Morán, G., Drevet, C., and Fernández-Martín, R. (2005) Convergent evolution of hydroxylation mechanisms in the fungal kingdoms: molybdenum cofactor-independent hydroxylation of xanthine via α-ketoglutarate dependent dioxygenase. *Molec. Microbiol. 57*, 276-290.

(26) Montero-Morán, G. M., Li, M., Rendon-Huerta, E., Jourdan, F., Lowe, D. J., Stumpff-Kane, A. W., Feig, M., Scazzocchio, C., and Hausinger, R. P. (2007) Purification and characterization of the Fe(II)- and α-ketoglutarate-dependent xanthine hydroxylase from *Aspergillus nidulans*. *Biochemistry 46*, 5293-5304.

(27) Albert, A., and Brown, D. J. (1954) Pruine studies. Part I. Stability to acid and alkali. Solubility. Ionization. Comparison with pteridines. *J. Chem. Soc.*, 2060-2071.

(28) Dornow, a., and Hinz, E. (1958) Syntheses of nitrogen-containing heterocycles. XVIII. ortho-condensations of heterocyclic *o*-aminocarboxylic acid derivatives. *Chem. Ber. 91*, 1834-1840.

(29) Altschul, S. F., Madden, T. L., Schaffer, A. A., Zhang, J. H., Zhang, Z., Miller, W., and Lipman, D. J. (1997) Gapped BLAST and PSI-BLAST: A new generation of protein database search programs. *Nucl. Acids Res. 25*, 3389-3402.

(30) Schäffer, A. A., Aravind, L., Madden, T. L., Shavirin, S., Spouge, J. L., Wolf, Y. I., Koonin, E. V., and Altschul, S. F. (2001) Improving the accuracy of PSI-BLAST protein database searches with composition-based statistics and other refinements. *Nucleic Acids Research 29*, 2994-3005.

(31) Ginalski, K., Elofsson, A., Fisher, D., and Rychlewski, L. (2003) 3D-Jury: a simple approach to improve protein structure predictions. *Bioinformatics 19*, 1015-1018.

(32) Muckstein, U., Holfacker, I. L., and Stadler, P. F. (2002) Stochastic pairwise alignments. *Bioinformatics 18 (Suppl. 2)*, S153-S160.

(33) Feig, M., Rotkiewicz, P., Kolinski, A., Skolnick, J., and Brooks, C. L., III. (2000) Accurate reconstruction of all-atom protein representations from side-chain-based low-resolution models. *Proteins 41*, 86-97.

(34) Feig, M., Karanicolas, J., and Brooks, C. L., III. (2004) MMTSB tool set: enhanced sampling and multiscale modeling methods for applications in structural biology. *J. Molec. Graphics Modeling 22*, 377-395.

(35) Zhang, C., Liu, S., Zhu, Q. Q., and Zhou, Y. Q. (2005) A knowledge-based energy function for protein-ligand, protein-protein, and protein-DNA complexes. *J. Med. Chem. 48*, 2325-2335.

(36) Feig, M., and Brooks, C. L., III. (2002) Evaluating CASP4 predictions with physical energy functions. *Proteins: Struct. Funct. Genet. 49*, 232-245.

(37) Samudrala, R., and Moult, J. (1998) An all-atom distance-dependent conditional probability discriminatory function for protein structure prediction. *J. Mol. Biol. 275*, 895-916.

(38) Stumpff-Kane, A. W., and Feig, M. (2006) A correlation-based method for the enhancement of scoring functions on funnel-shaped energy landscapes. *Proteins:*

Struct., Funct. Bioinform. 63, 155-164.

(39) Kalliri, E., Grzyska, P. K., and Hausinger, R. P. (2005) Kinetic and spectroscopic investigation of Co^{II}, Ni^{II}, and *N*-oxalylglycine inhibition of the Fe(II)/α-ketoglutarate dioxygenase, TauD. *Biochem. Biophys. Res. Commun. 338*, 191-197.

(40) Baader, E., Tschank, G., Baringhaus, K. H., Burghard, H., and Gunzler, V. (1994) Inhibition of prolyl 4-hydroxylase by oxalyl amino acid derivatives in vitro, in isolated microsomes and in embryonic chicken tissues. *Biochem. J. 300*, 525-530.

(41) Cunliffe, C. J., Franklin, T. J., Hales, N. J., and Hill, G. B. (1992) Novel inhibitors of prolyl 4-hydroxylase. 3. Inhibition by the substrate analogue N-oxaloglycine and its derivatives. *J. Med. Chem. 35*, 2652-2658.

(42) Chan, D. A., Sutphin, P. D., Denko, N. C., and Giaccia, A. J. (2002) Role of prolyl hydroxylation in oncogenically stabilized hypoxia-inducible factor-1α. *J. Biol. Chem. 277*, 40112-40117.

(43) McDonough, M. A., McNeill, L. A., Tilliet, M., Papmichael, C. A., Chen, Q.-Y., Banerji, B., Hewitson, K. S., and Schofield, C. J. (2005) Selective inhibition of factor inhibiting hypoxia-inducible factor. *J. Am. Chem. Soc. 127*, 7680-7681.

(44) Tramontano, A., and Morea, V. (2003) Assessment of homology-based predictions in CASP5. *Proteins: Struct. Funct. Genet. 53*, 352-368.

(45) Kryshtafovych, A., Venclovas, C., Fidelis, K., and Moult, J. (2005) Progress over the first decade of CASP experiments. *Proteins: Struct. Funct. Genet. S7*, 225-236.

(46) Clifton, I. J., McDonough, M. A., Ehrismann, D., Kershaw, N. J., Granatino, N., and Schofield, C. J. (2006) Structural studies on 2-oxoglutarate oxygenases and related double-stranded β-helix fold protein. *J. Inorg. Biochem. 100*, 644-669.

(47) Hoffart, L. M., Barr, E. W., Guyer, R. B., Bollinger, J. M., Jr., and Krebs, C. (2006) Direct spectroscopic detection of a C-H-cleaving high-spin Fe(IV) complex in a prolyl-4-hydroxylase. *Proc. Natl. Acad. Sci. USA 103*, 14738-14743.

(48) Busby, R. W., Chang, M. D.-T., Busby, R. C., Wimp, J., and Townsend, C. A. (1995) Expression and purification of two isozymes of clavaminate synthase and initial characterization of the iron binding site. General error analysis in

polymerase chain reaction amplification. *J. Biol. Chem. 270*, 4262-4269.

(49) Hegg, E. L., Whiting, A. K., Saari, R. E., McCracken, J., Hausinger, R. P., and Que, L., Jr. (1999) Herbicide-degrading α-keto acid-dependent enzyme TfdA: metal coordination environment and mechanistic insights. *Biochemistry 38*, 16714-16726.

(50) Müller, T. A., Fleischmann, T., van der Meer, J. R., and Kohler, H.-P. E. (2006) Purification and characterization of two enantioselective α-ketoglutarate-dependent dioxygenases, RdpA and SdpA, from *Sphingomonas herbicidovorans* MH. *Applied and Environmental Microbiology 72*, 4853-4861.

(51) Kahnert, A., and Kertesz, M. A. (2000) Characterization of a sulfur-regulated oxygenative alkylsulfatase from *Pseudomonas putida* S-313. *J. Biol. Chem. 275*, 31661-31667.

(52) Elion, G. B., Kovensky, A., and Hitchings, G. H. (1966) Metabolic studies of allopurinol, an inhibitor of xanthine oxidase. *Biochem. Pharmacol. 15*, 863-880.

(53) Edmondson, D., Ballou, D. P., Vn Heuvelen, A., Palmer, G., and Massey, V. (1973) Kinetic studies on the substrate reduction of xanthine oxidase. *J. Biol. Chem. 248*, 6135-6144.

(54) McWhirter, R. B., and Hille, R. (1991) The reductive half-reaction of xanthine oxidase. Identification of spectral intermediates in the hydroxylation of 2-hydroxy-6-methylpurine. *J. Biol. Chem. 266*, 23724-23731.

(55) Ivan, M., Kondo, K., Yang, H., Kim, W., Valiando, J., Ohh, M., Salic, A., Asara, J. M., Lane, W. S., and Kaelin, W. G., Jr. (2001) HIFα targeted for VHL-mediated destruction by proline hydroxylation: implications for O_2 sensing. *Science 292*, 464-467.

(56) Jaakkola, P., Mole, D. R., Tian, Y.-M., Wilson, M. I., Gielbert, J., Gaskell, S. J., von Kriegsheim, A., Hebestreit, H. F., Mukherji, M., Schofield, C. J., Maxwell, P. H., Pugh, C. W., and Ratcliffe, P. J. (2001) Targeting of HIF-α to the von Hippel-Lindau ubiquitylation complex by O_2-regulated prolyl hydroxylation. *Science 292*, 468-472.

(57) Hogan, D. A., Auchtung, T. A., and Hausinger, R. P. (1999) Cloning and characterization of a sulfonate/α-ketoglutarate dioxygenase from *Saccharomyces cerevisiae. J. Bacteriol. 181*, 5876-5879.

(58) Okamoto, K., Matsumoto, K., Hille, R., Eger, B. T., Pai, E. F., and Nishino, T. (2004) The crystal structure of xanthine oxidoreductase during catalysis: implications for reaction mechanism and enzyme inhibition. *Proc. Natl. Acad. Sci. USA 101*, 7931-7936.

(59) Truglio, J. J., Theis, K., Leimkühler, S., Rappa, R., Rajagopalan, K. V., and Kisker, C. (2002) Crystal structure of the active and alloxanthine-inhibited forms of xanthine dehydrogenase from Rhodobacter capsulatus. Structure 10, 115-125.

(60) Retailleau, P., Colloc'h, N., Vivarés, D., Bonneté, F., Castro, B., El Hajji, M., Mornon, J.-P., Monard, G., and Prangé, T. (2004) Complexed and ligand-free high-resolution structures of urate oxidase (Uox) from Aspergillus flavus: a reassignment of the active-site binding mode. Acta Crystallogr. D60, 453-462.

CHAPTER 4

Characterization of Active Site Variants of Xanthine Hydroxylase from *Aspergillus nidulans*

Tina Müller constructed the XanA variants and carried out oxygen consumption studies.

ABSTRACT

Xanthine/α-ketoglutarate (αKG) dioxygenase (XanA) is a non-heme mono-nuclear Fe(II) enzyme that decarboxylates αKG to succinate and CO_2 while catalyzing the hydroxylation of xanthine to generate uric acid. In the absence of a XanA crystal structure, a homology model was used to target several putative active site residues for mutagenesis. Wild-type XanA and ten enzyme variants were purified from recombinant *Escherichia coli* cells and extensively characterized. From analysis of the quenching of the endogenous fluorescence of XanA, the H149A, D151A, and H340A mutants displayed significant increases in K_d of Fe(II) and the K122A variant exhibited a large increase in K_d of αKG, consistent with the proposed roles of the corresponding residues in Fe(II)- and αKG-binding. The H149A and D151A variants were inactive whereas the H340A variant exhibited 0.13 U mg^{-1} (0.17 % of the wild-type enzyme). The N358A variant exhibited the next largest change in xanthine-related kinetics with a 12-fold larger K_m and 2-fold decrease in k_{cat} compared to wild-type XanA, pointing to a key role of Asn358 in catalysis. The E137A and D138A variants demonstrated enhanced activity with 9-methylxanthine, a poor substrate of the enzyme, consistent with Glu137 and Asp138 being proximal to N-9 of substrate. The Q356A and N358A variants had significantly increased K_i^{app} over control protein for 6,8-dihydroxypurine, identified as a slow-binding competitive inhibitor of XanA, suggesting that Gln356 and Asn358 hydrogen bond with the C-6 hydroxyl group of substrate. In contrast, the K_i^{app} decreased for the E137A and D138A proteins, consistent with repulsion between these carboxylates and the

deprotonated C-8 hydroxyl group suspected to bind Fe(II). Support for Cys357 residing at the active site was obtained by using thiol-specific reagents that inactivated wild-type enzyme with partial protection by substrate, whereas the C357A variant was resistant to these reagents. In the absence of substrates, the Q101A, Q356A, and C357A variants showed elevated ferroxidase activity, indicating increased oxygen reactivity of their metallocenters and/or enhanced Fe(II) access to those sites. These results were combined into a model depicting Fe(II) and substrate interaction with the XanA active site and provide insight into the specificity of the enzyme and selected aspects of its reactivity.

INTRODUCTION

Xanthine dehydrogenases and xanthine oxidases are molybdopterin cofactor (Moco)-containing enzymes that transform xanthine into uric acid (*1*). These enzymes are conserved throughout living organisms, including archaea, bacteria, fungi, plants, and metazoans. Surprisingly, mutants of *Aspergillus nidulans* with known defects in xanthine dehydrogenase activity (i.e., with mutations affecting the structural gene *hxA*, the *cnx* genes for Moco synthesis, or *hxB* for sulfuration of Moco) were found to retain the ability to grow on xanthine as sole nitrogen source (*2*). This capacity arises from an alternative xanthine-degrading activity encoded by the *xanA* gene found only in selected fungi (*3*). Recombinant His_6-tagged XanA protein was purified from both *A. nidulans* mycelia and *Escherichia coli* cells, extensively characterized, and shown to be an Fe(II)- and α-ketoglutarate (αKG)-dependent hydroxylase that catalyzes the reaction shown in Figure 2.1 (*4*). On the basis of its sequence similarity to taurine/αKG dioxygenase or TauD (*5*), a well-studied and crystallographically characterized member of the Fe(II)/αKG dioxygenase family (*6, 7, 8*), a homology model was constructed for XanA (*4*). The overall sequence identity of XanA and TauD is only 18 % over 280 residues and three loops in XanA could not be modeled; however, the relevant structural regions near the active sites are 33 % identical and it is reasonable to assume that the model captures the overall features correctly. The XanA model (Figure 4.1) predicts that (i) Fe(II) binds to the His149, Asp151, and His340 residues of the protein, (ii) αKG chelates the metal by using its C-1 carboxylate and C-2 keto group, with its C-1 carboxylate further stabilized by

FIGURE 4.1: Depiction of the putative active site pocket of XanA revealed from a homology model. His149, Asp151, and His340 side chains (blue) and αKG (yellow) coordinate the Fe(II)(orange sphere). Seven residues lining the putative active site and capable of participating in hydrogen-bonding interactions are colored green (Gln99, Lys122, Glu137, Asp138, Gln356, Cys357, Asn358), with another shown in purple (Gln101) at the active site entrance.

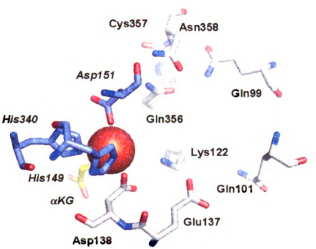

interaction with Lys122 and its C-5 carboxylate forming a salt bridge with Arg352, and (iii) xanthine binds in an active site pocket lined with potential hydrogen bond donors or acceptors (Gln99, Gln101, Glu137, Asp138, Lys122, Gln356, Cys357, and Asn358) whereas aromatic residues are not important for binding substrate.

In this study, the three residues thought to bind Fe(II) and each of the potential hydrogen-bonding residues at the XanA active site was replaced by Ala, a residue that is incapable of hydrogen bonding. Fluorescence quenching methods were used to assess the K_d values of Fe and αKG for the mutant enzymes. The kinetic properties of the variants were analyzed with xanthine, the alternate substrate 9-methylxanthine, and 6,8-dihydroxypurine (6,8-DHP), which was shown to be a slow-binding competitive inhibitor of XanA. Chemical modification studies were carried out with thiol-specific reagents for the wild-type enzyme and the C357A variant. Finally, the reactivity of each metallocenter with oxygen was examined in the absence of substrate. On the basis of these results, we identify critical residues that participate in binding of Fe(II), αKG, and the primary substrate, and we obtain insight into the enzyme reactivity.

EXPERIMENTAL PROCEDURES

Site-Directed Mutagenesis, Protein Overproduction, and Enzyme Purification. The Q99A, Q101A, K122A, E137A, D138A, H149A, D151A, H340A, Q356A, C357A, and N358A variants of XanA were created by mutagenesis of *xanA* (encoding a His_6-tagged version of XanA, termed wild-type XanA for convenience) in a modified version of vector pThioHisC (*4*) using the Quickchange II site-directed mutagenesis kit (Stratagene). Each mutation was confirmed by sequence analysis (Davis Sequencing, Davis, CA). Plasmids were transformed into XL1Blue *E. coli* cells (Stratagene) and the variant proteins were overproduced during cell growth in Luria Base Broth (Difco) and induced by using isopropyl-β-D-thiogalactopyranoside as described previously (*4*). Cultures were harvested by centrifugation at 8,000 *g* for 10 min at 4 °C, the cells were disrupted by use of a French pressure cell, membranes and insoluble materials were removed by ultracentrifugation (45 min at 100,000 *g*), and the wild-type and variant forms of XanA were purified by using Ni-loaded nitrilotriacetic acid (NTA)-bound resin, as previously reported (*4*).

Fluorescence Quenching Analyses of Fe(II) and αKG Binding. Fluorescence measurements were made on a luminescence spectrometer, model LS-50B (Perkin Elmer Limited, UK). The temperature of the cells was maintained at 25 °C. Fluorescence measurements were carried out at an excitation wavelength of 280 nm (10 nm band-width) with emission monitored from 300 to 400 nm (5 nm bandwidth). Samples were prepared in 50 mM Tris buffer, pH 8.0, and Fe(II) or αKG was added to 35 μM or 350 μM, respectively. The data were fit to equation 1, where [L] is the

ligand (Fe(II) or αKG) concentration.

$$\Delta\text{fluorescence} = \Delta\text{fluorescence}_{max}\,[L]/(K_d + [L]) \quad (1)$$

Enzyme Assays. Enzymatic assays of XanA and its variants were carried out at 25 °C by using the following typical assay conditions (total volume of 1 mL): 1 mM αKG, 40 μM $Fe(NH_4)_2(SO_4)_2$, and 200 μM xanthine in 50 mM MOPS buffer, pH 7.4 (*4*). For kinetic analyses, the concentrations of αKG or xanthine were varied while holding the concentrations of the other components constant. The absorbance at 294 nm was monitored to determine the uric acid production (overall change in ε_{294} of 10,200 M^{-1} cm^{-1}). Units of activity (U) were defined as μmol min^{-1} of uric acid produced and the specific activity (U mg^{-1}) was measured as μmol min^{-1} (mg of purified XanA)$^{-1}$ as described before (*4*). Analogous studies were carried out with 9-methylxanthine (Sigma-Aldrich), but in this case the absorbance at 291 nm was used to calculate the production of 9-methyluric acid (overall change in ε_{291} of 6,800 M^{-1} cm^{-1}). Trace activity was detected with 1-methylxanthine (Sigma-Aldrich), but complete kinetic studies could not be performed.

In addition to the spectrophotometric measure of xanthine conversion to uric acid (or the use of substituted xanthines to form substituted uric acids), the various forms of the enzyme were analyzed for ferroxidase activity (reduction of oxygen by using excess ferrous ions as reductant) by use of a Clark-type oxygen electrode. These assays were carried out in air-saturated MOPS medium (pH 7.4) at 25 °C. Less than 12% of the initial levels of O_2 were consumed in these assays, and the data were fit to equation 2. $[O_2]_t$ is the O_2 concentration at time t, $[O_2]_o$ is the initial O_2 concentration, v_b

is the background rate of O_2 reduction under the given conditions, v_o is the ferroxidase initial velocity, and k_{app} is the apparent first-order rate constant for the transition from v_o to v_b.

$$[O_2]_t = [O_2]_o - v_b t - (v_o - v_b)[1-\exp(-k_{app}t)]/k_{app} \quad (2)$$

As a complement to the electrode assay for O_2 reduction, the production of hydrogen peroxide was quantified by using a spectrophotometric assay. Timed aliquots of reaction mixtures were added to assay solutions containing 100 mM potassium phosphate (pH 5.0), 8.7 mM 2,2'-azino-bis(3-ethylbenzthiazoline-6-sulfonic acid) (ABTS), and approximately 0.003 units of horseradish peroxidase (Sigma-Aldrich). The oxidation of ABTS was monitored at 420 nm and compared to a standard curve generated with hydrogen peroxide.

A final method to assay the activity of the enzyme focused on quantification of the αKG consumed during the reaction. Aliquots (250 μL) of reaction mixtures were incubated for selected time periods, quenched by addition of 1 mL 0.5 mg/ml *o*-phenylenediamine (OPDA, Sigma-Aldrich) stock solution (dissolved in 1 M phosphoric acid, pH 2, containing 0.25% (v/v) β-mercaptoethanol), and the samples were heated for 3 min at 100 °C. The absorbance at 333 nm was monitored to determine αKG consumption by comparison to standard curves.

Kinetic Analysis of 6,8-DHP Inhibition. Spectrophotometric progress curves (containing 90 or more data points, typically at 15 s intervals) were initiated by adding XanA to solutions containing several fixed concentrations of substrate and selected concentrations of 6,8-DHP (graciously provided by D. J. Lowe and F.

Jourdan). The data were analyzed according to equation 3 by using a nonlinear regression program to give the individual parameters for each progress curve: A (absorbance at 294 nm), A_0 (for baseline correction), v_i (initial velocity), v_s (steady-state velocity), and k_{obs} (apparent first-order rate constant for the transition from v_i to v_s).

$$A = A_0 + v_s t + (v_i - v_s)[1 - \exp(-k_{obs} t)]/ k_{obs} \qquad (3)$$

RESULTS

Site-directed variants of recombinant *A. nidulans* XanA, an Fe(II)- and αKG-dependent hydroxylase of xanthine, were investigated to further characterize the protein features important to catalysis. In the absence of a crystal structure for XanA, we relied on a previously reported homology model of XanA (*4*) that identifies the likely triad of metal-binding residues and predicts the active site pocket is lined by eight residues capable of hydrogen bonding interactions with substrate. To test this hypothetical model, Ala was used to replace each of these residues and the enzymatic properties of the resulting variant proteins were characterized. In particular, the binding of Fe(II) and αKG to the XanA variants was assessed by fluorescence quenching methods and the kinetic properties were studied using xanthine, the alternative substrate 9-methylxanthine, and 6,8-DHP, a known XanA inhibitor (*4*). In addition, the behavior of wild-type enzyme and C357A variant were compared using thiol-specific chemical modification reagents. Finally, the ferroxidase activities of the active mutant proteins were examined in the absence of primary substrate.

Fe(II) and αKG Binding to XanA and its Variants. Eleven XanA variants (Q99A, Q101A, K122A, E137A, D138A, H149A, D151A, H340A, Q356A, C357A, and N358A) were produced in *E. coli* XL1Blue cells as His_6-tagged fusion proteins, along with the wild-type protein. Seven variant proteins were purified to homogeneity from cell extracts by Ni-NTA chromatography whereas three (H149A, D151A, and H340A) were enriched by this chromatographic step (Figure 4.2), and Q99A XanA failed to bind to Ni-loaded NTA resin. We interpret the Q99A XanA results to indicate protein

FIGURE 4.2: Denaturing polyacrylamide gel electrophoretic analysis of XanA variants purified from *E. coli*. Lane 1, markers; lane 2, Q101A (1.5 μg) ; lane 3, K122A (4.2 μg); lane 4, E137A (1.0 μg); lane 5, D138A (1.2 μg); lane 6, Q356A (0.5 μg); lane 7, C357A (0.3 μg); lane 8, N358A (6.4 μg); lane 9, H149A (0.17 μg); lane 10, D151 (0.8 μg); lane 11, H340A (0.13 μg) variant protein. Stacking and running gels contain 5 % and 12 % acrylamide, respectively.

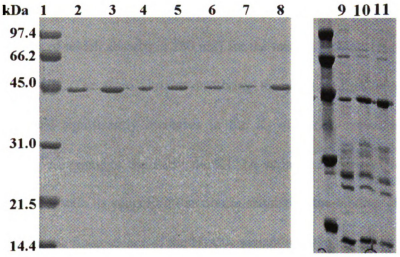

misfolding during overexpression, and this variant was not further investigated.

The binding of αKG and xanthine to XanA was previously shown to result in quenching of the endogenous fluorescence of the protein (*4*), thus allowing estimation of the K_d of the substrates. The apparent quenching of fluorescence by xanthine is complicated by the significant absorption of the excitation wavelength by the substrate, precluding the confident estimation of the K_d of xanthine. In contrast, the fluorescence quenching approach was extended to study the K_d of both αKG and Fe(II) (neither of which absorbs at 280 nm) for the mutant proteins (Figure 4.3 and 4.4, and Table 4.1). The three variants involving the putative ligands to the metallocenter displayed significantly increases in the K_d of Fe(II), consistent with their metal binding assignments. Similarly, the K122A variant exhibited an increased K_d of αKG, consistent with its suggested function in stabilizing the binding of the cosubstrate. Of interest, the fluorescence of the H149A variant was not quenched by addition of αKG perhaps suggesting that it may an important role in protein folding.

Kinetic Comparison of XanA and its Variants with Xanthine. Although all variants appeared to be equally overproduced, the Q99A, H149A, D151A, and H340A variants displayed no activity in cell extracts. When purified, H340A XanA exhibited trace activity (0.13 U mg^{-1}) corresponding to 0.17 % of that associated with wild-type enzyme. These four variants were not further analyzed kinetically. The kinetic parameters for XanA and the seven active mutant proteins are listed in Table 4.2. All of these variants exhibit perturbations in their K_m (xanthine), K_m (αKG), and k_{cat} compared to the control enzyme, consistent with the mutant proteins having

FIGURE 4.3: Fluorescence spectroscopic analysis of XanA interaction with Fe(II). The changes in the endogenous fluorescence (excitation at 280 nm and emission at 335 nm) due to quenching by Fe(II) were examined in 50 mM Tris buffer, pH. 8.0, solutions containing (A) 0.12 μM XanA, (B) 0.01 μM H149A, (C) 0.03 μM D151A, (D) 0.04 μM H340A, (E) 0.05 μM Q101A, (F) 0.12 μM K122A, (G) 0.05 μM E137A, (H) 0.07 μM D138A, (I) 0.02 μM Q356A, (J) 0.02 μM C357A, and (K) 0.07 μM N358A at 25 °C. Fe(II) concentrations ranged from 0-35 μM.

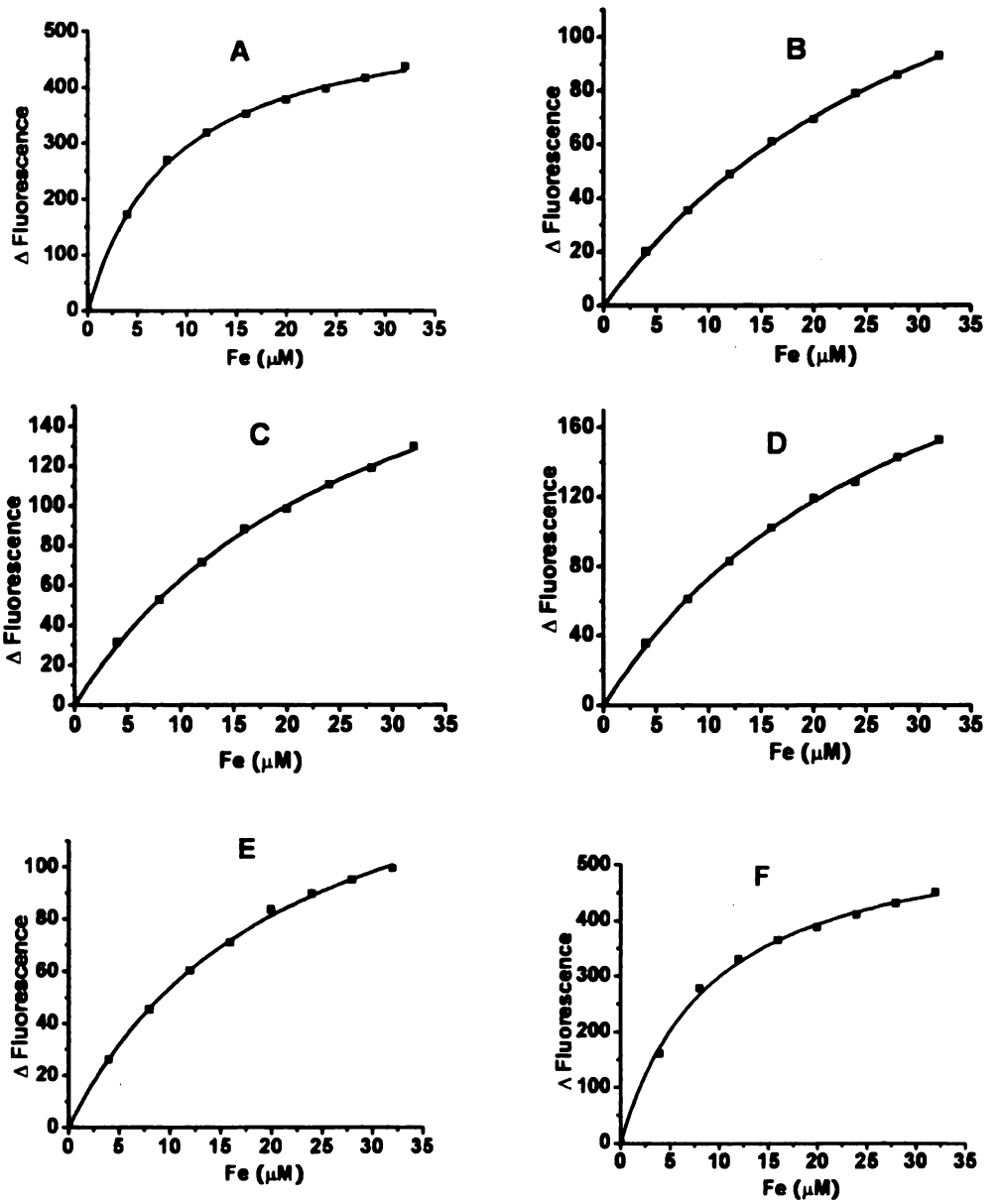

FIGURE 4.3:

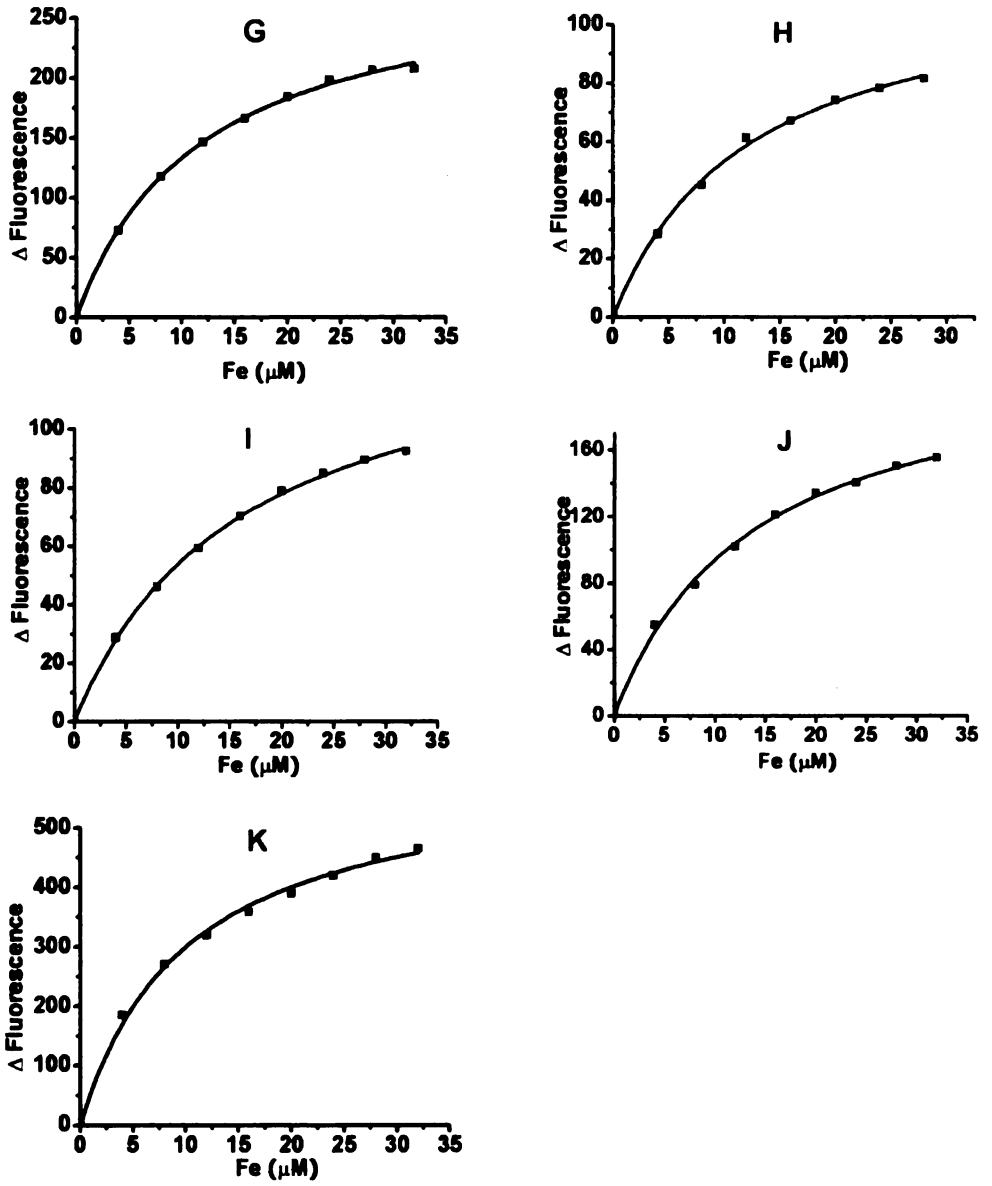
G
Δ Fluorescence
Fe (μM)
H
Δ Fluorescence
Fe (μM)
I
Δ Fluorescence
Fe (μM)
J
Δ Fluorescence
Fe (μM)
K
Δ Fluorescence
Fe (μM)

FIGURE 4.4: Fluorescence spectroscopic analysis of XanA interaction with αKG. The changes in the endogenous fluorescence due to quenching by αKG in 50 mM Tris, pH. 8.0, buffer were examined in solutions containing (A) 0.12 μM XanA, (B) 0.03 μM D151A, (C) 0.04 μM H340A, (D) 0.50 μM Q101A, (E) 0.12 μM K122A, (F) 0.13 μM E137A, (G) 0.18 μM D138A, (H) 0.05 μM Q356A, (I) 0.10 μM C357A and (J) 0.11 μM N358A, at 25 °C.

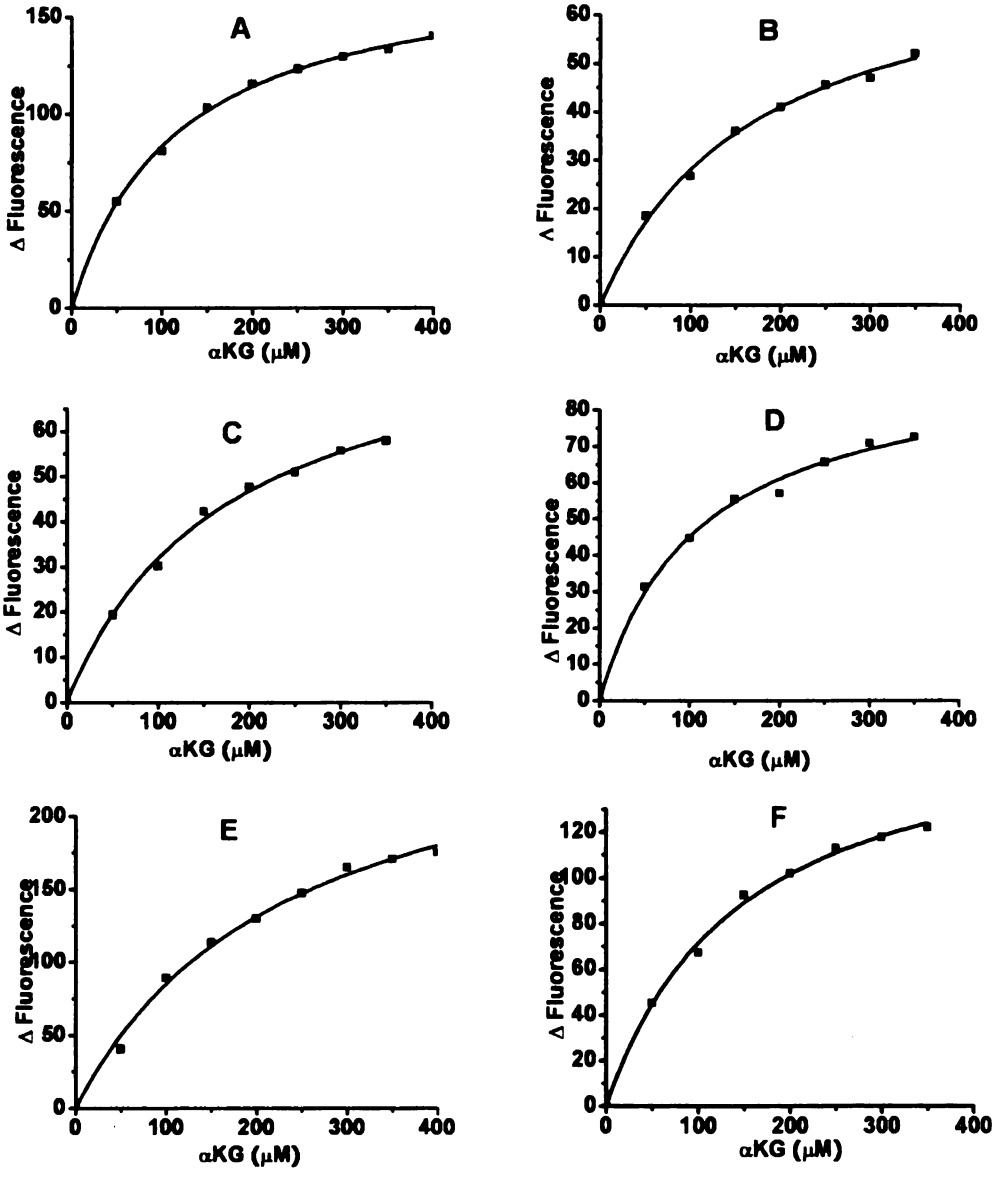

FIGURE 4.4:

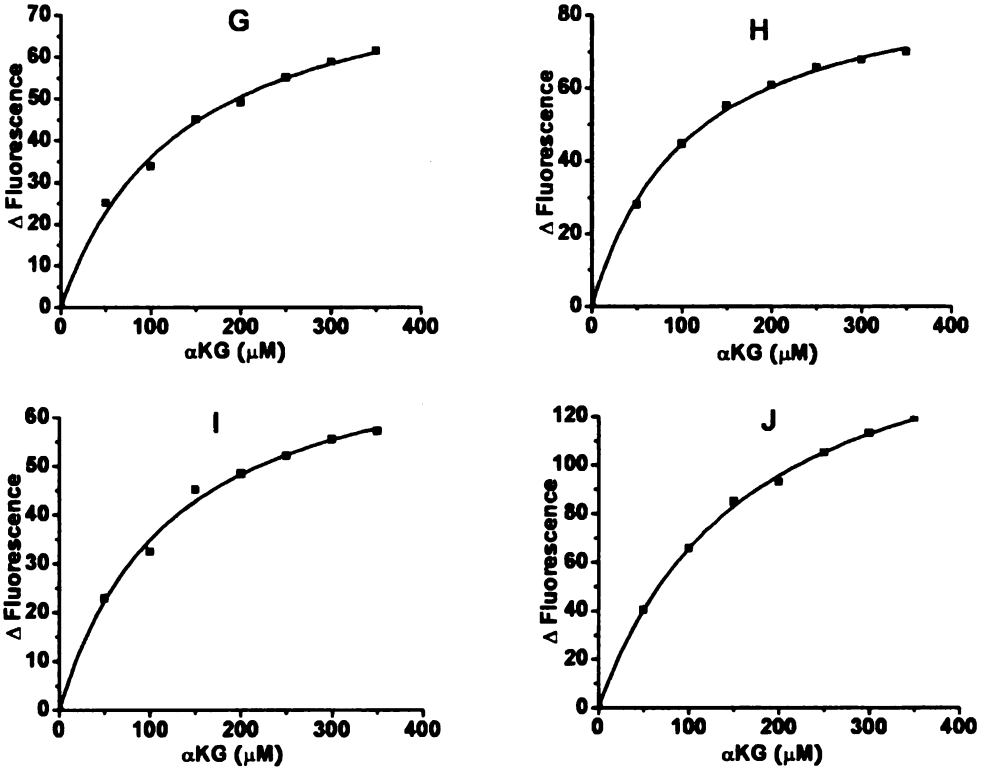

TABLE 4.1: Determination of K_d of Fe(II) and αKG for XanA and Selected Variants[a]

Mutant	K_d of Fe(II) (μM)	K_d of αKG (μM)
XanA	8.5 ± 0.3	115 ± 5
Q101A	21.5 ± 1.2	108 ± 12
K122A	9.3 ± 0.6	236 ± 29
E137A	11.7 ± 0.6	146 ± 13
D138A	12.3 ± 1.0	136 ± 14
H149A	36.8 ± 1.3	ND[b]
D151A	28.2 ± 1.4	169 ± 16
H340A	30.7 ± 1.4	175 ± 16
Q356A	15.9 ± 0.6	108 ± 6
C357A	13.5 ± 0.9	124 ± 14
N358A	10.1 ± 1.0	168 ± 9

[a] Estimated on the basis of quenching of the endogenous fluorescence with excitation at 280 nm and emission at 335 nm at 25 °C. The protein concentrations: 0.12 μM for XanA, 0.01 μM for H149A, 0.03 μM for D151A, 0.04 μM for H340A, 0.05 μM for Q101A in the Fe(II) assay and 0.5 μM in the αKG assay, 0.12 μM for K122A, 0.05 μM for E137A with Fe(II) and 0.13 μM in the αKG assay, 0.07 μM for D138A in the Fe(II) assay and 0.18 μM in the αKG assay, 0.02 μM for Q356A in the Fe(II) assay and 0.05 μM in the αKG assay, 0.02 μM for C357A in the Fe(II) assay and 0.10 μM in the αKG assay, and 0.07 μM for N358A in the Fe(II) assay and 0.11 μM in the αKG assay. [b] ND, fluorescence quenching was not detected.

TABLE 4.2: Substrate, Cosubstrate, and Substrate Analog Kinetic Parameters of XanA and Selected Variants[a]

XanA sample	Xanthine[b]			αKG[c]			9-Methylxanthine[d]		
	K_m (μM)	k_{cat} (s^{-1})	k_{cat}/K_m ($\mu M^{-1} s^{-1}$)	K_m (μM)	k_{cat} (s^{-1})	k_{cat}/K_m ($\mu M^{-1} s^{-1}$)	K_m (mM)	k_{cat} (s^{-1})	k_{cat}/K_m ($mM^{-1} s^{-1}$)
Wild-Type	45 ± 4	72 ± 2	1.6	31 ± 2	67 ± 1	2.16	0.40 ± 0.07	3.8 ± 0.3	9.5
Q101A	122 ± 9	36 ± 1	0.30	59 ± 6	21 ± 1	0.36	0.78 ± 0.07	0.66± 0.03	0.85
K122A	88 ± 5	60 ± 1	0.68	32 ± 2	42 ± 1	1.31	0.88 ± 0.07	1.9 ± 0.1	2.16
E137A	71 ± 5	40 ± 1	0.56	41 ± 8	31 ± 1	0.76	1.09 ± 0.17	5.9 ± 0.5	5.41
D138A	69 ± 6	34 ± 2	0.49	53 ± 7	25 ± 1	0.47	0.58 ± 0.09	4.25 ± 0.24	7.33
Q356A	57 ± 5	35 ± 1	0.61	42 ± 3	28 ± 1	0.67	0.68 ± 0.07	1.4 ± 0.1	2.05
C357A	58 ± 5	32 ± 1	0.55	47 ± 4	19 ± 1	0.40	0.55 ± 0.05	4.5 ± 0.2	8.18
N358A	554 ± 24	38 ± 2	0.07	48 ± 8	17 ± 1	0.34	1.0 ± 0.4	1.26 ± 0.35	1.26

[a] Except for the compound being analyzed, the assay solutions contained 40 μM Fe(II), 1 mM αKG, and 200 μM xanthine in 50 mM MOPS buffer, pH 7.4, and were maintained at 25 °C. [b] Xanthine concentrations ranged from 0-250 μM, except for the N358A variant, which ranged from 0-400 μM. [c] αKG concentrations ranged from 0-500 μM. [d] 9-methylxanthine concentrations ranged from 0-1.0 mM.

modifications involving active site residues.

Alternative Substrates for XanA and its Variants. In agreement with prior results (*4*), XanA was shown to be incapable of using 3-methylxanthine, 6-methylpurine, or 7-methylxanthine as the primary substrate. In contrast, trace levels of activity were detected for 1-methylxanthine (about 10^{-4} of that observed for xanthine) when using highly concentrated enzyme solutions, and low levels of activity were observed with 9-methylxanthine. The absorbance spectra of the products arising from 1-methylxanthine and 9-methylxanthine exhibited features at 289 nm and 291 nm (Figure 4.5), consistent with the formation of 1-methyluric acid and 9-methyluric acid (*9*), respectively. Generation of the product from 9-methylxanthine was coupled to O_2 consumption, as shown by use of an oxygen electrode, and to the decomposition of αKG, as analyzed by the OPDA assay (data not shown).

The kinetic parameters associated with XanA utilization of 9-methylxanthine for wild-type enzyme and the seven variants are shown in Table 2. For wild-type XanA, the K_m of 9-methylxanthine is 8.9-fold larger than that for xanthine while the k_{cat} is approximately 5 % of that for the true substrate. Comparison of the data obtained for the control enzyme with those for the mutant proteins provides insight into potential protein interactions involving the 9-methyl group. For example the E137A variant exhibited a 1.6-fold increase in k_{cat} for 9-methylxanthine versus the wild-type enzyme. Although not statistically significant, a small increase (1.1-fold) in k_{cat} also was noted for the D138A variant. These results suggest that substituting Ala for the carboxylate at position 137, and perhaps also at position 138, partially compensates for the

FIGURE 4.5: UV-visible spectra of 1-methylxanthine, 9-methylxanthine, and their products. (A) Spectrum of 9-methylxanthine in assay solution (solid) and the sample after 30 min of reaction (dotted) at 25 °C. The assay solution included 40 μM Fe(II), 1 mM αKG, 3.6 μM XanA, and 200 μM 9-methylxanthine in 50 mM MOPS, pH 7.4. (B) Spectrum of 1-methylxanthine in assay solution (solid) and the sample after 100 min of reaction at 25 °C (dotted), using conditions as above. (C) The spectrum of the product arising from the enzymatic transformation of 1-methylxanthine was calculated from B (dotted line) by measuring the absorption at 290 nm (0.747 absorbance units), determining ε_{290} for 1-methylxanthine (1,497 M^{-1} cm^{-1}) and 1-methyluric acid (10,273 M^{-1} cm^{-1}), using these results to estimate that the concentrations of 1-methylxanthine (149 μM) and 1-methyluric acid (51 μM) which totaled to 200 μM, and subtracting the spectrum of 149 μM 1-methylxanthine from the spectrum of the mixture. This was compared to the spectrum of authentic 1-methyluric acid (solid line)

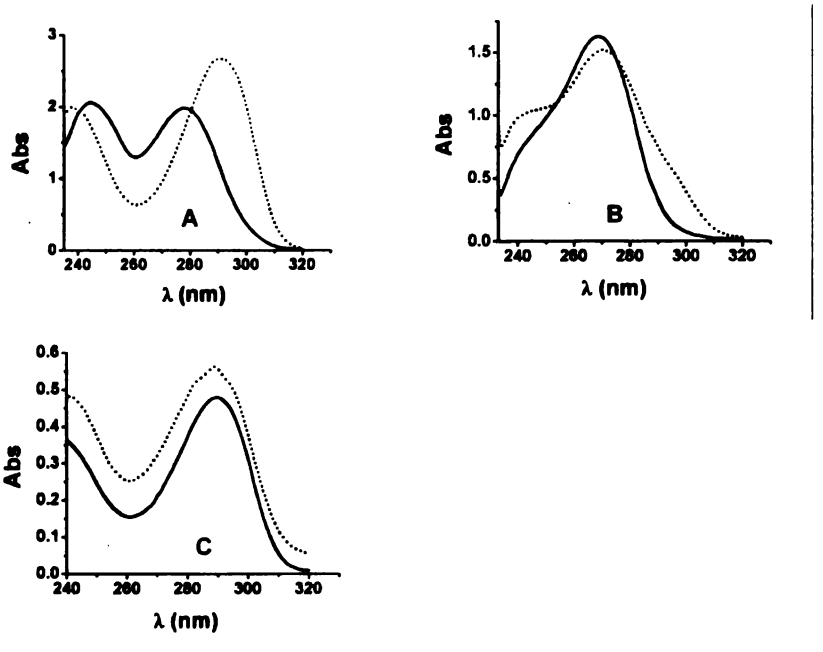

presence of a methyl group at N-9 of xanthine by allowing for more productive active site binding.

6,8-DHP Inhibition. 6,8-DHP was previously shown to inhibit wild-type XanA (*4*), but its mechanism of inhibition was not examined. By contrast only very modest inhibition was noted with 2,8-DHP, and 8-hydroxypurine did not inhibit the enzyme (*4*). These results indicated that XanA interactions with the C-6 oxygen were most important for inhibitor binding.

To examine the inhibitory effect of 6,8-DHP on XanA, progress curves of uric acid production were obtained under different inhibitor and substrate concentrations. The curves obtained for a constant substrate concentration with varied levels of inhibitor reveal a time-dependent inhibition of XanA by 6,8-DHP (Figure 4.6A) whereby the initial rate constant, v_i, decreases to a steady-state rate constant, v_s, with an apparent first-order rate constant, k_{obs}. The values of v_i, v_s, and k_{obs} were characterized according to equation 2 by using a variety of assay conditions. For varied inhibitor concentrations, k_{obs} exhibited a hyperbolic dependence on the concentration of 6,8-DHP (Figure 4.6B), consistent with a slow-binding inhibitory mechanism involving the reversible binding of inhibitor followed by a conformational change to create a tightly bound state (*10*). To distinguish the type of slow-binding inhibition mechanism, progress curves were obtained for a constant concentration of 6,8-DHP in the presence of varied substrate concentration (Figure 4.6C). A replot of k_{obs} versus substrate concentration reveals a negative slope (Figure 4.6D) and confirms the mechanism as being competitive (*11*), as depicted in Figure 4.7. Thus,

FIGURE 4.6: Interaction of XanA with 6,8-DHP. (A) Progress curves for XanA inhibition by varied concentrations of 6,8-DHP. 2.4 nM XanA was added to 50 mM MOPS buffer, pH 7.4, at 25 °C containing 40 μM Fe(II), 1 mM αKG, 200 μM xanthine, and 0 mM (■), 0.02 mM (●), 0.04 mM (▲), 0.06 mM (▼), 0.1 mM (♦) or 0.12 mM (◄) 6,8-DHP. The production of uric acid was monitored at 294 nm and the progress curves were fit to equation 1. (B) Dependence of k_{obs} on the concentration of 6,8-DHP. The curve was fit to equation 2. (C) XanA progress curves were obtained as above, but in the presence of 0.1 mM 6,8-DHP and 50 μM (◄), 100 μM (▼), 150 μM (▲), 200 μM (●) or 250 μM (■) xanthine. The progress curves were fit to equation 1. (D) Dependence of k_{obs} on the concentration of xanthine.

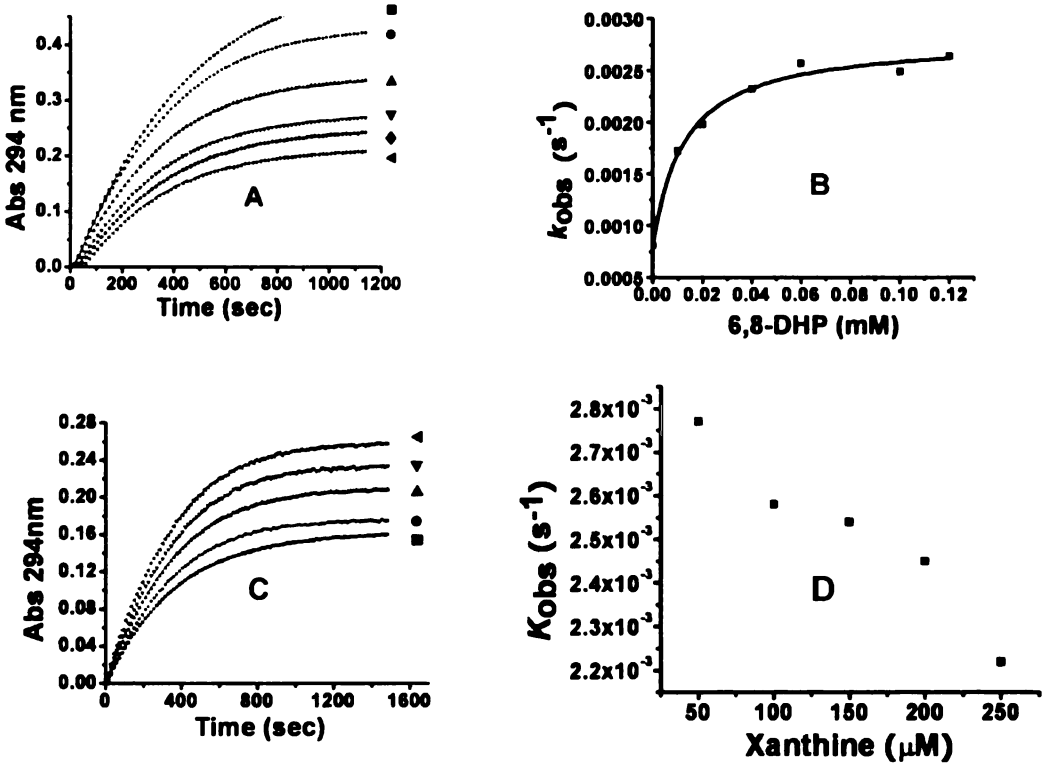

FIGURE 4.7: General mechanism for slow-binding inhibition.

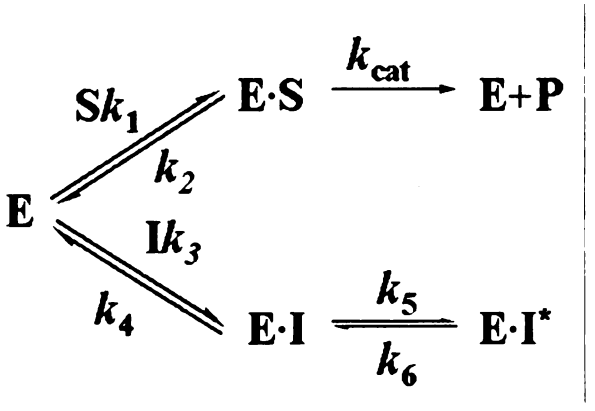

6,8-DHP competes with substrate to form an initial enzyme inhibitor complex (E·I) that slowly transforms to a more stable complex ($E{\cdot}I^*$). For such a mechanism, k_{obs} varies with the inhibitor concentration [I] according to equation 4 (*10*) , where $K_i = k_4/k_3$. This equation simplifies to equation 5 when one defines $K_i^{app} = K_i(1 + [S]/K_m)$.

$$k_{obs} = k_6 + k_5[I]K_i/(1 + [S]/K_m + [I]/K_i) \qquad (4)$$

$$k_{obs} = k_6 + k_5[I]/(K_i^{app} + [I]) \qquad (5)$$

Using the data from Figure 4.6B for wild-type XanA, $k_5 = 2.0 \times 10^{-3}$ s^{-1}, $k_6 = 8.1 \times 10^{-4}$ s^{-1}, and $K_i^{app} = 12.6$ μM. k_5 is larger than k_6 suggesting the rate of formation of $E{\cdot}I^*$ complex is much faster than its dissociation, which is in agreement with slow-binding inhibition mechanism.

The slow-binding inhibition kinetic properties of the active variant forms of XanA with 6,8-DHP were analyzed in a similar manner (see Figures 4.8-4.14) and the k_5, k_6 and K_i^{app} are compared to the control enzyme in Table 4.3. Compared with the K_i^{app} of 12.6 μM calculated for wild-type XanA, the values for the E137A and D138A proteins were smaller, ranging from 3.0-3.6 μM. This decrease in K_i^{app} is consistent with elimination of negative interactions between 6,8-DHP (possibly involving the deprotonated C-8 hydroxyl group that likely binds to Fe(II)) and the Glu137 or Asp138 carboxylates; i.e., the charge repulsion is eliminated in the two mutant proteins containing the small and hydrophobic Ala side chains. K_i^{app} increased significantly for both the Q356A and N358A proteins, suggesting that stabilizing interactions provided by the Gln356 and Asn358 side chains are abolished in these mutants. In particular, this result is consistent with hydrogen bonding between the C-6 hydroxyl group (or the corresponding keto tautomer) of 6,8-DHP and Gln356 and

FIGURE 4.8: Interaction of Q101A with 6,8-DHP. (A) Progress curves for Q101A XanA inhibition by varied concentrations of 6,8-DHP. 1.9 μM Q101A was added to 50 mM MOPS buffer, pH 7.4, at 25 °C containing 40 μM Fe(II), 1 mM αKG, 200 μM xanthine, and 0 mM (■), 0.01 mM (●), 0.02 mM (▲), 0.04 mM (▼), 0.06 mM (◀) or 0.08 mM (▶) 6,8-DHP. The production of uric acid was monitored at 294 nm and the progress curves were fit to equation 1. (B) Dependence of k_{obs} on the concentration of 6,8-DHP. The curve was fit to equation 2. (C) XanA progress curves were obtained as above, but in the presence of 0.1 mM 6,8-DHP and 50 μM (■), 100 μM (●), 150 μM (▲), 200 μM (▼) or 250 μM (◀) xanthine. The progress curves were fit to equation 1. (D) Dependence of k_{obs} on the concentration of xanthine.

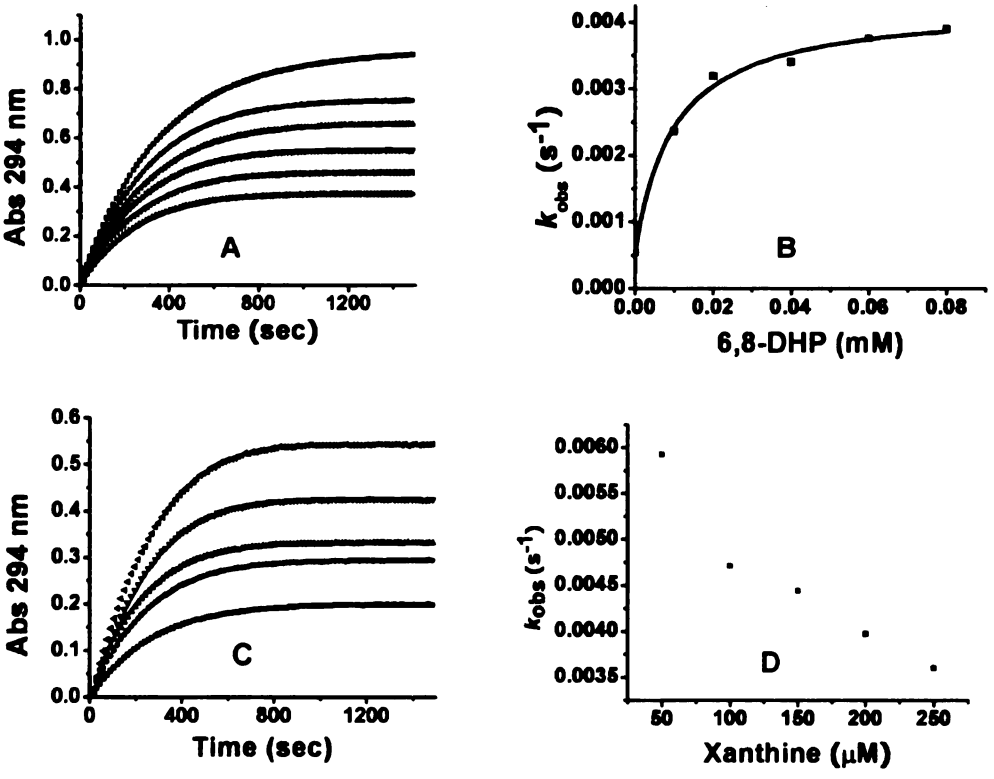

FIGURE 4.9: Interaction of K122A with 6,8-DHP. (A) 6.1 μM K122A was added to 50 mM MOPS buffer, pH 7.4, at 25 °C containing 40 μM Fe(II), 1 mM αKG, 200 μM xanthine, and 0 mM (■), 0.01 mM (●), 0.02 mM (▲), 0.04 mM (▼), 0.06 mM (◀), 0.08 mM (▶) or 0.1 mM (♦) 6,8-DHP. Panels B-D are the same as for Figure S3.

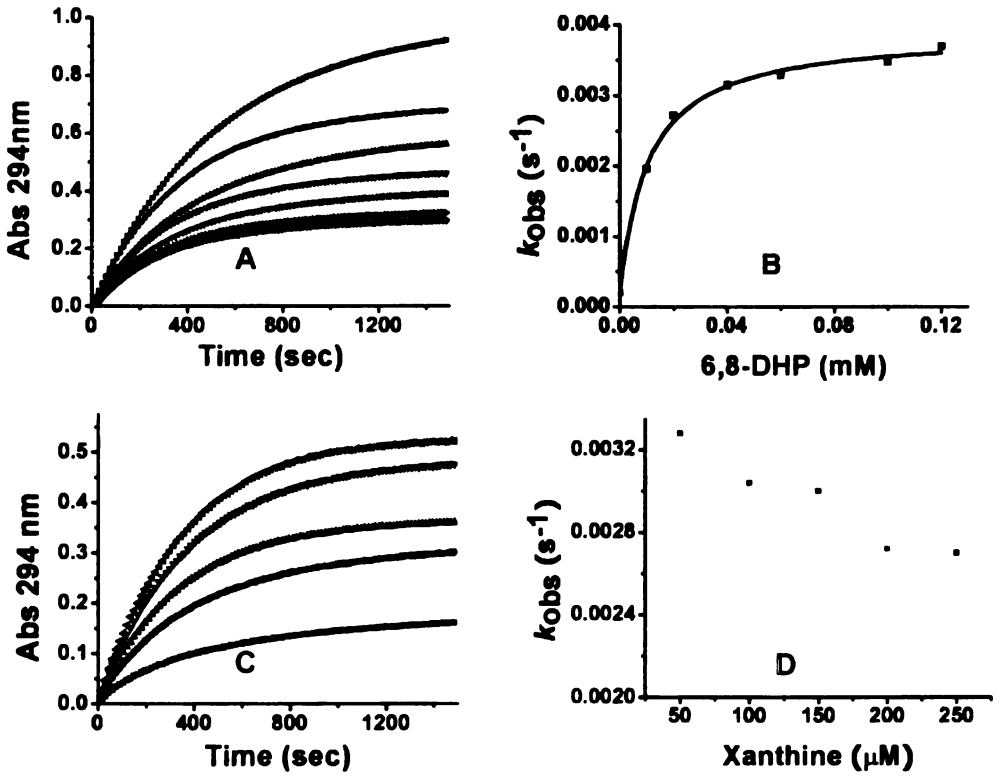

FIGURE 4.10: Interaction of E137A with 6,8-DHP. (A) 0.27 μM E137A was added to 50 mM MOPS buffer, pH 7.4, at 25 °C containing 40 μM Fe(II), 1 mM αKG, 200 μM xanthine, and 0 mM (■), 0.005 mM (●), 0.01 mM (▲), 0.02 mM (▼), 0.04 mM (◀), 0.06 mM (▶) or 0.08 mM (♦) 6,8-DHP. 0.54 μM E137A was used for plot (C) and (D). Panels B-D are the same as for Figure S3.

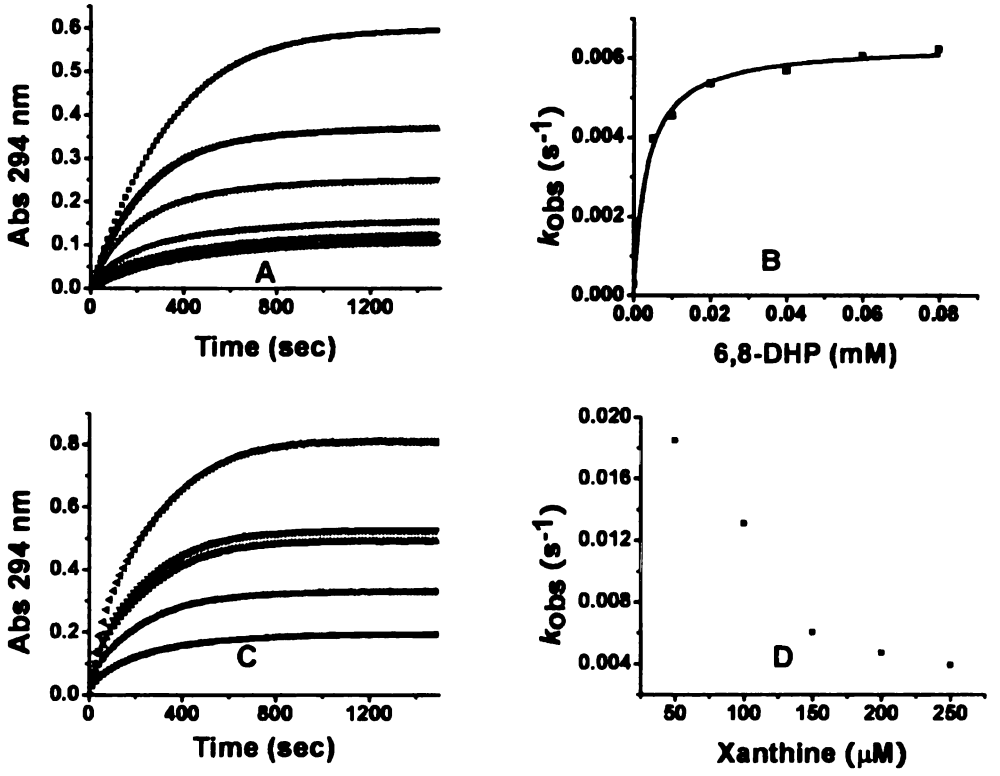

FIGURE 4.11: Interaction of D138A with 6,8-DHP. (A) 0.83 μM D138A was added to 50 mM MOPS buffer, pH 7.4, at 25 °C containing 40 μM Fe(II), 1 mM αKG, 200 μM xanthine, and 0 mM (■), 0.005 mM (●), 0.01 mM (▲), 0.02 mM (▼), 0.04 mM (◀), 0.06 mM (▶) or 0.08 mM (♦) 6,8-DHP. 1.6 μM D138A was used for plot (C) and (D). Panels B-D are the same as for Figure S3.

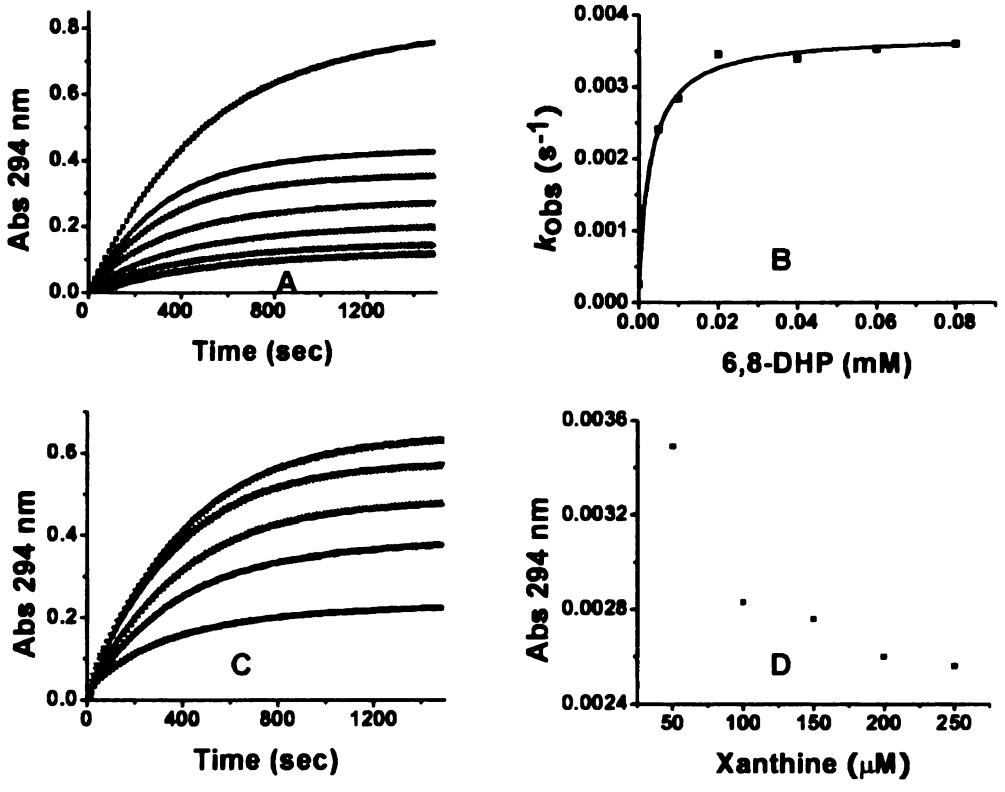

FIGURE 4.12: Interaction of Q356A with 6,8-DHP. (A) 53.5 nM Q356A was added to 50 mM MOPS buffer, pH 7.4, at 25 °C containing 40 μM Fe(II), 1 mM αKG, 200 μM xanthine, and 0 mM (■), 0.1 mM (●), 0.2 mM (▲), 0.3 mM (▼), 0.4 mM (◀) or 0.5 mM (▶) 6,8-DHP. Panels B-D are the same as for Figure S3.

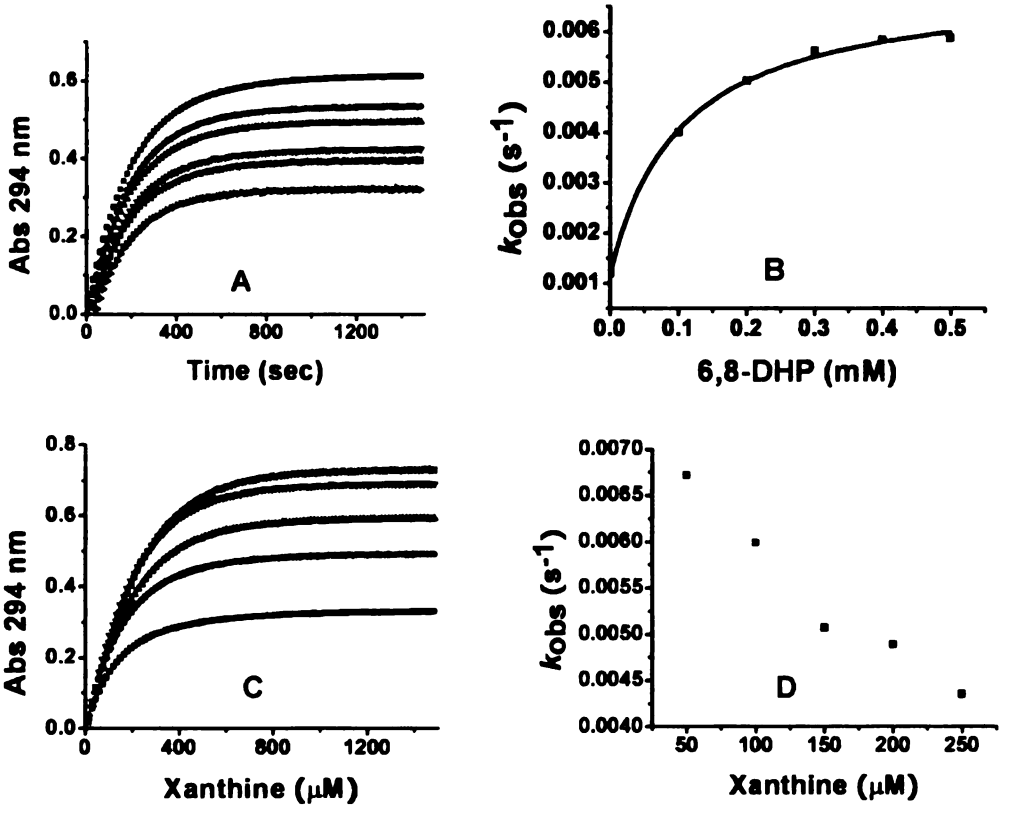

FIGURE 4.13: Interaction of C357A with 6,8-DHP. (A) 2.3 μM C357A was added to 50 mM MOPS buffer, pH 7.4, at 25 °C containing 40 μM Fe(II), 1 mM αKG, 200 μM xanthine, and 0 mM (■), 0.02 mM (●), 0.06 mM (▲), 0.10 mM (▼), 0.14 mM (◀) or 0.18 mM (▶) 6,8-DHP. Panels B-D are the same as for Figure S3.

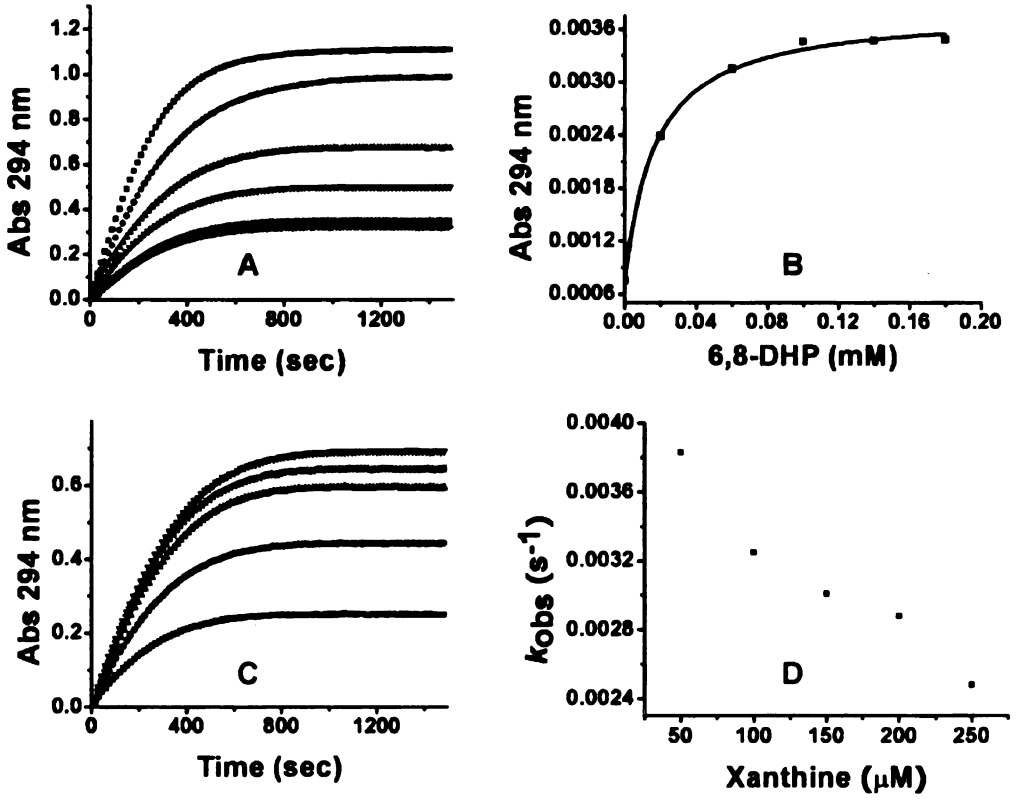

FIGURE 4.14: Interaction of N358A with 6,8-DHP. (A) 1.4 μM N358A was added to 50 mM MOPS buffer, pH 7.4, at 25 °C containing 40 μM Fe(II), 1 mM αKG, 200 μM xanthine, and 0 mM (■), 0.02 mM (●), 0.04 mM (▲), 0.10 mM (▼), 0.15 mM (◀), 0.20 mM (▶) or 0.30 mM (♦) 6,8-DHP. 2.3 μM N358A was used for plot (C) and (D). Panels B-D are the same as for Figure S3.

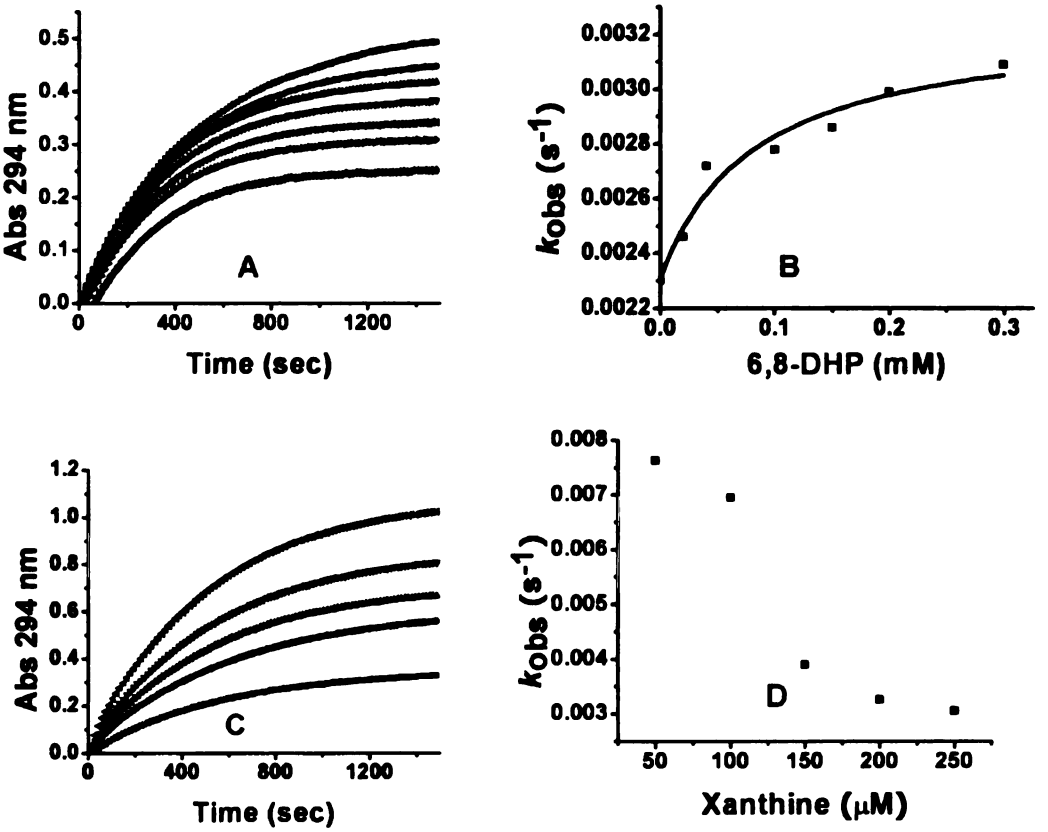

TABLE 4.3: Inhibition of Wild-Type XanA and its Variants by 6,8-DHP[a]

XanA sample	k_5 (s^{-1})	k_6 (s^{-1})	K_i^{app} (μM)
Wild-Type	$(2.0 \pm 0.1) \times 10^{-3}$	$(8.1 \pm 0.8) \times 10^{-4}$	12.6 ± 2.4
Q101A	$(3.7 \pm 0.2) \times 10^{-3}$	$(5.4 \pm 1.2) \times 10^{-4}$	9.8 ± 1.7
K122A	$(3.7 \pm 0.1) \times 10^{-4}$	$(2.0 \pm 0.1) \times 10^{-4}$	10.4 ± 1.1
E137A	$(3.8 \pm 0.1) \times 10^{-3}$	$(2.5 \pm 1.1) \times 10^{-4}$	3.1 ± 0.4
D138A	$(6.0 \pm 0.2) \times 10^{-3}$	$(3.1 \pm 1.7) \times 10^{-4}$	3.6 ± 0.4
Q356A	$(5.8 \pm 0.2) \times 10^{-3}$	$(1.2 \pm 0.1) \times 10^{-3}$	102 ± 12
C357A	$(3.1 \pm 0.1) \times 10^{-3}$	$(7.5 \pm 0.7) \times 10^{-4}$	16.6 ± 2.0
N358A	$(9.4 \pm 1.3) \times 10^{-4}$	$(2.3 \pm 0.1) \times 10^{-3}$	81 ± 39

[a] Kinetic analyses were carried out as described in the text, with the kinetic parameters defined according to equation 5.

Asn358. For most of the mutants, k_5 is larger than k_6; however, N358A exhibited the opposite result ($k_5 = 9.4 \times 10^{-4}$ s^{-1}, $k_6 = 2.3 \times 10^{-3}$ s^{-1}). This finding is consistent with the N358A enzyme lacking an important stabilizing hydrogen bond(s) to the C-6 hydroxyl group of 6,8-DHP, perhaps involved in the k_5 transition and formation of the $E{\cdot}I^*$ complex (Figure 4.5).

Identification of a Reactive Thiol at the XanA Active Site. The homology model of XanA depicts Cys357 at the active site (Figure 4.1), a prediction that was directly tested by chemical modification studies. As illustrated in Figure 4.15A, the incubation of XanA with various concentrations of 5,5'-dithiobis (2-nitrobenzoic acid) (DTNB or Ellman's reagent, specific for reacting with thiol groups) led to concentration-dependent, first-order losses of activity. Significantly, the added presence of xanthine provided some protection to the enzyme (Δ symbols in Figure 4.15A), consistent with a reaction between DTNB and a Cys residue at the active site. In contrast, αKG had much less of a protective effect when examined alone (□ symbols) or with xanthine (data not shown). Inactivation studies also were carried out with iodoacetamide (Figure 4.15B), a less specific reagent to thiol groups than DTNB. Higher concentrations of iodoacetamide were required to obtain XanA inactivation rates compared to DTNB. Either xanthine or αKG provided some protection against enzyme inactivation by this reagent, and the combined presence of xanthine and αKG provided increased protection against iodoacetamide. These results obtained with iodoacetamide agree well with those using DTNB and are consistent with the presence of a reactive Cys residue near the xanthine-binding site. When the DTNB

FIGURE 4.15: Inactivation of XanA by DTNB. (A) XanA (51 μg ml^{-1}) was incubated on ice with 0 (♦), 2.5 μM (■), 125 μM (▲), 750 μM (●) or 1.25 mM (◊) DTNB in 50 mM MOPS buffer, pH 7.4, for the indicated times, then diluted 100-fold into buffer containing 40 μM Fe(II)and 1 mM αKG. After blanking the spectrophotometer, xanthine was added to 200 μM. Additional samples containing 750 μM DTNB were examined with added 0.2 mM xanthine (--Δ--) or 1 mM αKG (--□--). The combination of added xanthine plus αKG was equivalent to added xanthine alone. (B) XanA inactivation by iodoacetamide. The enzyme (51 μg ml^{-1}) was incubated on ice with 0 (♦), 20 mM (▲), 50 mM (■), 60 mM (●) and 100 mM (x) iodoacetamide in 50 mM MOPS buffer, pH 7.4, for the indicated times, then diluted 100-fold into buffer containing 40 μM Fe(II)and 1 mM αKG. After blanking the spectrophotometer, xanthine was added to 200 μM. Additional samples containing 60 mM iodoacetamide were examined with added 0.2 mM xanthine (--+--) or 0.2 mM xanthine plus 1 mM αKG (--□--). The inclusion of αKG alone was equivalent to the case of added xanthine. (C) C357A XanA (51 μg ml^{-1}) was incubated on ice with 0 (♦), 15 μM (■), 0.75 mM (▲) and 1.25 μM (●) DTNB in 50 mM MOPS buffer, pH 7.4, for the indicated times, and diluted and assayed as above. (D) Time-dependent inactivation of wild-type XanA (■) and the C357A variant (♦).

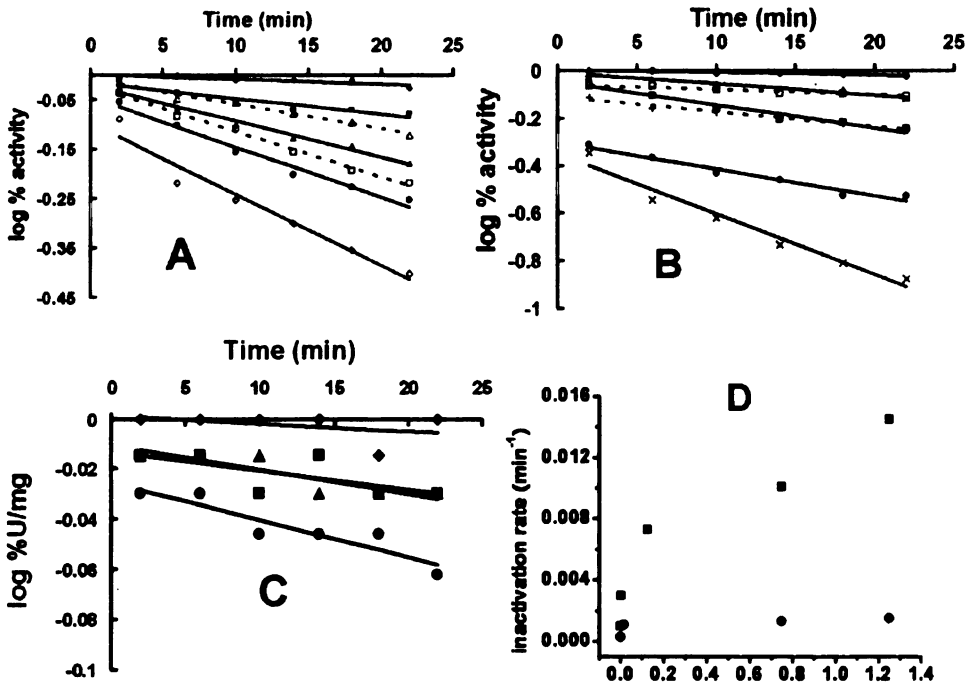

inactivation studies were repeated with the C357A variant enzyme, the reagent yielded very little inactivation compared to the control enzyme (Figure 4.15C and D). This result confirms the positioning of Cys357 at the XanA active site. During the course of the above studies, XanA was found to be labile when examined at dilute concentrations (e.g., 12 nM or 0.51 μg mL^{-1}), such as those used in routine enzyme assays, whereas the concentrated XanA samples were quite stable during storage. For example when highly diluted XanA was incubated at 25 °C in 50 mM MOPS buffer (pH 7.4), the activity decreased by ~70 % in about 6 min (Figure 4.16). Inclusion of 40 μM $Fe(NH_4)_2(SO_4)_2$ during this incubation stabilized the protein such that ~55 % activity was retained over this time period. Addition of both 40 μM $Fe(NH_4)_2(SO_4)_2$ and 1 mM αKG further stabilized the protein, with ~80 % activity remaining after 6 min. HPLC measurements showed no detectable change of αKG concentrations during these incubations. The approximately first-order loss of activity in the presence of 40 μM $Fe(NH_4)_2(SO_4)_2$ and 1 mM αKG was not affected by inclusion of 80 μM ascorbate (data not shown); however, the protein was found to be more stable in the absence of oxygen. The oxygen-dependent instability of XanA apoprotein hinted at the reactivity of a cysteine thiol in the protein. Consistent with this hypothesis, the activity of the Cys357 protein was quite stable when examined at dilute (12 nM) concentrations (Figure 4.16). This result confirms that metal-independent oxidation of Cys357 is associated with XanA inactivation; although the mechanism of this inactivation process remains unclear.

FIGURE 4.16: Time-dependent loss of XanA activity for highly diluted enzyme. Wild-type XanA was diluted to 0.51 μg ml^{-1} in aerobic buffer, 50 mM MOPS (pH 7.4), without additives (▼), with 40 μM Fe(II) (▲), and with 40 μM Fe(II) plus 1 mM αKG (●), or was diluted into anaerobic buffer (■). For comparison, the C357A variant (0.51 μg ml^{-1}) was examined in aerobic buffer (♦). At the indicated time points, the missing components were added and assays (25 °C) were initiated by adding 200 μM xanthine.

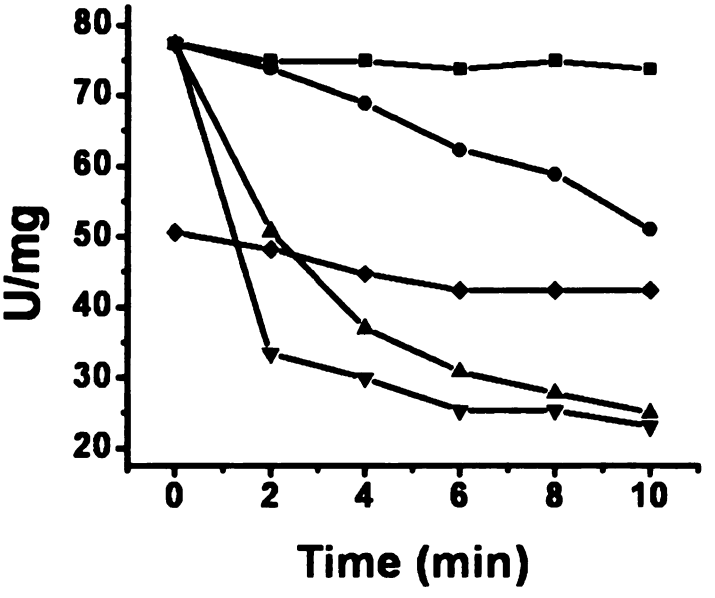

Oxygen Reactivity of XanA in the Absence of Primary Substrate. The addition of XanA to a buffered solution containing 40 μM Fe(II) led to a slow rate of O_2 consumption, similar to the background rate of consumption that occurred in the absence of enzyme (data not shown). For the Q101A, Q356A, and C357A mutant proteins, and to a lesser extent the E137A variant, a distinct pattern was observed with 15-20 μM O_2 being consumed with a much greater initial rate constant, denoted v_o in Table 4.4. This rapid phase of oxygen consumption also was observed for enzyme samples added to solutions containing Fe(II) plus αKG (Figure 4.17). The presence of cosubstrate often led to an increase in v_o, which is especially noticeable for the K122A and N358A variants (Table 4.4). Control experiments carried out with Q101A and E137A forms of XanA confirmed that the amount of oxygen consumed in this rapid process correlated with the concentration of added Fe(II), so that approximately twice the amount of O_2 was consumed when using 100 μM Fe(II). The use of higher concentrations of the metal ion in the assay allowed for a more reliable calculation of v_o for the wild-type enzyme (Table 4.4) even though the background rate of oxygen consumption also was increased.

We attribute the rapid phase of oxygen consumption in the above studies to enzyme-catalyzed ferroxidase activity in which the exogenous metal ions are used to provide electrons for the reduction of O_2 to hydrogen peroxide. Support for this activity was obtained by using the ABTS assay for quantifying peroxide production. To illustrate, the Q101A variant stimulated the production of hydrogen peroxide significantly faster than the wild-type protein, which generated H_2O_2 more rapidly

FIGURE 4.17: Oxygen consumption studies of XanA and its variants. An oxygen electrode was used to monitor O_2 consumption at 25 °C in 50 mM MOPS buffer, pH 7.4, containing 1 mM αKG and 40 μM Fe(II) (circles) or 100 μM Fe(II) (triangle), and 1 μM enzyme (wild-type, dark blue; Q101A, cyan; D138A, purple; C357A, green). Enzyme-free control samples (black symbols, no lines) were analyzed for comparison.

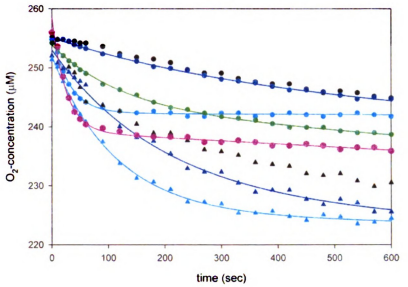

TABLE 4.4: Oxygen Reactivity of XanA and Selected Variants in the Absence of Primary Substrate[a]

Mutant	Fe(II) only	Fe(II) + αKG
	v_o ($\mu M\ s^{-1}$)	v_o ($\mu M\ s^{-1}$)
Wild-type	0.023 ±0.0001	0.030 ± 0.002 (0.136 ± 0.002)
Q101A	0.38 ± 0.008	0.46 ± 0.01 (0.240 ± 0.002)
K122A	0.051 ± 0.001	0.143 ± 0.001
E137A	0.17 ± 0.03	0.192 ± 0.018 (0.264 ± 0.004)
D138A	0.061 ± 0.003	0.097 ± 0.002
Q356A	0.39 ± 0.01	0.48 ± 0.03
C357A	0.70 ± 0.03	0.73 ± 0.01
N358A	0.064 ± 0.001	0.159 ± 0.002

[a] These representative data were obtained by using an oxygen electrode to measure the effects of adding enzyme samples (final concentrations of 1 μM) to solutions containing 50 mM MOPS buffer, pH 7.4, and 40 μM Fe (or 100 μM Fe for the values shown in parentheses), or the same plus 1 mM αKG. The data shown for each sample are derived from replicate measurements obtained on the same day. The immediate response (v_o) is attributed to ferroxidase activity with electrons from excess Fe(II) used to reduce oxygen.

than the non-protein controls (Figure 4.18) when assayed in the presence of 120 μM Fe(II) and 1 mM αKG. The rates of H_2O_2 production correlated with the rates of oxygen consumption for the mutant examined. The H_2O_2 produced in these reactions accounted for 48-63 % of the expected levels of this product (with the low stoichiometry likely due to the known Fe(III) inhibition of peroxidase). The increased levels of ferroxidase activity observed in several of the mutants compared to the wild-type enzyme could reasonably relate to increased accessibility of exogenous Fe(II) to the enzyme metallocenter or to altered binding of αKG resulting in enhanced metal center reactivity.

FIGURE 4.18: Hydrogen peroxide production by Q101A and wild-type XanA. The wild-type (●) and mutant (■) XanA samples (1 μM) were incubated with 120 μM Fe(II) and 1 mM αKG in 50 mM MOPS buffer, pH 7.4, at room temperature. At selected time intervals, aliquots were mixed with ABTS assay solution (pH 5.0) containing horseradish peroxidase and the absorbance was monitored at 420 nm. A non-protein control sample (▲) was examined for comparison.

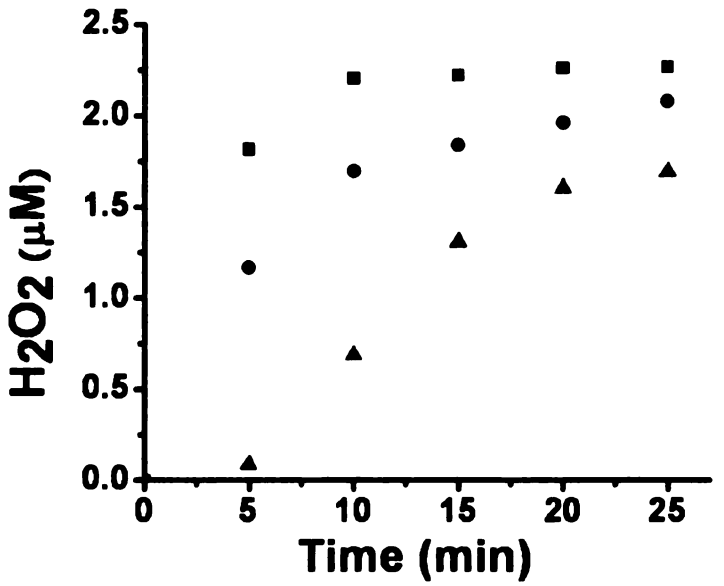

DISCUSSION

To identify active site residues and better define the reactivity of XanA, a recently identified Fe(II)/αKG-dependent xanthine hydroxylase (*4*), we extensively characterized a suite of enzyme variants (Q99A, Q101A, K122A, E137A, D138A, H149A, D151A, H340A, Q356A, C357A, and N358A variants). The residues targeted for mutagenesis, suspected metal ligands or potentially capable of hydrogen-bonding interactions with substrate, were selected on the basis of a homology model of the enzyme (*4*) that depicts them binding Fe(II) lining the active site pocket (Figure 4.1). Significantly, these residues are well conserved in sequences of XanA orthologues (*4*). For example, Gln101, His149, Asp151, His340, Gln356, Cys357, and Asn358 are universally conserved in the available XanA sequences. Gln99 often is present, but Val occupies this position in some representatives. Lys122, which was suggested to stabilize interactions with the C-1 carboxylate of αKG, either is retained or conservatively replaced by Arg or Thr. Although Asp, Gln, and Ser replace Glu137 in other XanA orthologues, these replacement residues are capable of similar hydrogen bond interactions. More flexibility exists for Asp138 which is replaced by Glu, Gln, His, and Lys in other XanA sequences. Aromatic residues are not predicted to lie near the active site, reducing the possibility of π-π stacking interactions with the base, though other hydrophobic residues are suggested to occur in this region. In addition to these various side chains, the substrate might also interact with unidentified backbone amide and carbonyl groups.

Model of Xanthine Binding Based on Kinetic Analyses of XanA and its Variants.

The results from our extensive kinetic analyses of wild type and variant XanA enzymes with substrates and inhibitors were combined along with determination of the K_d of Fe(II) and αKG along with the ferroxidase activities into a model for xanthine binding to XanA, as depicted in Figure 4.19 (with substrate entering the active site from the right and some hydrogen bonds likely to arise from interactions with backbone amide groups). In this figure, the Fe(II) is shown bound by the His149, Asp151, and His340 side chains, as is almost certain from sequence comparisons to other related enzymes (*4*). Mutations involving these residues abolished or greatly diminished activity and led to an increase in the K_d of Fe(II). Furthermore, αKG is illustrated as chelating the metal, in agreement with other members of this enzyme family, with stabilization provided by the appropriately positioned Arg352 (supported by sequence comparisons) and Lys122. Consistent with this role for Lys122, the K122A variant displayed an increase in the K_d of αKG. The primary substrate is shown binding to the enzyme active site via a constellation of hydrogen bonding interactions (some of which cannot be identified from our analyses), so that the disruption of any one hydrogen bond will lead to only modest effects on the kinetics. The K_m and k_{cat} parameters measured by steady-state kinetics for xanthine utilization by the wild type and variant enzymes cannot be used to directly infer which residues bind the substrate; however, this baseline information allows for such inferences to be made when combined with the data obtained from studies using 9-methylxanthine and 6,8-DHP. In addition, the ferroxidase measurements of the variants provide added insight about putative active site residues. The suspected positioning and role of each

FIGURE 4.19: Proposed xanthine binding on the active site.

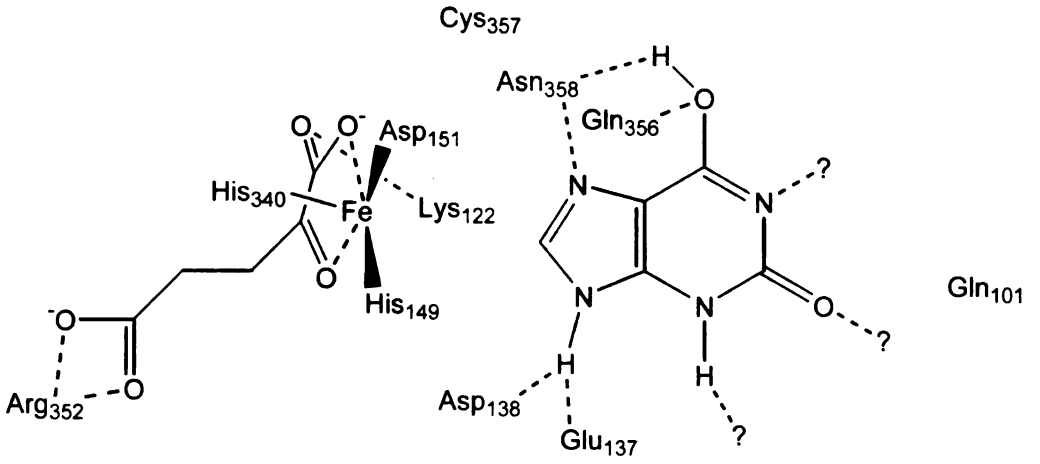

residue is described below.

The N358A variant displayed the largest reduction in k_{cat}/K_m of all mutants retaining significant activity, consistent with this side chain having a critical role in catalysis. This variant also gave rise to one of the largest effects when assessing K_i^{app} of 6,8-DHP inhibition, a result that can be interpreted as arising from the loss of a critical interaction involving the C-6 hydroxyl group of the inhibitor. Together, these results lead us to the depiction of Asn358 interacting with both the N-7 and the C-6 enol oxygen of xanthine (Figure 4.19). This mode of interaction with the substrate is compatible with the homology model (Figure 4.1) that predicts Asn358 is positioned deep in the active site near the metallocenter.

Gln356 also is shown interacting with the C-6 hydroxyl group of the substrate (Figure 4.19). Support for this interaction derives primarily from the significant increase in K_i^{app} of 6,8-DHP for the Q356A variant. The homology model predicts that this residue is positioned near Asn358 in the active site (Figure 4.1). Of interest, the Q356A variant exhibits enhanced ferroxidase activity that could be explained by increased access of exogenous Fe(II) to the metallocenter when this side chain is absent, in agreement with the model and Figure 4.19.

Cys357, located between Gln356 and Asn358, is present at the XanA active site as shown by the results of chemical modification studies-especially the finding that binding of substrate protects this residue from the thiol-specific reagents. The C357A variant was not susceptible to inactivation by these reagents. Further support for this residue being located near the XanA active site is derived from the increased

ferroxidase activity of the C357A variant, attributable to enhanced access to the bound metallocenter by exogenous Fe(II) when this thiol group is removed or to perturbation of the reactivity of the metal site. No specific interactions between Cys357 and substrate were identified experimentally (Figure 4.19), but removal of this side chain resulted in an increase in k_{cat} for 9-methylxanthine compared to the wild-type enzyme indicating a possible improvement in substrate orientation during catalysis. The homology model (Figure 4.1) predicts the thiol group does not point into the active site where xanthine binds, but small changes in torsion angles could reposition this side chain to allow for interaction with substrate. Significantly, changes in the kinetic properties of the C357A variant may be partially attributed to positional alterations of the adjacent Gln356 and Asn358 side chains.

Both Glu137 and Asp138 are proposed to accept hydrogen bonds from the proton at N-9 of xanthine (Figure 4.19). This suggestion is based primarily on the comparison of the kinetic properties for the wild-type protein versus the E137A and D138A variants when using xanthine and 9-methylxanthine. Notably, these mutant proteins exhibit greater k_{cat} than the control protein with this alternate substrate as if the absence of these side chains provides more optimized interactions with the substrate. Likely related to this finding, the E137A and D138A variants exhibit decreased K_i^{app} for 6,8-DHP compared to the wild-type protein. We attribute these results to a decreased repulsion of the deprotonated C-8 hydroxy group of the inhibitor (the form that is most likely to coordinate the metallocenter) by the variants, which lack the carboxylate groups. The homology model predicts that Asp138 lies

very close to the bound Fe(II), with Glu137 a short distance away (Figure 4.1). These residues are located on the opposite wall of the active site compared to the Gln356, Cys357, and Asn358 residues, consistent with the depiction in Figure 4.19.

The substitution of Gln101 by Ala leads to small effects on the substrate and inhibitor kinetic parameters of XanA, but a significant increase in ferroxidase activity. While we cannot suggest a specific site(s) of interaction between Gln101 and xanthine, we speculate (in Figure 4.19) that this residue restricts access to the active site by exogenous Fe(II). Compatible with this proposal, Gln101 is positioned near the active site entrance in the homology model (Figure 4.1).

Although the K_d of αKG is increased in the K122A variant, consistent with the earlier prediction that Lys122 interacts with the C-1 carboxylate of αKG (*4*), the substitution of this side chain by Ala had little effect on the kinetic parameters of the enzyme. Nevertheless, when compared to the very small ferroxidase activity of control enzyme the K122A variant exhibits a pronounced increase in ferroxidase activity in the presence of Fe(II) plus αKG over that of metal alone, suggesting that Lys122 is located near the αKG binding site and serves to minimize this aberrant activity.

Lack of Binding by Related Compounds. The proposed binding interactions for xanthine illustrated in Figure 4.19 are consistent with the exquisite specificity of XanA. Xanthine derivatives methylated at N-1, N-3, or the C-6 hydroxyl group are very poor or not substrates (*4*) because of steric clashes or the interruption of critical interactions. Although hypoxanthine (lacking the C-2 oxygen compared to xanthine)

might appear to closely mimic the normal substrate, this mono-hydroxylated compound will have too little resonance energy to overcome the lactam intrinsic stability so hypoxanthine will predominate as the C-6 keto tautomer (*4*), thus disrupting several features important to binding. Xanthine derivatives hydroxylated at C-8 (such as 6,8-DHP) cannot serve as substrates for the enzyme, but the hydroxyl group at C-8 could reasonably function as a metal ligand and contribute to inhibition. It is clear, however, that 8-hydroxypurine lacks many interactions proposed to be critical for binding xanthine, explaining why it is not an inhibitor of the enzyme (*4*). 2,8-DHP is a somewhat better inhibitor, but it still lacks several hydrogen bond interactions likely to be present with xanthine and exhibits only weak binding. By contrast, the model correctly predicts that 6,8-DHP should be a potent inhibitor due to the interactions involving its N-1, C-6 hydroxyl group, N-7, and N-9 proton, along with metal coordination by the C-8 hydroxyl group.

The product of the xanthine/αKG dioxygenase reaction, uric acid, does not significantly inhibit the enzyme despite its close structural resemblance to the substrate. A critical difference between xanthine and uric acid is the distinction in pK_a of the compounds. Whereas the pK_a of xanthine is 7.4 (*12*), that of uric acid is 5.8 with the singly ionized species identified as the deprotonated N-3 and the dianion shown to be the N-3 plus N-9 deprotonated species (*13*). Thus, in solution at neutral pH, uric acid is predominantly a species in which the C-2 enol is deprotonated while C-6 and C-8 are keto groups. The binding mode of substrate shown in Figure 4.19 is inconsistent with these interactions, perhaps leading to ejection of the product from

the active site.

To better understand the weak interaction of uric acid with XanA it is also instructive to examine the structure of a protein that specifically accepts uric acid as a substrate. Uric acid oxidase has been crystallized in the presence of several substrate analogues, including 9-methyluric acid (*14*). In that case, the compound binds as the 2,6,8-tri-keto species where both N-3 and N-7 are deprotonated. Specifically, a Gln OE1 hydrogen bonds to the N-1 proton, the C-2 keto oxygen hydrogen bonds to a backbone amide as well as to an Arg residue, the same Arg is bound by the deprotonated N-3, the C-6 keto oxygen binds a Gln EN2, the deprotonated N-7 binds to a backbone amide, and the C-8 keto group binds to another backbone amide. If the uric acid formed in XanA were to adopt this structure, many of the postulated hydrogen bond interactions suggested for xanthine would be disrupted. In addition, the C-8 keto oxygen would likely exhibit repulsion by the nearby Asp151. Thus, one can readily rationalize the dissociation of the product from XanA.

Comparison to Xanthine Binding in Other Systems. Although the structural details differ greatly, the general features of the proposed mode of xanthine binding in XanA resemble the suggested interactions of xanthine with xanthine hydroxylase (*15, 16*) and the fungal xanthine/uric acid transporter (*17, 18*). Similar to the proposed Gln356 and Asn358 hydrogen bonds to the xanthine C-6 enol proton, a Glu binds to the xanthine C-6 hydroxyl group in xanthine hydroxylase. In addition, the uncharacterized stabilization of the xanthine C-2 keto group in XanA is reminiscent of the C-2 keto group binding to an Arg residue in xanthine hydroxylase. Furthermore,

the potentially bridging interactions of XanA Asn358, between the N-7 and C-6 hydroxyl group of xanthine resemble the xanthine hydroxylase Glu interaction with both the N-3 and N-9 protons. No structure is available for any xanthine/uric acid transporter, but mutagenesis studies (*17, 18*) suggest that a particular Gln residue binds the deprotonated xanthine N-9 nitrogen, much like the model generated here. Final determination of XanA interactions with substrate must await elucidation of the crystal structure in the presence of substrate or inhibitor.

REFERENCES

(1) Hille, R. (2005) Molybdenum-containing hydroxylases. *Arch. Biochem. Biophys. 433*, 107-116.

(2) Darlington, A. J., and Scazzocchio, C. (1968) Evidence for an alternative pathway of xanthine oxidation in *Aspergillus nidulans*. *Biochim. Biophys. Acta 166*, 557-568.

(3) Cultrone, A., Scazzocchio, C., Rochet, M., Montero-Morán, G., Drevet, C., and Fernández-Martín, R. (2005) Convergent evolution of hydroxylation mechanisms in the fungal kingdoms: molybdenum cofactor-independent hydroxylation of xanthine via α-ketoglutarate dependent dioxygenase. *Molec. Microbiol. 57*, 276-290.

(4) Montero-Morán, G. M., Li, M., Rendon-Huerta, E., Jourdan, F., Lowe, D. J., Stumpff-Kane, A. W., Feig, M., Scazzocchio, C., and Hausinger, R. P. (2007) Purification and characterization of the Fe(II)- and α-ketoglutarate-dependent xanthine hydroxylase from *Aspergillus nidulans*. *Biochemistry 46*, 5293-5304.

(5) Eichhorn, E., van der Ploeg, J. R., Kertesz, M. A., and Leisinger, T. (1997) Characterization of α-ketoglutarate-dependent taurine dioxygenase from *Escherichia coli*. *J. Biol. Chem. 272*, 23031-23036.

(6) Hausinger, R. P. (2004) Fe(II)/α-ketoglutarate-dependent hydroxylases and related enzymes. *Crit. Rev. Biochem. Mol. Biol. 39*, 21-68.

(7) Clifton, I. J., McDonough, M. A., Ehrismann, D., Kershaw, N. J., Granatino, N., and Schofield, C. J. (2006) Structural studies on 2-oxoglutarate oxygenases and related double-stranded β-helix fold protein. *J. Inorg. Biochem. 100*, 644-669.

(8) Purpero, V., and Moran, G. R. (2007) The diverse and pervasive chemistries of the α-keto acid dependent enzymes. *J. Biol. Inorg. Chem. (On-line)*.

(9) H.S.Forrest, D. H., and J.M. Lagowski. (1961) Uric acid riboside. Part I. Isolation and reinvestigation of the sturcture. *J. Chem. Soc.*, 963-968.

(10) Morrison, J. F., and Walsh, C. T. (1988) The behavior and significance of slow-binding enzyme inhibitors. *Adv. Enzymol. Rel. Areas Mol. Biol. 61*, 201-301.

(11) Ha, T. J., and Kubo, I. (2007) Slow-binding inhibition of soybean lipoxygenase-1 by dodecyl gallate. *J. Agric. Food. Chem. 55*, 446-51.

(12) Dawson, R. M. C., Elliott, D. C., Elliott, W. H., and Jones, K. M. (1986) *Data for Biochemical Research*, Third ed., Clarendon Press, Oxford.

(13) Kahn, K., Serfozo, P., and Tipton, P. A. (1997) Identification of the true product of the urate oxidase reaction. *J. Am. Chem. Soc. 119*, 5435-5442.

(14) Retailleau, P., Colloc'h, N., Vivarés, D., Bonneté, F., Castro, B., El Hajji, M., Mornon, J.-P., Monard, G., and Prangé, T. (2004) Complexed and ligand-free high-resolution structures of urate oxidase (Uox) from *Aspergillus flavus*: a reassignment of the active-site binding mode. *Acta Crystallogr. D60*, 453-462.

(15) Okamoto, K., Matsumoto, K., Hille, R., Eger, B. T., Pai, E. F., and Nishino, T. (2004) The crystal structure of xanthine oxidoreductase during catalysis: implications for reaction mechanism and enzyme inhibition. *Proc. Natl. Acad. Sci. USA 101*, 7931-7936.

(16) Truglio, J. J., Theis, K., Leimkühler, S., Rappa, R., Rajagopalan, K. V., and Kisker, C. (2002) Crystal structure of the active and alloxanthine-inhibited forms of xanthine dehydrogenase from *Rhodobacter capsulatus*. *Structure 10*, 115-125.

(17) Goudela, S., Karatza, P., Koukaki, M., Frilingos, S., and Diallinas, G. (2005) Comparative substrate recognition by bacterial and fungal purine transporters of the NAT/NCS2 family. *Molec. Membrane Biol. 22*, 263-275.

(18) Koukaki, M., Vlanti, A., Goudela, S., Pantazopoulou, A., Gioule, H., Tournaviti, S., and Diallinas, G. (2005) The nucleobase-ascorbate transporter (NAT) signature motif in UapA defines the function of the purine translocation pathway. *J. Mol. Biol. 350*, 499-513.

CHAPTER 5

COORDINATION CHEMISTRY AT THE FE(II) SITE OF TAURINE/α-KETOGLUTARATE DIOXYGENASE AND *ASPERGILLUS NIDULANS* XANTHINE HYDROXYLASE BY VARIOUS SPECTROSCOPIES

Dr. John McCracken assisted with EPR and ESEEM analyses and performed the HYSCORE simulations; Efthalia Kalliri and Piotr Grzyska provided TauD and variant W248F; Dr. James Geiger simulated the structure of the NO-bound TauD active site.

ABSTRACT

Electronic spectroscopy and one- and two-dimensional electron spin echo envelope modulation (ESEEM) experiments have been used to study the coordination chemistry at the nitric oxide (NO)-bound non-heme Fe(II) sites of xanthine hydroxylase (XanA) and taurine/α-ketoglutarate (αKG) dioxygenase (TauD). NO, which serves as a surrogate for molecular oxygen, binds to the metallocenter and generates electronic transitions that were used to establish binding constants. The diatomic gas spin-couples to the integer spin Fe(II) to yield an $S = 3/2$ paramagnetic center with an axial EPR spectrum characterized by $g_{\perp} = 4.00$ and $g_{\|} = 2.00$. One-dimensional ESEEM spectra were taken across the EPR lineshape and show modulations from ^{14}N and ^{1}H. At $g = 4$ the contributions from these coupled nuclei overlap, making it necessary to use the two dimensional, 4-pulse hyperfine sublevel correlation spectroscopy (HYSCORE) method to resolve contributions from bound histidine nitrogens, coordinated H_2O, and ambient H_2O. For the extensively characterized enzyme TauD, HYSCORE spectra collected for samples in aqueous buffer and 60% $^{2}H_2O$-buffer show changes in H_2O and histidyl coordination as αKG and taurine are added to the enzyme. Prior to co-substrate addition, HYSCORE spectra show a substantial distribution of exchangeable, ^{1}H hyperfine couplings. When αKG is added, the ^{1}H HYSCORE is considerably altered with the dominant hyperfine coupling arising from an exchangeable, strongly coupled proton of rhombic symmetry. Subsequent addition of substrate taurine to yield the ternary complex (Fe(II)-NO/αKG/taurine) at the active site showed a new ^{1}H hyperfine interaction that

is not exchangeable in $^{2}H_2O$. The HYSCORE cross-peaks from this ^{1}H show a hyperfine tensor of axial symmetry characterized by a dipole-dipole distance of 3.2 Å and an isotropic contribution of 0.75 ± 0.3 MHz. X-ray crystal structure of TauD shows C7 of Trp248 lies around 4.5 Å to Fe(II), however, HYSCORE spectrum of W248F did not exhibit substantial difference than that of TauD. Analogous studies were carried out with the less well characterized enzyme XanA, providing the first spectroscopic information for this enzyme and yielding insights into the coordination properties of Fe(II) in this protein.

INTRODUCTION

The Fe(II)- and α-ketoglutarate (αKG)-dependent dioxygenases encompass a wide range of enzymes with diverse primary substrates (reviewed in (*1-3*)). To illustrate the versatility of this enzyme family, the prolyl, lysyl, and aspartyl(asparaginyl) hydroxylases catalyze posttranslational modifications of proteins (*4*), in some cases associated with hypoxic signaling (*5*). JmjC domain-containing proteins catalyze methylated-histone demethylation reactions (*6*). AlkB repairs 1-methyl-A or 3-methyl-C lesions in DNA (or RNA) by using an analogous oxidative dealkylation reaction (*7, 8*). The lipid-metabolizing enzyme phytanoyl-CoA hydroxylase participates in the metabolism of phytanic acid, and deficiency of this enzyme leads to Refsum disease (*9*). Finally, a wide variety of small molecules are synthesized or decomposed by members of this enzyme family. For example, plants synthesize gibberellins, flavonoids, and some alkaloids by action of these enzymes (*10*), thymine 7-hydroxylase sequentially hydroxylates the methyl group of free thymine (*11*), and TfdA, RdpA, and SdpA decompose specific phenoxyalkanoic acid herbicides by hydroxylation of their side chains (*12, 13*). The studies described here focus on two representative hydroxylases: TauD and XanA.

TauD or taurine/αKG dioxygenase, which catalyzes the reaction depicted in Figure 1.8., is the best-characterized member of this group of enzymes. The *Escherichia coli* enzyme is induced under conditions of sulfur starvation (*14*) and allows the cells to use taurine, a widely available sulfonate (*15*), as a sulfur source. The crystal structure of TauD has been reported (*16, 17*) and reveals a typical

2-His-1-carboxylate Fe(II)-binding motif of protein side chains (*18*), chelation of the metal by αKG, and the binding of primary substrate near to, but not directly coordinating, the metallocenter (Figure 5.1). The general mechanism of this enzyme (Figure 5.2) follows that proposed for another enzyme in this class approximately 25 years ago by Hanauske-Abel and Günzler (*19*). In the absence of the co-substrates (A), three side chain ligands and three water molecules bind the hexacoordinate Fe(II). The chelation of αKG to Fe(II) through the C-1 carboxylate and C-2 carbonyl moieties (B) displaces two of the waters, but leaves the final water bound resulting in low reactivity with oxygen (*20*). The addition of taurine (C) triggers release of the remaining water and creates a site for O_2 binding (D) that stimulates further oxidative chemistry. A critical Fe(IV)-oxo intermediate (E) was identified in this enzyme by a combination of stopped-flow ultraviolet-visible, continuous-flow resonance Raman, freeze-quench Mössbauer and extended x-ray absorbance fine structure approaches (*21-27*). This intermediate abstracts a hydrogen atom from substrate (F) and hydroxyl rebound leads to the product. Nitric oxide (NO) can be used as a surrogate for O_2, and the NO-bound form of this archetype enzyme has served as the paradigm for applying electron spin-echo envelop modulation (ESEEM) spectroscopy to the examination of substrate binding by use of deuterium labeled substrate (*28*).

XanA or xanthine/αKG dioxygenase is a recently identified member of the Fe(II)/αKG-dependent hydroxylases (*29*). This enzyme carries out the reaction shown in Figure 2.1, in which αKG decomposition is coupled to xanthine hydroxylation to form uric acid. XanA is found only in selected fungi (*29*) and its chemistry contrasts

FIGURE 5.1: TauD active site. The Fe(II) is bound to the His99, Asp101, and His255 side chains and is chelated by αKG. The substrate taurine binds near, but does not directly coordinate, the metal center.

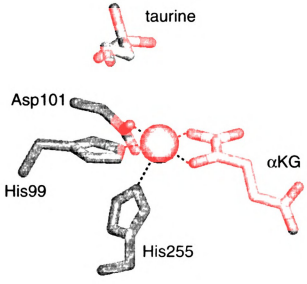

FIGURE 5.2: General mechanism of TauD.

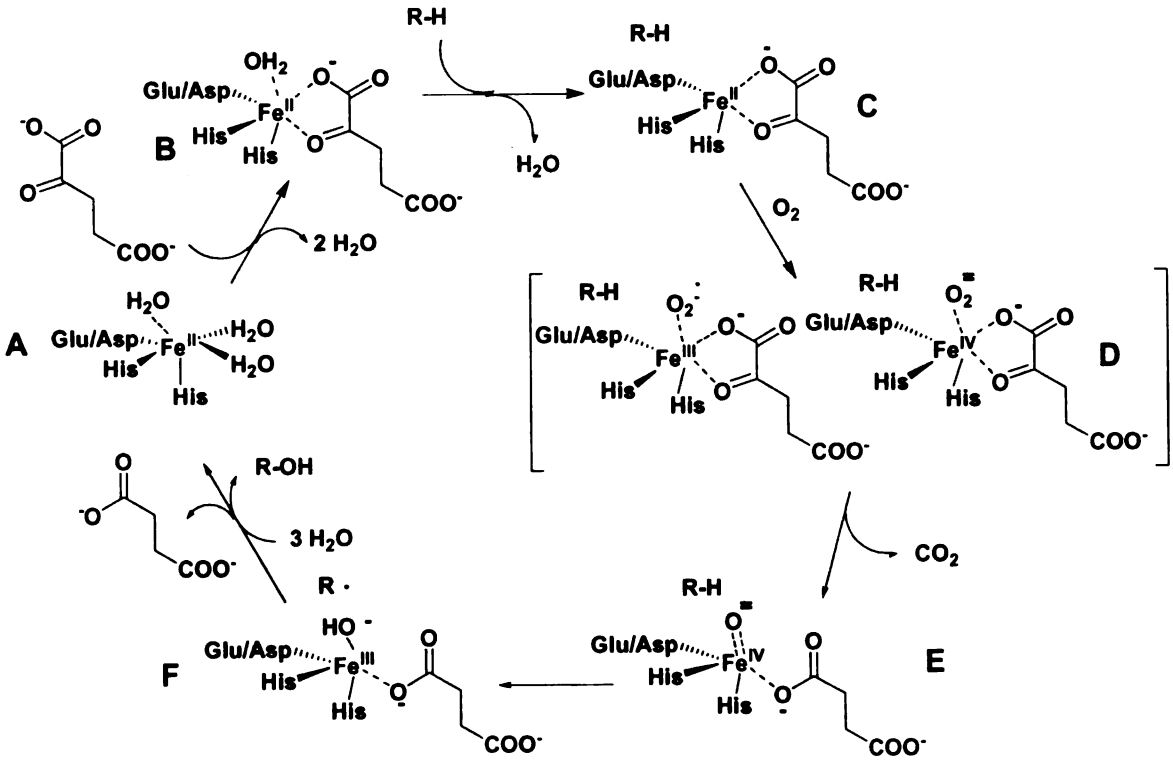

with the well-characterized metabolism of xanthine by the molybdopterin cofactor-containing enzymes that hydroxylate this substrate while transferring electrons to NAD (xanthine dehydrogenase) or oxygen (xanthine oxidase) (*30*). The recombinant His_6-tagged form of XanA from *Aspergillus nidulans* was purified from both its natural host and *E. coli* and extensively characterized (*31, 32*). The general protein properties differ for samples from the two sources, persumably due to the suspected lysosomal localization of the fungus-derived enzyme. Nevertheless, the enzymatic properties of the two forms of XanA are very similar and the general mechanism of this enzyme is suggested to parallel that of TauD (Figure 5.2). XanA is related in sequence to TauD (18% identity) and the latter structure was used to create a homology model of XanA (*31*); however, no crystal structure or spectroscopic studies of XanA have been reported.

Here, the metal ion coordination properties of the NO-bound forms of TauD and XanA are examined by electronic and one- and two-dimensional ESEEM spectroscopies. The spectroscopic results of the TauD model system are analyzed in terms of the known structure of this protein, and spectroscopic studies of a site-directed variant provide additional insights in the Fe(II) coordination environment. This spectroscopic approach is then applied to the XanA system to provide new structural insights into the active site of this poorly characterized system.

EXPERIMENTAL PROCEDURES

Materials. ^2H_2O was purchased from Cambridge Isotope Laboratories, Inc. (Andover, MA). Diethylammonium(Z)-1-(*N*,*N*-diethylamino)diazen-1-ium-1,2-diolate (DEA/NO) was purchased from Cayman Chemical (Ann Arbor, MI). An ammonium salt of taurine deuterated at C_1 (the carbon adjacent to the sulfonate group) was a gift from J. C. Price and J. M. Bollinger, and prepared as described (*22*). *N*-oxalylglycine (NOG) was a kind gift from N. Burzlaff. Other general chemicals were purchased from Sigma-Aldrich. ^2H-labeled αKG was prepared by 24h incubation of αKG in ^2H_2O at room temperature.

Enzyme Purification. TauD, XanA, and the W248F variant of TauD were purified as their His_6-tagged forms, as previously described (*26*). Concentration of the samples made use of Centriprep (Amicon Corp.) units with YM-10 membranes.

Analysis of Fe(II), αKG, and Substrate Binding to TauD and XanA by Using Electronic Spectroscopy. All stock solutions for UV-visible studies were prepared inside serum vials sealed with butyl rubber stoppers. Stock solutions of αKG (30 mM), taurine (100 mM), and xanthine (100 mM) were prepared in 50 mM Tris buffer (pH 8.0), and made anaerobic by 10 rounds of vacuum degassing and flushing with argon by using a vacuum manifold. Ferrous ammonium sulfate stock solutions (6 mM) were prepared by 10 rounds of degassing and flushing with argon inside sealed serum vials. Following the procedures reported for TauD (*20*), XanA (0.45 mM, in 50 mM Tris, pH 8.0) was made anaerobic by 10 rounds of degassing and flushing with argon in a 1 cm path length, 300-μl quartz cuvette fitted with a rubber stopper. After

blanking against the protein solution, spectra were recorded for samples to which anaerobic aliquots of Fe(II), αKG, or xanthine had been added.

Electronic Spectroscopy of NO-treated Samples. 10 mg DEA/NO was dissolved in 2 ml, 10 mM NaOH in tightly capped brown glass vials degassed as described above. The DEA/NO stock solutions were made anaerobic by 5 rounds of degassing and flushing with argon and stored at -80 °C. The concentrations were determined from product information ($\varepsilon_{250\ nm}$= 6,500 $M^{-1}\cdot cm^{-1}$) provided by Cayman chemical. Using a 50 µl syringe, the indicated concentrations of DEA/NO were added by to anaerobic protein samples in 300 µl quartz cuvettes fitted with rubber stoppers, and electronic spectra (300 nm to 800 nm) were recorded on a Shimadzu UV-2401PC spectrometer at 2 min intervals at 25 °C. Equation 1 was used for calculation of the dissociation constant, K_d, where the concentration of free NO is equal to the concentration of total NO added minus the concentration of enzyme-NO complex.

$$\text{Fraction of maximal NO-bound TauD complex} = [NO]/(K_d + [NO]) \qquad (1)$$

Electron Paramagnetic Resonance (EPR) Analyses. The samples from the quartz cuvettes described above were transferred to degassed EPR tubes by using a 1 ml syringe after incubation for approximately 35 min in the case of TauD or 50 min for XanA. The EPR samples were frozen and stored under liquid N_2. Additional protein samples were prepared by diluting the concentrated proteins into the desired volumes of 50 mM Tris, pH 8.0, prepared in 60% ^2H_2O.

Continuous wave-X band EPR spectra were recorded at 5 K on a Bruker ESP300E spectrometer equipped with an Oxford liquid He cryostat by using 100 KHz

modulation, 1.99 mW microwave power, and 9.58 GHz microwave frequency. One- and two-dimensional ESEEM spectra were recorded on a Bruker E-680X spectrometer operating at X-band and equipped with a model ER4118-MD-X-5-W1 probe that employs a 5 mm dielectric resonator. The sample temperature was maintained at 4.2 K using an Oxford Instruments liquid helium flow system equipped with a CF-935 cryostat and an ITC-503 temperature controller. ESEEM data were collected using a three-pulse, stimulated echo sequence (90°-τ-90°-T-90°) with τ = 120 ns; 90° microwave pulse widths of 16 ns (full width half maximum) and peak powers of 200 W. A four-step phase cycling sequence, (+x, +x, +x), (-x, +x, +x), (+x, -x, +x), and (-x, -x, +x), together with the appropriate addition and subtraction of the integrated spin-echo intensities served to actively remove the contributions of two-pulse echoes and baseline offsets from the data (*33*). An integration window of 48 ns was used to acquire spin-echo amplitudes, and data set lengths were 512 Points. Two dimensional ESEEM, also called hyperfine sublevel correlation spectroscopy (HYSCORE), data were collected using a four-pulse, stimulated echo sequence (90°-τ-90°-t_1-180 °-t_2 -90°) with τ = 120 ns, 90° microwave pulse widths of 16 ns and 200 W peak power; 180° microwave pulse widths of 28 ns and 200 W peak power; starting t_1 and t_2, 40 ns; and time increment, 28 ns. One- and two- dimensional ESEEM spectral processing involves removal of the ESEEM decay by subtraction of an exponential or polynomial decay feature, created with a Hamming window and Fourier Transformation. The absolute value, or square root of the resulting power spectrum, is displayed.

HYSCORE spectral simulations. HYSCORE spectral simulations were done in the time domain using the analytical expressions for S = 1/2, I = 1/2 HYSCORE modulation function developed by Gemperle, et al. together with the orientation averaging scheme developed by Hoffman and coworkers (*33, 34*). The output of these simulations was processed using the same scheme outlined above for the Bruker spectrometer via a program written for MATLAB.

RESULTS

Binding of αKG and Xanthine to Fe(II)-XanA Monitored by Electronic Spectroscopy. Anaerobic Fe(II)-bound TauD is known to form lilac-colored chromophores when incubated with αKG (λ_{max} 530 nm, ε_{530} 140-250 $M^{-1}\cdot cm^{-1}$) or αKG plus taurine (λ_{max} 520 nm, ε_{520} 254 $M^{-1}\cdot cm^{-1}$) (*20, 26, 35*), and these features have been attributed to metal-to-ligand charge-transfer transitions of six-coordinate and five-coordinate sites, respectively (*36-38*). For comparison, anaerobic solutions of Fe(II)-XanA were examined in a similar manner (Figure 5.3). The addition of αKG to Fe(II)-XanA yielded a very broad absorption spectrum centered at 506 nm with ε_{506} of 145 $M^{-1}\cdot cm^{-1}$. Subsequent binding of xanthine to αKG-Fe(II)-XanA yielded no significant shift in the absorption maximum, but led to enhanced definition of features at 470 and 580 nm while diminishing the overall signal intensity (ε_{506} 125 M^{-1} cm^{-1}). Unlike the case of TauD, where the addition of Fe(II) in the absence of co-substrates yielded a weak absorbance feature at ~650 nm due to metal interaction with low concentrations of an endogenous catechol arising from enzyme self-hydroxylation of Tyr73 (*35*), no analogous chromphore was observed in this region for Fe(II)-XanA.

Electronic Spectroscopy of NO complexes of TauD and XanA. The effects of added NO on the UV-visible spectra of various complexes of Fe(II)-bound TauD and XanA were examined, as shown for the substrate-αKG-Fe(II)-protein spectra in Figure 5.4. For each sample, NO binds to the Fe(II) site to form a yellow chromophoric species denoted $\{FeNO\}^7$ in the nomenclature of Feltham and Enemark (*39*). Only small differences were noted among the spectra of NO-treated Fe(II)-,

FIGURE 5.3: UV-visible absorption spectra of XanA complexes. (A) Spectra of anaerobic XanA (black), Fe(II)-XanA (red), αKG-Fe(II)-XanA (blue) and xanthine-αKG-Fe(II)-XanA (cyan) obtained in 50 mM Tris buffer, pH 8.0. The XanA subunit (0.45 mM) was mixed with ferrous ammonium sulfate (slightly <0.45 mM) and adjusted to contain 1 mM αKG and 1 mM xanthine. (B) Difference spectra of Fe(II)-XanA in the presence of αKG (solid) and αKG plus xanthine (dashed).

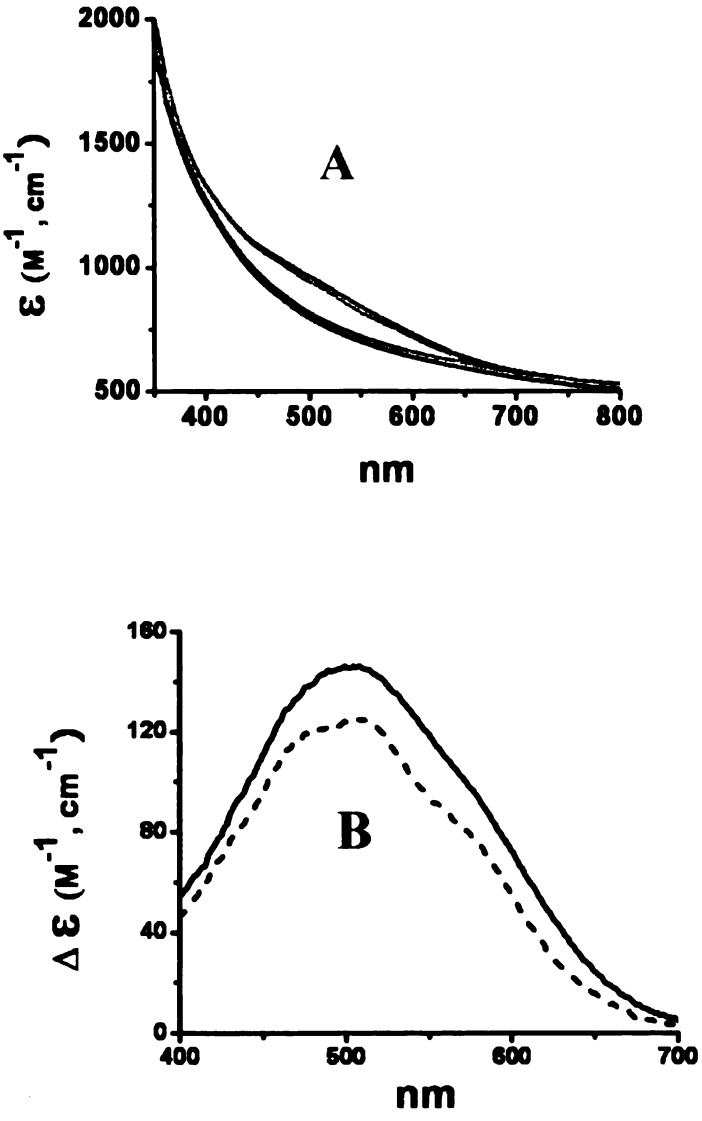

FIGURE 5.4: UV-visible absorption spectra of $\{FeNO\}^7$ complexes of TauD and XanA. The spectra of substrate-αKG-Fe(II)-protein complexes (0.45 mM protein subunit) were obtained prior to (solid lines) and after (dashed lines) incubation with 0.9 mM DEA/NO at 25 °C for (A) TauD (incubation time 35 min) and (B) XanA (incubation time 50 min). (C) Difference spectrum of xanthine-αKG-Fe(II)-XanA in the presence and absence of NO. (D) Difference spectrum of taurine-αKG-Fe(II)-TauD in the presence and absence of NO.

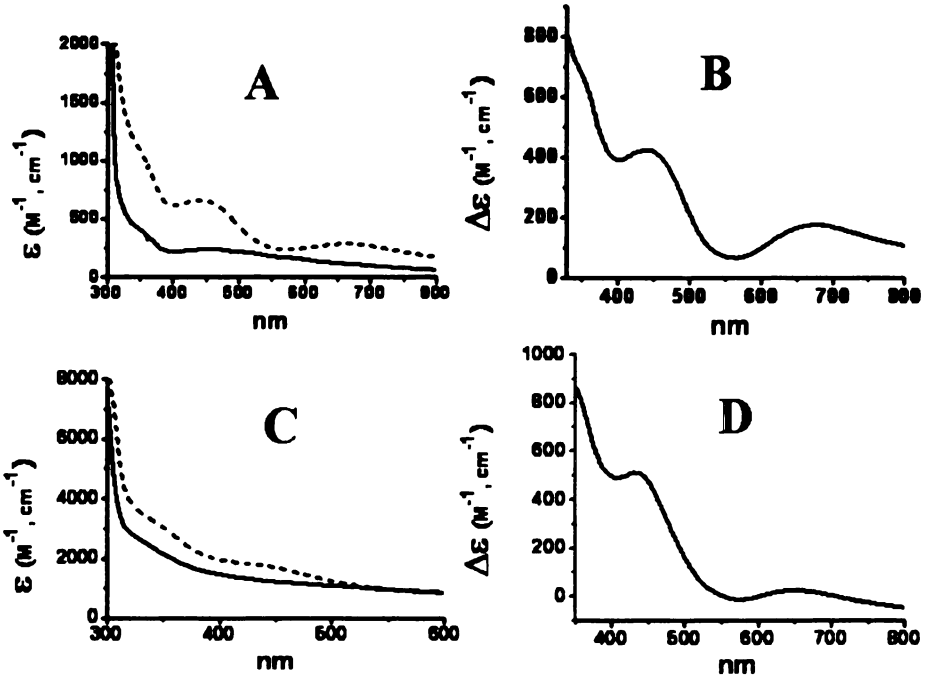

αKG-Fe(II)-, and substrate-αKG-Fe(II)-enzymes. In all cases, NO addition resulted in an intense transition near 450 nm ($\Delta\varepsilon_{443}$ 423 $M^{-1}\cdot cm^{-1}$ for TauD and $\Delta\varepsilon_{435}$ 518 $M^{-1}\cdot cm^{-1}$ for XanA) and a second less intense feature near 650 nm ($\Delta\varepsilon_{680}$ 180 $M^{-1}\cdot cm^{-1}$ for TauD and $\Delta\varepsilon_{650}$ 32 $M^{-1}\cdot cm^{-1}$ for XanA). These results are in close agreement with results previously reported for the herbicide-degrading Fe(II)/αKG hydroxylase TfdA (*40*).

To examine the binding affinity of NO for Fe(II)-TauD, αKG-Fe(II)-TauD, and taurine-αKG-Fe(II)-TauD, a series of binding curves were generated by monitoring the absorbance changes at 443 nm with varied NO concentrations (Figure 5.5A). The data were used to calculate K_d values of 0.178 mM for taurine-αKG-Fe(II)-TauD, 0.341 mM for αKG-Fe(II)-TauD, and 0.279 mM and for Fe(II)-TauD. The smallest K_d was noted for sample containing both the primary substrate and αKG, in agreement with the reported situation for TfdA (*40*).

Whereas the absorbance changes associated with the $\{FeNO\}^7$ species of TauD were typically complete within 35 min, in the case of the XanA complexes the $\{FeNO\}^7$ species were slower to develop and did not reach completion after 50 min (Figure 5.5B). These kinetics precluded calculation of K_d values for the XanA complexes, but it was shown that for identical concentrations of DEA/NO the $\{FeNO\}^7$ species was generated fastest in sample containing both substrate and αKG (Figure 5.5B).

EPR of $\{FeNO\}^7$ Adducts of TauD and XanA. X-band CW-EPR spectra for NO-treated Fe(II)-TauD, αKG-Fe(II)-TauD, taurine-αKG-Fe(II)-TauD, Fe(II)-XanA,

FIGURE 5.5: Thermodynamics and kinetics of NO binding to TauD and XanA. (A) NO binding curves were generated for the interaction of varied concentrations of DEA/NO with Fe(II)-TauD (dashed, ▲), αKG-Fe(II)-TauD (dotted, ●) and taurine-αKG-Fe(II)-TauD (solid, ■). The ordinate represents the fraction of NO-bound protein complex as monitored by the absorbance change at 443 nm after 35 min at 25 °C. The abscissa represents the free (unbound) NO concentration. (B) Kinetics of the absorbance changes at 435 nm for Fe(II)-XanA (●),αKG-Fe(II)-XanA (▲), xanthine-Fe(II)-XanA (▼) and xanthine-αKG-Fe(II)-XanA (■). DEA/NO (0.9 mM) was added to XanA (0.45 mM) containing ferrous ammonium sulfate (slightly < 0.45 mM), and αKG (1 mM), xanthine (1 mM), or both αKG and xanthine (1 mM each) were added to the sample that was incubated at 25 °C.

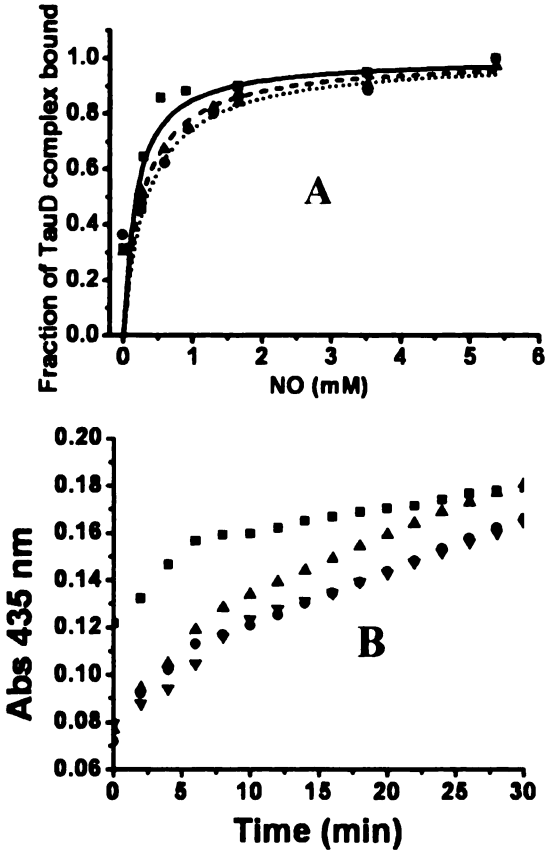

αKG-Fe(II)-XanA, and xanthine-αKG-Fe(II)-XanA were obtained to monitor the changes in the electronic environment of the enzyme metallocenters upon binding αKG and substrate (Figure 5.6). All the NO-bound samples possessed a nearly axial signal of $S = 3/2$ with $g_{\perp} = 4.00$ and $g_{\parallel} = 2.00$. This observation is typical for $\{FeNO\}^7$ complexes and arises from the $M_S = \pm 1/2$ Kramers doublet of the $S = 3/2$ coupled spin system. The lineshape reflects an axially symmetric zero field splitting interaction with its principal axis directed along $g_{\parallel}$ which approximates the Fe-NO bond (*41*). The region near $g_{\perp}$ was used to investigate structural changes since the $g_{\parallel} = 2.00$ signal was relatively weak and confounded by the signal arising from free NO. The EPR lineshapes of complexes Fe(II)-TauD and αKG-Fe(II)-TauD were almost identical, as shown in Figure 5.6A and B, and the calculated E/D value is 0.015 for both indicating a slight rhombic character. The terms D and E refer to axial and rhombic zero-field splitting constants, respectively, and the E/D ratio reflects the degree of rhombic distortion of the $\{FeNO\}^7$ center (with a purely axial geometry displaying $E/D \approx 0$ while a highly rhombic feature exhibits an $E/D \approx 0.33$). Addition of primary substrate, taurine, generated a more rhombic species with features at $g = 4.27$, 4.07 and 3.89. It is composed of two distinct populations: an axial species (E/D= 0.009, 68%) and a more-rhombic one (E/D= 0.03, 32%). Similar results were observed for XanA complexes. Both Fe(II)-XanA and αKG-Fe(II)-XanA exhibited axial signals ($E/D \approx 0$), whereas a more rhombic EPR lineshape with features at $g = 4.16$, 4.03 and 3.78 was observed after addition of xanthine. The more axial species (E/D = 0.01) accounts for 77% of the signal, whereas the remaining 23% comes from a more rhombic

FIGURE 5.6: EPR spectra of the $\{FeNO\}^7$ complexes of TauD and XanA. Samples (0.45 mM protein and slightly less than 0.45 mM ferrous ammonium sulfate) of (A) TauD or (D) XanA were examined alone or in the presence 1 mM αKG (B) and (E), or with 1 mM αKG plus 1 mM substrate after incubation (35 min for TauD (C), 50 min for XanA (F)) with 0.9 mM DEA/NO at 25 °C. The solid line represents experimental data and dashed line represents the simulation.

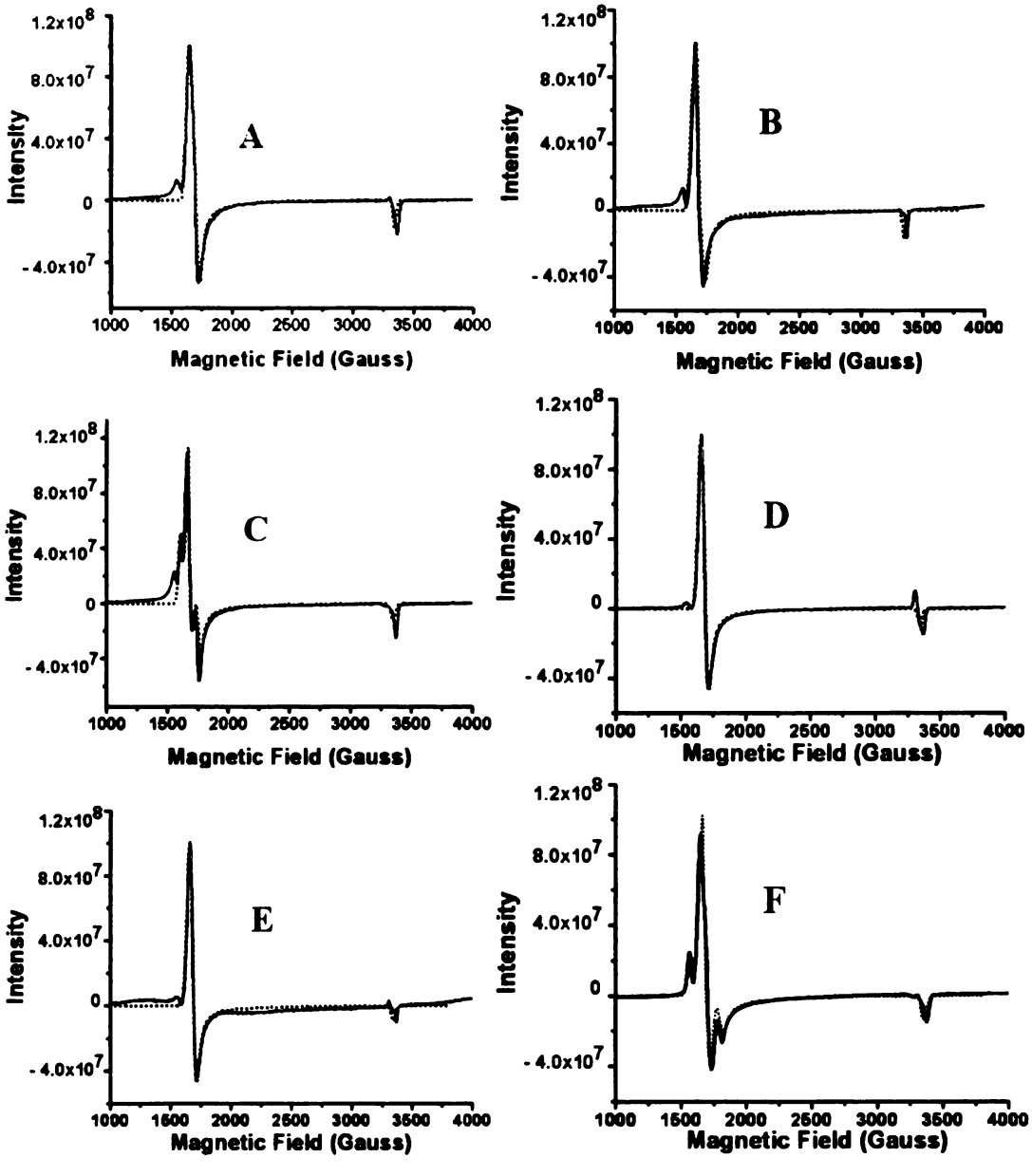

species (E/D = 0.045). A feature at g = 4.3 existed in all the spectra and was assigned to free Fe(III) ion.

One-Dimensional ESEEM of {FeNO}^{7} adducts of TauD and XanA. Across the EPR lineshape, two magnetic fields, 172.0 mT and 340.0 mT (around $g_\perp \doteqdot 4.00$ and $g_\parallel$ = 2.00), were selected to collect ESEEM spectra.

Three-pulse ESEEM spectra collected at 172.0 mT for Fe(II)-TauD, αKG-Fe(II)-TauD, and taurine-αKG-Fe(II)-TauD in Tris buffer prepared in H_2O are shown in Figure 5.7 A, C and E, and corresponding spectra collected in 60% ^2H_2O are shown in Figure 5.7 B, D and F. The sharp peak at a frequency around 7.4 MHz could be assigned to the matrix proton in the protein. This feature exists in all TauD complexes prepared in H_2O, but no in the ^2H_2O samples. The broad peaks from 9.5 MHz to 16 MHz could derive from one or more populations of strongly-coupled, and these couplings seem stronger in the presence of αKG or both αKG and taurine. The signal from 0 to 5 MHz is more complicated; it shows contributions from the histidyl ligands and more than one sets of strongly coupled protons. Compared to the spectra taken in H_2O, the signals from ^2H_2O prepared samples are cleaner. The significant ^2H modulation dominates the spectra at a frequency around 1.1 MHz as shown in Figure 5.7 B, D and F. However, the strong proton couplings in taurine-αKG-Fe(II)-TauD still exist and become more defined when comparing Figure 5.7 E and F.

The spectra that result from repeating the measurements for TauD samples at 340.0 mT are shown in Figure 5.7 G, I and K (H_2O) and Figure 5.7 H, J, and L (for samples prepared in 60% ^2H_2O). The feature at frequency 14.6 MHz is consistent with

FIGURE 5.7: One-dimensional ESEEM spectra of different TauD complexes prepared in H_2O and 60% ^2H_2O buffer at 172.0 mT and 340.0 mT. Fe(II)-TauD complex examined at 172.0 mT in H_2O buffer (A) and 60% ^2H_2O buffer (B), αKG-Fe(II)-TauD complex examined at 172.0 mT in H_2O buffer (C) and 60% ^2H_2O buffer (D), taurine-αKG-Fe(II)-TauD complex examined at 172.0 mT in H_2O buffer (E) and 60% ^2H_2O buffer (F). Fe(II)-TauD complex examined at 340.0 mT in H_2O buffer (G) and 60% ^2H_2O buffer (H), αKG-Fe(II)-TauD complex examined at 340.0 mT in H_2O buffer (I) and 60% ^2H_2O buffer (J), taurine-αKG-Fe(II)-TauD complex examined at 340.0 mT in H_2O buffer (K) and 60% ^2H_2O buffer (L). Protein concentration, 2 mM; ferrous ammonium sulfate, slightly less than 2 mM; αKG and taurine, 4 mM. ESEEM data were collected under the conditions as described in experimental procedures.

FIGURE 5.7:

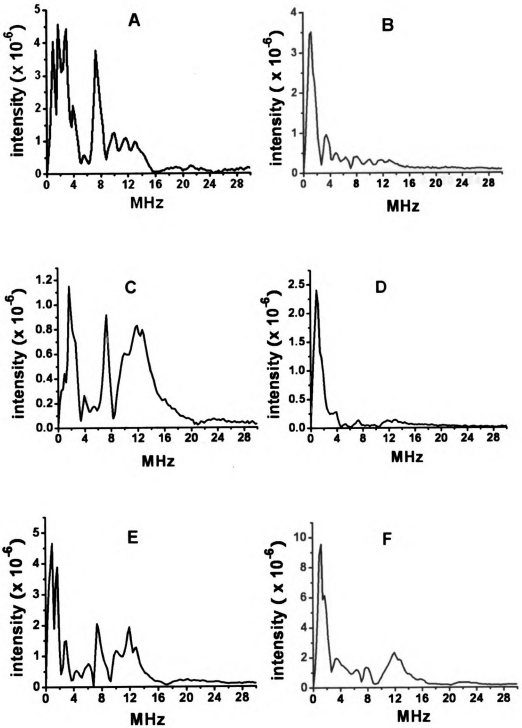

FIGURE 5.7:

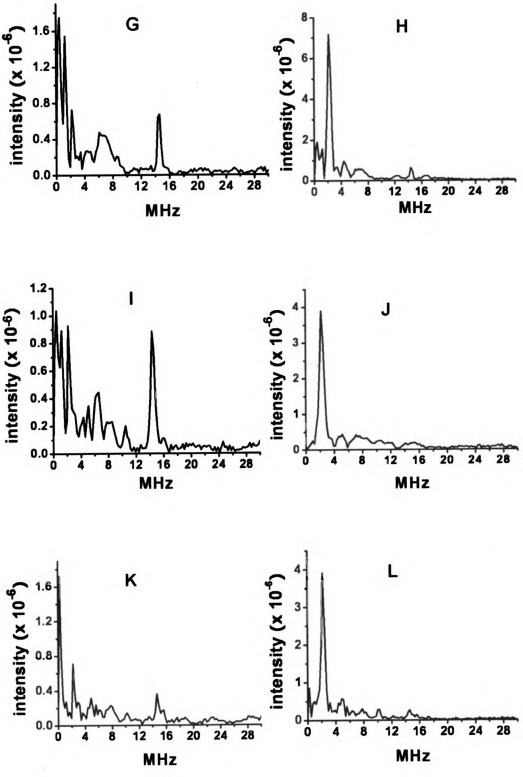

FIGURE 5.8: One-dimensional ESEEM spectra of different XanA complexes prepared in H_2O and 60% ^2H_2O buffer at 172.0 mT and 340.0 mT. Fe(II)-XanA complex examined at 172.0 mT in H_2O buffer (A) and 60% ^2H_2O buffer (B), αKG-Fe(II)-XanA complex examined at 172.0 mT in H_2O buffer (C) and 60% ^2H_2O buffer (D), xanthine-αKG-Fe(II)-XanA complex examined at 172.0 mT in H_2O buffer (E) and 60% ^2H_2O buffer (F). Fe(II)-XanA complex examined at 340.0 mT in H_2O buffer (G) and 60% ^2H_2O buffer (H), αKG-Fe(II)-XanA complex examined at 340.0 mT in H_2O buffer (I) and 60% ^2H_2O buffer (J), xanthine-αKG-Fe(II)-XanA complex examined at 340.0 mT in H_2O buffer (K) and 60% ^2H_2O buffer (L). Protein concentration, 0.45 mM; ferrous ammonium sulfate, slightly less than 0.45 mM; αKG and taurine, 1 mM. ESEEM data were collected under the conditions as described in experimental procedures.

FIGURE 5.8:

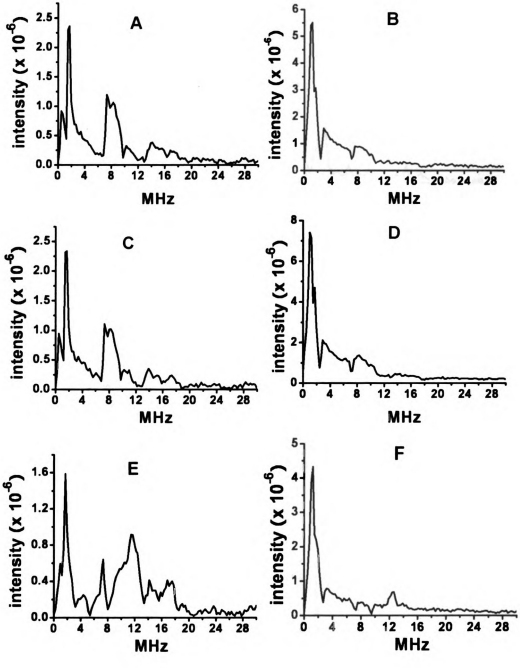

FIGURE 5.8:

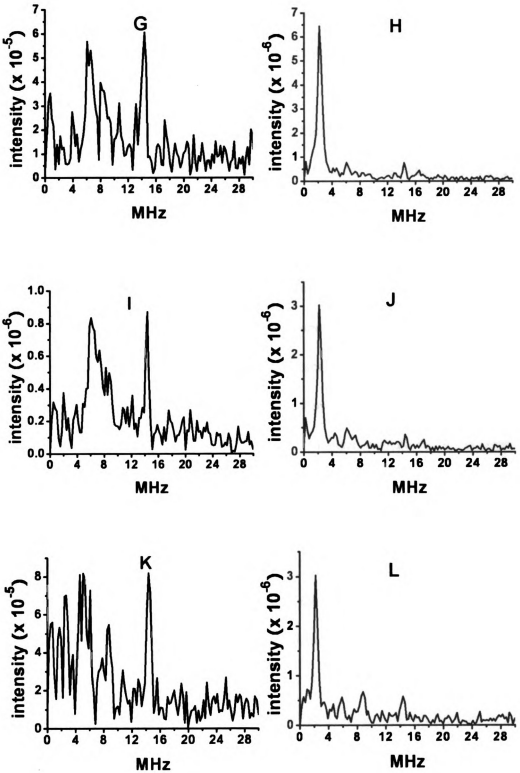

the proton Larmor frequency at $g = 2$. The low frequency region that contains ^{14}N and ^{1}H couplings are more complicated than was observed at $g = 4$ since bound NO might also contribute to this feature. A striking difference is that the broad peaks contributed from the strong proton couplings observed at $g = 4$ disappeared at $g = 2$ spectra.

The corresponding spectra obtained with XanA at the two fields (Figure 5.8) were very similar to those observed for TauD. For both enzymes, when probed at $g = 4$, the contributions from the coupled nuclei were overlapped making it necessary to use the two dimensional, 4-pulse HYSCORE method to resolve contributions from bound histidine nitrogens, coordinated H_2O, and ambient H_2O.

Two-Dimensional ESEEM of {FeNO}^{7} adducts of TauD. TauD was used as the model system to develop HYSCORE spectroscopy as a tool for analysis of Fe(II)/αKG dioxygenases. As described in the following paragraphs, the HYSCORE analysis of TauD included the use of H_2O and ^{2}H-labeled buffers, studies at several magnetic field strengths, examination of ^{2}H-labeled substrates, investigation of the effect of an inhibitor, and the study of W248F variant enzyme.

Comparison of HYSCORE spectra collected at 172.0 mT (perpendicular to the Fe-NO axis) for TauD samples prepared in aqueous buffer versus buffer containing 60% $^{2}H_2O$ reveal features associated with exchangeable protons and perturbations induced by the binding of co-substrates (Figure 5.9). In particular, the HYSCORE spectrum of the enzyme with Fe(II) alone shows two major cross-correlations in the (+,+) quadrant, Figure 5.9A. The stronger correlations lying in low frequencies (0.94, 1.86 MHz) and (1.77, 0.88 MHz), which are shown more clearly in Figure 5.10A, are

likely due to ^{14}N couplings. The HYSCORE spectrum also shows at least three pairs of high frequency correlations, (5.32, 9.14 MHz) (9.01, 5.76 MHz), (5.79, 9.57 MHz) (9.50, 5.89 MHz) and (4.1, 11.2 MHz) (11.3, 3.9 MHz). The correlations with higher frequencies exhibit a weak, disordered system of overlapping ^{1}H arches which most likely reflects a high degree of disorder at the site prior to co-substrate addition. When αKG was added, Figure 5.9C , the low frequency feature remains the same, whereas, the higher frequency correlations, (3.94, 11.58 MHz) (11.58, 3.78 MHz), (4.85, 11.64 MHz) (11.86, 4.33 MHz) and (5.37, 9.70 MHz) (9.70, 5.55 MHz), become better defined and take on the appearance of a wedge-shape that could be indicative of a ^{1}H hyperfine coupling of rhombic symmetry. Subsequent addition of substrate taurine to yield the NO-bound ternary taurine-αKG-Fe(II)-TauD complex at the active site yielded a new ^{1}H hyperfine coupling, at frequency correlations (4.48, 11.80 MHz) and (11.61, 4.73 MHz), with smoother contours and better resolution as shown in Figure 5.9E. In addition, there is a less resolved coupling at (2.1, 12.0 MHz) and (12.3, 2.2 MHz) lying right beside the major ^{1}H interactions. Figure 5.9B, D and F show the HYSCORE spectra at g = 4 of Fe(II)-TauD, αKG-Fe(II)-TauD and taurine-αKG-Fe(II) -TauD complexes prepared in 60% $^{2}H_2O$ buffer. Compared to signals in H_2O buffer, the low frequency couplings slightly changed in shape, Figure 5.10B, and in their correlation peaks (1.03, 2.04 MHz) and (2.07, 1.00 MHz). For complexes Fe(II)-TauD and αKG-Fe(II)-TauD, the cross peaks at high frequency disappeared from the spectrum when the samples are exchanged against $^{2}H_2O$ buffer, however, in the presence of taurine, this proton correlation is not exchangeable.

FIGURE 5.9: HYSCORE spectra of different TauD complexes prepared in H_2O and 60% ^2H_2O buffer at 172.0 mT. Fe(II)-TauD complex examined in H_2O buffer (A) and 60% ^2H_2O buffer (B), αKG-Fe(II)-TauD complex examined in H_2O buffer (C) and 60% ^2H_2O buffer (D), taurine-αKG-Fe(II)-TauD complex examined in H_2O buffer (E) and 60% ^2H_2O buffer (F). buffer. Protein concentration, 2 mM; ferrous ammonium sulfate, slightly < 2 mM; αKG and taurine, 4 mM.

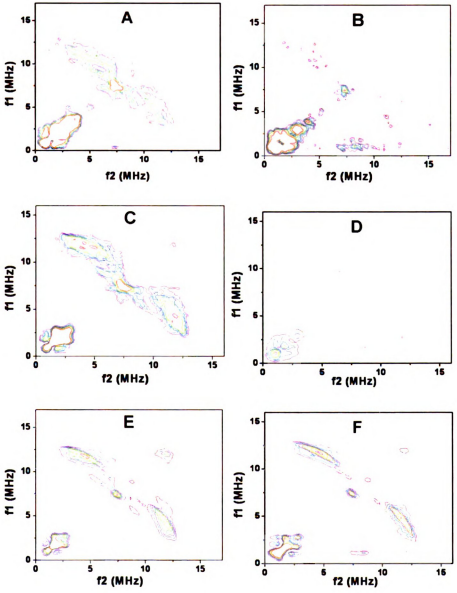

FIGURE 5.10: HYSCORE spectra of taurine-αKG-Fe(II)-TauD complex prepared in H_2O buffer at 172.0 mT (A), 340.0 mT (C) and 60% ^2H_2O buffer at 172.0 mT (B), 340.0 mT (D). All the spectra were examined at a threshold high enough to show ^{14}N couplings. Protein concentration, 2 mM; ferrous ammonium sulfate, slightly < 2 mM; αKG and taurine, 4 mM.

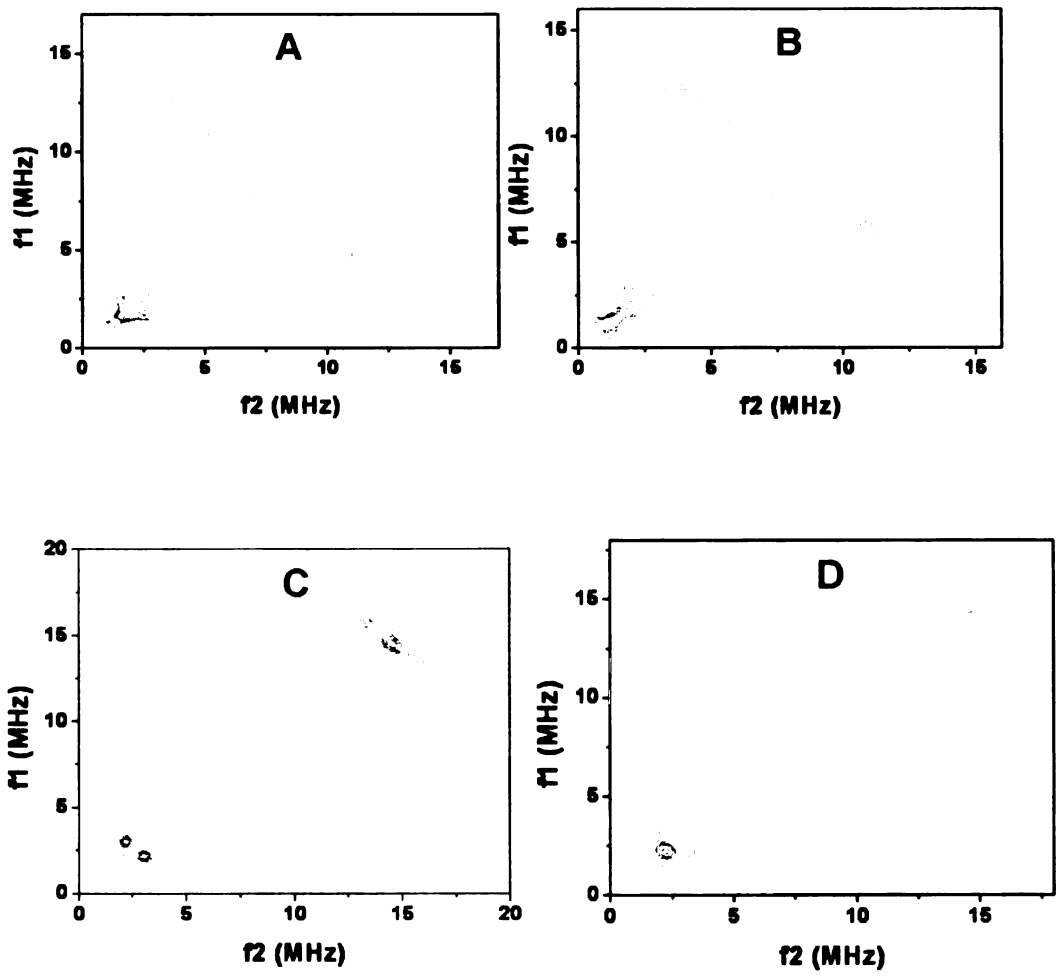

Figure 5.11 exhibits the HYSCORE spectra that result from repeating the measurement and processing procedure described for Figure 5.9 at 340.0 mT. An intact contour centered at the diagonal of (+,+) quadrant (14.5, 14.5 MHz) was observed for all three complexes, Fe(II)-TauD, αKG-Fe(II)-TauD and taurine-αKG-Fe(II)-TauD, whether they were prepared in H_2O or 60% ^2H_2O buffer. However, the feature at low frequency changed its appearance as substrate was added. Two weak ^{14}N couplings were shown for complexes Fe(II)-TauD and αKG-Fe(II)-TauD at correlations (2.26, 2.94 MHz) (2.94, 2.26 MHz) and (1.34, 3.34 MHz) (3.33, 1.35 MHz), Figure 5.11A and C. In the presence of taurine, only one coupling remained at correlations (2.15, 3.04 MHz) and (3.04, 2.16 MHz), Figure 5.11E. The low frequency couplings are very similar for all three complexes when they were prepared in ^2H_2O buffer, as illustrated in Figure 5.11B, D, F and 5.11D. This result is probably due to the dominate feature of ^2H signals. One significant change for the spectra taken at 340.0 mT compared to those taken at 172.0 mM is that the ^1H cross peaks at high frequency are no longer exist.

Three possibilities were considered to account for the origin of the non-exchangeable protons in NO-treated taurine-αKG-Fe(II)-TauD. First, this ^1H could come from C-3 of αKG. To test this option, NO-treated taurine-NOG-Fe(II)-TauD in H_2O was examined by HYSCORE spectroscopy. NOG is a known inhibitor of several Fe(II)/αKG-dependent dioxygenase family members (*42-45*), including XanA and TauD (*31, 46*), and is known to compete with αKG for binding to the metallocenter. The addition of NOG to Fe(II)-TauD yields a broad

FIGURE 5.11: HYSCORE spectra of different TauD complexes prepared in H_2O and 60% ^2H_2O buffer at 340.0 mT. Fe(II)-TauD complex examined at in H_2O buffer (A) and 60% ^2H_2O buffer (B), αKG-Fe(II)-TauD complex examined in H_2O buffer (C) and 60% ^2H_2O buffer (D), taurine-αKG-Fe(II)-TauD complex examined in H_2O buffer (E) and 60% ^2H_2O buffer (F). Protein concentration, 2 mM; ferrous ammonium sulfate, slightly < 2 mM; αKG and taurine, 4 mM.

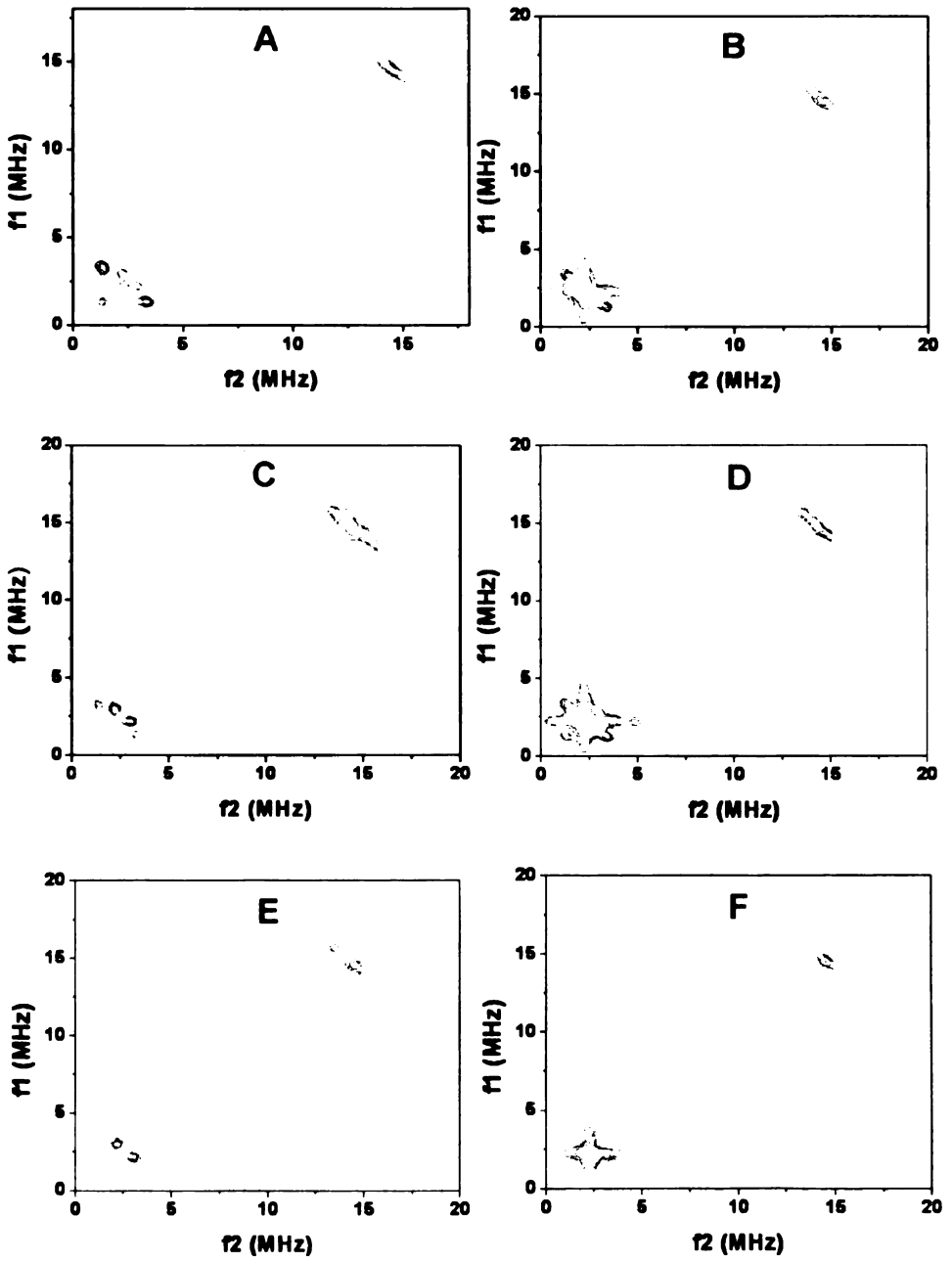

absorbance near 400 nm rather than the 530 nm MLCT feature observed for αKG (*46*). After adding taurine and NO to this sample, the protein complex exhibited an electronic spectrum with a well-defined peak at 408 nm and a feature between 550 nm and 800 nm, Figure 5.12A. Very similar ^{1}H cross peaks were observed in the HYSCORE spectrum of this sample in H_2O at 172.0 mT compared to that generated by adding NO to the taurine-αKG-Fe(II)-TauD complex (Figure 5.12B). This result suggested that the non-exchangeable proton likely does not arise from the C-3 position of αKG. Further confirmation of this point was obtained by using αKG that was incubated for 24 hr in $^{2}H_2O$ at 25 °C to exchange the protons at C-3. This sample was confirmed to be predominantly intact by the demonstration that its use generated 70% of the activity (k_{cat}) for freshly prepared αKG. When the 172.0 mT HYSCORE spectra of NO-treated tauine-^{2}H-labeled-αKG-Fe(II)-TauD (2 mM protein in 60% $^{2}H_2O$ or 0.45 mM TauD in 90% $^{2}H_2O$) were compared to the unlabeled samples, no significant differences were noted (Figure 5.13), again emphasizing that C-3 αKG protons are unlikely to be the source of non-exchangeable protons observed in the sample.

A second possible source of the non-exchangeable protons is from the primary substrate. To examine this option, HYSCORE spectra were obtained in H_2O for NO-treated taurine-αKG-Fe(II)-TauD where the taurine was deuterated at C_1. The non-exchangeable ^{1}H was still present in the HYSCORE spectra at 172.0 mT, although a slight change in the low frequency region was observed at 340.0 mT (Figure 5.14D), a new correlation appeared at (2.21, 2.21 MHz) compared to

FIGURE 5.12: UV-Vis spectra and HYSCORE of ternary complex taurine-NOG-Fe-(II)-TauD. (A) Left panel: UV-Vis Spectra of anaerobic TauD (black), Fe(II)-TauD (red), NOG-Fe(II)-TauD (blue) and taurine-NOG-Fe-(II)-TauD (cyan) obtained in 50 mM Tris buffer, pH 8.0. The TauD subunit (2 mM) was mixed with ferrous ammonium sulfate (slightly < 2 mM) and adjusted to contain 4 mM αKG and 4 mM taurine. Right panel, difference spectra of Fe(II)-TauD in the presence of NOG (solid) and NOG plus taurine (dashed). HYSCORE spectra of taurine-NOG-Fe(II)-TauD complex prepared in H_2O buffer at 172.0 mT (B) and 340.0 mT (C).

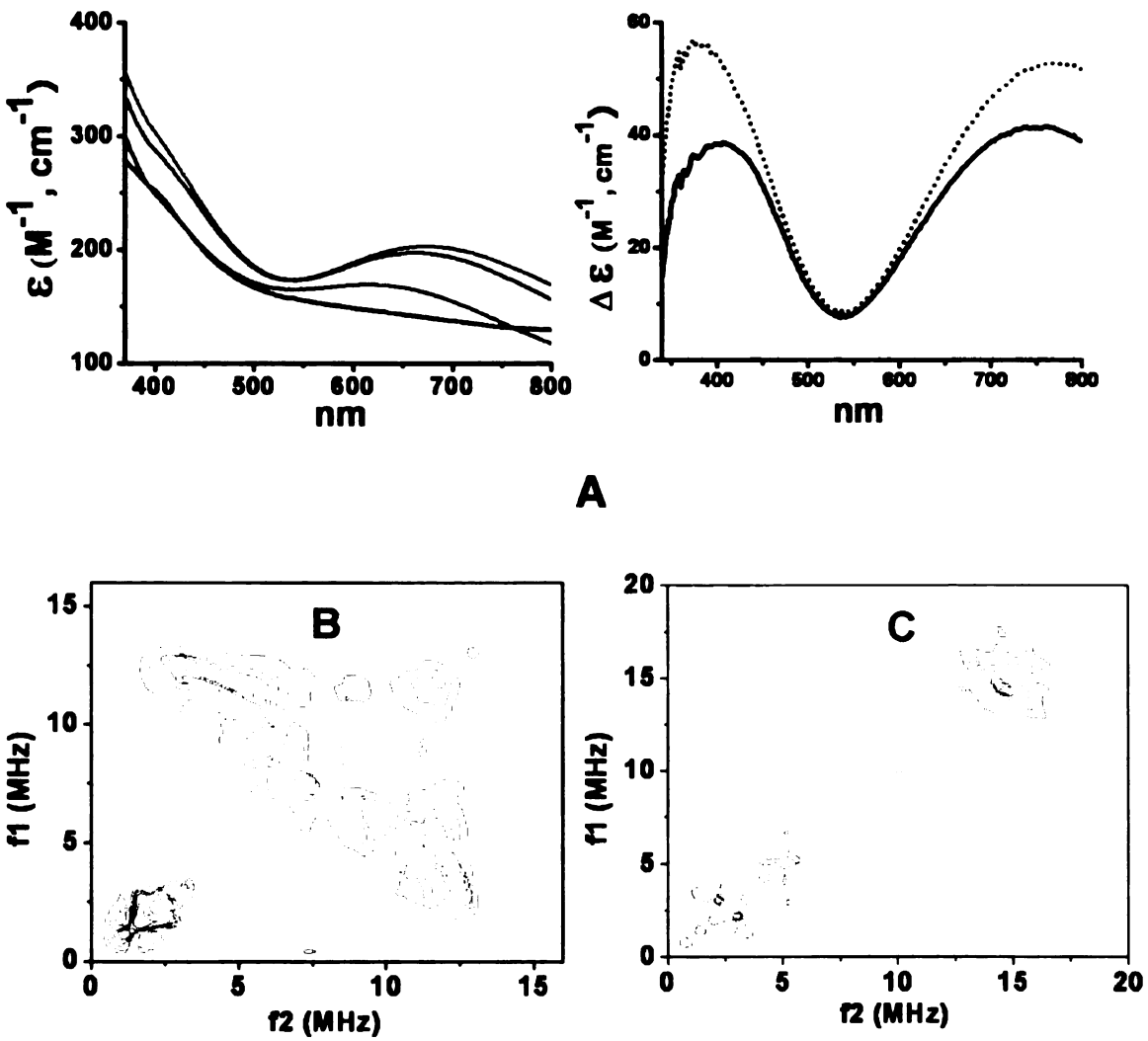

FIGURE 5.13: HYSCORE spectra at 172.0 mT of taurine-^{2}H-labeled-αKG-Fe(II)-TauD prepared in 60% $^{2}H_2O$ buffer (A) and 90% $^{2}H_2O$ buffer. Protein concentration for (A) is 2 mM and (B) is 0.45 mM; ferrous ammonium sulfate for (A) is slightly < 2 mM and (B) is < 0.45 mM; αKG and taurine, 4 mM for (A) and 1 mM for (B).

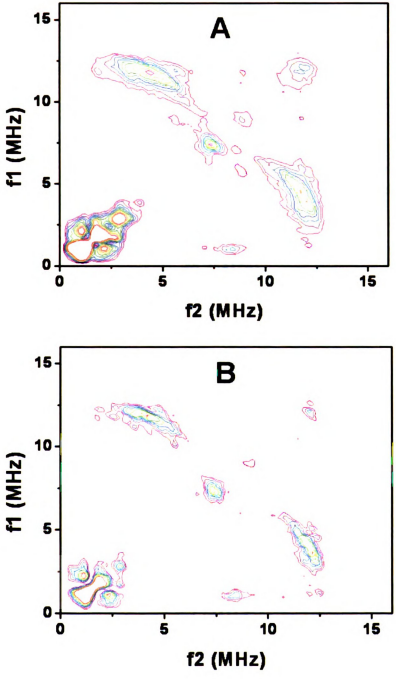

FIGURE 5.14: HYSCORE spectra of ^{2}H-labeled taurine-αKG-Fe(II)-TauD complex prepared in H_2O buffer at 172.0 mT (A) and 340.0 mT (B). Protein concentration, 2 mM; ferrous ammonium sulfate, < 2 mM; αKG and taurine, 4 mM.

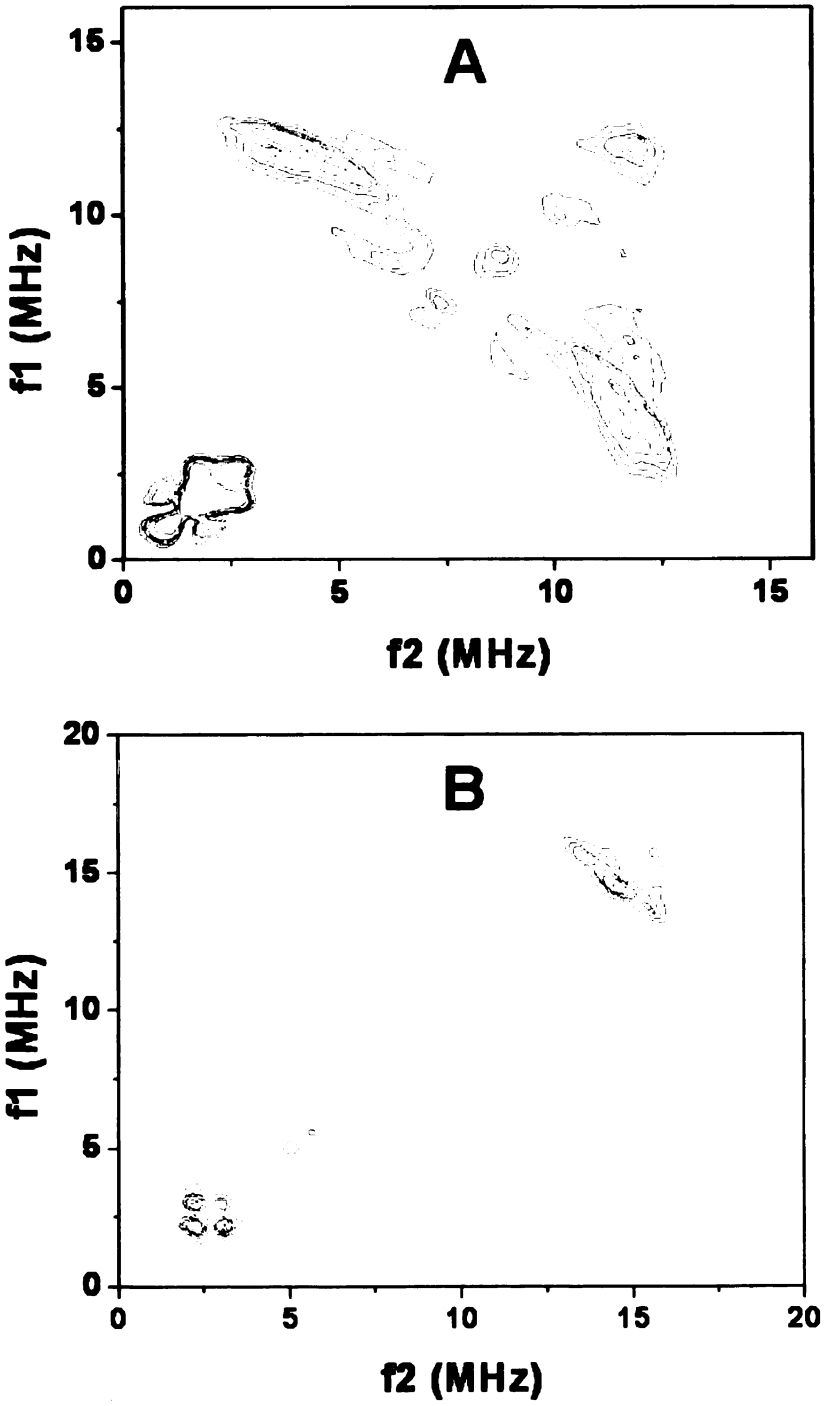

non-deuterated spectrum, Figure 5.10C.

The third possibility to account for the observed non-exchangeable ^1H is that it derives from a side chain of TauD. To attempt to identify this proton, the distance between the ^1H and Fe was estimated by analyzing the cross-peak lineshape of the HYSCORE spectrum for NO-treated taurine-αKG-Fe(II)-TauD in H_2O at 172.0 mT. These cross peaks are indicative of an axial hyperfine coupling and can be analyzed for their dipole-dipole and isotropic hyperfine contributions, $|T|$ and $|A_{iso}|$, respectively, using a graphical analysis developed by Dikanov and Bowman (*47*). In this analysis, an arc is constructed down the long-axis of the contour and correlated frequency pairs (ν_α,ν_β) are read from points along the arc. One then constructs a plot of ν_α^2 vs. ν_β^2 and extracts the slope, Q_α, and y-intercept, G_α, from a linear least squares fit to the points. A_{iso} and $|T|$ are then determined from knowing the Larmor frequency of the nucleus, ν_I, and the system of equations given below. ν_I , the ^1H Larmor frequency at $g = 4$, as 7.323 MHz, β (Bohr constant) is 9.27408×10^{-24} JT^{-1}, β_n (Bohr magneton constant) is 5.05082×10^{-27} JT^{-1}, g_e (electron g factor) is 4.00, g_n (nuclear g factor) is 5.586, and h (Planck's constant) is 6.62618×10^{-34} Js.

$$F_\alpha = [\pm 4\nu_I(Q_\alpha + 1)]/(Q_\alpha - 1) \qquad (2)$$

$$|T| = (2/3)\bullet\{\pm[G_\alpha(F_\alpha \pm 4\nu_I)]/2\nu_I - 4\nu_I^2 + F_\alpha^2/4\}^{1/2} \qquad (3)$$

$$A_{iso} = (F_\alpha - T)/2 \qquad (4)$$

$$T = g_e g_n \beta_e \beta_n / h r^3 \qquad (5)$$

In practice, the assignment of the labels α and β to the frequency pairs is arbitrary and one just has to pick a convention and stick to it. The signs for the first

term in the square root argument for calculating |T| are chosen to yield a real root. The result of using this system of equations is two unique pairs of values for A_{iso} and T. One set features A_{iso} and T parameters of the same sign, while for the other, A_{iso} and T have opposite signs. For the higher arc of Figure 5.9E, the ν_α^2 vs. ν_β^2 plot yielded Q_α = -0.6364 and G_α = 108.47 MHz^2. Plugging these numbers into equation 2-5 gave T = 5.0 MHz, A_{iso} = 1.1 MHz and r, the distance between the transition metal ion and nuclei of interest, approximate 3.2 Å.

A field dependent experiment was carried out for the taurine-αKG-Fe(II)TauD sample in 60% ^2H_2O at 172.0 mT, 182.0 mT, and 192.0 mT to further study the gradual hyperfine coupling changes and determine the A_{iso} and T values, Figure 5.15. After simulation, the non-exchangeable ^1H cross-peaks are characterized by A_{iso} = 0.75 ± 0.3 MHz, T = 5.0 MHz, and β_N = 90° (^1H is perpendicular to the Fe-NO bond axis). This result is consistent with the graphical analysis described above.

Examination of the TauD crystal structure reveals six residues that could position one or more protons at approximately this distance: the three metal ligands (His99, Asp101, and His255) and Asn95, Trp248, and Arg270, Figure 5.16A. Since the crystal structure was obtained under anaerobic conditions, the NO ligand was modeled into the crystal structure using bond lengths and angles from model compounds studies and placing the Fe-NO bond opposite to the axial histidine ligand (*41*). In particular, proton of C-7 in the benzene ring of Trp248 provided the shortest distance of 3.7 Å to the iron center, Figure 5.16B. To test the importance of the Trp248 C-7 proton relative to the HYSCORE spectrum, we made use of the W248F

variant that had previously been characterized and shown to retain 37% of the activity (k_{cat}) of wild-type TauD (*26*). In addition, this mutant protein exhibits UV-visible spectra similar to the control enzyme when incubated anaerobically with αKG and taurine. The taurine-αKG-Fe(II)-TauD W248F complex was treated with NO and examined by HYSCORE at 172.0 mT (Figure 5.17). When using 2 mM W248F, the ^{1}H hyperfine coupling was still clearly observed and remained non-exchangeable in 60% $^{2}H_2O$ buffer. Furthermore, the simulation result from taurine-αKG-Fe(II)-TauD resembled spectrum of taurine-αKG-Fe(II)-TauD W248F complex as illustrated in Figure 5.17C. Analogous experiments were not carried out with Arg270 mutants because this residue is well conserved in TauD sequences and we have found that the R270K variant is inactive. In the case of Asn95, the available variants (N95A and N95D) exhibit very large increases in K_m (taurine) and would not be suitable for these studies.

Two-Dimensional ESEEM of {FeNO}^{7} adducts of XanA. The HYSCORE spectra of XanA at 172.0 mT (Figure 5.18) and 340.0 mT (Figure 5.19) exhibited patterns very similar to TauD. A weak, exchangeable ^{1}H hyperfine coupling at (5.73, 9.23 MHz) and (9.37, 5.48 MHz) was observed before addition of αKG and xanthine; stronger, exchangeable ^{1}H couplings appeared when αKG was added; and further interaction of xanthine caused a new, non-exchangeable ^{1}H coupling at (4.25, 11.71 MHz) and (11.69, 3.78 MHz). The low frequency ^{14}N couplings are similar to TauD spectra in $^{2}H_2O$ prepared buffer, comparing Figure 5.20A to Figure 5.11A. When the 172.0 mT spectra were examined at a less sensitive contour or the spectra were

FIGURE 5.15: HYSCORE spectra of taurine-αKG-Fe(II)-TauD complex prepared in 60% $^{2}H_2O$ buffer at 172.0 mT (A), 182.0 mT (B) and 192.0 mT (C). Red dots are simulations. Protein concentration, 2 mM; ferrous ammonium sulfate, slightly < 2 mM; αKG and taurine, 4 mM.

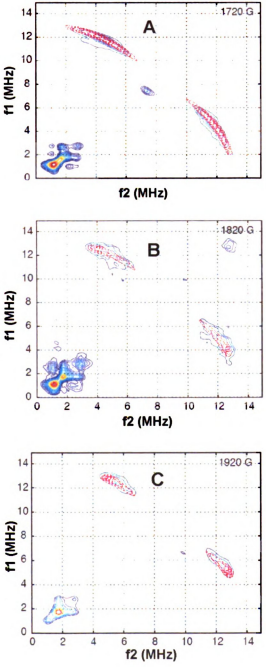

FIGURE 5.16: Two depictions of the TauD active site (A, B) and the XanA active site (C). αKG in stick form with its carbon atoms colored yellow is shown chelating the metal (red sphere). The three side chains that bind the metal are shown in stick form with carbon in yellow, oxygen in red and hydrogen in white. Residues located close to the metal center and potentially capable of accounting for the non-exchangeable hyperfine coupling with the paramagnetic center are shown in stick form with their carbon atoms in blue and nitrogen in dark blue. Panel B highlights the distance and geometry of Trp248 versus the NO-bound metal center of TauD. Panel C highlights the distance and geometry of Asp138 and ILe150 to metal center of XanA.

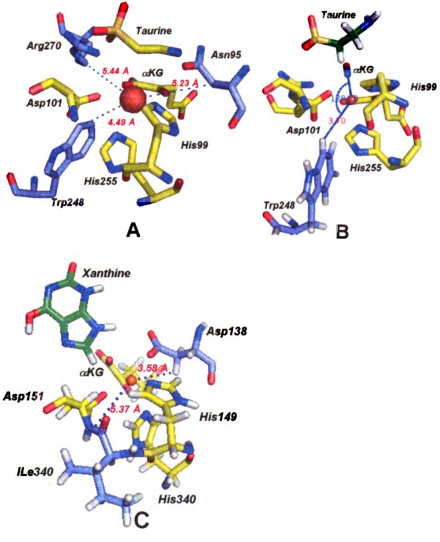

FIGURE 5.17: HYSCORE spectra at 172.0 mT of taurine-αKG-Fe(II)-TauD W248F prepared in H_2O buffer (A) and 60% ^2H_2O buffer (B). Protein concentration is 2 mM; ferrous ammonium sulfate, slightyly < 2 mM; αKG and taurine, 4 mM. Spectrum (C) shows the spectrum (A) overlapping with simulations in red.

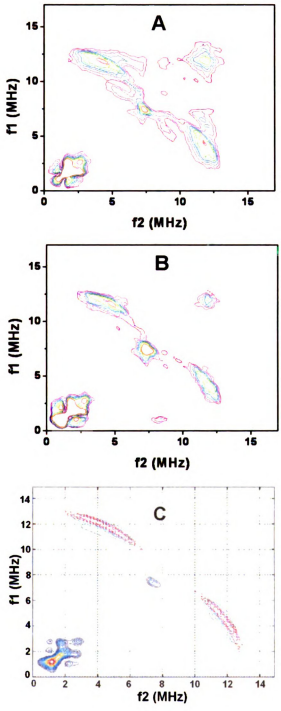

FIGURE 5.18: HYSCORE spectra of different XanA complexes prepared in H_2O and 60% ^2H_2O buffer at 172.0 mT. Fe(II)-XanA complex examined at in H_2O buffer (A) and 60% ^2H_2O buffer (B), αKG-Fe(II)-XanA complex examined in H_2O buffer (C) and 60% ^2H_2O buffer (D), xanthine-αKG-Fe(II)-XanA complex examined in H_2O buffer (E) and 60% ^2H_2O buffer (F). Protein concentration, 0.45 mM; ferrous ammonium sulfate, slightly < 0.45 mM; αKG and xanthine, 1 mM.

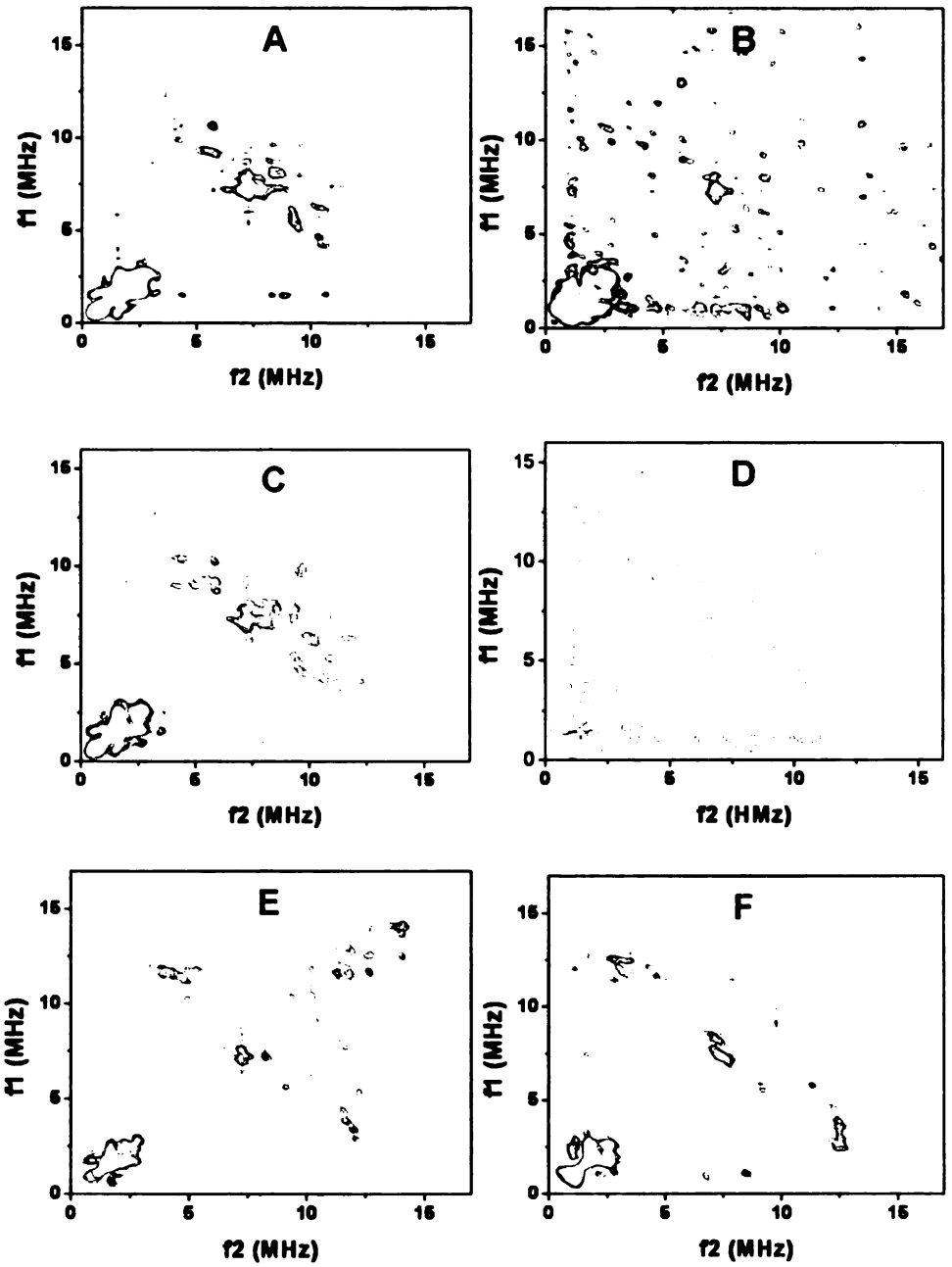

FIGURE 5.19: HYSCORE spectra of different XanA complexes prepared in H_2O and 60% ^2H_2O buffer at 340.0 mT. Fe(II)-XanA complex examined at in H_2O buffer (A) and 60% ^2H_2O buffer (B), αKG-Fe(II)-XanA complex examined in H_2O buffer (C) and 60% ^2H_2O buffer (D), xanthine-αKG-Fe(II)-XanA complex examined in H_2O buffer (E) and 60% ^2H_2O buffer (F). Protein concentration, 0.45 mM; ferrous ammonium sulfate, slightly < 0.45 mM; αKG and xanthine, 1 mM.

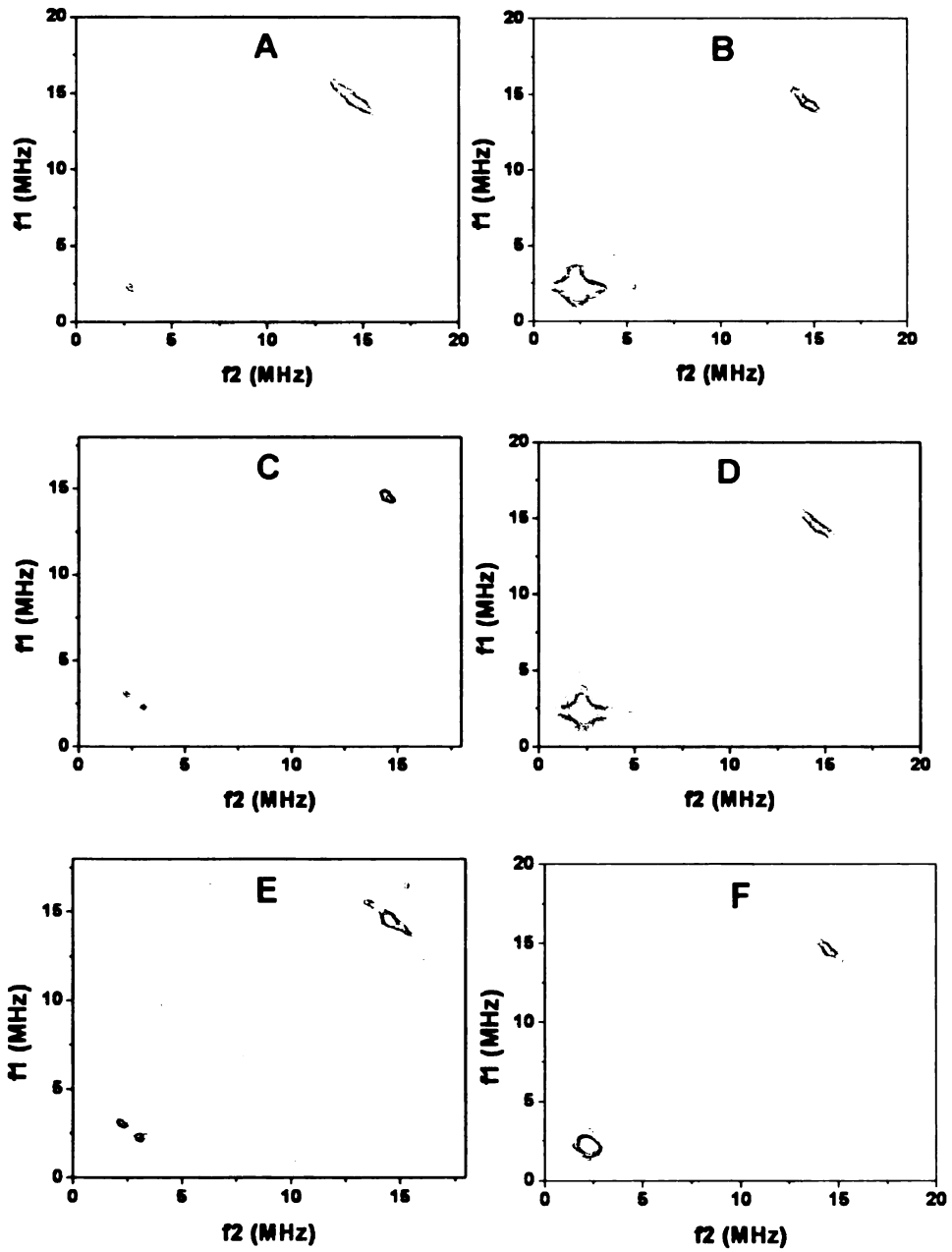

FIGURE 5.20: HYSCORE spectra of xanthine-αKG-Fe(II)-XanA complex prepared in H_2O buffer at 172.0 mT (A), 340.0 mT (C) and 60% ^2H_2O buffer at 172.0 mT (B), 340.0 mT (D). All the spectra were cut threshold high enough to show ^{14}N couplings. Protein concentration, 0.45 mM; ferrous ammonium sulfate, slightly < 0.45 mM; αKG and xanthine, 1 mM.

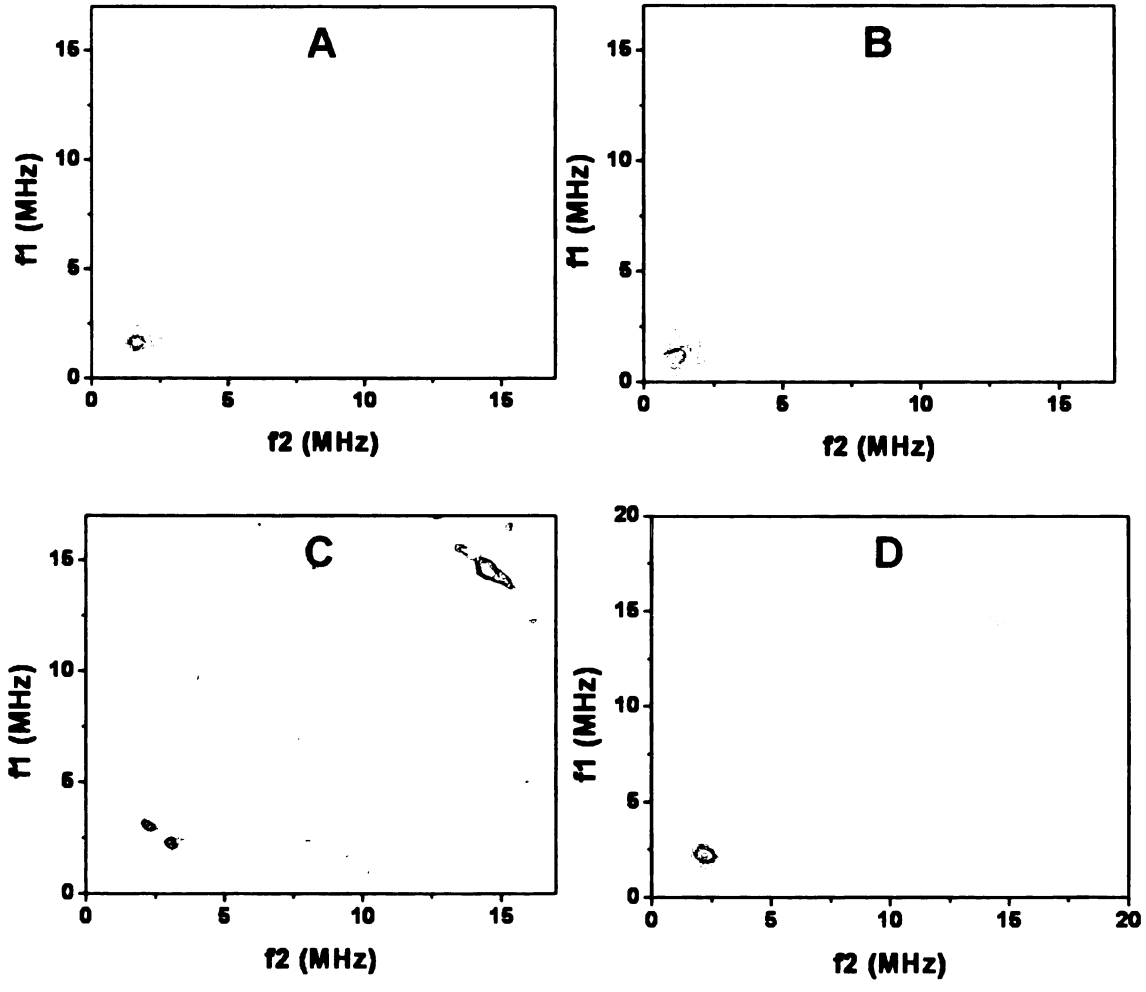

studied using 340.0 mT field, non-exchangeable protons were not convincingly observed and the features associated with nitrogen atoms were much less obvious than in the case of TauD. The potential donor of this non-exchangeable proton coule be Asp138, as shown in Figure 5.16C, or Ile150, which occupies the similar position of Trp248 in TauD.

DISCUSSION

Characterization of the coordination environment of most Fe(II) enzymes is hampered by the difficulty of obtaining high-quality crystal structures of these proteins under anaerobic conditions. One approach to overcome this hurdle is to make use of various spectroscopic methods to examine the active site environments. Whereas Fe(II) sites generally are uninformative when examined by electronic and EPR spectroscopies, prior studies with TauD (*20, 28*) and other Fe(II)/αKG dioxygenase family members (*40, 48*) have shown that the αKG-bound Fe(II) species exhibit a visible chromophore attributed to a MLCT transition (*36*) and that their NO-bound centers yield visible species that are paramagnetic and capable of study by EPR methods. Here, we use the highly soluble, easily obtained, and well-characterized TauD enzyme as a model system to extend these methods to include one- and two-dimensional ESEEM, and then we apply these methods to the study of XanA, a recently identified member of this group of enzymes.

As expected from TauD and other family members, αKG-Fe(II)-XanA exhibited characteristic MLCT transitions that were more defined in the presence of xanthine. Three partially resolved bands, 581 nm, 506 nm and 465 nm, could be assigned to electron transfer from Fe(II) d_{yz}, $d_{x^2-y^2}$, d_{z^2} to the π^* orbital of αKG respectively (*36*). In the presence of NO, XanA developed a distinct UV-visible spectrum as seen in many Fe(II) proteins. The two main features, were previously assigned by Solomon and coworkers to NO^- to Fe(III) charge transfer transitions, in which the most intense transition at 443 nm for TauD and 435 nm for XanA are due

to the interaction of the out-of-plane (the plane created by the bend Fe-N=O bond) NO^- $2\pi^*$ to Fe(III) d_{yz} orbitals, and the broad transitions around 650 nm for both enzymes could be due to the overlap of two transitions, the in-plane NO^- $2\pi^*$ to Fe(III) d_{xz} and Fe(III) d_{xy} to Fe(III) $d_{x^2-y^2}$ orbitals (*41*).

NO-treated TauD and XanA complexes in the absence of substrate exhibited a nearly axial signals of $S = 3/2$ resulting from the strong antiferromagnetic coupling of the high-spin Fe(III) ($S = 5/2$) with NO^- ($S = 1$) (*41*). In the presence of primary substrate, both enzymes exhibited a mixed signal at $g = 4$ composed of a major axial species (~70%) and a more rhombic one (~30%). Increasing the co-substrate or substrate ratio to protein from 2.0 to 5.0 did not alter the overall EPR lineshape and the percentages of each component. Moreover, the diagnostic MLCT transition related to αKG bidentate binding to Fe(II) did not increase when the ratios of added αKG or taurine to protein increased. These results indicated that the two different species were not caused by slow equilibrium between the protein and substrates, but more likely caused by slightly different ligand environments of the ternary complexes taurine-αKG-Fe(II)-TauD or xanthine-αKG-Fe(II)-XanA. Different environments could be associated with distinct Fe-NO angles arising from different ligand geometries of the equatorial histidine and aspartate. Both of the observed species could be catalytic relevant, or only one might lead to turnover. Neither UV-Vis nor HYSCORE spectroscopies are sensitive enough to discriminatethe basis of the two species.

One-dimensional ESEEM spectra of $\{FeNO\}^7$ adducts of TauD gave mixed

signals attributed to ^{14}N (bound histidine and NO) and ^{1}H (coordinated H_2O, ambient H_2O, and protons from the protein). Even though I could not clearly identify the source of each feature by 1-D ESEEM, the individual signals were useful for later studies. The general features of the spectra include the following, (i) Two distinct regions were present in the spectra including a low frequency region, from 0-5 MHz, and a high frequencydomain, usually above proton Larmor frequency. The high frequency signals are more resolved, especially, for the case of a non-exchangeable proton/protons that appears in the presence of substrate. (ii) The low frequency features are more complicated, probably due to a mixture of different ^{14}N and ^{1}H couplings. (iii) ESEEM spectra were dominated by ^{2}H modulations when protein samples were prepared in 60% $^{2}H_2O$ buffer.

The important advantage of HYSCORE techniques lies in the creation of cross peaks whose coordinates are nuclear frequencies from opposite-electron-spin manifolds. By using HYSCORE, our ability to identity couplings from different nuclei is greatly increased, as well as the capability to discriminate noise from signals. When TauD is incubated with Fe(II) alone, two water molecules should be coordinated to the Fe center, consistent with HYSCORE spectra at g = 4 which showed a substantial distribution of exchangeable ^{1}H hyperfine couplings attributed to accessible water molecules. There should be no bound water molecules when αKG is added, however, better defined proton couplings appeared in the spectrum. My explanation is that even though there is no metal bound water, some ambient water which binds near the $\{FeNO\}^7$ site are still close enough to modulate the electronic

center. Such protons may be attributed to the C-1 protonated carboxylate of αKG, or those interacting with the oxygen of the Fe-NO adduct. These proton cross-peaks disappear from the spectrum when the samples are exchanged against ^2H_2O buffer since they come from ambient water. The most interesting result is the appearance of the non-exchangeable proton in the ternary complex. This contribution is not derived from αKG or taurine, as shown from comparison studies of perdeuterated taurine and the αKG surrogate, NOG. Both graphical analysis and simulation of field dependent spectra for the taurine-αKG-Fe(II)-TauD sample gave consistent results: $A_{iso} \approx 1.0$ MHz, $T \approx 5.0$ MHz, $r \approx 3.2$ Å and this proton is perpendicular to Fe-NO bond axis, in agreement with the disappearance of cross-peaks at $g = 2$. Interestingly, xanthine-αKG-Fe(II)-XanA exhibited a very similar non-exchangeable ^1H signals with much lower intensity, while only exchangeable ^1H couplings were observed for complexes without primary substrate. From these observations, it appears that whatever residue gives rise to this strong signal, it is coupled to the $\{FeNO\}^7$ center in this unique fashion only when primary substrate is added. Perhaps this residue plays a role in positioning substrate or in guiding the chemistry of the center once the high valent iron-oxo intermediate is prepared. Based on TauD the crystal structure, this proton could be contributed from any of six residues, including the three metal ligands or Trp248, Asn95, and Arg270. W248F TauD has been used to test the importance of Trp248 and its HYSCORE spectrum showed no substantial difference with wild-type TauD. These results do not completely rule out Trp248 as a candidate for this coupling since the phenylalanine residue partially resembles tryptophan structurally, and it is

known that W248F retains 37% of the activity of wild-type TauD. The three metal ligands are less likely as a source of this proton since no non-exchangeable proton cross-peaks were observed for Fe(II)-TauD and αKG-Fe(II)-TauD. However, the nitrogen couplings were greatly affected by adding primary substrate, thus implying that the positions of metal ligands may shift upon addition of taurine to create an optimized site for O_2 coordination, compatible with the finding that NO has the greatest affinity to the enzyme in the presence of both co-substrate and substrate. Further mutagenesis studies will help to locate this proton; however, the mutants need to be active to confirm proper folding of the protein, so the residue could not simply be mutated to alanine. The lack of crystal structure of XanA makes it even more difficult to locate this proton donor. The HYSCORE spectra of XanA exhibited patterns very similar to TauD, however, the poor signal-to-noise ratio forces one to set the contour plot threshold high. As a result, only the most intense spots instead of complete contour were observed for XanA complexes and an accurate comparison with TauD results is difficult. To overcome this problem, I attempted to set the threshold of TauD HYSCORE spectra high enough so that only the most intense couplings can be seen, as shown in Figure 5.21. The comparison of XanA with this plot reveals that the correlations of proton hyperfine couplings are not exactly the same for XanA and TauD in the Fe(II) bound only and αKG-Fe(II) bound complexes, as shown in Figure 5.21 and Figure 5.18A, C and E. All the XanA samples exhibited a less sensitive contour and much less obvious signals than in the case of TauD, however, this loss of useful information is not just from the decreased sample

FIGURE 5.21: HYSCORE spectra at 172.0 mT of Fe(II)-TauD (A), αKG-Fe(II)-TauD (B), and taurine-αKG-Fe(II)-TauD complex prepared in H_2O buffer. The threshold of the spectra was adjusted to show [only] the most intense spots. Protein concentration, 2 mM; ferrous ammonium sulfate, slightly < 2 mM; αKG and taurine, 4 mM.

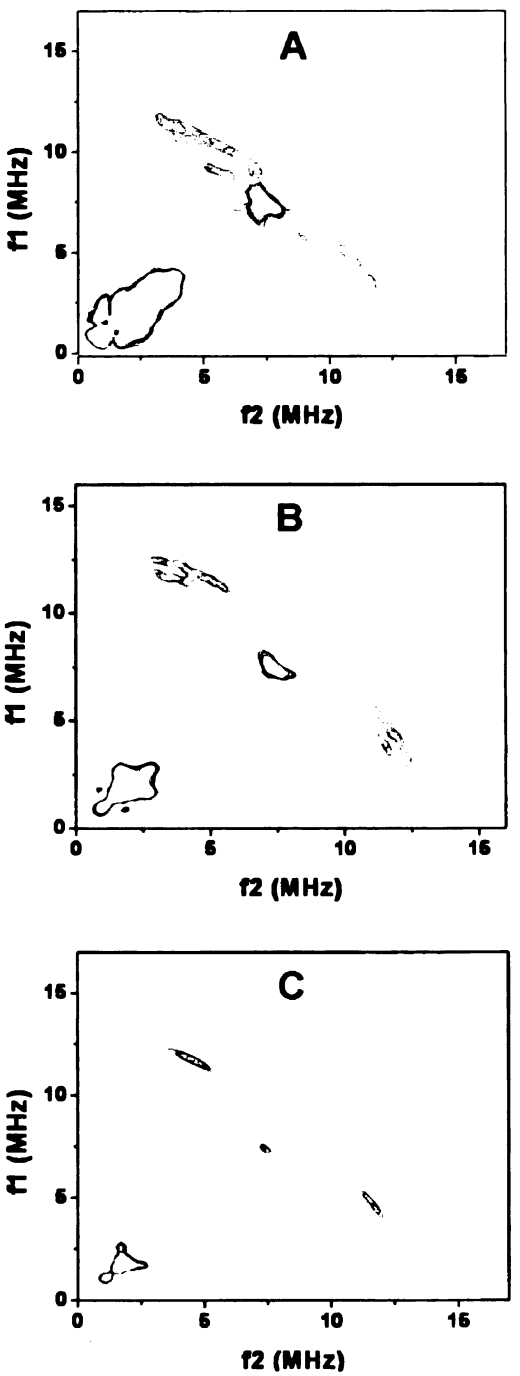

concentration of XanA, as compared with TauD at lower concentration (data not shown). These facts imply that structural differences exist between the two proteins. The differences could be associated with changes in the coordination geometry from metal ligands or αKG, or the active site may be affected by surrounding residues to different extents. Nevertheless, it is not surprising to see these differences based on discrepencies observed before (*32*), including selectivity for primary substrate, spacings between the conserved Asp to the distal His, solvent isotope effect, MLCT transitions of Fe(II)-αKG-protein complex, electronic rhombicity for the ternary complex, also the reactivity of the replaced proton (H at C-1 of taurine, H at C-8 of xanthine).

In summary, I applied different spectroscopies, including UV-Vis, EPR, and one- and two- dimensional ESEEM, to gain insights into XanA, a recently described Fe(II)/αKG hydroxylase family member that is the first representative to catalyze the oxidation of purine base. A well-characterized member, TauD, was used as a model system. αKG-Fe(II)-XanA exhibited characteristic MLCT transitions that were altered by the presence of xanthine verifying the αKG bidentate binding to Fe(II). NO treated XanA complexes developed similar spectra of UV-Vis, EPR, one- and two-dimensional ESEEM compared with those of TauD. This study provides the first spectroscopic information for XanA and yields insights into the coordination properties of Fe(II) in this protein. An non-exchangeable proton coupling signal was observed for the ternary complex, this new feature only exists in the presence of the primary substrate and may play an important role of positioning the substrate in the

binding pocket.

REFERENCES

(1) Hausinger, R. P. (2004) Fe(II)/α-ketoglutarate-dependent hydroxylases and related enzymes. *Critical Reviews in Biochemistry and Molecular Biology 39*, 21-68.

(2) Clifton, I. J., McDonough, M. A., Ehrismann, D., Kershaw, N. J., Granatino, N., and Schofield, C. J. (2006) Structural studies on 2-oxoglutarate oxygenases and related double-stranded β-helix fold protein. *Journal of Inorganic Biochemistry 100*, 644-669.

(3) Purpero, V., and Moran, G. R. (2007) The diverse and pervasive chemistries of the α-keto acid dependent enzymes. *J. Biol. Inorg. Chem. 12*, 587-601.

(4) Kivirikko, K. I., and Pihlajaniemi, T. (1998) Collagen hydroxylases and the protein disulfide isomerase subunit of prolyl 4-hydroxylase. *Advances in Enzymology and Related Areas of Molecular Biology 72*, 325-398.

(5) Schofield, C. J., and Ratcliffe, P. J. (2004) Oxygen sensing by hydroxylases. *Nature Reviews in Molecular Cell Biology 5*, 343-354.

(6) Tsukada, Y.-I., Fang, J., Erdjument-Bromage, H., Warren, M. E., Borchers, C. H., Tempst, P., and Zhang, Y. (2006) Histone demethylation by a family of JmjC domain-containing proteins. *Nature 439*, 811-816.

(7) Trewick, S. C., Henshaw, T. F., Hausinger, R. P., Lindahl, T., and Sedgwick, B. (2002) Oxidative demethylation by *Escherichia coli* AlkB directly reverts DNA base damage. *Nature 419*, 174-178.

(8) Aas, P. A., Otterlei, M., Falnes, P. O., Vagbe, C. B., Skorpen, F., Akbari, M., Sundheim, O., Bjoras, M., Slupphaug, G., Seeberg, E., and Krokan, H. E. (2003) Human and bacterial oxidative demethylases repair alkylation damage in both RNA and DNA. *Nature 421*, 859-863.

(9) Mukherji, M., Chien, W., Kershaw, N. J., Clifton, I. J., Schofield, C. J., Wierzbicki, A. S., and Lloyd, M. D. (2001) Structure-function analysis of phytanoyl-CoA 2-hydroxylase mutations causing Refsum's disease. *Human Molecular Genetics 10*, 1971-1982.

(10) Prescott, A. G., and John, P. (1996) Dioxygenases: molecular structure and role in plant metabolism. *Annual Review of Plant Physiology and Plant Molecular Biology 47*, 245-271.

(11) Thornburg, L. D., Lai, M.-T., Wishnok, J. S., and Stubbe, J. (1993) A non-heme iron protein with heme tendencies: an investigation of the substrate specificity of thymine hydroxylase. *Biochemistry 32*, 14023-14033.

(12) Fukumori, F., and Hausinger, R. P. (1993) Purification and characterization of 2,4-dichlorophenoxyacetate/α-ketoglutarate dioxygenase. *Journal of Biological Chemistry 268*, 24311-24317.

(13) Müller, T. A., Zavodszky, M. I., Feig, M., Kuhn, L. A., and Hausinger, R. P. (2006) Structural basis for the enantiospecificities of *R*- and *S*-phenoxypropionate/α-ketoglutarate dioxygenases. *Protein Science 15*, 1356-1368.

(14) Eichhorn, E., van der Ploeg, J. R., Kertesz, M. A., and Leisinger, T. (1997) Characterization of α-ketoglutarate-dependent taurine dioxygenase from *Escherichia coli*. *Journal of Biological Chemistry 272*, 23031-23036.

(15) Kertesz, M. A. (1999) Riding the sulfur cycle - metabolism of sulfonates and sulfate esters in Gram-negative bacteria. *FEMS Microbiology Reviews 24*, 135-175.

(16) Elkins, J. M., Ryle, M. J., Clifton, I. J., Dunning Hotopp, J. C., Lloyd, J. S., Burzlaff, N. I., Baldwin, J. E., Hausinger, R. P., and Roach, P. L. (2002) X-ray crystal structure of *Escherichia coli* taurine/α-ketoglutarate dioxygenase complexed to ferrous iron and substrates. *Biochemistry 41*, 5185-5192.

(17) O'Brien, J. R., Schuller, D. J., Yang, V. S., Dillard, B. D., and Lanzilotta, W. N. (2003) Substrate-induced conformational changes in *Escherichia coli* taurine/α-ketoglutarate dioxygenase and insight into the oligomeric structure. *Biochemistry 42*, 5547-5554.

(18) Koehntop, K. D., Emerson, J. P., and Que, L., Jr. (2005) The 2-His-1-carboxylate facial triad: a versatile platform for dioxygen activation by mononuclear non-heme iron(II) enzymes. *Journal of Biological Inorganic Chemistry 10*, 87-93.

(19) Hanauske-Abel, H. M., and Günzler, V. (1982) A stereochemical concept for the catalytic mechanism of prolylhydroxylase. Applicability to classification and design of inhibitors. *Journal of Theoretical Biology 94*, 421-455.

(20) Ryle, M. J., Padmakumar, R., and Hausinger, R. P. (1999) Stopped-flow kinetic analysis of *Escherichia coli* taurine/α-ketoglutarate dioxygenase: interactions with α-ketoglutarate, taurine, and oxygen. *Biochemistry 38*,

15278-15286.

(21) Price, J. C., Barr, E. W., Tirupati, B., Bollinger, J. M., Jr., and Krebs, C. (2003) The first direct characterization of a high-valent iron intermediate in the reaction of an α-ketoglutarate-dependent dioxygenase: a high-spin Fe(IV) complex in taurine/α-ketoglutarate dioxygenase (TauD) from *Escherichia coli*. *Journal of Biological Chemistry 42*, 7497-7508.

(22) Price, J. C., Barr, E. W., Glass, T. E., Krebs, C., and Bollinger, J. M., Jr. (2003) Evidence for hydrogen abstraction from C1 of taurine by the high-spin Fe(IV) intermediate detected during oxygen activation by taurine:α-ketoglutarate dioxygenase (TauD). *Journal of the American Chemical Society 125*, 13008-13009.

(23) Proshlyakov, D. A., Henshaw, T. F., Monterosso, G. R., Ryle, M. J., and Hausinger, R. P. (2004) Direct detection of oxygen intermediates in the non-heme Fe enzyme taurine/α-ketoglutarate dioxygenase. *Journal of the American Chemical Society 126*, 1022-1023.

(24) Riggs-Gelasco, P. J., Price, J. C., Guyer, R. B., Brehm, J. H., Barr, E. W., Bollinger, J. M., Jr., and Krebs, C. (2004) EXAFS spectroscopic evidence for an Fe=O unit in the Fe(IV) intermediate observed during oxygen activation by taurine:α-ketoglutarate dioxygenase. *Journal of the American Chemical Society 126*, 8108-8109.

(25) Price, J. C., Barr, E. W., Hoffart, L. M., Krebs, C., and Bollinger, J. M., Jr. (2005) Kinetic dissection of the catalytic mechanism of taurine:α-ketoglutarate dioxygenase (TauD) from *Escherichia coli*. *Biochemistry 44*, 8138-8147.

(26) Grzyska, P. K., Ryle, M. J., Monterosso, G. R., Liu, J., Ballou, D. P., and Hausinger, R. P. (2005) Steady-state and transient kinetic analyses of taurine/α-ketoglutarate dioxygenase: effects of oxygen concentration, alternative sulfonates, and active site variants on the Fe(IV) intermediate. *Biochemistry 44*, 3845-3855.

(27) Sinnecker, S., Svensen, N., Barr, E. W., Ye, S., Bollinger, J. M., Jr., Neese, F., and Krebs, C. (2007) Spectroscopic and computational evaluation of the structure of the high-spin Fe(IV)-oxo intermediates in taurine: alpha-ketoglutarate dioxygenase from Escherichia coli and its His99Ala ligand variant. *J Am Chem Soc 129*, 6168-79.

(28) Muthakumaran, R. B., Grzyska, P. K., Hausinger, R. P., and McCracken, J. (2007) Probing the Fe-substrate orientation for taurine/a-ketoglutarate

dioxygenase using deuterium ESEEM spectroscopy. *Biochemistry in press.*

(29) Cultrone, A., Scazzocchio, C., Rochet, M., Montero-Morán, G., Drevet, C., and Fernández-Martín, R. (2005) Convergent evolution of hydroxylation mechanisms in the fungal kingdoms: molybdenum cofactor-independent hydroxylation of xanthine via α-ketoglutarate dependent dioxygenase. *Molecular Microbiology 57*, 276-290.

(30) Hille, R. (2005) Molybdenum-containing hydroxylases. *Archives of Biochemistry and Biophysics 433*, 107-116.

(31) Montero-Morán, G. M., Li, M., Rendóm-Huerta, E., Jourdan, F., Lowe, D. J., Stumpff-Kane, A. W., Feig, M., Scazzocchio, C., and Hausinger, R. P. (2007) Purification and characterization of the FeII- and a-ketoglutarate-dependent xanthine hydroxylase from Aspergillus nidulans. *Biochemistry 46*, 5293-5304.

(32) Montero-Morán, G. M., Li, M., Rendón-Huerta, E., Jourdan, F., Lowe, D. J., Stumpff-Kane, A. W., Feig, M., Scazzocchio, C., and Hausinger, R. P. (2007) Purification and characterization of the Fe(II)- and α-ketoglutarate-dependent xanthine hydroxylase from *Aspergillus nidulans. Biochemistry 46*, 5293-5304.

(33) Gemperle, C., Aebli, G., Schweiger, A., and Ernst, R. R. (1990) PHase cycling in pulse EPR. *J. Magn. Reson. 88*, 241-256.

(34) Hoffman, B. M., Venters, R. A., and Martinsen, J. (1985) General theory of polycrystalline ENDOR patterns. Effects of finite EPR and ENDOR component linewidths. *J. Magn. Reson. 62*, 537-542.

(35) Grzyska, P. K., Müller, T. A., Campbell, M. G., and Hausinger, R. P. (2007) Metal ligand substitution and evidence for quinone formation in taurine/α-ketoglutarate dioxygenase. *Journal of Inorganic Biochemistry 101*, 797-808.

(36) Pavel, E. G., Zhou, J., Busby, R. W., Gunsior, M., Townsend, C. A., and Solomon, E. I. (1998) Circular dichroism and magnetic circular dichroism spectroscopic studies of the non-heme ferrous active site in clavaminate synthase and its interaction with α-ketoglutarate cosubstrate. *Journal of the American Chemical Society 120*, 743-753.

(37) Zhou, J., Kelly, W. L., Bachmann, B. O., Gunsior, M., Townsend, C. A., and Solomon, E. I. (2001) Spectroscopic studies of substrate interactions with clavaminate synthase 2, a multifunctional α-KG-dependent non-heme iron enzyme: correlation with mechanisms and reactivities. *Journal of the American Chemical Society 123*, 7388-7398.

(38) Ho, R. Y. N., Mehn, M. P., Hegg, E. L., Liu, A., Ryle, M. A., Hausinger, R. P., and Que, L., Jr. (2001) Resonance Raman studies of the iron(II)-α-keto acid chromophore in model and enzyme complexes. *Journal of the American Chemical Society 123*, 5022-5029.

(39) Enemark, J. H., and Fleltham, R. D. (1974) Principles of structure, bonding, and reactivity for metal nitrosyl complexes. *Coordination Chemistry Reviews 13*, 339.

(40) Hegg, E. L., Whiting, A. K., Saari, R. E., McCracken, J., Hausinger, R. P., and Que, L., Jr. (1999) Herbicide-degrading α-keto acid-dependent enzyme TfdA: metal coordination environment and mechanistic insights. *Biochemistry 38*, 16714-16726.

(41) Brown, C. A., Pavlovsky, M. A., Westre, T. E., Zhang, Y., Hedman, B., Hodgson, K. O., and Solomon, E. I. (1995) Spectroscopic and theoretical description of the electronic structure of $S = 3/2$ iron-nitrosyl complexes and their relation to O_2 activation by non-heme iron enzyme active sites. *Journal of the American Chemical Society 117*, 715-732.

(42) Baader, E., Tschank, G., Baringhaus, K. H., Burghard, H., and Gunzler, V. (1994) Inhibition of prolyl 4-hydroxylase by oxalyl amino acid derivatives in vitro, in isolated microsomes and in embryonic chicken tissues. *Biochemical Journal 300*, 525-530.

(43) Cunliffe, C. J., Franklin, T. J., Hales, N. J., and Hill, G. B. (1992) Novel inhibitors of prolyl 4-hydroxylase. 3. Inhibition by the substrate analogue N-oxaloglycine and its derivatives. *Journal of Medicinal Chemistry 35*, 2652-2658.

(44) Chan, D. A., Sutphin, P. D., Denko, N. C., and Giaccia, A. J. (2002) Role of prolyl hydroxylation in oncogenically stabilized hypoxia-inducible factor-1α. *Journal of Biological Chemistry 277*, 40112-40117.

(45) McDonough, M. A., McNeill, L. A., Tilliet, M., Papmichael, C. A., Chen, Q.-Y., Banerji, B., Hewitson, K. S., and Schofield, C. J. (2005) Selective inhibition of factor inhibiting hypoxia-inducible factor. *Journal of the American Chemical Society 127*, 7680-7681.

(46) Kalliri, E., Grzyska, P. K., and Hausinger, R. P. (2005) Kinetic and spectroscopic investigation of Co^{II}, Ni^{II}, and *N*-oxalylglycine inhibition of the Fe^{II}/α-ketoglutarate dioxygenase, TauD. *Biochemical and Biophysical Research Communications 338*, 191-197.

(47) Dikanov, S. A., and Bowman, M., K. (1995) Cross-peak lineshape of two-dimensional ESEEM spectra in disordered S=1/2, I=1/2 spin systems. *Journal of Magnetic Resonance A 116*, 125-128.

(48) Hogan, D. A., Smith, S. R., Saari, E. A., McCracken, J., and Hausinger, R. P. (2000) Site-directed mutagenesis of 2,4-dichlorophenoxyacetic acid/α-ketoglutarate dioxygenase. Identification of residues involved in metallocenter formation and substrate binding. *Journal of Biological Chemistry 275*, 12400-12409.

CHAPTER 6

CONCLUSIONS AND FUTURE RESEARCH

CONCLUSIONS

Moco-independent *Aspergillus nidulans* xanthine hydroxylase (XanA) was purified as the His_6-tagged recombinant protein from both the fungus and a heterologous bacterial host and characterized as a novel member of Fe(II)/αKG-dependent dioxygenase superfamily (*1*). Ferrous XanA catalyzes xanthine hydroxylation to uric acid, concomitant with the oxidative decarboxylation of αKG, forming succinate and carbon dioxide. Comparison of XanA isolated from *A. nidulans* and *E. coli* revealed very different quaternary structures and posttranslational modifications; however, the kinetic properties of XanA purified from both hosts are very similar (*E. coli* : ~70 U mg $^{-1}$, K_m of 31 μM for αKG, and K_m of 45 μM for xanthine at pH 7.4; *A. nidulans* : 30 U mg $^{-1}$, and K_m values of 50 μM and 46 μM at pH 7.0). Fe(II) is irreplaceable for enzyme activity and some divalent metals, such as Ni(II), Zn(II) and Cu(II), are competitive inhibitors of Fe(II). A solvent isotope effect was observed upon substituting H_2O with ^2H_2O. This result suggests that a chemical group possessing an exchangeable proton such as Fe(III)-OOH or Fe(III)-OH is important in the rate-determining step of the overall reaction. Although the xanthine C-H bond is broken at C-8 during turnover, substitution of the proton at this position by ^2H did not lead to a substrate isotope effect. This result demonstrates that C-H cleavage is not the rate-determining step in the reaction. The co-substrate can be substituted by α-ketoadipate, but not by other α-keto acids tested. NOG, a known inhibitor of several other representatives of this superfamily, is a competitive (with αKG) inhibitor of XanA with a K_i of 0.12 μM. XanA displays high specificity

towards its primary substrate. 9-methylxanthine and 1-methylxanthine act as alternative substrates with significant activity loss, respectively around 20 and 10^{-4} times less than xanthine. 6,8-DHP is a competitive, slow-binding inhibitor with K_i^{app} of 12.6 μM, while 2,8-DHP and 8-HP have almost no inhibitory effect, indicating the potentially important role of the C-6 carbonyl or enol for primary substrate binding. The above studies represent the first biochemical characterization of purified xanthine/αKG dioxygenase, and provide valuable baseline information to carry out further mechanistic and spectroscopic studies.

Fe(II)/αKG-dependent dioxygenases catalyze a wild range of reactions and utilize substrates ranging from small molecules, such as taurine, to large polymers, such as proteins or DNA/RNA (*2*). It is well known that the highly conserved DSBH structure acts as a stable platform to anchor the Fe(II) and αKG (*2*). The metal ion is ligated by the three residues forming a conserved HXD/EX$_n$H motif, while αKG binds Fe(II) in a bidentate fashion through the C-1 carboxylate and C-2 keto groups. The most interesting question is how to bind different substrates within this scaffold to carry out the unique reactions for each enzyme. A homology model of XanA was generated on the basis of the structure of the related enzyme TauD (*1*). The XanA protein is predicted to contain the DSBH comprised of eight β-strands with the Fe(II) binding ligands (His149, Asp151, and His340), and the co-substrate positioned to chelate Fe(II) in a bidentate fashion. The αKG C-5 carboxylate is predicted to form a salt bridge with Arg352, while Lys122 is well positioned to stabilize the C-1 carboxylate of the co-substrate. Xanthine binds in an active site pocket lined with

potential hydrogen bond donors or acceptors (Gln99, Gln101, Glu137, Asp138, Lys122, Gln356, Cys357, and Asn358). Ala was chosen to replace each of the potential hydrogen-bonding residues at the XanA active site and the eight single mutants were constructed and purified. After analyzing the kinetic properties of the variants with xanthine, the alternate substrate 9-methylxanthine, 6,8-DHP and thiol-specific reagents, critical residues that participate in binding of the primary substrate were identified and a model for xanthine binding to XanA was proposed, Figure 4.17. Xanthine is shown binding to the enzyme active site via a constellation of hydrogen bonding interactions which explains the high selectivity towards the primary substrate. The xanthine binding model derived from my extensive kinetic comparisons will need to be verified by crystal structure determination, but crystals of XanA are not available currently.

After carrying of biochemical characterization and mutational/kinetic studies (focusing on the primary substrate binding mode) of XanA, my ultimate goal and the most challenging part of this project was to further uncover the mechanism of this enzymatic reaction by using of spectroscopic methods. Knowing the structures of each intermediate is the key to understand the mechanism. I started with investigating the coordination chemistry of different enzyme complexes: XanA-Fe, XanA-Fe(II)-αKG and XanA-Fe(II)-αKG-xanthine. I confirmed the bidentate binding of αKG to Fe(II) by observing the diagnostic MLCT features around 500 nm by UV-Vis spectroscopy of the XanA-Fe(II)-αKG and XanA-Fe(II)-αKG-xanthine complexes. Consistent with a shift from 6-coordinate to 5-coordinate geometry, I

observed enhanced definition of the spectroscopic features after adding substrate. Since high spin Fe(II) is EPR silent, I used NO, a good O_2 surrogate, to bind Fe(II) to form an $\{FeNO\}^7$ complex which is EPR active. I found that adding primary substrate disturbs the electronic environment of Fe(II) and this is supported by the more rhombic EPR line shape for XanA-Fe(II)-aKG-xanthine compared with XanA-Fe(II) or XanA-Fe(II)-aKG. Electron nuclear hyperfine coupling between Fe(II) and surrounding ligands was investigated by using one- and two-dimensional ESEEM spectroscopies. In this part, I used TauD as a reference and examined even more extensively than XanA. One-dimensional ESEEM spectra for both XanA and TauD show modulations from ^{14}N and ^{1}H. At g = 4, the contributions from these coupled nuclei are overlapped making it necessary to use the two dimensional, 4-pulse HYSCORE method to resolve contributions from bound histidine nitrogens, coordinated H_2O, and ambient H_2O. For TauD-Fe(II), HYSCORE spectra show a substantial distribution of exchangeable, ^{1}H hyperfine couplings. When co-substrate αKG is added, the ^{1}H HYSCORE is considerably altered with the dominant hyperfine coupling arising from an exchangeable, strongly-coupled proton of rhombic symmetry. Subsequent addition of substrate taurine, to yield the ternary complex at the active site, showed a new, ^{1}H hyperfine interaction that was not exchangeable in $^{2}H_2O$. The HYSCORE cross-peaks from this ^{1}H show a hyperfine tensor of axial symmetry characterized by a dipole-dipole distance of 3.2 Å and an isotropic contribution of 1.1 MHz. Comparison of these data with the X-ray crystal structure of TauD and the results of parallel studies of TauD variants suggests that this ^{1}H is likely from W248.

However, the W248F variant did not show any substantial difference in its spectral features compared with those of wild-type TauD. Interestingly, XanA-Fe(II)-αKG-xanthine exhibited very similar non-exchangeable ^{1}H signals with much lower intensity. Exchangeable ^{1}H hyperfine couplings were also observed for XanA-Fe(II) and the XanA-Fe(II)-αKG complex. This comparison study suggested that the coordination chemistry of TauD and XanA are very similar, even though the origin of this strong, non-exchangeable ^{1}H is still unclear, its appearance in both enzyme complexes means this structural change induced by adding primary substrate could be quite common for this superfamily and important for understanding the mechanism.

FUTURE RESEARCH

Constructing Double or Triple Mutants. Eight single mutants (Q99A, Q101A, E137A, D138A, K122A, Q356A, C357A, and N358A) were constructed and, except Q99A, all of them exhibited substantial activities. This finding suggested that modifying only one residue will not cause significant change of primary substrate binding. Double or even triple mutants might affect xanthine binding more efficiently. N358A has shown the most significant K_m change, so it could be considered first; Q99A can be excluded; C357A did not show any direct interaction with substrate based on the homology model, so it could be considered the last possibility. So (Q101A, N358A), (K122A, N358A), (E137A, N358A), (D138A, N358A) and (Q356A, N358A) could be the first set of double mutants to try out.

Determination of Dissociation Constant (K_d). Dissociation constant (K_d) is a more accurate parameter than K_m to examine substrate binding. Fluorescence spectroscopy was applied to try to determine the K_d. Fluorescence measurements were carried out at an excitation wavelength of 280 nm with emission monitored from 300 to 400 nm. The binding of Fe, αKG and xanthine each quenched the endogenous fluorescence of the proteins. However, the quenching by xanthine is artificial since xanthine absorbs at 268 nm which is too close to the excitation wavelength 280 nm. So the quenching observed upon adding xanthine is actually caused by fewer photons being absorbed by the protein. So finding a better to determine the dissociation constant (K_d) of xanthine would be very helpful to understand primary substrate binding mode for XanA.

Steady-State and Transient Kinetic Studies by Stopped-Flow UV-Vis spectroscopy. Stopped-flow UV-Vis spectroscopy is a powerful technique to detect intermediates forming within ms to s. The chromophores associated with XanA-Fe(II)-αKG and XanA-Fe(II)-αKG-xanthine could be examined to see if their formation is fast enough to be catalytically relevant. Next, the oxygen reactivity of XanA-Fe(II)-αKG and XanA-Fe(II)-αKG-xanthine could be examined. The Fe(IV)=O^{2-} intermediate has been observed by stopped-flow methods applied to three family members, and in each case exhibited an absorption near 318 nm by UV/Vis. We could assess whether a similar signal is formed in XanA. To enhance the chances of observing this species, one can attempt to slow down the decay reaction. Using ^2H_2O instead of H_2O may be a useful approach since XanA is known to exhibit a significant solvent isotope effect.

Alternatively, the intermediate may be longer-lived in the presence of a poor substrates, such as using 9-methylxanthine instead of xanthine. Probably the best approach is to use 8-^{2}H-xanthine instead of xanthine. Even though I did not observed any isotope effect during steady-state kinetic studies, the deuterated substrate is likely to reduce the rate of the hydrogen abstraction in the reaction and should facilitate the transient kinetic approaches. If transient absorption changes are observed with wild-type XanA, single or double mutants which are potentially important for substrate binding or enzymatic reactions also could be examined by this technique.

Resonance Raman and Mössbauer Spectroscopy. The UV-Vis spectrum provides information on electron transitions, but in order to further define the properties of the Intermediate species, more sophisticated methods need to be applied, such as resonance Roman and Mössbauer spectroscopy. For RR, typical vibrational modes of each intermediate, combining the information from modeling studies and other members of this superfamily, could help us assign each species. Mössbauer spectroscopy is very sensitive to Fe redox state and coordination, and it detects the Fe center no matter whether it is paramagnetic or diamagnetic, so it is a very powerful technique to investigate Fe-containing proteins. So, freeze-quench Mössbauer analyses may be a useful tool for further studies.

More HYSCORE Spectroscopy studies. In order to assign the non-exchangeable ^{1}H in the TauD-Fe(II)-αKG-taurine complex to certain residue, more single mutants

could be prepared, such as substitutions involving Asn95 and Arg270, which also lie within 5 Å around Fe(II) of TauD. The metal binding ligands are also possible targets to examine if incorporation of deuterated histidine and aspartate could be accomplished. The same strategy is applicable for wild-type XanA and mutants such as D138A (this residue lies within 5Å around Fe(II) of XanA), and might be the first mutant to examine. Another interesting study is to assign the strong couplings we observed at $g_{\|}$ = 2.00 (not observed at $g_{\perp} \approx 4.00$) for both TauD and XanA. It could come from NO or axial histidine ligand as shown in Figure 6.1.

Problems Application of many techniques mentioned above, such as, HYSCORE, RR, Mössbauer, even UV-Vis, require substantial amounts of concentrated (at least 0.5 mM), active and stable protein. XanA isolated from *E. coli* barely meets this requirement and only freshly prepared protein can be used. So, the further studies of the XanA enzyme mechanism will benefit from additional investigation designed to improve the protein yield and stability.

From my HYSCORE study, I found the non-exchangeable ^{1}H only appearing when the primary substrate is present. This suggests that a protein structural change is induced by adding substrate. Mutation of targeted residues could help to locate this proton; however, the mutants need to be active to confirm proper folding of the protein. That is why we could not simply mutate the metal ligands to alanine. Further mutagenesis studies will need to take this problem into account.

FIGURE 6.1: HYSCORE spectra of NO treated ternary complex TauD-Fe-αKG -taurine in 50 mM Tris-H_2O, pH = 8.0 at (A) 3400 G and (B) 1720G.

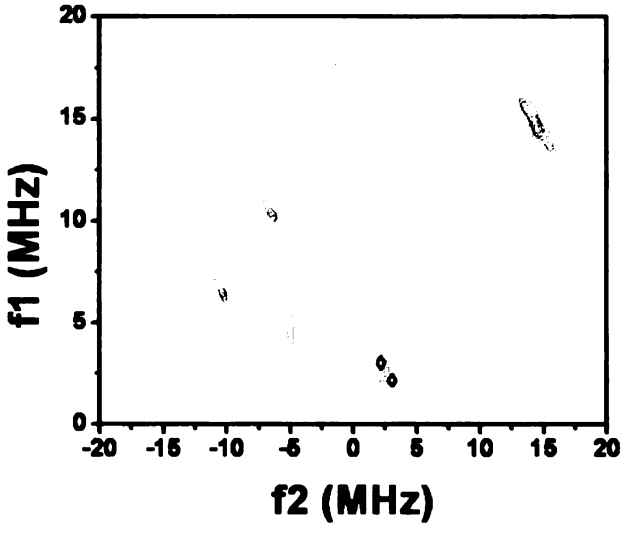

A

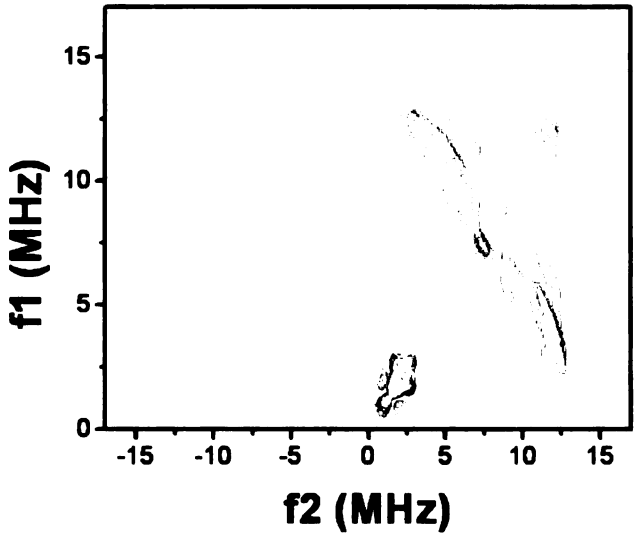

B

REFERENCES

(1) Montero-Morán, G. M., Li, M., Rendon-Huerta, E., Jourdan, F., Lowe, D. J., Stumpff-Kane, A. W., Feig, M., Scazzocchio, C., and Hausinger, R. P. (2007) Purification and characterization of the Fe(II)- and α-ketoglutarate-dependent xanthine hydroxylase from *Aspergillus nidulans*. *Biochemistry 46*, 5293-5304.

(2) Hausinger, R. P. (2004) Fe(II)/α-ketoglutarate-dependent hydroxylases and related enzymes. *Crit. Rev. Biochem. Mol. Biol. 39*, 21-68.